이학박사학위논문

Deformation microstructures and petro-fabrics of blueschist, eclogite and mantle peridotite: Implication for seismic properties in the subduction zone

청색편암, 에클로자이트, 그리고 감람암의 변형 미세구조와 암석조직: 섭입대의 지진파 비등방성에 대한 적용

2014 년 08 월

서울대학교 대학원

지구환경과학부

조 이

Deformation microstructures and petro-fabrics of blueschist, eclogite and mantle peridotite: Implications for seismic properties in the subduction zone

청색편암, 에클로자이트, 그리고 감람암의 변형 미세구조와 암석조직: 섭입대의 지진파 비등방성에 대한 적용

지도교수 **정 해 명**

이 논문을 이학박사 학위논문으로 제출함

2014 년 08 월

서울대학교 대학원

지구환경과학부

조 이

조이의 이학박사 학위논문을 인준함

2014 년 08 월

위 원 장 : 조 문 섭 (인)

부위원장 : 정 해 명 (인)

위 원 : 길 영 우 (인)

위 원 : 이 준 기 (인)

위 원 : 김 영 희 (인)

Doctoral Thesis

Deformation microstructures and petro-fabrics of blueschist, eclogite and mantle peridotite: Implications for seismic properties in the subduction zone

Yi Cao

A dissertation submitted in partial fulfillment of
the requirements for the degree of
Doctor of Philosophy

School of Earth and Environmental Sciences

Seoul National University

August 2014

ABSTRACT

Deformation microstructures and petro-fabrics of blueschist, eclogite and mantle peridotite: Implications for seismic properties in the subduction zone

Yi Cao
School of Earth and Environmental Sciences
The Graduate School
Seoul National University

The deformation microstructures, petro-fabrics and associated mineral and rock chemical compositions of natural blueschist, eclogite and peridotites which were derived from two ancient subduction zones (i.e. North Qilian orogenic belt and Qinling orogenic belt) in China were analyzed in detail with the purpose of understanding the complex geodynamic processes and their seismic implications at a subduction zone setting. The calculated seismic properties of the lithologically different and variously deformed blueschists and eclogites suggest that (1) blueschists and foliated eclogites have larger seismic anisotropies and approximately 3–12% lower velocities compared to the nearly isotropic massive eclogite and mantle peridotite, and thus can explain the gradual diminishing of low velocity upper layer and deceasing of seismic anisotropy with the depth of subduciton; (2) a moderate trench-parallel fast anisotropy can be effectively induced by deformed oceanic crust in a high-angle

(> 45–60 °) subducting slab, with a delay time in the range from 0.03–0.09 s (lower bound for massive LBS) to 0.1–0.3 s (upper bound for foliated epidote blueschist); and (3) large eclogite bodies can potentially be detected in a shallow blueschist-rich accretion wedge owing to the fairly large reflection coefficients between blueschists and eclogites (R_c = 0.04–0.20), by using the high-resolution seismic reflection experiments. In the cases of mantle peridotites, a variety of olivine fabrics (i.e. B-, C- and A-/D-type) were observed in the harzburgites and/or dunites which were believed to represent a highly refractory remnant after ~25–30% fractional melting in the fore-arc lithospheric mantle of both North Qilian and Qinling subduction zones. The presumably prevailing A-/D-type olivine fabric is supposed to weaken the trench-parallel seismic anisotropy and affect the serpentinization related seismic properties in the fore-arc mantle. By contrast, the wet C- and B-type olivine fabrics were considered to be developed at low-stress, high-temperature and high-stress, low-temperature conditions, respectively. The transition of olivine fabrics from C- to B-type might reflect a cooling process and incidental transitions of fast shear wave polarization anisotropy from trench-normal to trench-parallel directions during the subduction zone evolution and/or subsequent exhumation process. However, several ambiguities which are particularly concerned with the genetic relations between wet (B- and C-types) and dry (A- or D-type) olivine fabrics in the evolutionary fore-arc mantle are still not fully clarified in this thesis and necessitate more detailed laboratory

microstructural analysis and field structural surveys in future studies.

……

Key words: blueschist, eclogite, peridotite, plastic deformation, subduction zone, seismic properties

Student number: 2011-31268

CONTENTS

CHAPTER 1

Introduction

Subduction zones are the regions where one oceanic plate moves under another plate and sinks into the deep mantle as the plates converge (Fig. 1.1). During the subduction process, a portion of the sediments, oceanic crust and mantle lithosphere of the subducting plate would be partially melted and dehydrated/devolatilized to generate magmas and whereby contribute incidentally to the formation of continental crust, whereas the rest portion of the descending oceanic plate would be transformed and transported as residues downward to the lowermost mantle and recycled as mantle plumes (e.g., Stern, 2002, Tatsumi, 2005). This large-scale geodynamic process has been operating since the early age of the Earth, and has no doubt significant implications for many global geodynamic issues such as material recycle, crust and mantle evolution, plate tectonics, and mantle convection, which have attracted vast attentions of numerous Earth scientists for over the past few decades.

As shown in Fig. 1.1., the subduction zone typically consists of four major components: incoming plate, downgoing plate, mantle wedge and arc-trench complex. The mechanical and seismic structures in the shallow layers of incoming plate and arc-trench complex can be relatively better constrained

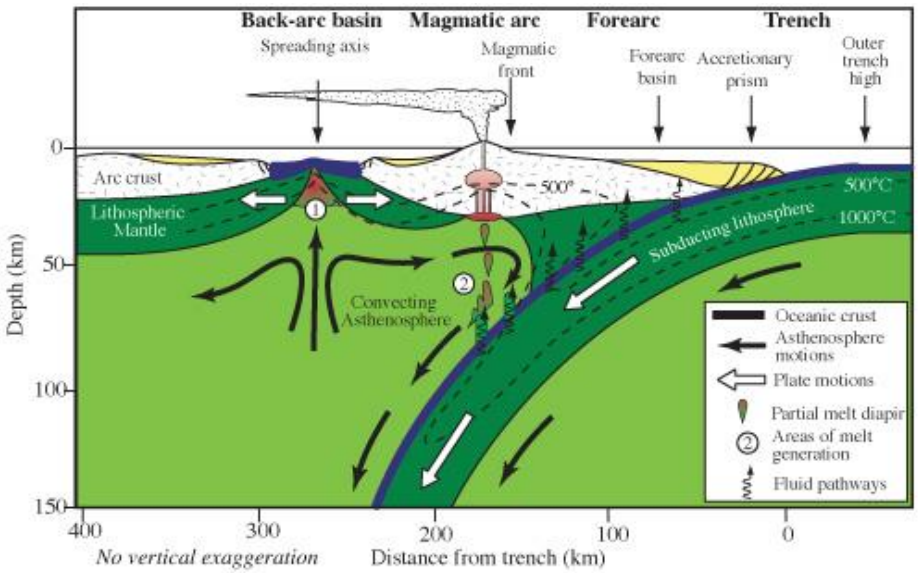

Fig. 1.1. Schematic illustration of the shallow part of subduction zone (upper 150 km, showing the principal crustal and upper mantle components and their interactions. The location of mantle wedge is conventionally referred to the part of mantle beneath the overriding plate and between the trench and the most distal part of the arc where subduction-related igneous or fluid activity is found. Adapted from "Subduction zones," by R. J. Stern, 2002, *Reviews of Geophysics* 40(4), 1-42. Copyright 2002 by the American Geophysical Union.

using high-resolution seismic reflection and/or direct core-drilling methods (e.g., Calvert, 2011, Fujie *et al.*, 2013, Horine *et al.*, 1990, MacLeod, 1994). In contrast, the rheological characteristics and seismic structures in the deeper portions of downgoing slab and mantle wedge are loosely constrained, because of the dramatic decreasing of seismic resolutions (e.g., tomography and seismic reflection) and the limited accessibilities of natural samples in the depths (e.g., Hasegawa *et al.*, 1994, Zhao, 2004, Zhao, 2012). As an alternative, the experimental and numerical simulations are thus often applied to understand the geodynamic issues that occurred in the deep subduction zone (e.g., Arcay *et al.*, 2005, Le Voci *et al.*, 2014b, Li *et al.*, 2014, MacDougall *et al.*, 2014, van Keken, 2003).

Despite the limited accessibilities, the natural samples derived from the deep mantle can provide the most direct evidence of the geological and geodynamic processes that have occurred in the history of subduction zone. In the cases of subducting slab and mantle wedge, the most commonly recovered rocks include various mantle peridotites and high-pressure metamorphic rocks (e.g., blueschist and eclogite) which occur either as xenoliths in arc magmas or high-pressure terranes in orogenic belts. The complex partial melting, melt-rock reaction, high-pressure metamorphism, and plastic deformation processes, as well as the associated seismic properties in mantle wedge and subducting slab can thus be undoubtedly revealed by investigating these deep-seated rocks. In this thesis, I will tentatively address these issues by analyzing the

deformation microstructures, petro-fabrics, mineral and whole-rock compositions of the natural blueschists, eclogites and peridotites that were originated from two ancient subduction zones in the following four chapters.

Chapter 2 will be focused on two types of high-pressure metamorphic rocks (i.e. epidote blueschist and low-temperature eclogite) from the North Qilian suture zone, NW China (e.g., Song *et al.*, 2007b, Wu *et al.*, 1993). Different deformation microstructures that ranges from weakly strained massive eclogite to intensively strained eclogites were also distinguished. The combination of lithologically and texturally different samples offer a rare chance to explore how the subducting oceanic crust changes its deformational and seismic properties (i.e. velocities and anisotropies) with the phase transformation from blueschist to eclogite during the subduction process. The calculated seismic velocities and anisotropies of blueschist and eclogite will be further discussed to evaluate their roles in affecting the trench-parallel seismic anisotropy in the fore-arc region, and to assess their implications on detecting eclogite bodies in subduction channel using seismic reflection technique.

Chapter 3 can be regarded as a complementary section to Chapter 2, in which another type of high-pressure metamorphic rock (i.e. lawsonite blueschist) from the same locality was studied. Two types of lawsonite blueschist that contain either weakly or strongly strained textures, and two subtypes of strongly strained lawsonite bluechist that exhibit either simple shear

or pure shear dominant deformation regimes were distinguished and analyzed. The comparisons of deformation microstructures and mineral fabrics between differentially deformed samples provide a valuable insight into how textures and fabrics evolve in response to increasing strain and various deformation geometries. Besides epidote blueschist, lawsonite blueschist is supposed to be another major component in the subducting oceanic crust. The combination of calculated seismic properties of the epidote and lawsonite blueschists may thus yield more precise constraints on the seismic velocity and anisotropy of an actual subducting oceanic crust.

In Chapter 4, the focus will be switched to the peridotites that are derived from the mantle wedge in the ancient North Qilian subduction zone (e.g., Song *et al.*, 2009b). The mineral compositions, water contents and mineral fabrics were measured to investigate the relations between partial melting, melt-rock reaction and plastic deformation processes that occurred in the fore-arc mantle. The mineral fabrics of harzburgites and antigoritites were later used to calculate the seismic velocities and anisotropies, and to further discuss their seismic implications on the trench-parallel polarization anisotropy and the related serpentinization process in the fore-arc mantle.

Chapter 5 will deal with the similar research scenario as Chapter 4, by focusing on different peridotite samples from Qinling orogenic belt, central China (e.g., Song *et al.*, 2005). Because the petrogenesis of these peridotites is

highly disputed in literature, I will first constrain their provenance to a fore-arc lithospheric mantle using various mineral compositions and whole-rock geochemical data. In the context of this specified geological setting, the olivine fabric data measured from texturally different samples and their geodynamic implications will be discussed. Lastly, the post-kinematic metamorphic evolutions of these peridotites will be addressed.

Notes:

Chapter 2 has been published

Cao, Y., Jung, H., Song, S. G. (2013). Petro-fabrics and seismic properties of blueschist and eclogite in the North Qilian suture zone, NW China: Implications for the low-velocity upper layer in subducting slab, trench-parallel seismic anisotropy, and eclogite detectability in the subduction zone. *Journal of Geophysical Research: Solid Earth* **118**, 3037-3058.

Chapter 3 has been published

Cao, Y., Jung, H., Song, S. (2014). Microstructures and petro-fabrics of lawsonite blueschist in the North Qilian suture zone, NW China: Implications for seismic anisotropy of subducting oceanic crust. *Tectonophysics* **628**, 140-157.

CHAPTER 2

Petro-fabrics and seismic properties of blueschist and eclogite in the North Qilian suture zone, NW China

Abstract

The potential seismological contributions of metamorphosed and deformed oceanic crust in a subduction zone environment were studied in a detailed petro-fabric analysis of blueschist and eclogite in the North Qilian suture zone, NW China. The calculated whole-rock seismic properties based on the measured lattice preferred orientations (LPOs) of the constituting minerals show increasing P-wave and S-wave velocities and decreasing seismic anisotropies from blueschist to eclogite, mainly due to the decreasing volume proportion and deformation extent of glaucophane. The low velocity of the upper layer in the subducting oceanic crust can be explained by the existence of blueschist and foliated eclogite, which induces a 3–12% reduction in velocity compared to that induced by the surrounding mantle rocks. This low-velocity layer may gradually disappear when blueschist and foliated eclogite are replaced by massive eclogite at a depth in excess of 60–75 km for the paleo North Qilian subduction zone. Trench-parallel seismic anisotropy with a moderate delay

time (0.1–0.3 s) can only effectively contribute to deformed blueschist and eclogite in a high-angle (>45–60 °) subducting slab, regardless of the direction of slab movement. The calculated reflection coefficients (R_c = 0.04–0.20) at the lithologic interfaces between eclogite and blueschist imply that it may be possible to detect eclogite bodies in shallow subduction channels using high-resolution seismic reflection profiles. However, the imaging of eclogite bodies located in deep subduction zones could be challenging.

2.1. Introduction

The transition between blueschist and eclogite is a common process that occurs in the 'cold' (high P/T thermal gradient) oceanic crust during subduction or exhumation, as indicated by the co-occurrence of eclogite and associated blueschist on the macro- or micro-scale. Rock assemblages of eclogite and blueschist in many subduction or suture zones have been reported, such as Sivrihisar Massif, Turkey (e.g., Davis & Whitney, 2006), the Motagua fault zone, Guatemala (e.g., Tsujimori *et al.*, 2006), Pam Peninsula, New Caledonia (e.g., Clarke *et al.*, 1997), Franciscan Complex, California (e.g., Maruyama & Liou, 1988), Pinchi fault zone, British Columbia (e.g., Ghent *et al.*, 1993), North Qilian, NW China (e.g., Wu *et al.*, 1993) and Tianshan, NW China (e.g., Gao *et al.*, 1999). Because the transformation of blueschist into eclogite is associated with a series of dehydration reactions, it is considered the most

important process in controlling the HP-UHP metamorphism of oceanic crust, the generation of arc-magmas, the upper plane seismicity or maximum depth of intra-slab earthquakes in the double seismic zone and the depth of low-velocity upper layers in subducting slabs (e.g., Hacker *et al.*, 2003a, Hacker *et al.*, 2003b, Hasegawa *et al.*, 1994, Kirby *et al.*, 1996, Peacock, 1993, Peacock & Hyndman, 1999, Peacock & Wang, 1999, Poli & Schmidt, 2002). Therefore, thorough investigations of these facies transition processes can shed significant light on geodynamic evolution of subduction zones.

Previous studies on seismic properties of blueschist and eclogite mainly focused on the seismic velocities and anisotropies of these rocks, and most of these investigations were concentrated on medium- and high-temperature (MT and HT) eclogites, which are simply composed of a bi-mineralic assemblage of garnet and omphacite (e.g., Abalos *et al.*, 2011, Bascou *et al.*, 2001, Christensen & Mooney, 1995, Fountain *et al.*, 1994, Fujimoto *et al.*, 2010, Kern *et al.*, 1999, Kern *et al.*, 2002, Mauler *et al.*, 2000, Rudnick & Fountain, 1995, Sun *et al.*, 2012, Wang *et al.*, 2009, Wang *et al.*, 2005a, Warner *et al.*, 1996, Zhang *et al.*, 2008); only a few recent studies focused on blueschist (Bezacier *et al.*, 2010b, Cao *et al.*, 2014, Cao *et al.*, 2013, Chantel *et al.*, 2012, Fujimoto *et al.*, 2010, Kim *et al.*, 2013a, Kim *et al.*, 2013b, Mookherjee & Bezacier, 2012). Based on these studies, some general conclusions have been reached: (1) eclogite commonly shows very high P-wave (8.0-8.6 km/s) and S-wave velocities (4.5–4.9 km/s) comparable to those of mantle peridotite (Rudnick & Fountain, 1995),

which are significantly higher than those of blueschist (V_p = 7.3–7.6 km/s) (Fujimoto *et al.*, 2010); and (2) the P-wave anisotropies of eclogite (AV_p < 3%) are generally much weaker than those of blueschist (AV_p > 10 %) (Bascou *et al.*, 2001, Fujimoto *et al.*, 2010). Even so, the seismic properties of blueschist and low-temperature (LT) eclogite in which the hydrous phases of glaucophane, epidote and lawsonite present prevalently are still poorly understood.

Seismic anisotropies, particularly polarization anisotropies, are widely observed in subduction zones (e.g., Huang *et al.*, 2011b, Long & van der Hilst, 2005, Nakajima & Hasegawa, 2004, Nakajima *et al.*, 2006, Park & Levin, 2002, Russo & Silver, 1994, Smith *et al.*, 2001), which are typically characterized by trench-parallel and trench-normal fast shear-wave polarization directions in the fore-arc and back-arc regions, respectively (Huang *et al.*, 2011b, Nakajima & Hasegawa, 2004). To explain this unique trench-parallel seismic anisotropy, many distinct mechanisms have been proposed, including mantle flow parallel to trenches associated with slab roll-back (Long & Silver, 2008, Russo & Silver, 1994), crustal foundering (Behn *et al.*, 2007) or oblique subduction (Mehl *et al.*, 2003), the water-induced B-type lattice preferred orientation (LPO) of olivine (Jung & Karato, 2001a, Jung *et al.*, 2006, Karato *et al.*, 2008, Kneller *et al.*, 2008), the LPO of serpentine (Jung, 2011, Katayama *et al.*, 2009) the pressure-induced B-type LPO of olivine (Jung *et al.*, 2009c, Ohuchi *et al.*, 2011) and anisotropy in the fore-arc crust (Huang *et al.*, 2011b). Because both blueschist and eclogite are dominating and can be strongly deformed in a ‘cold’

subducting slab, it is expected that the seismic anisotropy in subduction zones might also be affected by these rocks. However, such contributions of blueschist and eclogite to the seismic anisotropy in the fore-arc region are poorly understood. Fujimoto *et al.* (2010) recently measured the P-wave velocity and anisotropy of lawsonite and epidote blueschist at 1 GPa and room temperature (the cracks were assumed to be closed under these conditions) using the ultrasonic pulse transmission technique. They observed direction-dependent P-wave velocities showing the slowest V_p normal to the foliation (7.0–7.2 km/s) and the fastest V_p sub-parallel to the lineation (7.4–7.6 and 7.9 km/s for lawsonite and epidote blueschist, respectively), resulting in a P-wave anisotropy of 4.0% in lawsonite blueschist and 8.9–10.7% in epidote blueschist. Bezacier *et al.* (2010b) calculated the seismic anisotropy of blueschist and glaucophane-bearing eclogite based on the LPO of major constituent minerals. Their results also show that blueschist presents much stronger anisotropies (AV_p = 16.1%, max. AVs = 10.3%) than eclogite (AV_p = 2.9%, max. AVs = 1.7%) and exhibits the fastest and slowest P-waves parallel to the lineation and perpendicular to the foliation, respectively. These data thus imply that shear-wave splitting with a delay time (approximately 0.16 s) can be produced by a 7 km thick blueschistic oceanic crust.

The previous studies mentioned above suggest that seismic anisotropy in 'cold' subduction zones can be potentially affected by blueschist and eclogite. To understand the petrology and seismic properties of blueschist and LT

eclogite in subducting slabs, we measured the chemical compositions and LPOs of major constituent minerals from natural blueschists and eclogites in the North Qilian suture zone, NW China. Herein, we discuss their implications for the depth of the low-velocity upper layer of the associated subducting oceanic crust and the seismic anisotropy and seismic detectability of eclogite in the corresponding subduction zone.

2.2. Geological setting

The North Qilian suture zone is a NW-SE trending orogenic belt between the Alashan Block to the north and the Qilian-Qaidam Block to the south in the NW part of China (Fig. 2.1a). Many pieces of petrological, geochemical and geochronological evidence have suggested that this orogenic belt represents a typical oceanic-type subduction zone of the early Paleozoic (see Song *et al.* (2009a) for a review). This suture zone is composed of early Paleozoic subduction zone complexes, including ophiolite suits, high-pressure (HP) metamorphic belts, island-arc volcanic rocks and granitic plutons, Silurian flysch formations, Devonian molasses and Carboniferous to Triassic sedimentary cover sequences (e.g., Song *et al.*, 2013a, Song *et al.*, 2009a, Song *et al.*, 2007b). Two sub-belts are further identified within the HP metamorphic belts (Wu *et al.*, 1993): (1) a low-grade blueschist slice characterized by a typical mineral assemblage of lawsonite (Lws) + glaucophane (Gln) +

pumpellyite (Pmp) + albite (Ab) + chlorite (Chl) ± aragonite (Arg) ± epidote (Ep) (lawsonite-blueschist) in the north (Zhang *et al.*, 2009) and (2) three high-grade blueschist slices A, B and C, with a typical assemblage of Gln + Ep + phengite (Ph) ± garnet (Grt) (epidote-blueschist) enclosing massive blocks of lawsonite-bearing eclogite in the south (Song *et al.*, 2007b, Zhang & Meng, 2006, Zhang *et al.*, 2007). The mineral abbreviations above were adopted from Whitney and Evans (2010).

As shown in Fig. 2.1b, high-grade blueschist slices A, B and C trend NW-SE and stretch sub-parallel to each other, intruding into island-arc volcanic complexes. In the flanks of each slice, blueschist is strongly retrograded into greenschist. The eclogite occurs as massive blocks measuring tens to hundreds of square meters in size, surrounded by blueschist, meta-greywacke, meta-pelite, marble and meta-chert (Song *et al.*, 2007b). Based on mineral assemblage, North Qilian eclogite can be divided into two categories: (1) phengite-eclogite, with a peak-stage mineral assemblage of Grt + omphacite (Omp) + Ph + rutile (Rt) + quartz (Qtz) ± Gln ± Ep, showing protoliths geochemically similar to ocean island basalt (OIB) or enrich-type mid-ocean ridge basalt (E-type MORB) (classifications and descriptions of MORB are referred to Sun *et al.* (1979) and Tarney *et al.* (1980)), and (2) epidote-eclogite, with a mineral assemblage of Grt + Omp + Ep + Gln + Rt + Qtz, primarily corresponding to normal-type (N-type) MORB (Song *et al.*, 2009a, Song *et al.*, 2006). Lawsonite occurs as inclusions in garnet in both types of eclogite (Song

et al., 2007b, Zhang & Meng, 2006, Zhang *et al.*, 2007). According to field appearance and microstructure, these eclogites can be sub-divided into massive and foliated eclogite (Cao *et al.*, 2011, Song *et al.*, 2007b). Massive and foliated eclogites mostly occur as isolated blocks within mafic or felsic blueschist matrix. In addition, many massive eclogite bodies also contain various retrograde and foliated overprintings due to heterogeneous deformation.

Using a Grt-clinopyroxene (Cpx)-Phn thermobarometer (Ravna & Terry, 2004) and phase equilibrium diagram (Powell *et al.*, 1998), the peak P-T conditions of massive eclogite were determined to be 2.10–2.65 GPa and 460–590 ℃ within the lawsonite stability field (Cao *et al.*, 2011, Song *et al.*, 2007b, Wei *et al.*, 2009, Zhang *et al.*, 2007), which are consistent with the recognition of lawsonite as an inclusion in the garnet of eclogite (Song *et al.*, 2007b, Zhang & Meng, 2006, Zhang *et al.*, 2007). Along with lawsonite blueschist outcropped in low-grade blueschist slices to the north (Wu *et al.*, 1993, Zhang *et al.*, 2009), the oceanic crust was inferred to have experienced a metamorphic transition from lawsonite blueschist to lawsonite eclogite during subduction. This notion is also supported by the growth history of garnet (occurring in the stability field of lawsonite) in massive eclogite determined using phase equilibria modeling in the NCKFMASHO system (Wei *et al.*, 2009). In contrast, foliated eclogite (epidote eclogite) is most likely the retrograded and deformed product of massive eclogite during decompression, as evidenced by the transition in

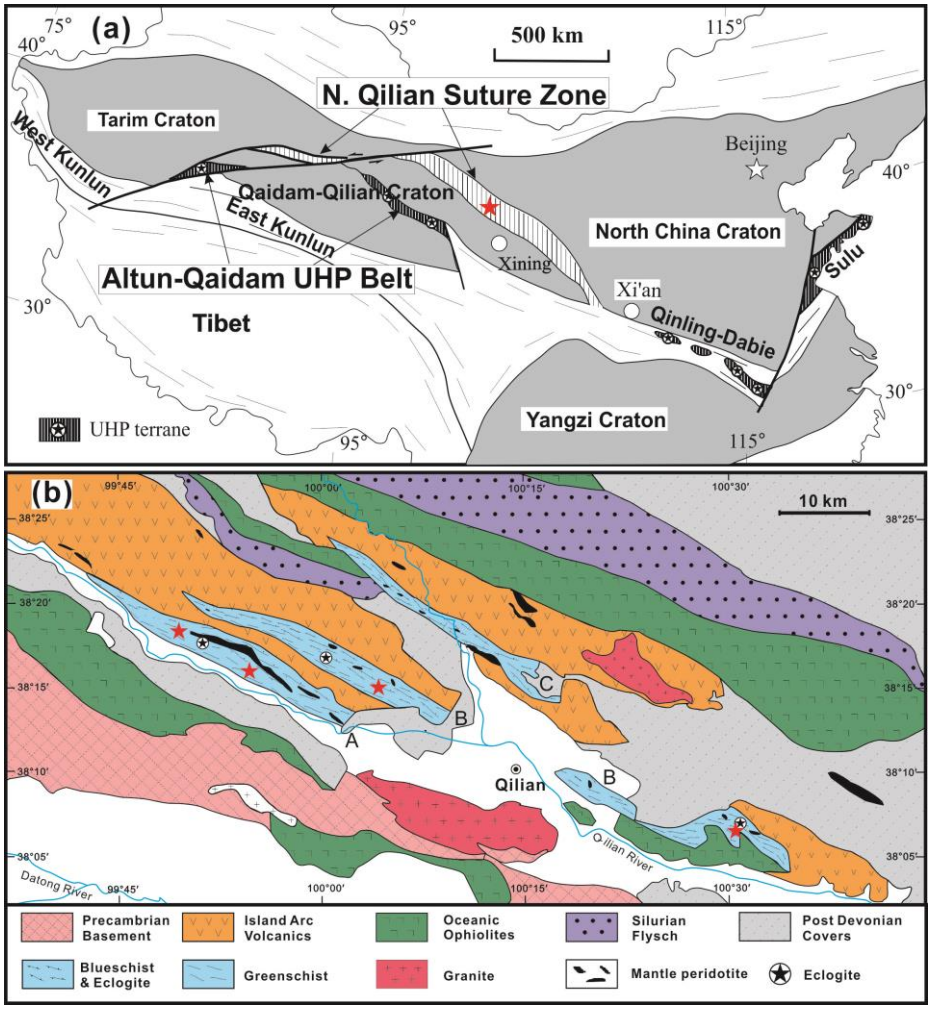

Fig. 2.1. (a) Geological map showing the major tectonic units of China. Red star represents the study area. (b) Magnified geological map of the study area shown as red star in Fig. 2.1a, the central part of North Qilian suture zone. Red stars denote the sample localities in this study. Modified after Song *et al*., (2006, 2009).

texture, variations in mineral composition and decreasing P-T conditions (1.8-2.2 GPa and 450-480 ℃) (Cao *et al.*, 2011, Song *et al.*, 2007b). The eclogite-facies meta-pelite (with or without Mg-carpholite) shows similar P-T results, 2.1–2.6 GPa and 470–540 ℃, comparable to those of massive eclogite (Song *et al.*, 2007b, Wei & Song, 2008); this confirms that the North Qilian metamorphic belt is the result of 'cold' oceanic-type subduction ('cold' subduction generally indicates a subducting thermal gradient less than 8 ℃/km).

The petro-genesis of epidote blueschist is ambiguous due to insufficient textural observations of these facies transitions: Epidote blueschist can be either retrograded from epidote eclogite or transformed from lawsonite blueschist. Although the transition from lawsonite blueschist to epidote blueschist was clearly observed in the low-grade blueschist slices of the Qilian region (Zhang *et al.*, 2009), it is not assured that this process also occurred in the high-grade blueschist slices. Moreover, no lines of textural evidence are available to confirm whether epidote blueschist is derived from greenschist. Because the outcrops of epidote eclogite are much smaller in scale than those of the blueschist slices, epidote blueschist retrograded from epidote eclogite may only make up a small portion of the epidote blueschist. Hence, we consider that most of the exposed epidote blueschists in the high-grade blueschist slice originated from shallower depths without transforming into eclogite before exhumation.

The uplift age of high-grade epidote-blueschist and the peak eclogitic metamorphism age of eclogite have been well reported. The Ar-Ar ages of

glaucophane and phengite (462–448 Ma) from epidote-blueschist are consistently younger than the eclogitic zircon ages (489–464 Ma) obtained from SHRIMP U-Pb dating (Liou *et al.*, 1989, Liu *et al.*, 2006, Song *et al.*, 2004b, Song *et al.*, 2006, Wu *et al.*, 1993, Zhang *et al.*, 2007, Zhang *et al.*, 1997), clearly indicating a progressive evolution from early subduction to later exhumation.

2.3. Petrography

2.3.1. Blueschist

All of the blueschist and eclogite samples were collected from the three high-grade blueschist slices (Fig. 2.1b and Table 2.1). The felsic blueschist is characterized by a mineral assemblage of Gln + Qtz + Ep + Ph + Grt + sphene (Spn) (Fig. 2.2a), which is associated with a meta-greywacke origin. The mafic blueschist consists of an assemblage of Gln + Ep + Spn ± Ph ± Grt (Fig. 2.2c-d), indicating protoliths similar to those of oceanic basalt or gabbro. The volume proportion of garnet is very low, except for one sample (QL-68) in which the garnet fraction is approximately 10 vol.%, evenly distributed throughout the matrix (Fig. 2.2d). All samples are strongly deformed, as indicated by extremely elongated and aligned crystals of glaucophane, epidote or phengite. The grain size of glaucophane and epidote vary from 100 to 1000 μm in length and from 200 to 500 μm in length, respectively.

Table 2.1. Results of studied blueschist and eclogite.

Sample	Rock type	Density (g/cm^3)	Mineral volume fraction (%)[a]								Bulk M-index	V_p[b] (km/s)	V_s[b] (km/s)	Poisson's ratio	AVp (%)	Max. AVs (%)
			Gln	Ep	Omp	Grt	Ms	Qtz	Rt	Spn						
QL-47	Felsic blueschist	2.97	44	16	-	+	10	30	-	+	0.15	6.91 ±0.5	4.20 ±0.2	0.21	15.1	11.14
QL-53	Mafic blueschist	3.24	50	50	-	+	+	+	-	+	0.12	7.56 ±0.5	4.39 ±0.1	0.25	13.6	8.39
QL-68		3.16	90	+	-	10	+	+	-	+	0.08	7.89 ±0.5	4.60 ±0.1	0.24	13.4	6.77
QL-73		3.09	95	5	-	-	+	+	-	+	0.18	7.68 ±0.5	4.51 ±0.2	0.24	24.6	14.66
QL-40	Foliated eclogite	3.34	30	30	30	10	+	+	+	+	0.12	7.92 ±0.3	4.53 ±0.1	0.26	6.7	4.57
QL-74		3.20	65	5	25	5	+	+	+	+	0.08	7.83 ±0.4	4.59 ±0.1	0.24	9.6	5.12
08BSY-30		3.29	45	40	7	8	+	+	+	-	0.14	7.73 ±0.4	4.45 ±0.1	0.25	10.2	8.09
08BSY-38		3.40	20	20	43	17	+	+	+	-	0.13	8.04 ±0.2	4.60 ±0.1	0.26	5.4	3.66
QL-33	Porphyroclastic eclogite	3.46	+	10	70	20	+	+	+	-	0.12	8.23 ±0.1	4.70 ±0.03	0.26	2.5	1.72
Q05-1	Massive eclogite	3.49	5	3	65	27	+	+	+	-	0.04	8.28 ±0.1	4.74 ±0.02	0.26	1.4	1.03

[a] The errors of mineral volume fraction are less than 10% for a fairly homogeneous sample.

[b] V_p and V_s calculated at ambient conditions.

Mineral abbreviation: glaucophane (Gln), epidote (Ep), omphacite (Omp), garnet (Grt), muscovite (Ms), quartz (Qtz), rutile (Rt), and sphene (Spn).

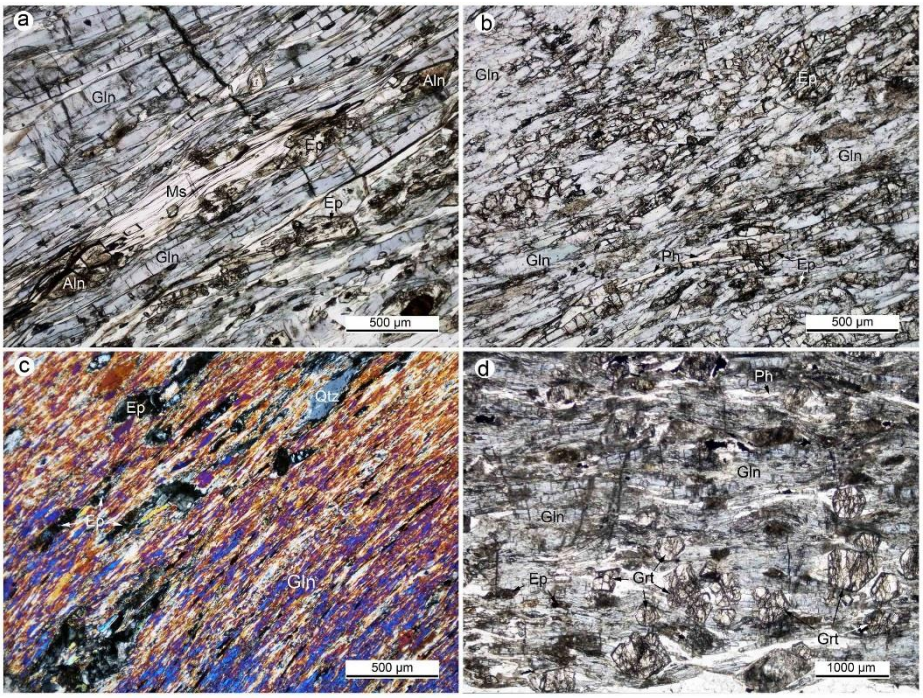

Fig. 2.2. Photomicrographs showing strongly foliated high-grade blueschists. (a) Felsic blueschist (QL-47). (b, c) Garnet-poor mafic blueschist (QL-53 and QL-73). Grain-size and volume content of Gln is finer and higher in (c) (QL-73). (d) Garnet-rich mafic blueschist (QL-68).

2.3.2. Eclogite

The petrography of both massive and foliated eclogite has been described in part by Cao *et al.* (2011). The massive eclogite is weakly deformed and shows a nearly random-oriented peak metamorphic assemblage of Grt + Omp + Ph + Rt ± Lws (inclusion in Grt) (Fig. 2.3a). Intra-crystal plastic micro-structures (e.g., undulatory extinctions, sub-grains) are frequently observed in omphacite, suggesting that dislocation creep is the dominant deformation mechanism in massive eclogite. However, in some domains, the massive eclogite is overprinted by fine-grained and retrograded aggregates of Gln + Ep (Cao *et al.*, 2011). The foliated eclogites are more strongly deformed than the massive ones. They exhibit well-defined foliation and are composed of a fine-grained mineral assemblage of Omp + Ep + Gln + Ph + Rt, which surrounds idioblastic to weakly elongated garnet (Figs. 2.3e,f). Significant variations in chemical composition were found in Grt, Omp and Ep between massive and foliated eclogite, represented by a decreasing CaO content in garnet and an increasing Fe^{2+} or Fe^{3+} content in omphacite and epidote (Cao *et al.*, 2011). Diffusive mass transfer (DMT) with concomitant anisotropic growth assisted by fluids was considered to be responsible for the deformation of the foliated eclogite. Consequently, the foliated eclogite was thought to be retrograded and deformed from its massive counterpart during exhumation. In this study, we discerned another eclogite with porphyroclastic texture. This type of eclogite is characterized by two distinct domains of coarse-grained Omp grains and a

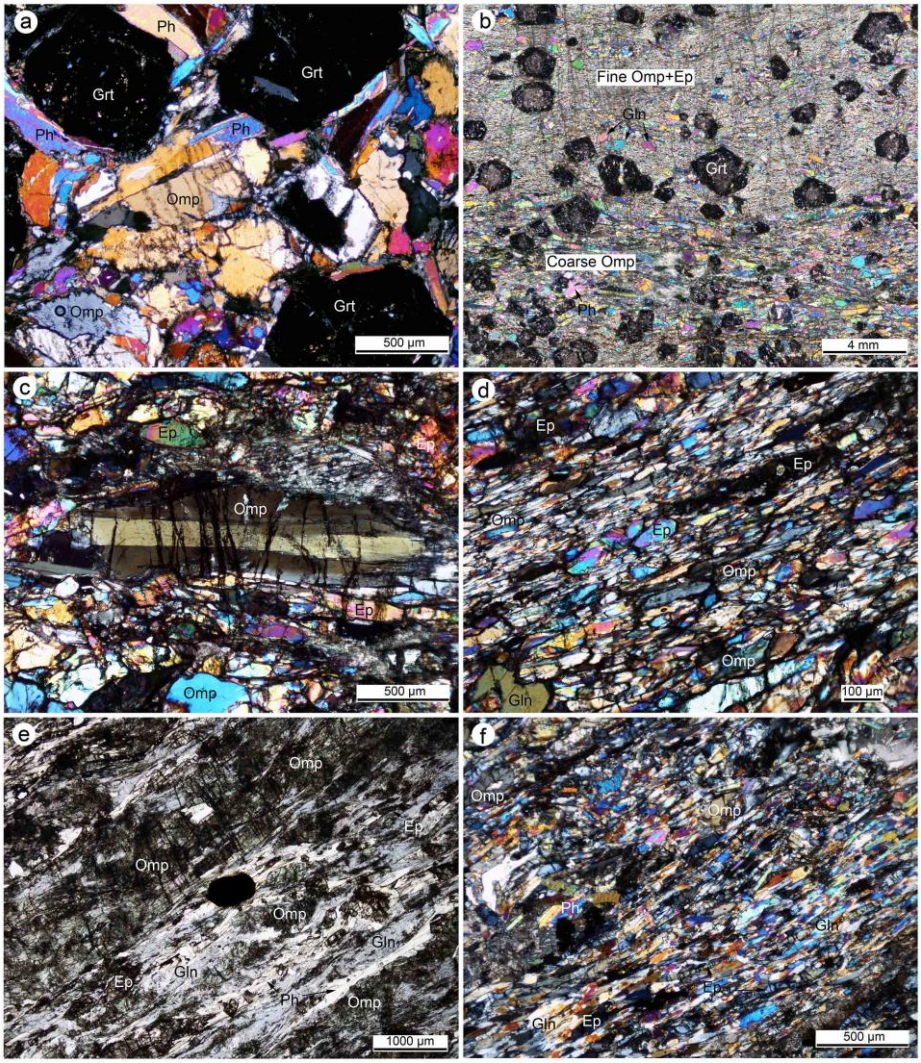

Fig. 2.3. Photomicrographs showing three texturally different eclogites. (a) Massive eclogite displaying coarse-grained and poly-granular texture (Q05-1). (b) Porphyroclastic eclogite is strongly deformed, exhibiting oriented coarse-grained Omp domain and fine-grained Omp+Ep domain with sharp boundary (QL-33). (c) Elongated coarse Omp grain showing tilt boundary parallel to foliation in coarse-grained Omp domain of (b). (d) Fine-grained Omp+Ep crystals form well-defined foliation in (b). (e, f) Foliated eclogite. (e) Mineral inter-bands of Omp and Gln (QL-74), implying similar rheological strength between Omp and Gln. Ep grains commonly occur in the Gln-rich band. (f) Remarkable foliation defined by fine-grained Omp+Gln+Ep aggregates (QL-40).

fine-grained or recrystallized assemblage of Omp + Ep + Ph + Rt in the specimen. Both of these domains are strongly deformed and display coherent foliations, which are crosscut by large and euhedral glaucophance crystals (Figs. 2.3b-d).

2.4. Mineral chemical compositions and P-T estimations

Chemical composition analyses of sodic-amphibole and epidote in blueschist and eclogite were conducted using an electron probe micro-analyzer (EPMA) JXA-8900R at National Center for Inter-University Research Facilities (NCIRF) of SNU, Seoul, Korea. The system was running under the following conditions: 15 kV accelerating voltage, 1 nA current and 1–5 μm beam size. Additional chemical compositions of major constituting minerals in eclogite are detailed by Cao *et al.* (2011).

As shown in Fig. 2.4a, all sodic-amphiboles belong to glaucophane, except for some located in the crossite field in foliated eclogite. A negative trend between X_{Mg} [Mg/(Mg+Fe^{2+})] and Y_{Fe} [Fe^{3+}/(Fe^{3+}+Al)] is observed. There is no difference in the Y_{Fe} in Gln between eclogite and blueschist, whereas the X_{Mg} in Gln is remarkably higher in eclogite (approximately 0.7–0.9) than blueschist (approximately 0.6–0.8), without significant variations between massive and foliated eclogite or mafic and felsic blueschist.

The Ps value [Fe^{3+}/(Fe^{3+}+Al)] of epidote varies over a large range (0.10–

0.22) in foliated eclogite and mafic blueschist and is low (0.10–0.18) and high (0.22–0.24) in massive eclogite and felsic blueschist, respectively (Fig. 2.4b). Ps value is used to indicate the mole fraction of the pistacite component in epidote, which ranges from pure clinozoisite (Ps_{00}) to Ps_{33} (Deer *et al.*, 1966).

Based on mineral assemblages, volume proportion and composition between blueschist and eclogite, a potential reaction consuming glaucophane and epidote to produce garnet and omphacite is inferred to take place during the eclogitization of blueschist:

$$Gln^1 + Ep^1 = Grt + Omp + Gln^2 + Ep^2 + H_2O$$

The reverse reaction indicates blueschist overprinting over eclogite during exhumation.

As suggested by X_{Mg} in glaucophane and the Ps value in epidote, an increasing P-T condition from blueschist to eclogite is implied. The approximate P-T conditions for eclogite and blueschist are estimated using the Grt-Omp-Ph (-Ky) geothermobarometry from Ravna and Terry (2004) and the average P-T calculation mode of THERMOCALC 3.33 (Powell *et al.*, 1998) with the updated database of Holland and Powell (1998). The activities of mineral end-members are calculated using AX 2.0 (details of AX program can be obtained from Tim Holland's web page https://www.esc.cam.ac.uk/research/research-groups/holland/ax), assuming unit activity for H_2O, quartz and albite. A coexisting eclogitic mineral assemblage of Grt + Omp + Ph is used in the geothermobarometry, whereas in

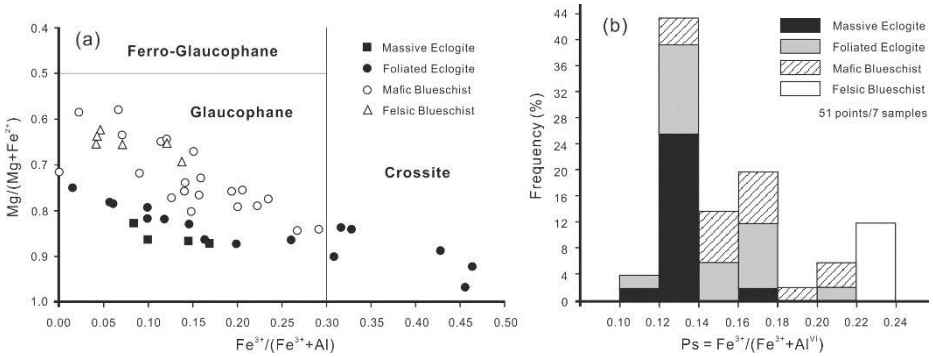

Fig. 2.4. Diagrams showing the variations in composition of sodic-amphiboles (a) and epidotes (b) in blueschist and eclogite.

the average P-T estimation mode, typical mineral assemblages of Grt + Omp + Gln + Ep + Ph + Qtz and Grt + Gln + Ep + Ph + Ab + Qtz are applied for eclogite and blueschist, respectively. As shown in Table 2.2, eclogite exhibits distinctively higher pressure results (1.8–2.1 ± 0.3 GPa, 1σ confidence interval) than those of blueschist (0.5–1.4 ± 0.6 GPa, 1σ confidence interval), which are similar to the results obtained from Grt-Omp-Ph geothermobarometry (P = 1.7–2.6 GPa, integrated with previously reported data). The massive eclogite presents the highest pressure conditions (P = 2.1–2.6 GPa). A large temperature difference exists between two P-T estimation methods, as characterized by much lower temperature results for eclogite when Grt-Omp-Ph geothermobarometry is applied (T = 342–480 ℃). Using the average P-T calculation mode, the temperature is better constrained for eclogite (521–582 ± 54 ℃, 1σ confidence interval) than blueschist (481–625 ± 102 ℃, 1σ confidence interval). Overall, these P-T results are consistent with those of previous studies for eclogite (Cao *et al.*, 2011, Song *et al.*, 2007b, Wei *et al.*, 2009) and blueschist (Li, 2010).

2.5. Lattice preferred orientations

Thin-sections of XZ plane (foliation-normal and lineation-parallel) were made and polished under 1 μm diamond paste and SYTON (0.06 μm colloidal silica) fluid, to remove all the surface damage. The specimens were later lightly

Table 2.2. P-T results of eclogites and blueschist estimated using Grt-Omp-Ph (-Ky) geothermobarometry of Ravna & Terry (2004) and Thermocalc 3.33 of Powell *et al.* (1998) and their corresponding P-wave velocities.

Sample	Lithology	Grt-Omp-Ph geothermobarometry		V_p[a] (km/s)	Average P-T conditions by Thermocalc 3.33				V_p[b] (km/s)	sd (V_p)[b] (km/s)
		P (kbar)	T (℃)		P (kbar)	sd (P)	T (℃)	sd (T)		
08BSY-30		16.6	342	7.93	17.7	3.8	527	65	7.88	0.05
QL-40	Foliated eclogite	18.8	411	8.14	18.7	3.3	534	56	8.09	0.04
QL-74		19.1	428	8.05	18.7	4.1	521	72	8.00	0.05
QL-33	Fine grains in Porphyroclastic eclogite	19.0	419	8.45	18.3	3.1	554	47	8.38	0.04
Q05-1	Massive eclogite	23.0[c]	480[c]	8.54	20.6[d]	1.9[d]	582[d]	32[d]	8.45	0.02
QL-53					13.7	6.6	625	111	7.49	0.09
QL-68	Mafic				7.0	5.4	491	104	7.73	0.18
Q7-53[e]	blueschist				7.8	6.3	536	113		
Q7-60[e]					5.2	4.3	481	79		

[a] Average V_p calculated using P-T results from Grt-Omp-Ph geothermobarometry.

[b] Average V_p calculated using P-T results from Average P-T condition by Thermocalc 3.33, standard deviation (sd).

[c] Data from Cao *et al.* (2011).

[d] Data from Wei *et al.* (2009).

[e]Recalculated using mineral chemical composition data from Li (2010).

coated with ~3 nm carbon layer to prevent charging in the SEM. Afterwards, the LPO of minerals were manually acquired in these thin-sections using the HKL electron back-scattered diffraction (EBSD) system attached to a JEOL-6380 SEM at SEES in SNU, Korea. The working parameters for EBSD measurement were a 20 kV acceleration voltage, 15 mm working distance and spot size of 60, with 70 °specimen tilt. The SEM was operated in high vacuum. To avoid repeated data collection, grains showing different Kikuchi patterns (or electron back-scattered patterns, EBSPs) from their neighbors were manually selected for EBSD pattern acquisition and indexing. The indexing of a collected EBSP from a mineral grain was completed by searching for an optimal match between the observed EBSP and simulated ones with all possible orientations. The crystal structures used for simulating EBSPs are from *American Mineralogist Crystal Structure Database*. This indexing process can be conveniently done by using HKL Channel 5.0 software.

2.5.1. LPO of glaucophane

Glaucophane in most blueschists presents a typical fabric type (point-type or SL-type), which is characterized by having its [001] axes parallel to lineation and its [100] axes and (110) pole normal to the foliation, while having its [010] axes align sub-perpendicular to lineation in the foliation (Figs. 2.5a,b). This type of glaucophane fabric is well consistent with the findings of most previous studies on natural blueschists (Bezacier *et al.*, 2010b, Fujimoto *et al.*, 2010, Kim *et al.*, 2013a, Kim *et al.*, 2013b, Teyssier *et al.*, 2010), as well as other

species of amphibole in natural amphibolites (Cao *et al.*, 2010, Tatham *et al.*, 2008). In contrast, a different type of glaucophane LPO (girdle-type or L-type) is observed in garnet-rich blueschist and eclogite (Figs. 2.5c,d), with its [100] and [010] axes and (110) pole forming a girdle nearly normal to lineation and the maximum of its [001] axes still aligning parallel to lineation.

To quantify the strength of LPOs, we calculated the misorientation index (M-index) (Skemer *et al.*, 2005). M-index is defined by $M = \frac{1}{2}\int \left| R^T(\theta) - R^0(\theta) \right| d\theta$. It describes the difference between the observed distribution of uncorrelated misorientation angles $R^0(\theta)$ (obtained from EBSD data) and distribution of uncorrelated misorientation angles $R^T(\theta)$ for a theoretically random fabric. The range of M-index is from 0 (random fabric) to 1 (single crystal fabric).

The fabric strength of glaucophane is significantly higher for the SL-type (M = 0.13–0.24) than for the L-type (M = 0.06–0.14), in which the massive eclogite (Q05-1) showed the lowest fabric strength (M = 0.06). Hence, the differences in fabric type and strength in glaucophane between garnet-poor blueschist and garnet-rich blueschist or eclogite are most likely due to the LPO randomization effect of garnet, whereas the lower fabric strength of glaucophane in massive rather than foliated or porphyroclastic eclogite is credited to the weaker extent of deformation in massive eclogite. Although strong glaucophane LPOs indicate that dislocation creep may be the principal

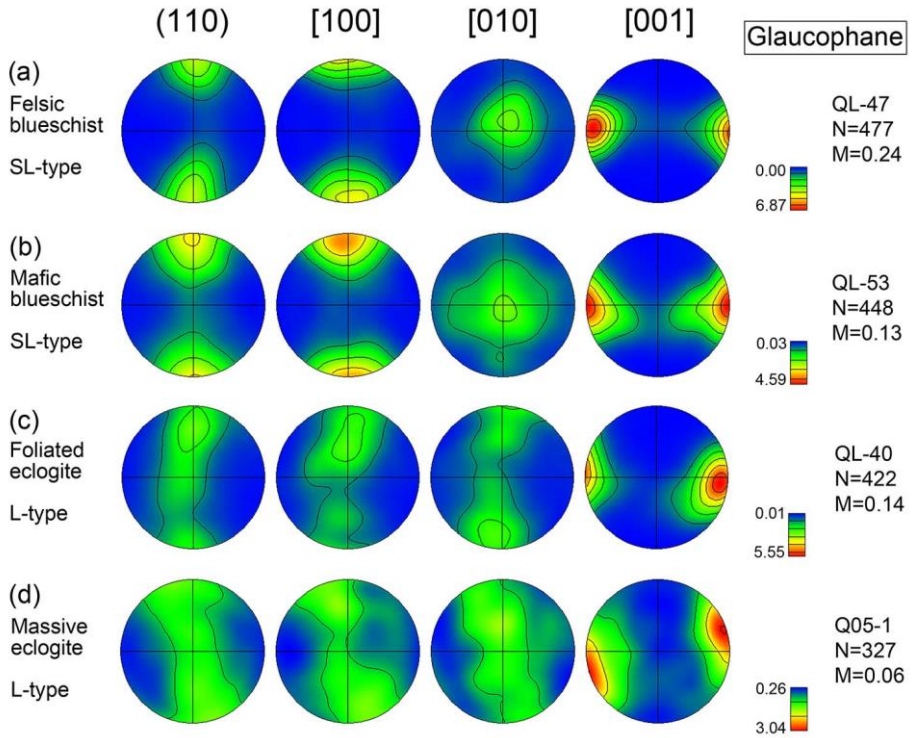

Fig. 2.5. LPO of glaucophane in representative blueschist (a, b) and eclogite (c, d). Pole figures are shown in upper hemisphere and equal-area projection, with a half-width of 30 ° and cluster size of 5 °. E-W and N-S directions denote lineation and foliation normal, respectively. N is number of grains; M is M-index of LPO.

deformation mechanism, as suggested by many TEM observations in which [001](100), [001]{hk0}, [100](010) and 1/2<110>{110} are the dominant slip systems in naturally and experimentally deformed amphiboles (Biermann, 1981, Biermann & Vanroermund, 1983, Morrison-Smith, 1976, Reynard *et al.*, 1989, Skrotzki, 1992), the lack of features indicating intra-crystal plasticity (e.g., undulatory extinctions, kink bands) and frequent chemical zonation patterns in glaucophane indicate that diffusive mass transfer (DMT) creep assisted by fluids might also be important for accommodating the deformation of glaucophane.

2.5.2. LPO of epidote

The LPO of epidote in blueschist and eclogite showed a [010] axis that has a strong maximum aligning sub-parallel to lineation, with a weak girdle parallel to foliation. The maximum of the [001] axes is concentrated normal to foliation with or without a girdle normal to lineation, and the [100] axes commonly forms a girdle normal to lineation with its maximum in the foliation plane (Fig. 2.6). Both the [010] and [001] axes display higher maximum densities than those of the [100] axes and (110) pole. Based on the distribution of the [001] axes, epidote fabric can be sub-divided into [001] point-type (SL-type, Figs. 2.6a,c,d) and [001] girdle-type (L-type, Fig. 2.6b). The fabric strength of epidote is higher in blueschist and foliated or porphyroclastic eclogite (M = 0.10-0.24) than in massive eclogite (M = 0.06).

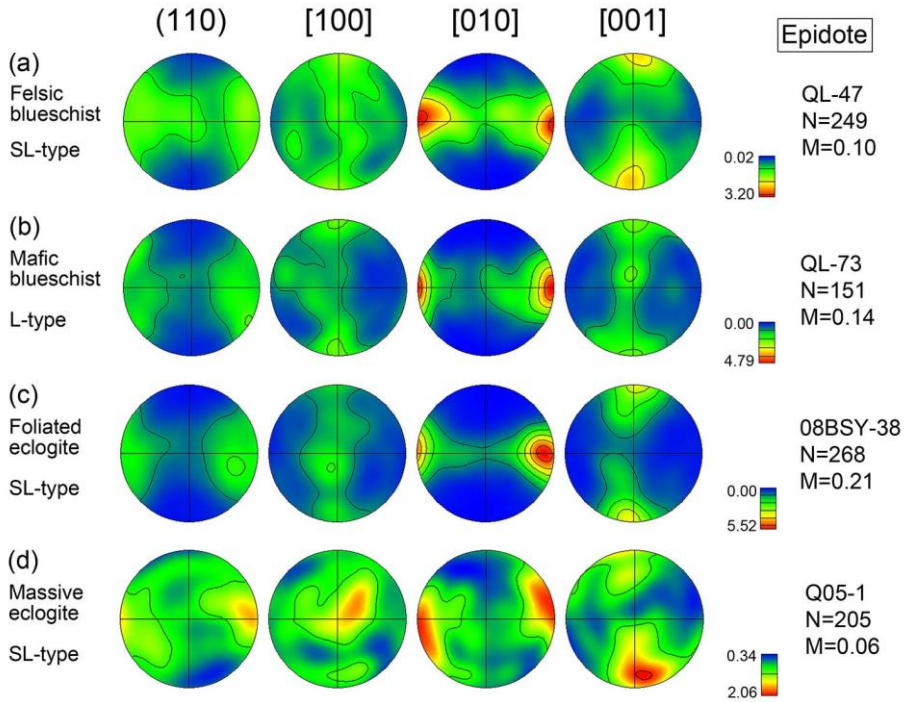

Fig. 2.6. LPO of epidote in representative blueschist (a, b) and eclogite (c, d). Pole figures are shown in upper hemisphere and equal-area projection, with a half-width of 30 ° and cluster size of 5 °. E-W and N-S directions denote lineation and foliation normal, respectively. N is the number of grains, and M is the M-index of LPO.

2.5.3. LPO of omphacite

The LPOs of omphacite in porphyroclastic and foliated eclogites are shown in Fig. 2.7. Omphacite presents a consistent fabric type (SL-type) among all samples, represented by a [001] axes concentrated parallel to lineation with a girdle in foliation, a [010] axes aligning normal to foliation, and a [100] axes aligning sub-perpendicular to lineation within foliation. The M-index varies in the range of 0.06-0.16 and is the lowest for massive eclogite, suggesting the weakest degree of deformation. The increase in fabric strength with enhanced deformation is also clearly confirmed by the M-index between coarse-grained (M = 0.11) and fine-grained omphacite (M = 0.16) in the porphyroclastic eclogite (Figs. 2.7b,c).

2.5.4. LPO of garnet

The LPO of garnet in garnet-rich blueschist and eclogite were examined. Because garnet crystals are large in size (1–5 mm), only a limited number of grains were measured in thin sections. As shown in Figs. 2.8a and b, the fabric of garnet is nearly random in all samples, suggesting that garnet most likely rotates as a rigid block in the matrix under deformation.

2.5.5. LPO of phengite and quartz

The fabric of phengite and quartz were only measured in felsic blueschist (Figs. 2.8c,d). The LPO of phengite is characterized by a strong maximum of the [001] axes normal to the foliation, with the [100] axes, [010] axes and (110)

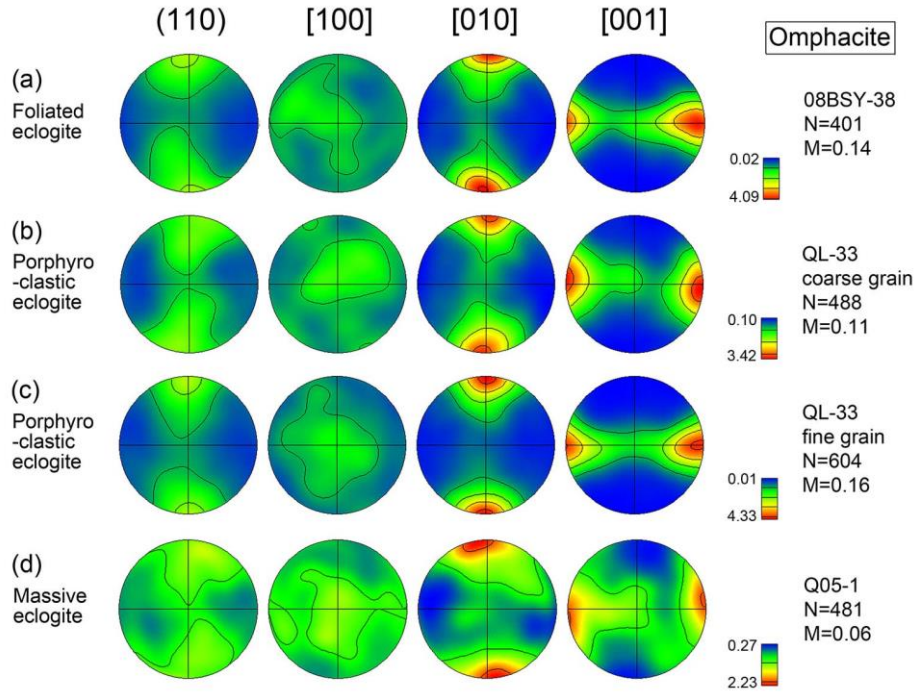

Fig. 2.7. LPO of omphacite in representative eclogite. All samples show SL-type fabric. Pole figures are shown in upper hemisphere and equal-area projection, with a half-width of 30 ° and cluster size of 5 °. E-W and N-S directions denote lineation and foliation normal, respectively. N is the number of grains, and M is the M-index of LPO. (a) and (d) are from Cao *et al.* (2011).

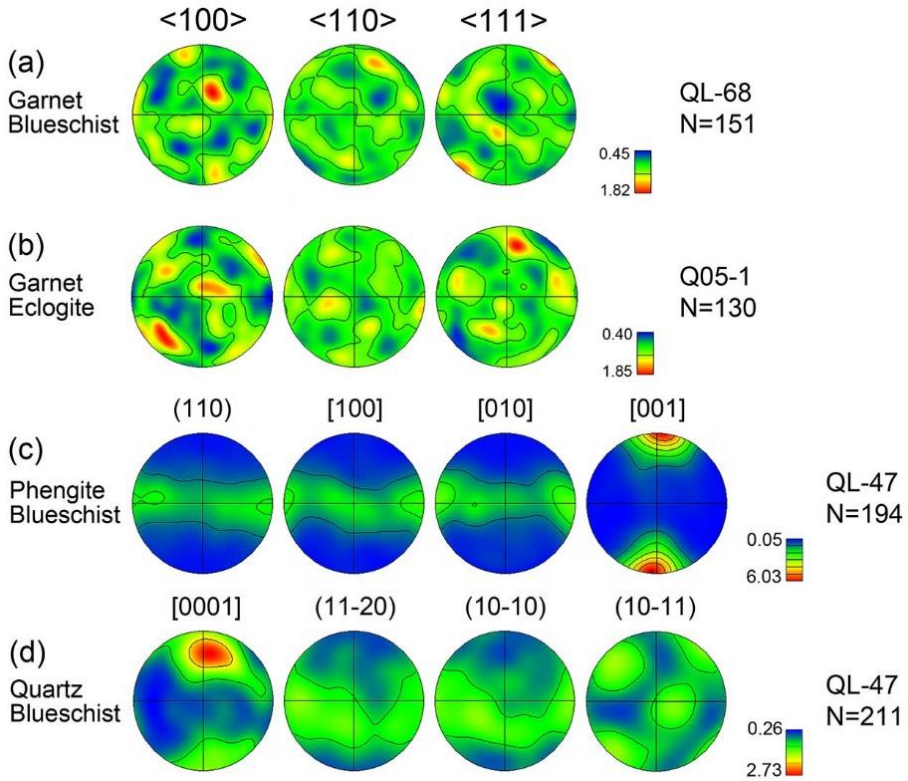

Fig. 2.8. LPO of garnet, phengite and quartz in blueschist and eclogite. Pole figures are shown in upper hemisphere and equal-area projection, with cluster size of 5 °and half-widths of 20 °for garnet and 30 °for phengite and quartz. E-W and N-S directions denote lineation and foliation normal, respectively. N is the number of grains. (a) Garnet-rich blueschist; (b) massive eclogite; (c and d) felsic blueschist.

pole distributing in a girdle parallel to foliation and their weak maxima aligning parallel to lineation. Quartz shows a *c*-axes normal to foliation, with the $(11\bar{2}0)$ and $(10\bar{1}0)$ poles forming a girdle parallel to foliation (Fig. 2.8d).

2.6. Rock seismic properties

The rock seismic properties of blueschist and eclogite were calculated based on the single-crystal elastic constants, crystal density, LPOs and volume proportions of major constituent minerals using the Voigt-Reuss-Hill (VRH) averaging scheme and David Mainprice's petro-physical software (Mainprice, 1990). Specifically speaking, the seismic velocities and anisotropies of a multimineralic rock are estimated by solving the Christoffel equation. To solve this equation, the macroscopic elastic tensor $<C_{ij}>$ and density of rock are required. The macroscopic elastic tensor can be calculated by integration of elastic stiffnesses of all mineral grains (C_{ij}) over all orientations assuming an averaging method (e.g., Vogit, Reuss, Hill or Geometric). The orientation of a single crystal is manifested as triplet of Euler angle which can be obtained from EBSD measurements, and bulk density of a rock is averaged from densities and volume proportions of major constituent minerals. The average V_p and V_s were calculated as $\left(V_{p\max}+V_{p\min}\right)/2$ and $\left(V_{s1\max}+V_{s1\min}+V_{s2\max}+V_{s2\min}\right)/4$, respectively ($V_{s1\max}$ and $V_{s1\min}$ are the maximum and minimum velocity of fast shear wave over all directions. Likewise, $V_{s2\max}$ and $V_{s2\min}$ are the maximum and

minimum velocity of slow shear wave over all directions).

Volume proportions of minerals in a normalized mineral assemblage of Gln + Ep ± Grt ± Ms ± Qtz and Omp + Ep + Grt ± Gln were used in the calculation of the seismic properties of blueschist and eclogite, respectively (Table 2.1). For a better estimation of the seismic properties of porphyroclastic eclogite, the coarse and fine grained omphacite were treated separately. We used the elastic stiffnesses from Bezacier *et al.* (2010b) for glaucophane, Ryzhova *et al.* (1966) for epidote, Vaughan and Guggenheim (1986) for phengite, and McSkimin *et al.* (1965) for quartz. To obtain the appropriate single-crystal elastic properties for omphacite ($Di_{0.5}$,$Jd_{0.4}$,$Ae_{0.1}$) and garnet ($Grs_{0.25}$,$Pyr_{0.20}$,$(Alm,Spss)_{0.55}$ in eclogite) ($Grs_{0.35}$,$Pyr_{0.05}$,$(Alm,Spss)_{0.60}$ in blueschist), an average of the elastic stiffness of the end-members was used, assuming that the elastic stiffnesses C_{ij} were linearly related to the molar fraction of constituent end-members (Collins & Brown, 1998, Zhang *et al.*, 2008). The elastic constants for end-members of omphacite and garnet were from Aleksandrov *et al.* (1964), Bass (1989), Kandelin and Weidner (1988), Levien *et al.* (1979), O'Neill *et al.* (1991), Wang and Simmons (1974). The calculated single-crystal elasticity of omphacite was similar to that reported by Bhagat *et al.* (1992).

Besides, seismic properties of each monomineralic aggregate with a given texture were also calculated to compare with the seismic properties of multimineralic rocks they constitute. This exercise could clarify the role of each monomineralic aggregate and different texture (LPO) in contributing to the

seismic properties of a multimineralic rock.

2.6.1. Glaucophane polycrystals

As shown in Fig. 2.9, the glaucophanes of SL- and L-type fabrics show similar patterns of P-wave anisotropy and polarization anisotropy. The P-wave velocity is maximum sub-parallel to the lineation and minimum normal to the foliation. The strong and weak polarization anisotropies are mostly aligned at low and high angles to the foliation, respectively. The direction of fast shear-wave polarization is aligned sub-parallel to the lineation when the shear-wave propagates normal to the foliation, whereas fast shear-wave polarization is nearly parallel to foliation when the incident ray is at a low angle to foliation. As for the glaucophane aggregates exhibiting SL-type LPO, the P-wave anisotropy (AV_p) is in the range of 21–26% and the maximum polarization anisotropy (max. AV_s) ranges from 11% to 16%. The seismic anisotropy patterns of glaucophane showing SL-type fabric are similar to those showing L-type fabric, where the latter presents a lower magnitude of anisotropy (AV_p = 8–15%, max. AV_s = 5–8%), with the lowest value in the massive eclogite.

2.6.2. Epidote polycrystals

The seismic anisotropy patterns of epidote are similar to those of glaucophane, with the fastest and slowest P-wave velocities parallel to lineation and normal to foliation, respectively. The magnitude of S-wave polarization anisotropy (AVs) is low in the direction sub-normal to the foliation. The fast

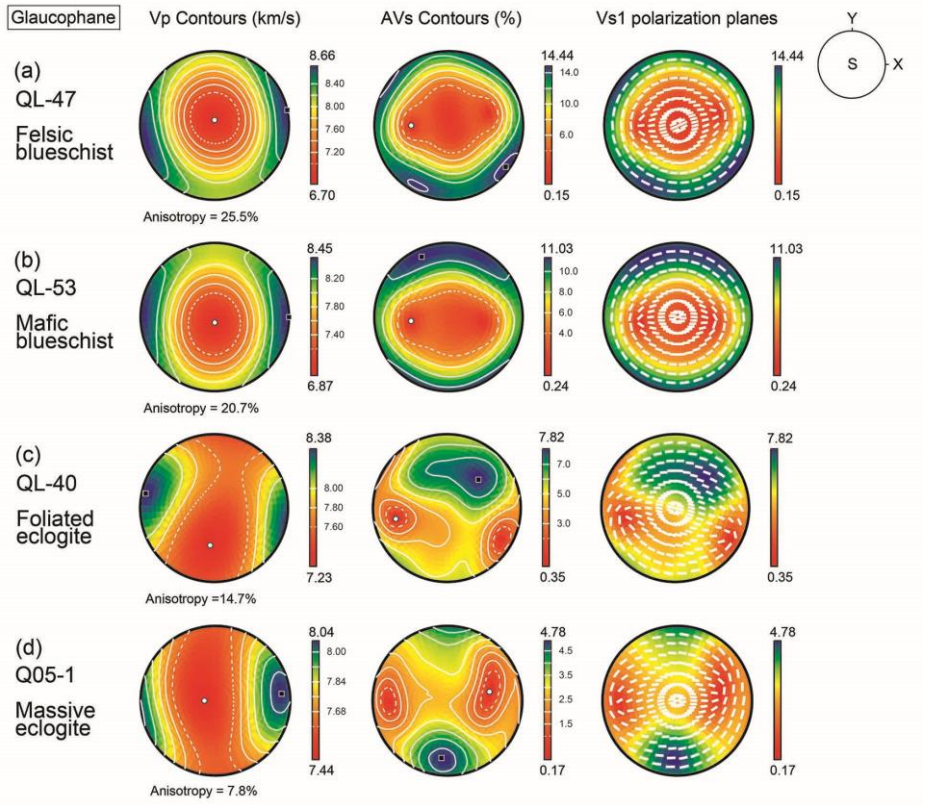

Fig. 2.9. Seismic anisotropy of glaucophane aggregate in representative blueschist (a and b) and eclogite (c and d). Data are presented on the foliation plane (XY) with equal-area and upper hemisphere projection. The reference frame of X and Y is as shown in the figure.

shear wave polarizes sub-parallel to foliation when the incidence angle of the shear wave is low relative to foliation, whereas the polarization direction of the fast S-wave has a tendency to align sub-normal to the lineation when the shear wave propagates normal to foliation (Fig. 2.10). The seismic anisotropies of epidote aggregates vary from 4% to 11% for P-waves and from 4% to 12% for maximum polarization anisotropy, which are lower than those of SL-type glaucophane. Moreover, epidote in massive eclogite shows the lowest seismic anisotropies.

2.6.3. Omphacite polycrystals

The patterns of P-wave anisotropy in omphacite aggregate resemble those of glaucophane and epidote, which show the fastest and slowest P-wave velocities parallel to the lineation and normal to the foliation, respectively (Fig. 2.11). These results are consistent with those of most previous calculations and laboratory observations of deformed eclogites [*Abalos et al.*, 2011; *Bascou et al.*, 2001; *Mauler et al.*, 2000; *Zhang et al.*, 2008]. The patterns of S-wave polarization anisotropy (AV_s) are more complicated, and the polarization direction of the fast shear wave is mostly sub-parallel to lineation for a foliation-normal incident seismic ray, except for the sample 08BSY-38. However, the magnitudes of the P-wave and shear wave polarization anisotropies of omphacite (AV_p and max. AV_s = 1.3–3.2%) are much smaller than those of glaucophane and epidote. The average velocities of P-waves and shear waves are higher than those of glaucophane and epidote aggregates.

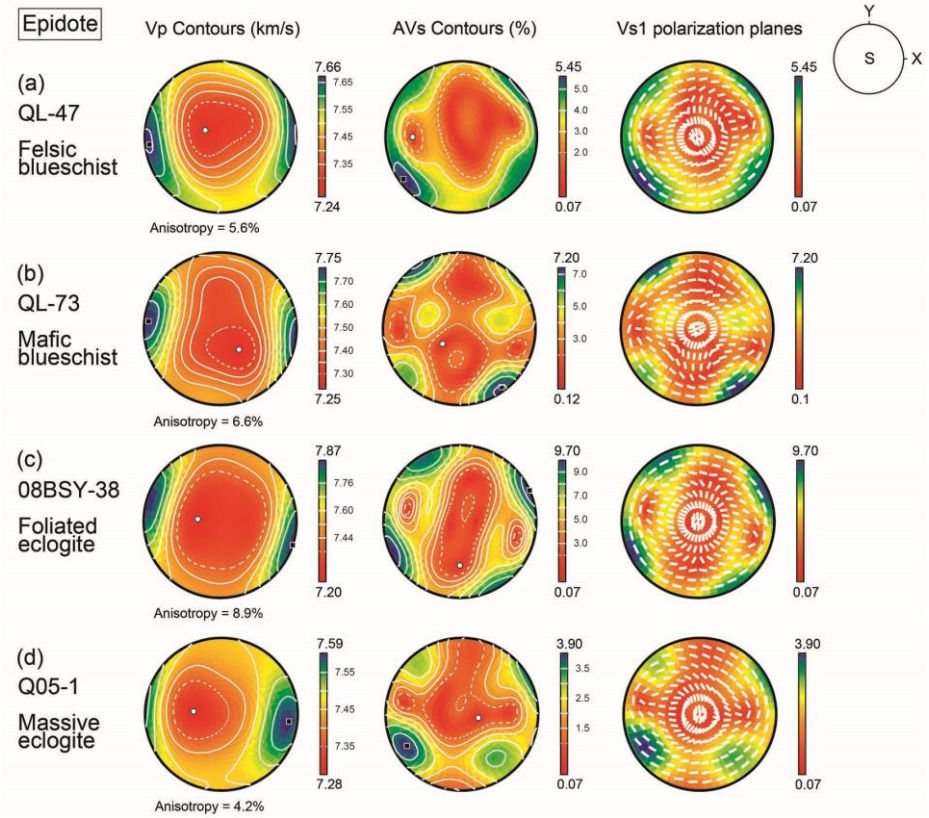

Fig. 2.10. Seismic anisotropy of epidote aggregate in representative blueschist (a and b) and eclogites (c and d). Data are presented on foliation plane (XY) with equal-area and upper hemisphere projection. The reference frame of X and Y is as shown in the figure.

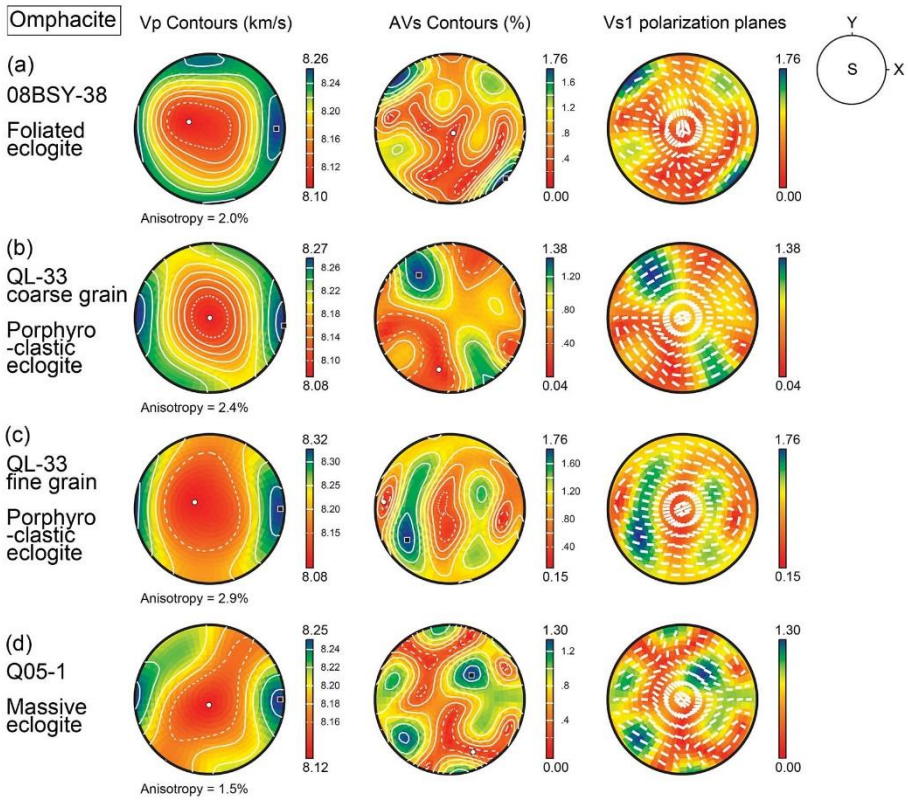

Fig. 2.11. Seismic anisotropy of omphacite aggregate in three representative texturally different eclogite type. (a) Foliated eclogite; (b and c) porphyroclastic eclogite; (d) massive eclogite. Data are presented on the foliation plane (XY) with equal-area and upper hemisphere projection. The reference frame of X and Y is as shown in the figure.

2.6.4. Garnet, phengite and quartz polycrystals

The garnets in both garnet-rich blueschist and eclogite exhibit a quasi-isotropic pattern of seismic anisotropy (AV_p = 0.1%, AV_s = 0.1–0.3%), mainly due to their nearly random fabrics and weak single crystal anisotropy of garnet per se. The P-wave velocity of garnet aggregates is approximately 8.80 km/s, with only subtle differences between garnet-rich blueschist and eclogite. It has the highest velocities among all blueschistic and eclogitic minerals (Figs. 2.12a,b). Phengite aggregate is seismically very anisotropic, with similar anisotropic patterns to those of glaucophane, epidote and omphacite, which show the fastest and slowest P-wave velocities parallel to lineation and normal to foliation (AV_p = 37%), respectively. The S-wave polarization anisotropy is also significantly parallel to foliation and becomes weaker towards the normal to foliation (AV_s = 32%). The fast-shear wave polarizes sub-normal to the lineation for vertical propagation along foliation, whereas it tends to polarize sub-parallel to foliation when the shear-wave propagates at high angles relative to the foliation normal (Fig. 2.12c). The seismic anisotropies are distinct in quartz aggregate (Fig. 2.12d). This aggregate shows the fastest V_p aligned sub-normal to foliation and the slowest V_p sub-parallel to foliation, which yields a P-wave anisotropy of 6%. The pattern of polarization anisotropy is complex and characterized by polarization directions in which the fast shear wave is aligned sub-normal to lineation when the S-waves propagate sub-normal to foliation.

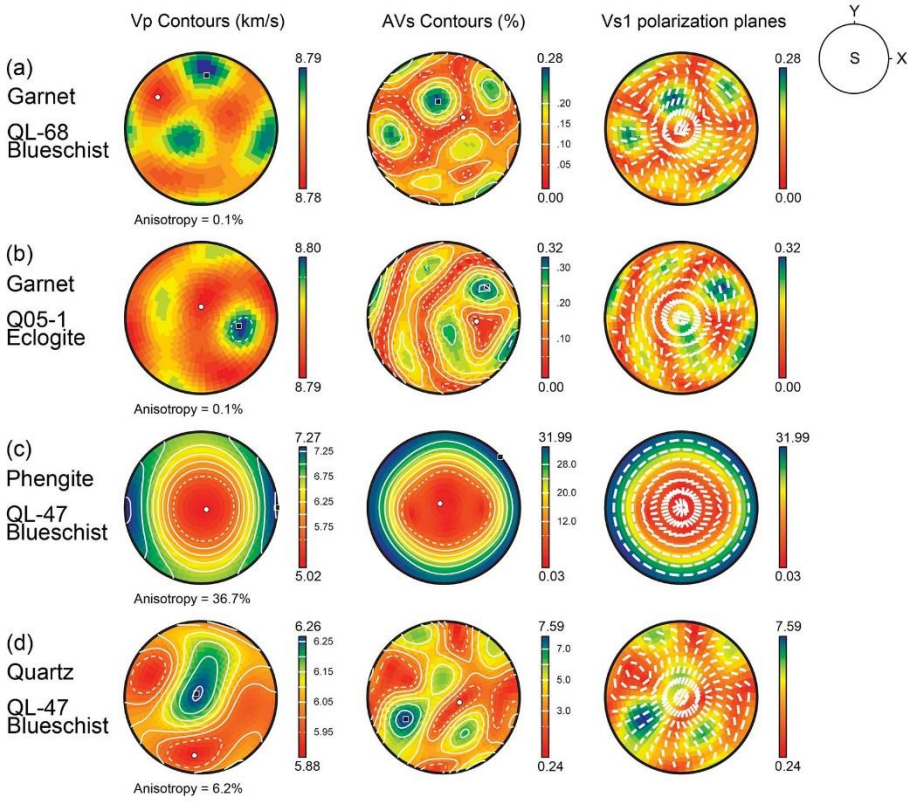

Fig. 2.12. Seismic anisotropy of garnet aggregate in blueschist (a) and eclogite (b); as well as phengite (e) and quartz (f) aggregate in felsic blueschist. Data are presented on the foliation plane (XY) with equal-area and upper hemisphere projection. The reference frame of X and Y is as shown in the figure.

2.6.5. Whole-rock

As observed in Fig. 2.13, the P-wave velocity is the fastest in the direction parallel to lineation and decreases to a minimum toward the normal to foliation in blueschists and eclogites. The magnitude of polarization anisotropy is high in the direction sub-parallel to the foliation and decreases gradually along the normal to the foliation. The polarization direction of the fast shear wave is mostly sub-parallel to the lineation in the direction nearly normal to foliation, and it becomes foliation-parallel when the incidence angle of the shear wave becomes low to foliation. The AV_p and maximum AV_s for blueschist are in the range of 13–25% and 7–15%, respectively. The massive and porphyroclastic eclogites show lower AV_p (1.4% and 2.5%) and max. AV_s (1.1% and 1.7%) than those of the foliated ones (AV_p = 5–10%, max. AV_s = 3.7–8.1%) (Figs. 2.13 and 2.14a). An overall positive correlation between bulk seismic anisotropies and bulk M-index are observed in the whole rock (Fig. 2.14a), in which the fabric strength (Bulk M-index) of the whole rock is averaged based on the M-index of the LPO and volume contents of each constituent mineral.

Owing to high volume percentage and high seismic anisotropies of glaucophane aggregate in blueschist, the anisotropic pattern of blueschist resembles to that of glaucophane aggregate. Because omphacite, glaucophane, epidote and phengite show similar patterns of P-wave anisotropy but less similar patterns of polarization anisotropy (Figs. 2.9-2.12), the bulk seismic anisotropy of P-waves can also be averaged from the seismic anisotropies of

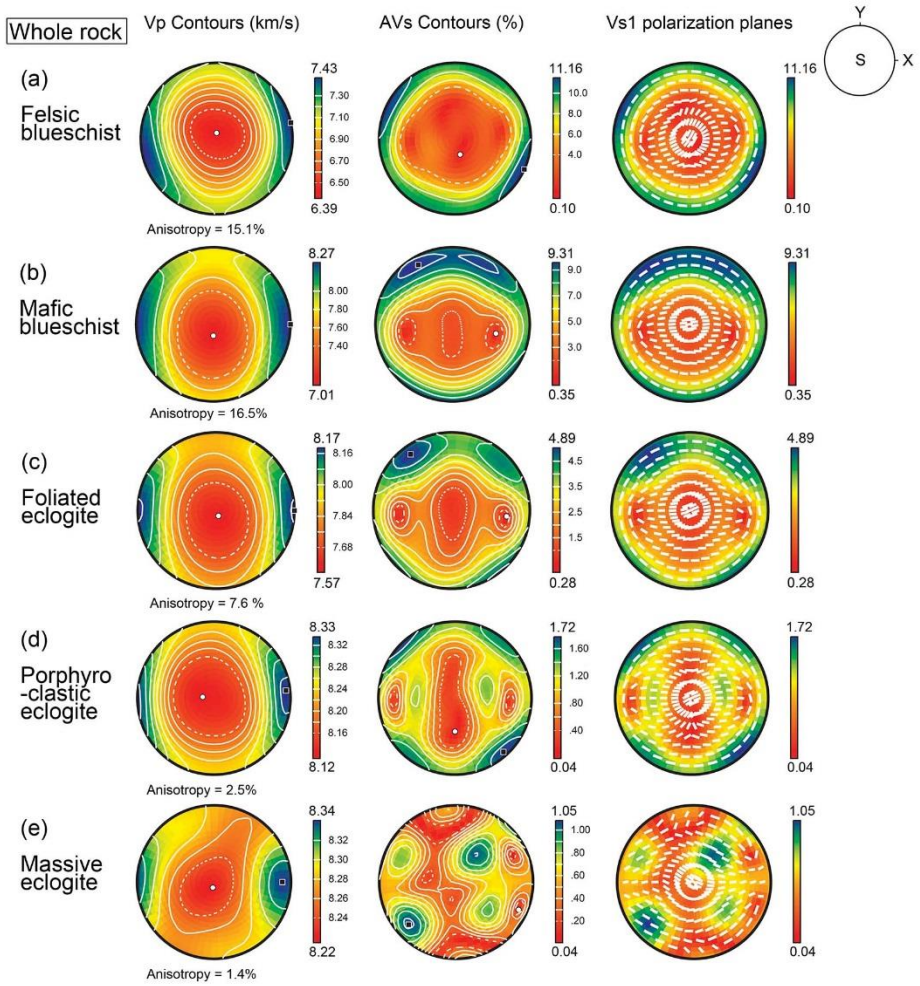

Fig. 2.13. Seismic anisotropy of blueschist (a and b) and eclogite (c and d). (b) is averaged seismic anisotropy of mafic blueschists. (c) is averaged seismic anisotropy of foliated eclogites. Data are presented on the foliation plane (XY) with equal-area and upper hemisphere projection. The reference frame of X and Y is as shown in the figure.

each constituent mineral assemblage weighted by its volume contents. However, quartz displays opposite seismic anisotropy patterns (in particular P-wave anisotropy) to those of Gln, Ep and Phn in felsic blueschist (Fig. 2.12d). We thus take account of the cancellation effects of quartz using a negative volume content of quartz in this averaging method. The bulk seismic anisotropies obtained from this averaging method are overall equal to but slightly higher than those conventionally calculated using LPOs and the volume proportions of constituent minerals, as observed from the plotted data, which lie somewhat above the dividing line (slope, k = 1), excluding those for the felsic blueschist. These subtle discrepancies are most likely caused by small differences in the seismic anisotropy patterns, which are ignored in the averaging method. In addition, the P-wave anisotropy shows relatively better internal correlation (R^2 = 0.99) and consistency (k = 0.96) than the shear wave splitting anisotropy (R^2 = 0.94, k = 0.89) (Fig. 2.14c). This result can be explained by the more consistent patterns of P-wave anisotropy among different minerals, compared to those of polarization anisotropy.

These results also suggest that the contributions of each of the different mineral aggregates towards the overall anisotropy can be quantitatively estimated by multiplying the magnitude of seismic anisotropy and volume proportion of each monomineralic assemblages (Table 2.3). Because of large seismic anisotropy features and high volume proportions of glaucophane aggregate in blueschists and foliated eclogite, glacuophane aggregate makes the

Table 2.3. Contributions of different mineral assemblages to the bulk seismic anisotropies.

Sample	Rock type	Gln (%)		Ep (%)		Omp (%)		Grt (%)		Ms (%)		Qtz (%)	
		AVp	AVs_{max}	AVp	AVs_{max}	AVp	AVs_{max}	AVp	AVs_{max}	AVp	AVs_{max}	AVp	AVs_{max}
QL-47	Felsic blueschist	81	78	6	11					26	39	-13	-28
QL-53	Mafic blueschist	75	63	25	37								
QL-68		100	100					0	0				
QL-73		99	98	1	2								
QL-40	Foliated eclogite	61	46	29	45	10	8	0	0				
QL-74		94	87	3	5	3	7	0	0				
08BSY-30		57	43	41	55	2	2	0	0				
08BSY-38		54	36	31	46	15	18	0	1				
QL-33	Porphyroclastic eclogite			29	45	71	54	1	1				
Q05-1	Massive eclogite	26	19	8	9	64	66	2	7				

greatest contribution of bulk seismic anisotropies. In contrast, lack of glauophane in massive and porphyroclastic eclogites leads omphacite aggregate to dominate the overall seismic anisotropies. The role of epidote aggregate is diverse and dependent on their relative volume proportions in the rocks, and garnet aggregate has almost negligible contributions in the bulk seismic anisotropies. As a whole, the degrees of seismic anisotropy of different mineral aggregates and whole rocks follow in the order Gln > Bulk > Ep > Omp > Grt, suggesting that the high seismic anisotropies of whole rocks are primarily controlled by glaucophane aggregate (Fig. 2.14b).

The P-wave and S-wave velocities at ambient conditions are the lowest and highest in the felsic blueschist (V_p = 6.91 ± 0.52 km/s; V_s = 4.20 ± 0.17 km/s) and porphyroclastic or massive eclogite (V_p = 8.23–8.28 ± 0.11 km/s; V_s = 4.70–4.74 ± 0.03 km/s), respectively. However, there are no significant differences in V_p or V_s within the azimuthal anisotropies between mafic blueschists (V_p = 7.56–7.89 ± 0.54 km/s; V_s = 4.39–4.60 ± 0.24 km/s) and foliated eclogite (V_p = 7.73–8.04 ± 0.40 km/s; V_s = 4.45–4.60 ± 0.13 km/s). The calculated P-wave velocities of mafic blueschist are close to those of epidote blueschist (7.2–7.9 km/s) experimentally measured at 1 GPa and room temperature (Fujimoto *et al.*, 2010). The massive and porphyroclastic eclogites show lower calculated V_p (8.2–8.3 km/s) than those of fresh rutile eclogite at 500–600 MPa and room temperature (~ 8.5 km/s from Sun *et al.* (2012); Wang *et al.* (2009); 8.3–8.4 km/s from Abalos *et al.* (2011)). This is probably due to higher glaucophane

and epidote volume proportions in our studied massive and porphyroclastic eclogites than those fresh eclogites. In contrast, the calculated V_p of foliated eclogites are close to those of retrograded eclogites measured at 500–600 MPa and room temperature (7.0–7.9 km/s) (Abalos *et al.*, 2011, Sun *et al.*, 2012, Wang *et al.*, 2009). The calculated S-wave velocities of massive and porphyroclastic eclogites vary within the range of those of measured fresh eclogites (4.7–4.9 km/s), whereas, foliated eclogites show slightly higher S-wave velocities than those measured retrograde eclogites (4.0–4.3 km/s) (Abalos *et al.*, 2011, Sun *et al.*, 2012, Wang *et al.*, 2005a). The mean Poisson's ratios are in the range of 0.23–0.26 in mafic blueschists and eclogites, which are higher than the ratio of felsic blueschist (approximately 0.21) and similar to the laboratory-measured ratio of mafic HP metamorphic rocks (Kern *et al.*, 1999) (Fig. 2.14d).

2.7. Discussions

2.7.1. Low velocity upper layer in subducting slab

When epidote blueschist transitions to epidote eclogite with the increasing depth of subducting oceanic crust, the hydrous minerals Gln + Ep could be progressively dehydrated to form the anhydrous phases of Grt + Omp. As shown in the V_p-V_s diagram, because the average P-wave and S-wave velocities in Gln and Ep are lower than those in Grt and Omp, the mafic blueschist and

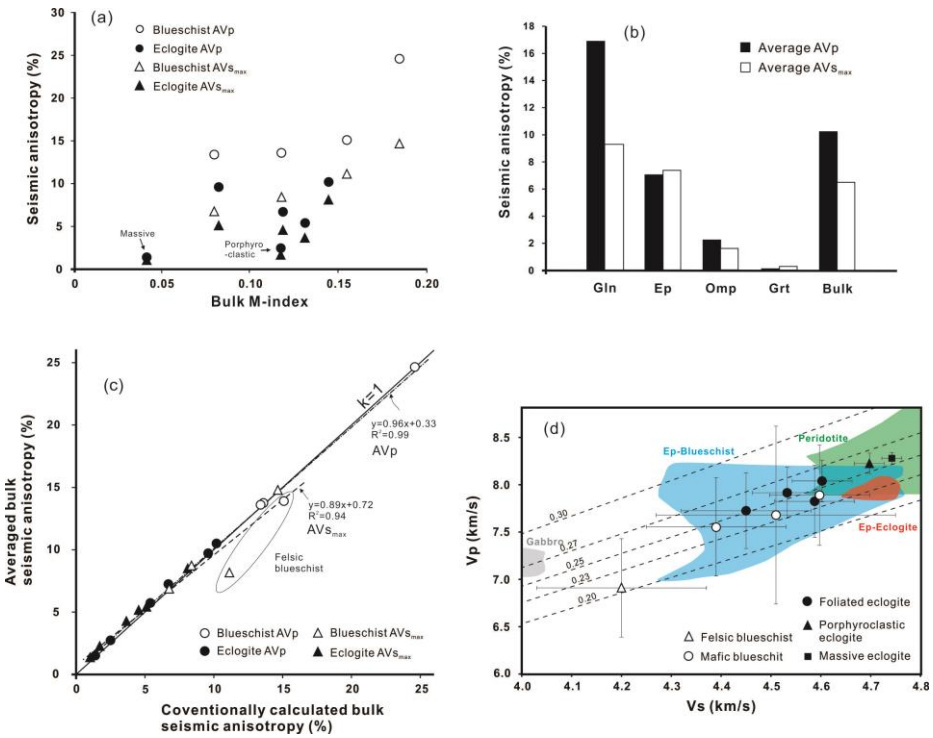

Fig. 2.14. Seismic properties of blueschist and eclogite. (a) An overall positive trend between seismic anisotropies and bulk fabric strength (bulk M-index). (b) Average seismic anisotropies of Gln, Ep, Omp and Grt, as well as those of the whole rocks. (c) The relationships between seismic anisotropies calculated using two different methods are shown. Averaged bulk seismic anisotropy is defined as that averaged from the seismic anisotropy of each constituent mineral assemblage weighted by its volume contents. Conventionally calculated bulk seismic anisotropy refers to that calculated directly using LPOs and volume proportions of constituent minerals. (d) The relationship between V_p and V_s in blueschist and eclogite under ambient conditions; error bars denote the azimuthal anisotropies and dashed lines indicate the Poisson's ratios. Areas of gabbro (grey), epidote blueschist (blue), epidote eclogite (red) and peridotite (green) at ambient conditions are modified from Bezacier *et al.* (2010). In only the lower-left region, approximately 1/3 of the total area for peridotite is displayed.

foliated eclogite show lower velocities, which are located within the epidote blueschist area, compared to those of porphyroclastic and massive eclogite plotted within the peridotite area (Fig. 2.14b). Moreover, the velocities are relatively higher in foliated eclogite than in mafic blueschist (Table 2.1). In addition, the differences in seismic velocities between eclogite in this study and epidote eclogite from Bezacier *et al.* (2010b) may be due to the mineral volume composition differences between the studied eclogite samples.

The rock seismic properties were calculated using single-crystal elasticities measured under ambient conditions, without available relevant data under high P-T conditions. These calculated results are supposed to correspond with projected velocities (V_{p0}) at room P-T derived from laboratory-measured velocities for a crack-free sample under high P-T conditions. To compare P-wave velocities in the oceanic crust with those in the surrounding mantle, it is important to know the in-situ P-wave velocities $V_p(P,T)$ at various depths using the following equation:

$$V_p(P,T) = V_{p0} + \left(dV_p/dP\right)P + \left(dV_p/dT\right)T \quad , \tag{1}$$

where $\partial V_p/\partial P$ is the pressure derivative and $\partial V_p/\partial T$ is the temperature derivative. The experimentally measured pressure and temperature derivatives of rocks are largely dependent on the rock types and less so on mineral volume proportions and compositions, as well as directions (Kern *et al.*, 1999, Kern *et al.*, 2002, Wang *et al.*, 2009, Wang *et al.*, 2005a). For simplicity, we only considered the differences in rock type using a $\partial V_p/\partial P$ value of 0.2 km s^{-1}

GPa^{-1} and a $\partial V_p/\partial T$ value of -3.6 × 10^{-4} km s^{-1} ℃$^{-1}$ for epidote blueschist (Fujimoto *et al.*, 2010) and average $\partial V_p/\partial P$ and $\partial V_p/\partial T$ values of 0.2 km s^{-1} GPa^{-1} and -4.2 × 10^{-4} km s^{-1} ℃$^{-1}$ for massive eclogite (with weakly retrograde metamorphism), respectively (Wang *et al.*, 2009). Because the pressure and temperature derivatives for foliated eclogite (retrograded epidote eclogite) are not currently available, the mean $\partial V_p/\partial P$ and $\partial V_p/\partial T$ values between those of epidote blueschist and massive eclogite were used. The P-wave velocities of blueschist and eclogite corresponding to the rocks' respective P-T conditions were thus calculated (Table 2.2). The average V_p of blueschist under the blueschist facies condition is 7.5–7.7 km/s, which is slightly lower than the V_p under ambient conditions (7.6–7.9 km/s). In contrast, the average V_p values of eclogite under the eclogite facies condition are in the range of 7.9–8.1 km/s and 8.4–8.5 km/s for foliated and porphyroclastic or massive eclogite, respectively, which are higher than the V_p under ambient conditions (7.7–7.9 km/s and 8.2–8.3 km/s).

Therefore, the blueschist and foliated eclogite are capable of reducing V_p by 3–12% relative to the value for the adjacent mantle (V_p 8.3–8.5 km/s), whereas the V_p of massive and porphyroclastic eclogite is 1.4% less to even 1.8% higher than that of the surrounding mantle. Therefore, the low-velocity upper layer (approximately 3–7% velocity lows) can be mainly attributed to the existence of blueschist and foliated eclogite, and a transition from blueschist to eclogite implies a progressive loss of velocity contrast with the surrounding

mantle peridotite with depth (Bezacier *et al.*, 2010b, Nakajima *et al.*, 2009a, Nakajima *et al.*, 2009b). In addition, the seismic anisotropies of Gln and Ep are remarkably higher than those of Grt and Omp (Fig. 2.14c); hence, a decrease in azimuthal and polarization anisotropy might also be expected during the blueschist to eclogite transformation in subducting oceanic crust.

Many tomographic images showing the continuous distribution of a low-velocity layer (approximately 3–7% velocity low) downward to 100–250 km in the subducting oceanic crust (e.g., Abers, 2000, Hasegawa *et al.*, 1994, Lin *et al.*, 1999) indicate the existence of lawsonite eclogite in a 'cold' subducting slab (Connolly & Kerrick, 2002), where epidote is no longer stable. Above a depth of 100 km, both epidote blueschist/eclogite and lawsonite blueschist/eclogite may control the low-velocity layer. The calculated pressure of massive eclogite (P = 2.1–2.6 GPa) suggests that the maximum depth of the low-velocity upper layer in subducting oceanic crust may reach at least 60–75 km in the North Qilian paleo-subduction zone. Because massive eclogite is supposed to have experienced metamorphic stages of lawsonite blueschist/eclogite facies during subduction, this inferred depth of the low-velocity zone most likely reflects the consumption of Lws + Gln to Grt + Omp by metamorphic reactions at a shallower mantle, which may be caused by the higher thermal gradient of the oceanic slab during subduction or thermal relaxation during exhumation.

2.7.2. Polarization anisotropy in subduction zone

As observed in the polarization anisotropy patterns, the polarization

direction of fast shear is mostly sub-parallel to the lineation when a shear wave propagates sub-normal to the foliation for mafic blueschists and eclogites (Figs. 2.13b-d). For felsic blueschist, this polarization direction becomes sub-normal to lineation due to the influence of quartz and phengite (Fig. 2.13a). The lineation direction is often parallel to the direction of tectonic transport, which can be dip-slip, strike-slip or a combination of the two. In the fore-arc region where the subduction of the slab is nearly flat, the incidence direction of near-vertically traveling shear waves is sub-normal to the foliation. In this case, the trench-normal and trench-parallel polarization direction of fast shear-wave propagation can be induced by deformed blueschist and eclogite under the dip-slip and strike-slip motion of the slab, respectively (Figs. 2.15a,b). However, the magnitude of polarization anisotropy is small in the foliation normal direction (AV_S = 1–3%) for foliated eclogite and blueschist, which only accounts for a delay time of 0.02–0.05 s, assuming a 7 km-thick oceanic crust composed of homogenously deformed foliated eclogite and mafic blueschist. We ignored the felsic blueschist because the sedimentary layer is very thin in the oceanic crust. This calculated value is apparently too small to interpret the naturally observed delay times of 0.1–0.3 s (e.g., Nakajima & Hasegawa, 2004, Nakajima *et al.*, 2006, Yang *et al.*, 1995) and 1–2 s (e.g., Anglin & Fouch, 2005, Long & van der Hilst, 2006, Smith *et al.*, 2001). If the subduction angle of the slab is larger than 45 °for strike-slip and 60 °for dip-slip, the incidence direction of near-vertically travelling fast shear wave is sub-parallel to foliation and thus

polarizes parallel to the trench in both of the subduction models (Figs. 2.15c,d). The induced delay time could reach 0.1–0.3 s for mafic blueschist and 0.10–0.15 s for foliated eclogite, because the larger polarization anisotropy (AV_s = 4–9%) and longer ray path passing through the subducting oceanic crust (approximately 10–14 km) could be sampled by an upward-traveling shear wave. In this case, the blueschist and foliated eclogite may make a moderate contribution to the observed trench-parallel anisotropy and delay time (dt = 0.1–0.3 s) in the fore-arc region. In an extreme case, if the subducting crust is abnormally thick, e.g., in central Alaska, where the oceanic crust is as thick as 15–20 km (Rondenay *et al.*, 2008), a much larger delay time could be expected from a deformed and steeply subducted oceanic crust (0.2–0.8 s for mafic blueschist and 0.2–0.4 s for foliated eclogite). However, we cannot rule out other mechanisms such as the B-type LPO of olivine (Jung & Karato, 2001a), the LPO of antigorite (Jung, 2011, Katayama *et al.*, 2009) and trench-parallel mantle flow (Long & Silver, 2008, Smith *et al.*, 2001) to explain trench-parallel seismic anisotropy, particularly for much longer delay times (dt = 1–2 s).

However, the model we applied to interpret the polarization anisotropy in the subduction zone is over-simplified, and the induced delayed time tends to be over- or under-estimated for two main reasons:

(1) The oceanic crust is assumed to be composed solely of foliated eclogite and strongly deformed mafic blueschist, neglecting the weakly deformed massive eclogite. Field observations show that some blueschists are less

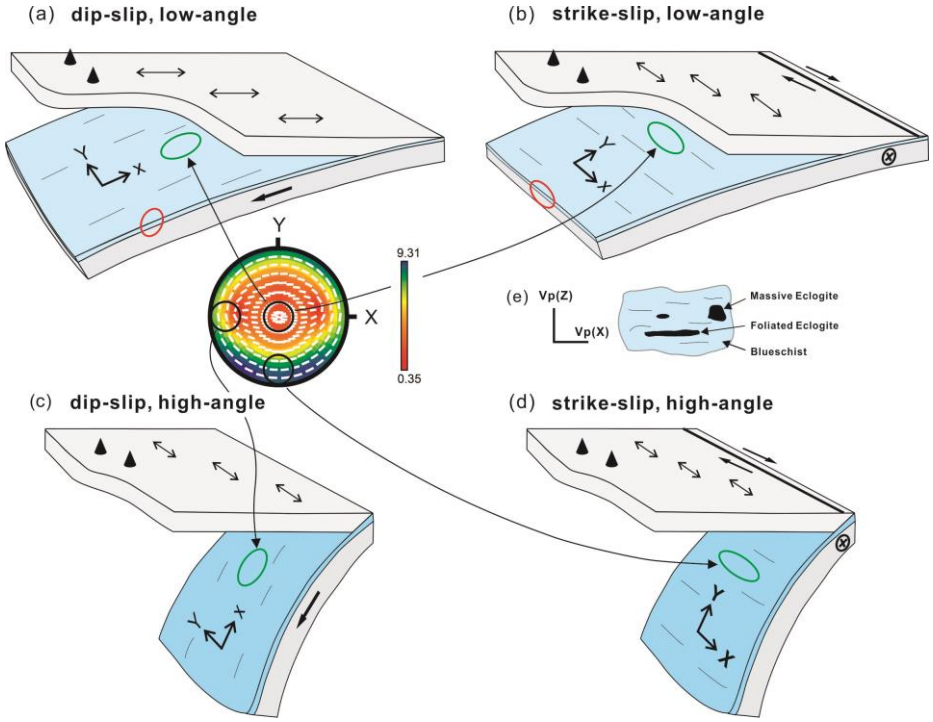

Fig. 2.15. Schematic diagrams showing influence of deformed eclogite and blueschist on the polarization anisotropy of fast shear wave in the fore-arc region. (a) Dip-slip, low-angle subduction, (b) strike-slip, low-angle subduction, (c) dip-slip, high-angle subduction, and (d) strike-slip, high-angle subduction. Thin solid lines indicate lineation in the subducting slab, and double-headed arrows denote the expected polarization directions of the fast shear wave. X denotes lineation and Y is perpendicular to lineation and lying on foliation plane. Trench-parallel seismic anisotropy of fast shear wave is seen in (b), (c) and (d). (e) The occurrences of eclogite and blueschist in the oceanic crust as indicated by the red ellipses in (a) and (b).

strongly deformed or display micro-fold structures compared to the strongly foliated blueschist shown in this study.

(2) The effect of the lawsonite LPO on seismic anisotropy is not considered. Although the outcropped rocks contain no lawsonite, petrographic observations and phase equilibrium studies suggest that lawsonite may exist in blueschist and eclogite during subduction. Based on the single-crystal elasticity of lawsonite, lawsonite shows maximum polarization anisotropy parallel to the a- and b-axes (max. AV_s = 64.63%) (Sinogeikin *et al.*, 2000). Therefore, a favored LPO with the a- or b-axes sub-normal to foliation could significantly increase the polarization anisotropy and induced delay time (assuming nearly horizontal shearing) and lead to the under-estimations of the delay time made in this study. This type of LPO has been reported by Teyssier *et al.* (2010), where the a- and c-axes are found clustering normal to the foliation and parallel to the lineation, respectively. However, an opposite LPO type of lawsonite characterized by the a-axes aligning parallel to lineation and c-axes preferentially oriented normal to foliation, respectively, has also been found (Fujimoto *et al.*, 2010). More detailed studies on the LPOs of lawsonite and their influences on seismic anisotropies must be conducted in the future.

2.7.3. Detectability of eclogite in the subduction channel

In the exhumation path of eclogite toward the surface, progressive shearing would cause a mixture or interlayering between deep-origin eclogite and shallow-origin blueschist. This concept is supported by the field occurrence of

eclogite blocks surrounded or layered by blueschist or meta-sedimentary rocks. Assuming the bodies are sufficiently thick to be imaged, the seismic reflection method can be employed to detect eclogite bodies in subduction channels (e.g., near-vertical reflection) based on the reflectivity of the lithologic interface. The calculation of impedance contrast or the reflection coefficient (R_c) depends on the propagation directions of P-waves and the structural reference frame corresponding to different subduction models (dip-slip and strike-slip).

In shallow subduction zones (<25 km), the slab subducts at an extremely low angle of approximately 5 ° (Hasegawa *et al.*, 1994); and the foliation of a rock is sub-parallel to the slab surface; thus, the incidenting P-wave waves used in a near-vertical reflection mode exhibit nearly normal incidence angle to the surface of a subducting slab or the foliation of a rock (Z direction). Because P-waves display no distinct velocity contrast along all directions sub-perpendicular to foliation, the horizontal components of P-waves likely do not affect the detectability of eclogite. For simplicity, we used ambient values of V_p in the range of 0-30 ° oblique to the Z-axes to calculate the reflection coefficients at different lithologic contacts (Fig. 2.15e), because the average P-wave velocities of eclogite and blueschist at shallow depths (e.g., P-T condition corresponding to blueschist facies) are likely no more than 0.04 km/s higher than those under ambient conditions.

$$R_c = \left[\rho_1 V_{p1}(Z') - \rho_2 V_{p2}(Z')\right] / \left[\rho_1 V_{p1}(Z') + \rho_2 V_{p2}(Z')\right], \quad (2)$$

where ρ_1 and ρ_2 are the densities of rocks 1 and 2 and $V_{p1}(Z')$ and $V_{p2}(Z')$

are the velocities of P-wave with normal incidence to the lithogical interface (Z-direction, perpendicular to foliation) of rocks 1 and 2, respectively (Ji *et al.*, 1993). As shown in Table 2.4, the reflection coefficients larger than 0.1 are associated with the interfaces between massive eclogite and blueschist and those between felsic blueschist and eclogite, which are required for strong seismic reflectors (Warner & McGeary, 1987). The interfaces between massive and foliated eclogite, mafic and felsic blueschist, and foliated eclogite and mafic blueschist produce reflection coefficients of 0.04-0.09, which are capable of generating fair reflectors (Fountain *et al.*, 1994). The reflection coefficients for weakly deformed or almost randomly oriented rocks can also be calculated using the average P-wave velocity at different lithologic interfaces:

$$R_c = \left[\rho_1 V_{p1} - \rho_2 V_{p2} \right] / \left[\rho_1 V_{p1} + \rho_2 V_{p2} \right]. \quad (3)$$

where V_{p1} and V_{p2} are the average P-wave velocities of rocks 1 and 2, respectively, and the other notations are the same as in (2).

The reflection coefficients at the same lithologic contacts are smaller when using formula (3) than those calculated using formula (2) (Table 2.5), suggesting a strengthening effect on reflectivity due to the increase of elastic anisotropy induced by the fabric associated with deformation. The similar average P-wave velocities between mafic blueschist and foliated eclogite (Fig. 2.14b, Table 2.1) imply that it is difficult to distinguish between them using seismic reflectivity (R_c approximately 0.032) (Table 2.5); however, it becomes easier if P-waves traveling sub-parallel to the direction normal to foliation are

taken into account (R_c = 0.042–0.055) (Table 2.4). Although the reflection coefficients between massive and foliated eclogite are large enough (R_c = 0.053–0.069) (Tables 2.4 and 2.5), it is probably difficult to distinguish between them because many massive eclogites are also heterogeneously retrograded as observed in the outcrops. In addition, both mafic blueschist and eclogite contacting with felsic blueschist are characterized by large reflection coefficients, which may also make them easy to be imaged.

In addition to the reflection coefficient, however, another two factors (depth and size) could restrict the detectability of eclogite. Because both the horizontal and vertical resolutions of seismic waves decrease strongly with depth due to the loss of high-frequency components, large eclogite bodies are required for detection at great depths. For example, assuming a fairly high-frequency reflection wave (2–10 Hz) could reach depths of 30–50 km below the mantle wedge with an average velocity of 7–8 km/s, a minimum vertical size of 0.2–1.0 km and horizontal size of 7–20 km is required to detect eclogite bodies. The field observations made in this study and over the world suggest that the sizes of eclogite outcrops vary mostly in the order of tens of meters to hundred meters. However, the outcropped eclogite bodies may have been fragmented by brittle fractures during exhumation, and their original dimension could be larger at greater depths. Nevertheless, it seems that a single eclogite body is often too small to be imaged at depths of 30–50 km in near-vertical incidence seismic profiles. Conversely, when eclogite bodies occur at shallower depths,

Table 2.4. P-wave velocities sub-perpendicular to foliation and reflection coefficients at the interfaces between eclogite and blueschist.

Lithology	$V_p(Z')$[a] (km/s)	Massive eclogite	Foliated eclogite	Mafic blueschist	Felsic blueschist
Massive eclogite	8.22	0	0.063-0.069	**0.105-0.124**	**0.197-0.204**
Foliated eclogite	7.57		0	0.042-0.055	**0.135-0.137**
Mafic blueschist	7.01			0	0.082-0.093
Felsic blueschist	6.39				0

[a]V_p at ambient condition.
Reflection coefficients (R_c) are derived from densities and P-wave velocities calculated in the range of 0-30 ° oblique to the normal of foliation. Bold-type values denote high reflection coefficients $R_c \geq 0.100$.

Table 2.5. Average P-wave velocities and reflection coefficients at the interfaces between eclogite and blueschist.

Lithology	Average V_p[a] (km/s)	Massive eclogite	Foliated eclogite	Mafic blueschist	Felsic blueschist
Massive eclogite	8.28	0	0.053	0.085	**0.169**
Foliated eclogite	7.87		0	0.032	**0.117**
Mafic blueschit	7.64			0	0.086
Felsic blueschit	6.91				0

[a]V_p at ambient condition.
Reflection coefficients (R_c) are derived from densities and average P-wave velocities. Bold-type values denote high reflection coefficients $R_c \geq 0.100$.

near or within the accretion wedge (<30 km depth), where the higher-frequency contents of seismic waves (10–40 Hz) can be received, large individual eclogite bodies can likely be resolved (In this case, the vertical resolution is 50–200 m and horizontal resolution (Fresnel zone) is less than 3.5–7 km assuming an average velocity of 7–8 km/s for blueschist and eclogite). Because we have no precise knowledge of the size of eclogite bodies or their spatial variation in the subducting slab, the estimated reflection coefficients between eclogite and blueschist (R_c = 0.04–0.20) provide some useful information regarding the possible detectability of eclogite in the subduction channel, and more high-resolution vertical reflection experiments must be conducted to test this hypothesis in the future.

2.8. Conclusions

The detailed petro-fabric analysis of blueschist and eclogite in the North Qilian suture zone, NW China allows us to examine the seismological implications of deformed oceanic crust under 'cold' subduction zone conditions. Based on the LPOs and single-crystal elasticity of constituent minerals, the seismic velocities and anisotropies of blueschist and eclogite have been calculated. The massive and porphyroclastic (glaucophane-poor) eclogite display the highest P-wave and S-wave velocities, which are close to those of mantle peridotite, whereas the mafic blueschist and foliated eclogite (glaucophane-rich) show lower and similar P-wave and S-wave velocities (approximately 3–12% lower than adjacent mantle). Combined with the estimated P-T results derived from blueschist (P = 0.5–1.4 ±0.6 GPa), foliated eclogite (P = 1.7–2.1 GPa) and massive eclogite (P = 2.1–2.6 GPa), a gradual decrease in velocity contrast with the surrounding mantle with depth is

expected, and the maximum depth of the low-seismic-velocity layer in the subducting slab could reach at least 60–75 km in the paleo North Qilian subduction zone.

The P-wave anisotropy and polarization anisotropy decrease from blueschist (AV_p = 13–25%; max. AV_s = 7–15%), through foliated eclogite (AV_p = 5–10%; max. AV_s = 4–8%), to massive or porphyroclastic eclogite (AV_p = 1–3%; max. AVs = 1–2%), which is mainly controlled by a decrease in both the volume proportion and deformation degree of glaucophane. The direction of fast shear-wave polarization is consistent with the orientation of lineation in blueschist and eclogite, which is determined by the direction of slab movement at the convergent boundary. Trench-parallel fast shear-wave anisotropy is difficult to explain based on the marginal delay time (0.02–0.05 s) induced by deformed blueschist and eclogite in a low-angle subducting slab, even if a significant strike-slip component is involved at the convergent boundary. However, a trench-parallel fast anisotropy with a moderate delay time (0.1–0.3 s) can be effectively induced by deformed oceanic crust in a high-angle (>45–60 °) subducting slab, irrespective of the directions of slab movement. The effect of lawsonite LPO on the seismic anisotropy is not considered here, but it should not be ignored in the future.

The detection of eclogite bodies in subduction channels using high-resolution seismic reflection experiments is challenging. The calculated reflection coefficients at the lithologic interfaces between eclogite and blueschist are fairly large (R_c = 0.04–0.20) and should allow for the resolution of eclogite bodies in seismic reflection images. However, small eclogite bodies may limit this detection in deep subduction channels. The detection of eclogite in shallow accretion wedges is currently more plausible.

CHAPTER 3

Microstructures and petro-fabrics of lawsonite blueschist in the North Qilian suture zone, NW China

Abstract

We conducted a detailed study on the microstructures and petro-fabrics of massive and foliated lawsonite blueschist (LBS) in North Qilian suture zone, NW China. The lattice preferred orientation (LPO) of glaucophane and lawsonite in foliated lawsonite blueschist (LBS) is considered to be dominantly formed by the deformation mechanism of dislocation creep and rigid-body rotation, respectively. The LPO of glaucophane is mainly characterized by the [001] axis aligning parallel to lineation and the [100] axis and (110) pole plunging perpendicular to foliation. In contrast, the LPO of lawsonite features the maximum [010] axis concentrated close to lineation and the [001] axis strongly clustered normal to foliation. The preferred orientation of [010] axis of lawsonite parallel to lineation is supported by a two-dimensional numerical modeling using the finite-volume method (FVM). The mineral LPOs are much stronger in foliated LBS than in massive LBS. In addition, a kinematic vorticity analysis suggests that both pure shear dominant (W_m = 0.18–0.26) and simple shear dominant (W_m = 0.86–0.93) deformation regimes are present in foliated LBS. The [001] axis and (010) pole of glaucophane, and the [100] and [010] axes of lawsonite, tend to distribute in a foliation-parallel girdle in the pure shear dominant samples, but simple shear dominant samples display more

lineation-parallel concentrations of a [001] axis of glaucophane and a [010] axis of lawsonite. Because the whole-rock seismic anisotropies in foliated LBS are significantly higher than those in massive LBS and a counteracting effect on seismic anisotropies occurs between glaucophane and lawsonite, the delay time of fast S-wave polarization anisotropy induced by an actual subducting oceanic crust with a high subducting angle (> 45–60 °) is expected to range from 0.03 to 0.09s (lower bound for massive LBS) and from 0.1 to 0.3s (upper bound for foliated epidote blueschist).

3.1. Introduction

Subduction zones are regions where sediments, oceanic crust, and oceanic mantle lithosphere are extensively recycled into the Earth's mantle and re-equilibrated therein (Stern, 2002). Depending on the P-T stability fields of hydrous silicate minerals, a variety of such minerals can occur over wide temperatures and depths in the subducted oceanic crust and in the slab-mantle boundary (Poli & Schmidt, 2002, Schmidt & Poli, 1998). Hydrous minerals are therefore considered to have enormous implications for the transportation of water, rheology, seismicity, and seismic properties within the subducted oceanic crust (e.g., Abers, 2000, Hacker *et al.*, 2003a, Hacker *et al.*, 2003b, Hilairet *et al.*, 2007, Jung *et al.*, 2009a, Jung *et al.*, 2004, Kirby *et al.*, 1996, Mainprice & Ildefonse, 2009).

Blueschist is an important high pressure (HP) and low temperature (LT) metamorphic rock dominated by hydrous minerals (e.g., glaucophane, lawsonite, epidote, chlorite, and pumpellyite). It forms the major portion of old and cold, as well as some relatively young and warm oceanic crusts, prior to its transformation into eclogite with progressive subduction. A number of

experimental and thermodynamic phase equilibrium modelings using basaltic compositions have delineated the P-T stability field of blueschist. These results suggest that two main blueschist sub-facies – lawsonite blueschist (LBS, dominated by glaucophane and lawsonite) and epidote blueschist (EBS, dominated by glaucophane and epidote) – occur at different P-T conditions (e.g., Evans, 1990, Forneris & Holloway, 2003, Oh & Liou, 1998, Peacock, 1993, Schmidt & Poli, 1998). Because lawsonite blueschist is stable at a lower temperature and higher pressure within a larger P-T space (P = 0.5–2.5 GPa, T = 200–500 ℃) than epidote blueschist (P = 0.5–2.0 GPa, T = 300–550 ℃) (the P-T boundary between LBS and EBS is positive, and ranges from 0.5 GPa at 300 ℃ to 2.0 GPa at 500 ℃, see Fig. 3.2), it is expected that lawsonite blueschist may constitute a significant portion of an old and metamorphosed oceanic crust that was subducted to a depth of greater than 70 km (Peacock, 1993). As potential evidence for this argument, findings of lawsonite (or its pseudomorphs from blueschist) have been reported in many subduction and suture zones in the world, such as in the Franciscan Complex, California (e.g., Maruyama & Liou, 1988); Ile de Groix, France (e.g., Ballevre *et al.*, 2003); Kurosegawa Zone, SW Japan (e.g., Maruyama *et al.*, 1984); North Qilian, NW China (e.g., Wu *et al.*, 1993); Pam Peninsula, New Caledonia (e.g., Clarke *et al.*, 1997); Sesia Zone, Western Alps, Italy (e.g., Pognante, 1989); Zermatt-Saas Zone, Western Alps (Angiboust *et al.*, 2009), Switzerland; Seward Peninsula, Alaska (e.g., Forbes *et al.*, 1984); Tavşanlı Zone, Turkey (e.g., Okay, 1984); Syros, Cyclades, Greece (e.g., Philippon *et al.*, 2013). An in-depth investigation of the deformation microstructures and rheological properties of blueschist, in particular lawsonite blueschist, is therefore of extreme importances for gaining an understanding of the mechanical strength and seismic properties (velocity and anisotropy) of the subducted oceanic crust.

However, only a few recent studies have been concerned with the

deformation microstructures and seismic properties of deformed natural blueschist (Bezacier *et al.*, 2010b, Cao *et al.*, 2013, Fujimoto *et al.*, 2010, Kim *et al.*, 2013a, Kim *et al.*, 2013b, Teyssier *et al.*, 2010), or have been focused on investigating the single crystal structures and elasticities of glaucophane and lawsonite at high pressures (Chantel *et al.*, 2012, Mookherjee & Bezacier, 2012, Reynard & Bass, 2014). Based on these studies, several important findings and implications have been obtained: (1) The major constituent minerals (e.g., glaucophane, lawsonite, and epidote) in deformed blueschist can exhibit strong lattice preferred orientation (LPOs); and thus (2) cause moderate seismic anisotropies that might be partly responsible for the trench-parallel shear wave polarization anisotropy observed in fore-arc regions; (3) lawsonite blueschist has a contrastingly weaker anisotropy than epidote blueschist due to the destructive and constructive seismic anisotropic patterns between lawsonite and glaucophane, and between epidote and glaucophane, respectively; and (4) the low seismic velocity upper layer in the subducting slab can be explained by the existence of glaucophane, lawsonite, and epidote in blueschist and low-T eclogite.

In this study, we concentrate on the microstructures and petro-fabrics of both weakly and strongly deformed natural lawsonite blueschists collected from the North Qilian suture zone, NW China. This differs from previous studies in that the comparisons between weakly and strongly deformed samples can help to provide greater details of the deformation mechanism, evolution of mineral fabric with deformation, and the seismic anisotropy of the subducting oceanic crust.

3.2. Geological setting

The North Qilian suture zone is an elongated NW-SE trending belt which is located in the northern margin of the Qilian orogenic belt, which is the central part of the Qinling-Qilian-Kunlun Fold System, or the Central China orogenic belt (Song *et al.*, 2013a, Song *et al.*, 2009a, Song *et al.*, 2006, Yin *et al.*, 2008) (Fig. 3.1a). The North Qilian orogenic belt is considered to be a typical oceanic-type subduction zone at the early Paleozoic (490–440 Ma); which is corroborated by a suite of subduction complexes including a Neoproterozoic to Early Paleozoic ophiolite sequence, HP metamorphic belts, island-arc volcanic rocks and granitoid plutons, Silurian flysch formation, Devonian molasses, and a Carboniferous to Triassic sedimentary cover sequence (see the review of Song *et al.*, 2013a). The HP metamorphic belt mainly consists of blueschist, eclogite, meta-graywacke, meta-pelite, and associated ophiolitic rocks. Based on mineral and rock assemblages, two sub-belts of HP metamorphic rocks are characterized: high-grade blueschist belts (slices A, B, and C) in the southeast and a low-grade blueschist belt (slice D) in the northwest (Fig. 3.1b) (see the review of Song *et al.*, 2009a, Wu *et al.*, 1993).

The high-grade blueschist belt is NW-SE-trending, and unconformably overlain by an island-arc volcanic sequence (Fig. 3.1b). It is majorly composed of epidote blueschist with a typical mineral assemblage of glaucophane (Gln) + epidote (Ep) + phengite (Ph) ± garnet (Grt), and other blueschist-facies meta-greywacke/-pelite. The occurrence of eclogite lenses and eclogite-facies meta-greywacke/-pelite layers within the blueschist-facies rocks suggest a precedent high-grade or high-pressure metamorphism (Song *et al.*, 2007b). The findings of lawsonite inclusions in eclogitic garnets (Song *et al.*, 2007b, Zhang & Meng, 2006, Zhang *et al.*, 2007) and carpholite in meta-pelite (Song *et al.*, 2007b), further indicate that an eclogite-facies metamorphism occurred at low

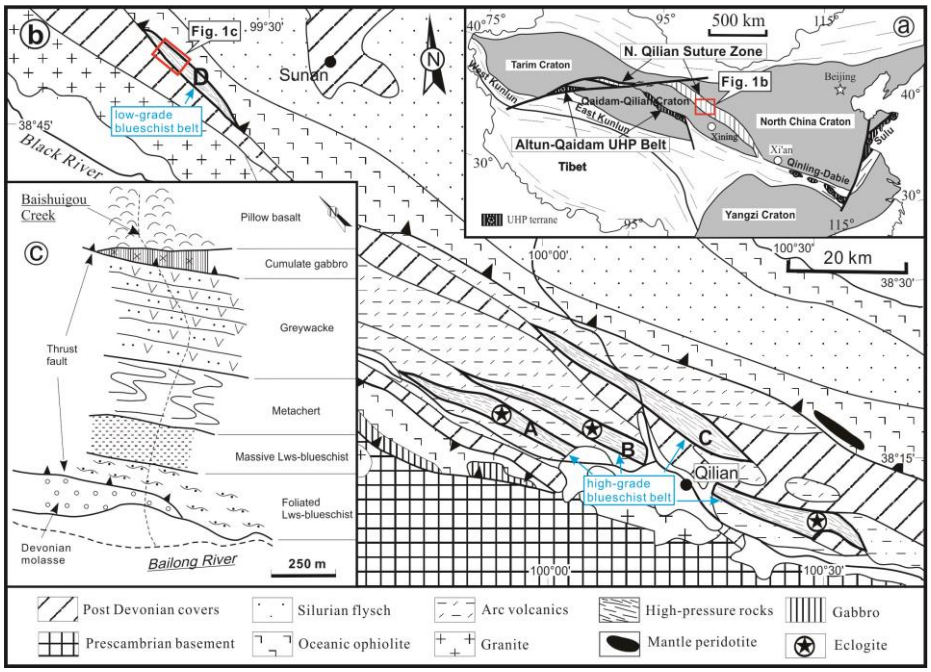

Fig. 3.1. (a) Schematic geological maps showing the major tectonic units of China. (b) Geological map showing the middle part of the North Qilian suture zone, where: A-C indicate the high-grade blueschist (epidote blueschist) belt and D denotes the low-grade blueschist (lawsonite blueschist) belt. (c) The rock assemblage of low-grade blueschist belt. Figures were modified after Song et al. (2006, 2009).

temperature, indicative of a "cold" oceanic-type subduction. These petrographic observations also agree well with P-T estimates (using a phrase equilibrium diagram or Grt-clinopyroxene (Cpx)-Ph thermobarometer) of blueschist, eclogite and eclogite-facies meta-pelite. Many studies have yielded P-T conditions of 2.1–2.6 GPa and 460–590 ℃, and 1.8–2.2 GPa and 450–550 ℃ for peak lawsonite eclogite-facies and retrograde epidote eclogite-facies metamorphism, respectively (Cao *et al.*, 2011, Song *et al.*, 2007b, Wei & Song, 2008, Wei *et al.*, 2009, Zhang *et al.*, 2007), as well as an epidote blueschist-facies metamorphic condition of 0.5–1.4 GPa and 480–620 ℃ (Cao *et al.*, 2013, Li, 2010) (Fig. 3.2). In addition, Cao *et al.* (2013) and Cao *et al.* (2011) examined the mineral chemical compositions and petro-fabrics of both blueschist and eclogite, and found that whole-rock seismic anisotropy and velocity decreases and increases with a transformation from blueschist to eclogite, respectively.

The low-grade blueschist belt also occurs as an elongated zone (~ 20 km in length and ~ 1 km in width) extending from NW to SE (Fig. 3.1b), with a well-preserved cross-section exposed in Baishuigou Creek (Fig 3.1c). This blueschist belt is thrust southwestwards onto the Devonian molasses to the south, and overlain by an ophiolitic sequence to the north. The belt consists of a metamorphic rock assemblage of blueschist, meta-chert, and meta-greywacke, which changes sequentially from SW to NE. Based on field occurrence and microstructures, the low-grade blueschist can be subdivided into areas of massive lawsonite blueschist in the north and foliated lawsonite blueschist in the south. In Baishuigou Creek, the massive lawsonite blueschist occurs as a 10 m × 20 m sized block and is composed of glaucophane and lawsonite (Lws), with minor amounts of pumpellyite (Pmp), chlorite (Chl), and albite (Ab). In contrast, the foliated lawsonite blueschist is strongly deformed and featured by intense foliation and isoclinal folds in the outcrops. The mineral assemblage is

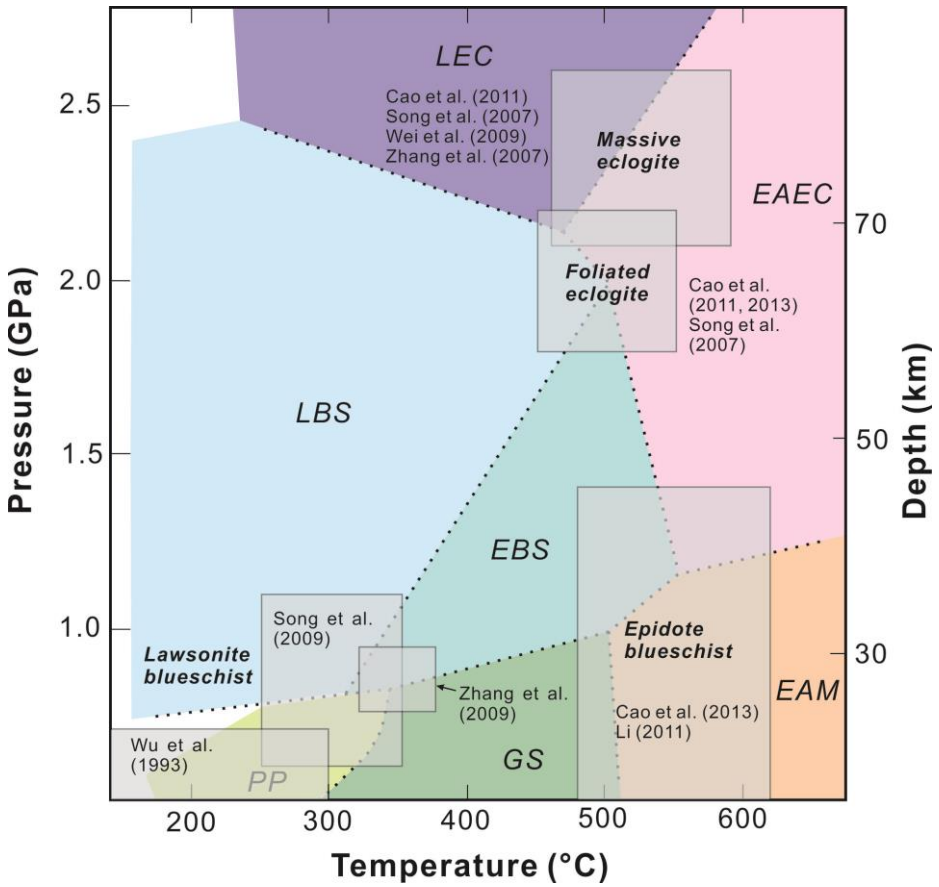

Fig. 3.2. P-T diagram showing the equilibrated P-T conditions of low-grade blueschist belt (lawsonite blueschist) and high-grade blueschist belt (epidote blueschist, massive and foliated eclogite) in North Qilian suture zone. Metamorphic facies boundaries were adopted from Liou et al. (1998) and Zhang et al. (2009). *LEC*: lawsonite eclogite facies, *LBS*: lawsonite blueschist facies, *EBS*: epidote blueschist facies, *EAEC*: epidote-amphibole eclogite facies, *EAM*: epidote amphibolite facies, *GS*: greenschist facies, and *PP*: prehnite-pumpellyite facies.

mostly represented as Pmp + Gln + Lws + Chl + Ab + Qtz. In contrast to the high-grade blueschist belt, only sparse P-T estimations were available for the low-grade blueschist. Wu *et al.* (1993) first reported P-T conditions of 0.4–0.7 GPa and 150–250 ℃, based on the first appearance of Lws, aragonite (Arg) and Pmp in lawsonite blueschist. Based on mineral reactions that produce and/or consume Lws, Pmp, Arg, and Ab, Song *et al.* (2009a) recently determined P-T conditions of 0.6–1.1 GPa and 250–350 ℃. Similarly, Zhang *et al.* (2009) employed a P-T pseudosection calculation using Domino/Theriak software, and obtained comparable results of 0.80–0.95 GPa, 335–355 ℃ and 0.75–0.85 GPa, 320–350 ℃, for massive and foliated lawsonite blueschist, respectively. However, the exact deformation P-T condition is not well constrained, although it is supposed to be similar to the metamorphic P-T condition.

3.3. Description of samples

The lawsonite blueschist samples in this study were collected from Baishuigou Creek, ca. 20 km west of the town of Sunan, in Gansu Province, NW China (Fig. 3.1). Ten massive samples and three foliated samples were selected for analysis.

3.3.1. Massive lawsonite blueschist

Massive lawsonite blueschist generally displays a homogeneous texture with hardly any discernible foliation and lineation on either field- or hand-specimen scale. However, two subtypes of the massive lawsonite blueschist can still be categorized, based on an integrated consideration of their optical microstructures (Fig. 3.3) and lawsonite fabrics (see below). For convenience, we named them M1 type (Figs. 3.3a-c) and M2 type (Figs. 3.3d-f). Both M1

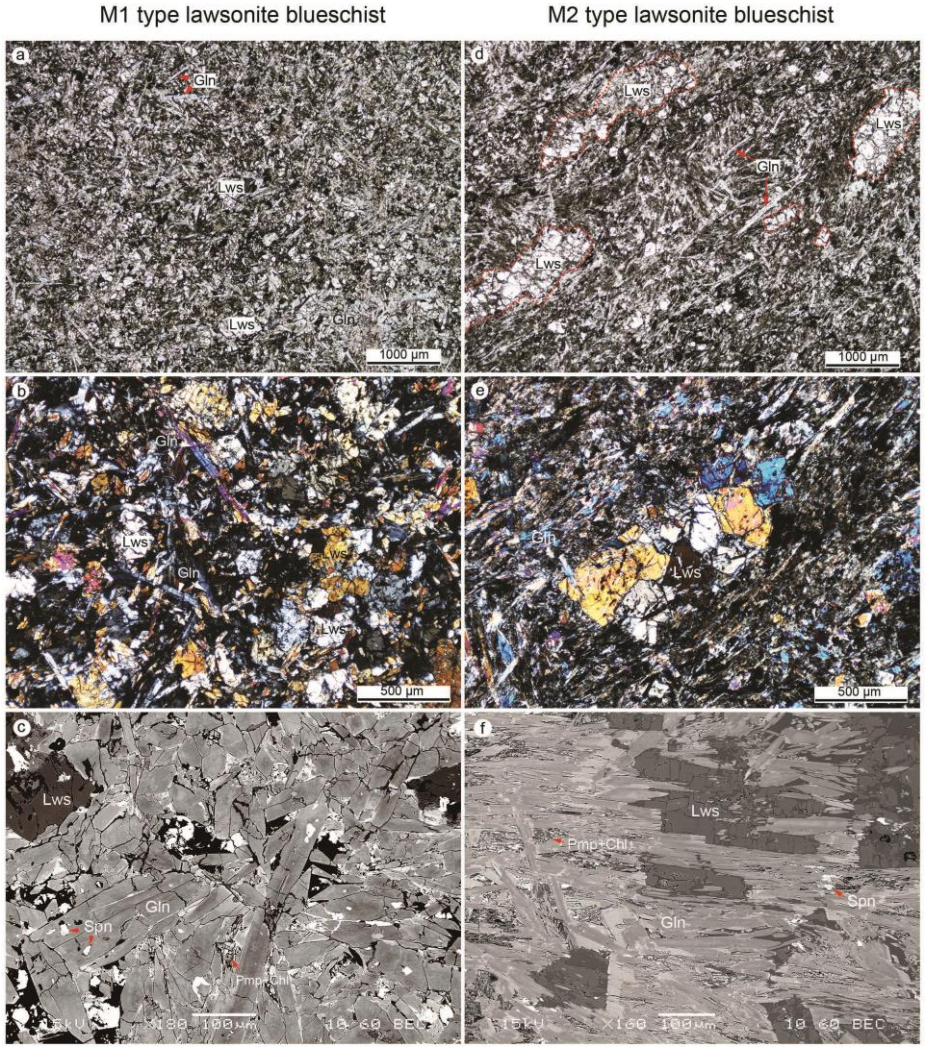

Fig. 3.3. Photo-micrographs showing the representative microstructures of two subtypes of massive lawsonite blueschist: M1 type (a-c) and M2 type (d-f). (a) and (d) are the plane-polarized optical images; (b) and (e) are the cross-polarized optical images; (c) and (f) are electron back-scattered images; (d) elongated and oriented lawsonite aggregates are outlined with a red-dotted line; (e) close-up image showing an oriented lawsonite aggregate in which poly-crystals are random in orientation. (a-c) shows the texture of the exhibited random orientation of euhedral glaucophane and lawsonite; (d-f) displays moderate foliation composed of oriented glaucophane and lawsonite. In (c) a weak chemical heterogeneity is indicated by relatively darker cores and brighter rims in the glaucophane crystals. In (f), glaucophane displays a similar, but abrupt, composition transition from core to rim compared to (c). These features of glaucophane might imply an increasing Fe and Ca content from core to rim (c,f). In addition, cracks are frequently observed in lawsonite grains (c,f).

and M2 types have the same mineral assemblage of Gln + Lws + Pmp + Chl + sphene (Spn), in which Gln and Lws are dominant. The lawsonite crystals are euhedral (columnar, rectangular, rhombic, or polygonal), and large in size (0.2–1.0 mm in diameter), occurring as isolated single crystals or aggregates in the glaucophane matrix. Lawsonite crystals or aggregates in the M1 type are randomly oriented, but they frequently form elongated aggregates aligning sub-parallel to each other with random orientations in a single aggregate in the M2 type. Likewise, in the M1 type, the glaucophane crystals are column or needle shaped (up to ~ 1.0 mm in length) and randomly orientated, but are relatively smaller in size and aligned preferentially sub-parallel to the lawsonite aggregates in the M2 type. These microstructures indicate that the M2 type is probably more highly strained than the M1 type. In addition, the chemical pattern of glaucophane in the M1 type is gently varied (Fig. 3.3c), whereas the glaucophane in the M2 type shows a more abrupt change in chemical composition (Fig. 3.3f).

3.3.2. Foliated lawsonite blueschist

In contrast, the foliated lawsonite blueschist is significantly deformed, as indicated by the well-defined foliation and lineation defined by elongated and oriented fine-grained glaucophane or chlorite crystals (Fig. 3.4). The mineral assemblage is typically characterized by Gln + Lws + Chl + Pmp + Ab + Qtz, with varying mineral modal abundances among different domains in one sample (Figs. 3.4a-c). Lawsonite crystals are euhedral and display variable oblique angles between the long axis and foliation. In some samples, lawsonite crystals with large aspect ratios (R > 3) and oblique at a high angle to foliation are frequently observed (Figs. 3.4d and e). The orientations of the lawsonite long axis against foliation are dependent on their aspect ratios, since they tend to align parallel to foliation above a critical aspect ratio value (see section 5).

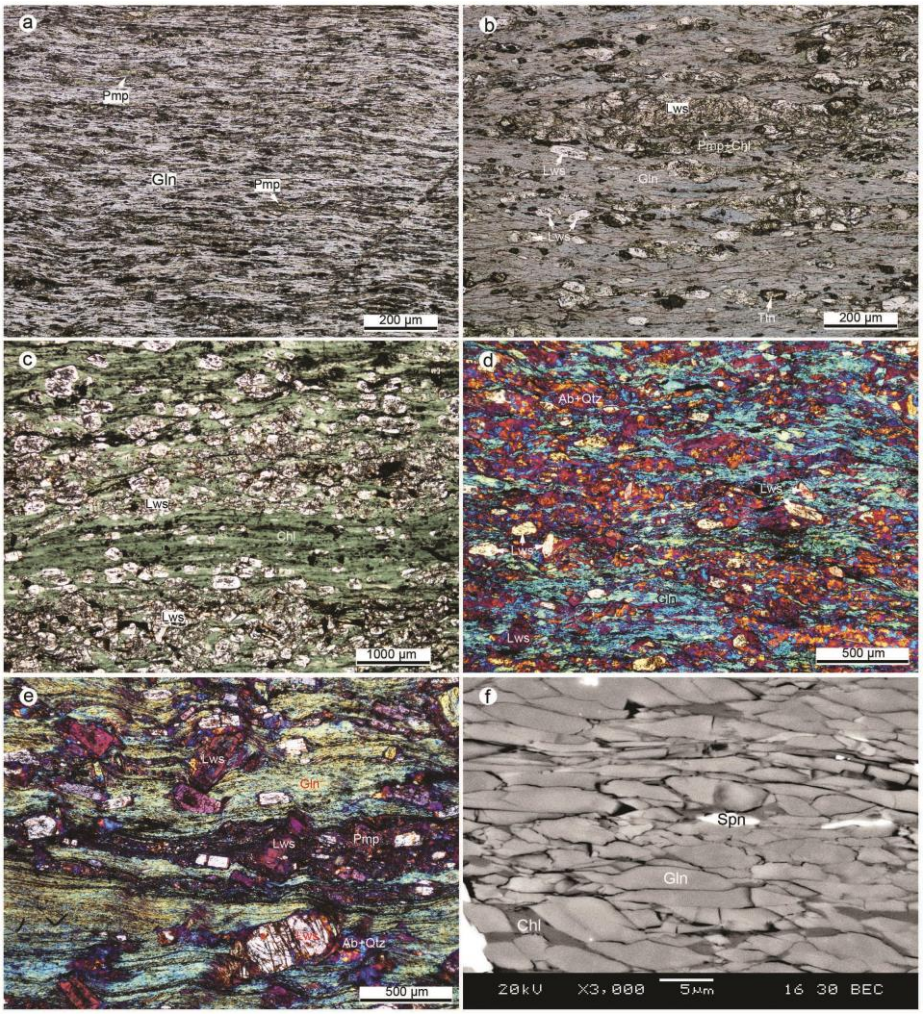

Fig. 3.4. Photo-micrographs showing the representative microstructures of foliated lawsonite blueschist: (a-c) plane-polarized optical images taken from three different domains in a single sample; (a) Gln + Pmp domain (11QL-24-1); (b) Lws + Gln + Pmp + Chl domain (11QL-24-2); (c) Lws + Chl domain (11QL-24-4). (d) and (e) are cross-polarized images of (d) 2S12 and (e) 2S30, where isolated lawsonite crystals of large aspect ratios aligning at a high angle to foliation can be observed; (f) electron back-scattered image showing well oriented fine-grained glaucophane matrix containing conformably aligned interstitial chlorite and sphene.

In comparison with massive lawsonite blueschist, glaucophane in the foliated lawsonite blueschist has an anhedral shape with an extremely small grain size (~5–10 μm in length) and a smaller aspect ratio (Fig. 3.4f). The composition of fine-grained glaucophane may vary slightly, as suggested by its fairly homogeneous brightness under a back-scattered image (Fig. 3.4f).

3.4. Lattice preferred orientations

Fine-polished thin-sections were used to measure the LPOs of glaucophane and lawsonite, under an electron back-scattered diffraction (EBSD) system (JEOL JSM6380 with HKL channel 5 housed at the School of Earth and Environmental Science, Seoul National University). The system operates in an experimental environment of 20 kV acceleration voltage, 15 mm working distance, and a spot size of 60. To avoid repeated data collection, we indexed the EBSD patterns manually for every grain where the Kikuchi pattern was obviously different from those of neighboring grains. Because the structural framework is difficult to ascertain in massive LBS, we used thin-sections taken from arbitrary directions for EBSD analysis. The obtained LPOs of glaucophane and lawsonite were later rotated by aligning the clusters of the [001] and [100] axes of glaucophane parallel to lineation and perpendicular to foliation, respectively (because this is the only fabric type that has been reported for natural glaucophane, see Fig. 3.11 for the 3D crystal shapes of lawsonite and glaucophane) (Bezacier *et al.*, 2010b, Cao *et al.*, 2013, Fujimoto *et al.*, 2010, Kim *et al.*, 2013a, Kim *et al.*, 2013b, Teyssier *et al.*, 2010). In contrast, since the structural reference frame of foliated lawsonite blueschists is clear, and EBSD analysis was conducted on *XZ* thin-sections (*X*: parallel to lineation, *Z*: normal to foliation).

Both the pole figures and the inverse pole figures were drawn from individual orientation data (Euler angle triplets), which were obtained from EBSD measurements, using plotting programs of *PFctf* and *IPFctf* developed by David Mainprice. To quantify the strength of the LPOs, we applied both M-index (Skemer *et al.*, 2005) and J-index (Bunge, 1982) algorithms. The misorientation index (M-index) is defined by $M = \frac{1}{2}\int \left| R^T(\theta) - R^0(\theta) \right| d\theta$, which describes the differences between the observed $R^0(\theta)$ (obtained from EBSD data) from a real fabric and the modeled distribution of uncorrelated misorientation angles $R^T(\theta)$ for a theoretically random fabric. The M-index ranges from 0 (random fabric) to 1 (single crystal fabric). In contrast, the J-index is defined as $J \equiv \int \left[f(g) \right]^2 dg$, where $f(\phi_1, \psi, \phi_2)$ is the orientation distribution functions (ODFs), ϕ_1, ψ, ϕ_2 is the Euler angle triplet, and *dg* is a volume element in Euler angle space. The J-index theoretically ranges from 1 (random fabric) to infinity (single crystal fabric). We also used the pfJ index and ipfJ index, which are similar to the J-index, to describe the sharpness of a pole figure and an inverse pole figure, respectively. Because the values of J-index, pfJ and ipfJ index are dependent on number of discrete data in the orientation distribution function (ODF) (e.g., number of grains in LPO measurement) and arbitrary numerical parameters (e.g., the Gauss half width (GHW)) (Skemer *et al.*, 2005), the same GHW of 8.5 degrees was used in all calculations to minimize the systematic error. Even so, J-index, pfJ and ipfJ index may still not be powerful enough to distinguish the samples with similar fabric strengths due to their non-uniqueness and variable number of grains in the LPO measurement, whereas M-index could be more satisfying in this case.

3.4.1. LPO of glaucophane

The glaucophane in two subtypes of massive lawsonite blueschist displays a weak LPO (girdle-type or L-type), which is characterized by a [001] axis aligning parallel to lineation, both a [100] axis and a (110) pole forming girdles nearly normal to lineation with their maxima sub-perpendicular to foliation, and a (010) pole also lying in a girdle with its maximum sub-perpendicular to the lineation in the foliation (Figs. 3.5a and b). This fabric type of glaucophane has also been reported from garnet-rich blueschist and eclogite (Cao *et al.*, 2013), suggesting that the L-type fabric of glaucophane in massive lawsonite blueschist may result from the fabric randomization effect by a large abundance of rigid lawsonite crystals (similar to the effect of rigid garnet crystals) and/or by a weak deformation. In contrast, foliated lawsonite blueschist mostly shows a strong glaucophane fabric (point-type or SL-type), as featured by a [001] axis parallel to lineation, a [100] axis and a (110) pole perpendicular to foliation, and a (010) pole normal to lineation in the foliation (Fig. 3.5c). This is a typical fabric for natural glaucophane and other species of amphibole reported in many previous studies (Bezacier *et al.*, 2010b, Cao *et al.*, 2010, Cao *et al.*, 2013, Fujimoto *et al.*, 2010, Kim *et al.*, 2013b, Tatham *et al.*, 2008, Teyssier *et al.*, 2010). In addition, we also observed another glaucophane fabric (S-type) that exhibits clear foliation-parallel girdles of both [001] axis and (010) pole with the same maxima orientations as those in the SL-type fabric (Fig. 3.5d). The fabric patterns of L-type, SL-type and S-type were originally defined by Helmstaedt *et al.* (1972) and later updated by Zhang *et al.* (2006).

These different LPOs of glaucophane can also be presented in the inverse pole figures (Fig. 3.6). SL- and L-type fabrics display strong concentrations of [001] axes of glaucophane parallel to lineation (Figs. 3.6a-c), whereas the S-type fabric shows a girdle distribution of lineation parallel to the plane

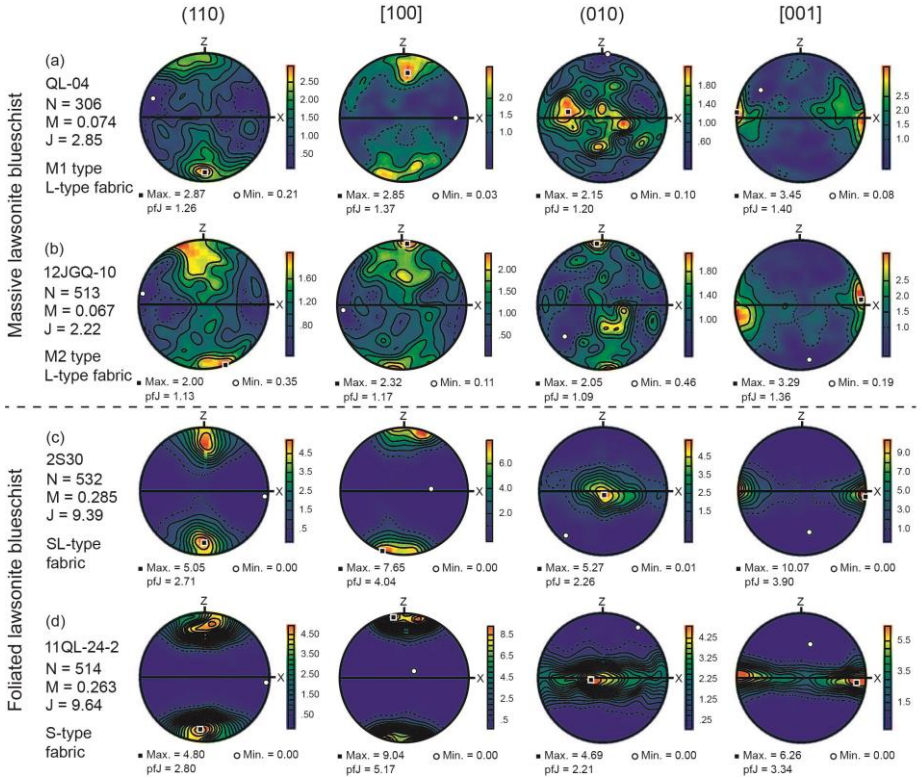

Fig. 3.5. Pole figures of glaucophane in representative massive (a) M1 type and (b) M2 type, and (c, d) foliated lawsonite blueschist. Pole figures are presented in upper hemisphere and equal-area projection, with a default Gauss half width of 8.5 degrees. Denotations: X: lineation, Z: foliation normal, N: number of grains, M: M-index, J: J-index, pfJ: pole figure J-index. Because two opposite XZ sections in a sample after cutting can be used for LPO measurement, it is not matter to use either upper or lower hemisphere projection.

containing a [010] and [001] axis, with its maximum aligning to the [001] axis (Fig. 3.6d). The maximum of foliation normal direction (*Z*) is consistent with the $[\bar{1}00]$ and [101] axes of glaucophane in the SL- and S-type fabrics (Figs.3.6c and d). However, in the L-type fabric, it forms a clear girdle sub-parallel to the (001) plane with its maximum aligning sub-parallel to the $[\bar{1}00]$ and [101] axes (Figs. 3.6a and b).

The strength of the L-type fabric is significantly weaker in massive LBS (M = 0.06–0.09, J = 1.9–3.6) than those of the SL- and S-type fabrics in foliated LBS (M = 0.40–0.29, J = 6.7–17.8) (Table 3.1). Therefore, a combined variation of the fabric pattern and fabric strength of glaucophane between the two types of LBS is especially indicative of the increasing degree of deformation from massive to foliated LBS. In addition, although the mineral textures suggest that the M2 type is relatively more strongly deformed than the M1 type LBS, the fabric strength of glaucophane is not significantly different between these two subtypes.

3.4.2. LPO of lawsonite

Even though the fabric is very weak, a non-random LPO of lawsonite is still discerned in the massive LBS. Different from glaucophane, two subtypes (M1 and M2) of the massive LBS present distinctive fabrics for lawsonite (Figs. 3.7a and b). The most important difference is that the maximum of the [001] axis is aligned close to the center of the pole figure normal to lineation in foliation in the M1 type LBS, whereas it tends to align sub-perpendicular to foliation in the M2 type LBS. This characteristic is also exhibited in the inverse pole figures of lawsonite, which features *Y*- and *Z*-directions concentrated sub-parallel to the [001] axis in the M1 and M2 type massive LBS, respectively (Figs. 3.6a and b). The distribution of the [100] and [010] axes is diffused, with

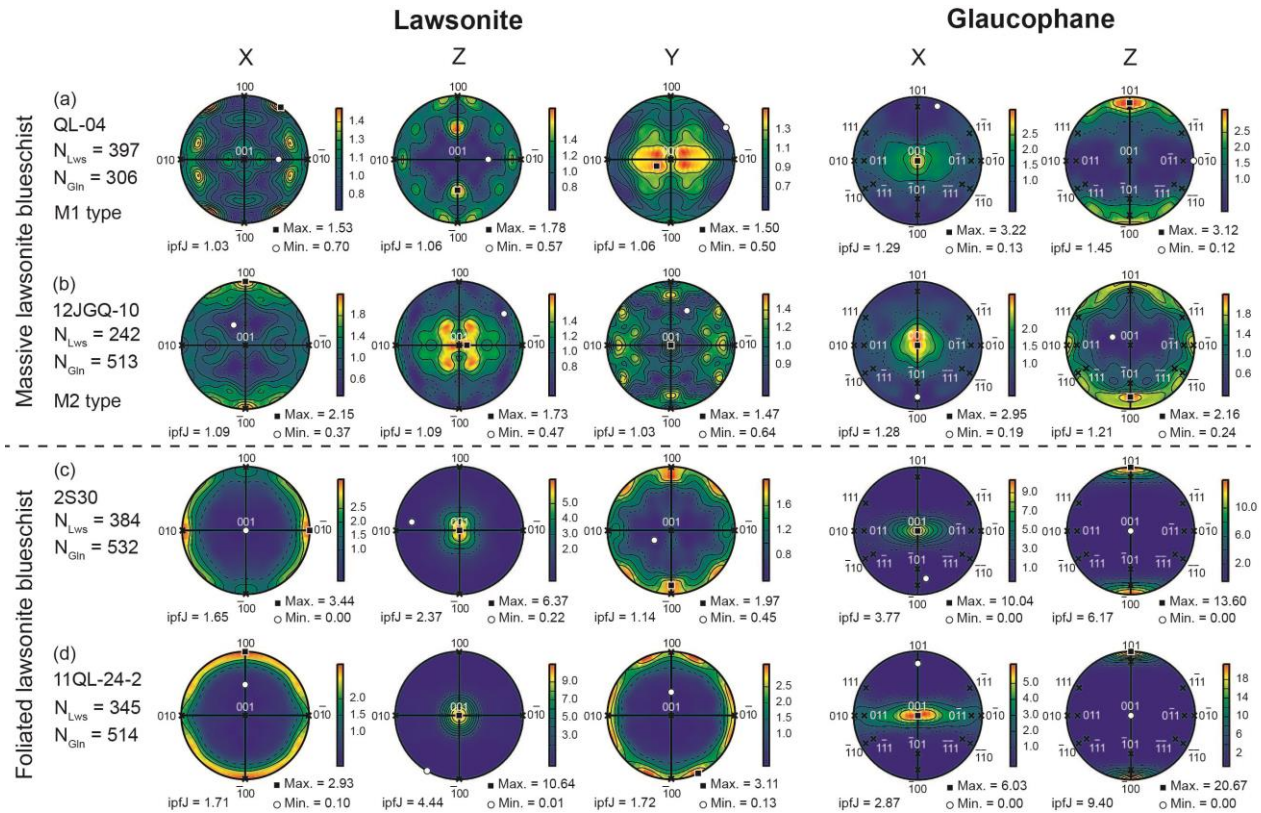

Fig. 3.6. Inverse pole figures of lawsonite and glaucophane in representative massive (a) M1 type and (b) M2 type, and (c, d) foliated lawsonite blueschist. N_{Lws} and N_{Gln} are the numbers of lawsonite and glaucophane grains, respectively. X: lineation, Z: foliation normal, Y: orthogonal to both X and Z, ipfJ: inverse pole figure J-index.

Table 3.1. Fabric strengths of glaucophane and lawsonite aggregates for massive and foliated lawsonite blueschist.

Sample	Rock type (LBS)	Glaucophane aggregates											Lawsonite aggregates									
		M-index	J-index	pfJ index				ipfJ index					M-index	J-index	pfJ index			ipfJ index				
				[100]	[010]	001]	[110]	X	Z	Y	X+Z	Z/X			[100]	[010]	[001]	X	Z	Y	X+Z	Z/X
08QS-16	M1 type	0.086	3.61	1.17	1.3	1.72	1.2	1.68	1.24	1.22	2.92	0.74	0.048	1.87	1.1	1.15	1.16	1.06	1.04	1.07	2.1	0.98
08QS-18-1	M1 type	0.075	3.03	1.21	1.2	1.79	1.23	1.75	1.27	1.2	3.02	0.73	0.05	1.99	1.12	1.1	1.14	1.04	1.03	1.06	2.07	0.99
12JGQ-12	M1 type	0.064	2.25	1.09	1.19	1.42	1.1	1.4	1.13	1.09	2.53	0.81	0.049	2.36	1.16	1.15	1.2	1.12	1.05	1.07	2.17	0.94
QL-03	M1 type	0.064	2.29	1.16	1.07	1.29	1.12	1.3	1.13	1.07	2.43	0.87	0.049	1.96	1.09	1.15	1.14	1.04	1.01	1.04	2.05	0.97
QL-04	M1 type	0.074	2.85	1.37	1.2	1.4	1.26	1.29	1.45	1.11	2.74	1.12	0.046	1.7	1.09	1.09	1.11	1.03	1.06	1.06	2.09	1.03
08QS-18-2	M2 type	0.084	2.59	1.16	1.29	1.7	1.16	1.58	1.12	1.2	2.7	0.71	0.053	2.19	1.17	1.18	1.18	1.07	1.07	1.02	2.14	1.00
12JGQ-06	M2 type	0.067	2.24	1.21	1.21	1.44	1.15	1.38	1.23	1.09	2.61	0.89	0.05	2.29	1.24	1.11	1.25	1.15	1.12	1.04	2.27	0.97
12JGQ-10	M2 type	0.067	2.22	1.17	1.09	1.36	1.13	1.28	1.21	1.04	2.49	0.95	0.05	2.47	1.19	1.14	1.18	1.09	1.09	1.03	2.18	1.00
12JGQ-17	M2 type	0.064	2.84	1.3	1.08	1.45	1.25	1.47	1.35	1.06	2.82	0.92	0.046	1.97	1.15	1.13	1.17	1.05	1.06	1.04	2.11	1.01
QL-02	M2 type	0.064	1.93	1.12	1.08	1.35	1.12	1.3	1.09	1.07	2.39	0.84	0.05	1.7	1.1	1.08	1.12	1.06	1.06	1.02	2.12	1.00
11QL-24-1*	Foliated	0.402	17.80	4.81	3.4	5.98	3.34	5.53	8.49	3.14	14.02	1.54										
11QL-24-2*	Foliated	0.263	9.64	5.17	2.21	3.34	2.8	2.87	9.4	2.34	12.27	3.28	0.23	6.25	1.95	1.7	4.56	1.71	4.44	1.72	6.15	2.60
11QL-24-4*	Foliated												0.205	4.39	1.44	1.71	3.24	1.36	3.03	1.58	4.39	2.23
2S12	Foliated	0.191	6.69	2.62	1.55	3.99	2.24	3.38	4.11	1.51	7.49	1.22	0.164	3.88	1.48	1.56	2.95	1.49	2.86	1.36	4.35	1.92
2S30	Foliated	0.285	9.39	4.04	2.26	3.9	2.71	3.77	6.17	2.17	9.94	1.64	0.149	3.02	1.32	1.57	2.56	1.65	2.37	1.14	4.02	1.44

* Different domains in the same sample 11QL-24.

LBS is lawsonite blueschist, X is lineation, Z is foliation-normal, Y is orthogonal to X and Z; X+Z = ipfJ(X) + ipfJ(Z); Z/X = ipfJ(Z) / ipfJ(X)

their maxima mostly aligning either at low angles around lineation, or sub-normal to foliation. In contrast, the fabrics of lawsonite in the foliated LBS are much stronger (Figs. 3.7c and d). Similar to the M2 type LBS, lawsonite in foliated LBS displays a very strong concentration of [001] axis perpendicular to foliation. In addition, the [100] and [010] axes form girdles parallel to foliation, with the maxima of [010] axes clustering close to lineation. Because both foliated and M2 type LBS are more strongly deformed than the M1 type LBS, the transition of the concentration of the lawsonite [001] axes from aligning parallel to normal to foliation, probably results from the increasing degree of deformation.

Similar to glaucophane, the fabric strength of lawsonite in massive LBS (M = 0.05, J = 1.7–2.5) is significantly smaller than that in foliated LBS (M = 0.15–0.23, J = 3.0–6.3), and there is no significant fabric strength difference of lawsonite between the M1 and M2 type LBS, although deformation is relatively stronger in the M2 type than in the M1 type LBS (Table 3.1).

3.5. Vorticity analysis

The kinematic vorticity number (W_k) is a measure of the non-coaxiality that is involved in the progressive deformation history (Means *et al.*, 1980). It can be expressed as a ratio of the rotational to the stretching components in the velocity field, as $W_k = 0$ for coaxial deformation and $W_k = \infty$ for rigid body rotation. For plane strain deformation, W_k ranges from 0 to 1, which corresponds to a non-linear transition from pure shear to simple shear (an equal contribution of pure shear and simple shear components at $W_k = 0.71$) (Law *et al.*, 2004). Because the vorticity of deformation in natural rock may vary with space and time (e.g., non-steady state deformation), a mean kinematic vorticity

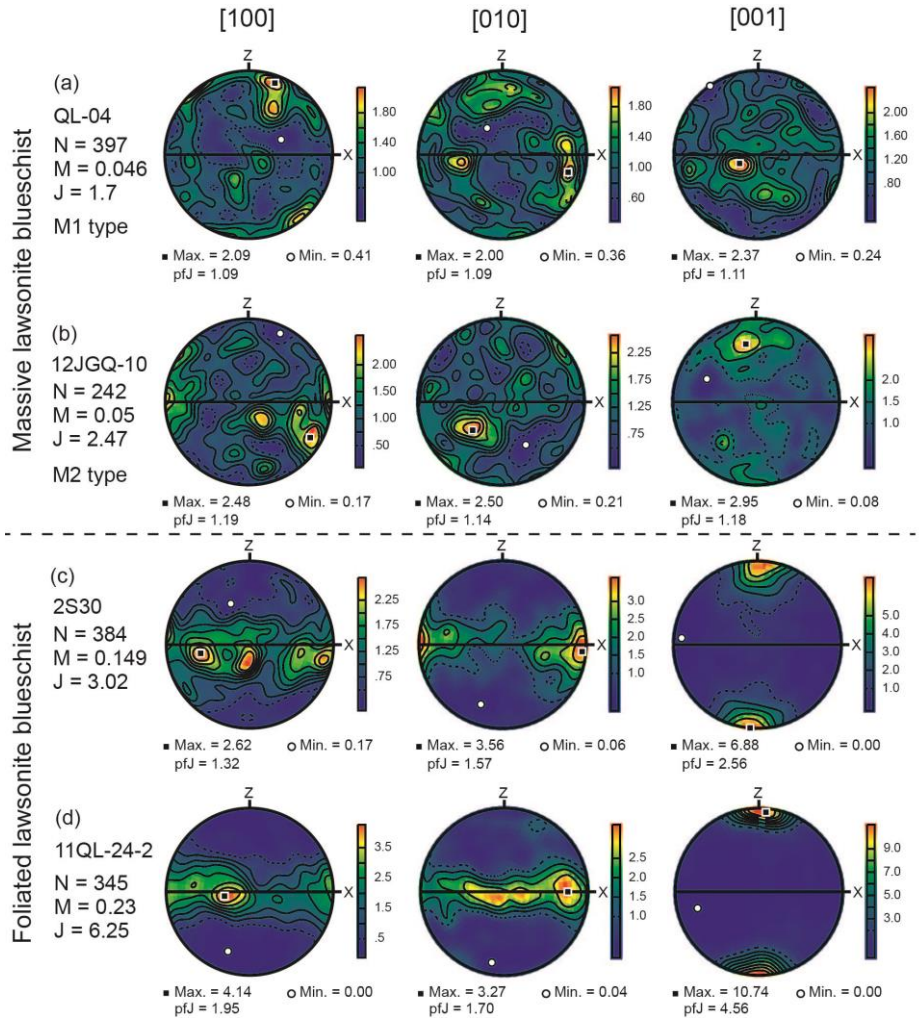

Fig. 3.7. Pole figures of lawsonite in representative massive (a) M1 type and (b) M2 type, and (c, d) foliated lawsonite blueschist. Pole figures are presented in upper hemisphere and equal-area projection, with a default Gauss half width of 8.5 degrees. X: lineation, Z: foliation normal, N: number of grains, M: M-index, J: J-index, pfJ: pole figure J-index.

number W_m (in which the vorticity is integrated over space and time) is more appropriate to use (Passchier, 1988).

There exist three techniques for quantifying the vorticity number in a deformed natural rock using a two-dimensional *XZ* thin-section (Law *et al.*, 2004); herein, we employ the method proposed by Wallis *et al.* (1993). This method is based on analyzing the orientations and aspect ratios of rigid porphyroclasts rotating in a homogeneously deformed matrix, and determining the critical aspect ratio (R_c) below which porphyroclasts rotate continuously (and hence display no shape preferred orientation), and above which they achieve a stable alignment parallel to foliation (Law *et al.*, 2004). In another word, this statement assumes that the variations in the orientation of rigid porphyroclasts and the inferred vorticity values are only controlled by their aspect ratios, and are not affected by interactions between the porphyroclasts (e.g., Passchier, 1987, Tikoff & Teyssier, 1994, Wallis, 1995) and slip at the interfaces between porphyroclasts and their matrix (e.g., Johnson *et al.*, 2009, Marques *et al.*, 2007). In the case of plane strain, the mean kinematic vorticity number W_m can be calculated as $W_m = \left(R_c^2 - 1\right) \Big/ \left(R_c^2 + 1\right)$ (Passchier, 1987), where R_c is the critical aspect ratio.

The S-L tectonite structure consisting of foliation and lineation is very well developed in our studied foliated lawsonite blueschist, indicating that the deformation may not deviate far from plane strain (Teyssier *et al.*, 2010). The lawsonite grains are mostly isolated and surrounded by deflected fine-grained Gln and/or Chl matrix (e.g., Fig. 3.4b-e), suggesting that the lawsonite was probably formed prior to deformation and that there was no significant interaction between the lawsonite crystals during deformation. In addition, the very fine-grained matrix may imply that glaucophane was deformed by recovery and dynamic recrystallization processes, which probably minimizes

the slip along lawsonite boundaries (Teyssier *et al.*, 2010). Based on these textures, we considered that lawsonite could be treated as a rigid porphyroclast rotating in a ductile matrix, and that the estimation of kinematic vorticity using the above-mentioned relationship between W_m and R_c is reasonable. Because lawsonite grains are frequently observed in contact with each other, which could imply interactions between porphyroclasts, we chose domains without significant grain-to-grain interactions among lawsonite crystals for the vorticity analysis.

As shown in Fig. 3.8, two distinct W_m values are found in foliated LBS. Two different lawsonite-rich domains in a single sample display a very low W_m value (0.18–0.26) (Fig. 3.8a), corresponding to dominant pure shear deformation. In contrast, the other two samples have remarkably higher values of W_m (0.86–0.93) (Fig. 3.8b), indicative of dominant simple shear deformation. It is of interest to notice that Teyssier *et al.* (2010) studied the lawsonite vorticity of blueschist layers in the Sivrihisar Massif, Turkey and reported vorticity values in-between our results of W_m = 0.4–0.6.

3.6. Rock seismic properties

To obtain the rock seismic velocity and anisotropy, it is necessary to solve the Christoffel equation, which requires the macroscopic elastic tensor $<C_{ij}>$ and density of a rock. From a microscopic point of view, the macroscopic elastic tensor can be considered as an integration of the elastic stiffness of all mineral grains (C_{ij}) over all orientations of a rock. To complete this integration, it is necessary to use one of several averaging schemes (e.g., Vogit, Reuss, VRH, and Geometric). The density of rock is generally regarded as the average density of all the major constituent minerals weighted by their volume

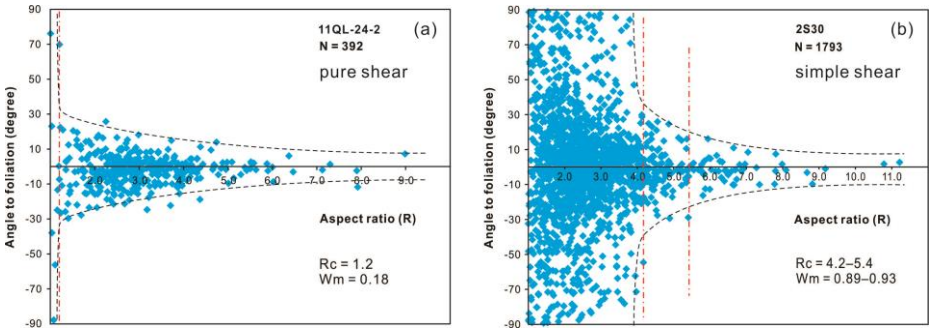

Fig. 3.8. Aspect ratio versus angle to foliation for lawsonite grains in representative foliated lawsonite blueschists for (a) pure shear and (b) simple shear deformation regime. Dashed lines are the overall envelopes of data points, and the vertical dash-dotted lines denote the chosen critical aspect ratio (R_c) used to estimate mean kinematic vorticity W_m. The choice of R_c was based on two criteria: (1) the value at which the envelope of a data point shows an abrupt change of slope; and (2) the value above which the angle to foliation is < 30 ° and below which the amplitude of the angle to foliation can reach above 30 °.

percentages. This complicated calculation process can be conveniently accomplished using petro-physical software (Mainprice, 1990), based on the single crystal elastic constants, crystal density, lattice-preferred orientations (LPOs), and the volume proportions of constituent minerals.

To calculate the seismic properties of lawsonite blueschist in this study, we used normalized volume proportions of a simplified bi-mineralogical assemblage of Gln + Lws (except for one foliated sample that contained a high abundance of albite) because of their dominant modal proportions (> 95 vol.% in total). The macroscopic elasticity stiffness tensor of blueschist is computed from the single-crystal elasticity stiffness tensors of glaucophane (Bezacier *et al.*, 2010b), lawsonite (Sinogeikin *et al.*, 2000) and albite (Aleksandrov *et al.*, 1974), assuming the Voigt-Reuss-Hill (VRH) averaging scheme. It is, however, noteworthy that the axis designation of the *a* and *b* axes of lawsonite generally used in single-crystal elastic stiffness (a = 8.79, b = 5.85, c = 13.13; e.g., Baur, 1978, Comodi & Zanazzi, 1996) is opposite to that commonly used for LPO measurements (a = 5.86, b = 8.81, c = 13.15; e.g., Libowitzky & Armbruster, 1995, Meyer *et al.*, 2001, Pawley & Allan, 2001), and that both single-crystal elastic stiffness and mineral LPOs are required in the calculation of seismic properties of polycrystals and whole rocks. We therefore modified the order of the elasticity stiffness tensor (C_{ij}) of a single-crystal lawsonite to make it consistent with the designations of the crystallographic axis which was used to measure the lawsonite LPO. Although this correction induces a little change of the seismic properties of polycrystals and whole rocks due to a small difference of seismic properties along *a* and *b* axes of lawsonite single-crystal (see section *6.1*), it is still necessary to point out and correct this problem.

3.6.1. Single crystal

Identical to the result of Bezacier *et al.* (2010b), the seismic properties of

glaucophane single crystal are characterized by the fastest (9.27 km/s) and slowest (6.30 km/s) P-wave velocities aligning parallel to the [001] and [100] axis, respectively, which yield a large P-wave anisotropy (AV_p) of 38.1%. The shear-wave polarization anisotropy forms a high-value girdle sub-parallel to the (100) plane, with its maximum (max. AV_s = 27.30%) close to the [001] axis (Fig. 3.9a). The P-wave velocity in the lawsonite single crystal is also the fastest (9.15 km/s) along the [001] axis, but is the slowest (7.23 km/s) sub-parallel to the [110] axis. This velocity pattern produces a lower P-wave anisotropy (AV_p = 23.5%) compared to that of the glaucophane. Both [010] and [100] axes show similar intermediate P-wave velocities and the largest magnitude of shear-wave polarization anisotropy (Fig. 3.9a).

3.6.2. Glaucophane polycrystals

Glaucophane aggregates of SL- and L-type fabrics display an overall consistent P-wave anisotropy pattern (Figs. 3.9b-d), which is characterized by maximum and minimum P-wave velocities aligning parallel to lineation and normal to foliation, respectively. This P-wave anisotropy pattern can be well interpreted by the glaucophane fabric of the [001] axis (fastest V_p direction) that is concentrated parallel to lineation and the [100] axis (slowest V_p direction) that is plunging perpendicular to foliation. However, the fast P-wave velocity shows a much stronger girdle distribution sub-parallel to foliation in the S-type glaucophane fabric, although the maximum velocity still aligns along the lineation (Fig. 3.9e). The strong polarization anisotropies (AV_s) in the glaucophane aggregates within the massive LBS lie mostly at a low angle to foliation and a high angle to lineation, whereas weak polarization anisotropies dominantly form a girdle along the *XZ* direction, with their minimum close to lineation. In contrast, the glaucophane aggregates in foliated LBS exhibit a more symmetrical pattern of polarization anisotropy, such as strong and weak

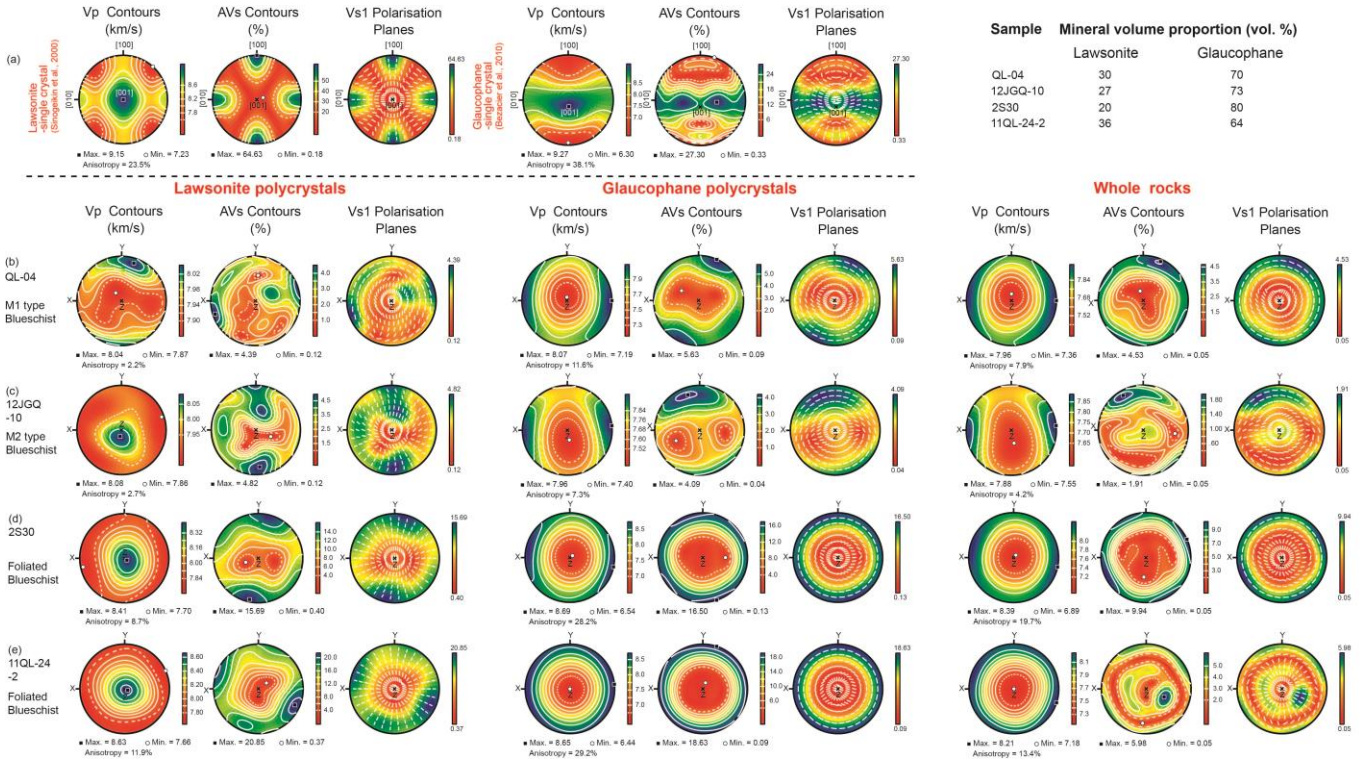

Sample	Mineral volume proportion (vol. %)	
	Lawsonite	Glaucophane
QL-04	30	70
12JGQ-10	27	73
2S30	20	80
11QL-24-2	36	64

Fig. 3.9. Seismic anisotropies of (a) lawsonite and glaucophane single crystals, (b) M1 type, (c) M2 type, and (d, e) foliated lawsonite blueschist. Data are presented on a [100]-[010] plane for single crystals and on a foliation plane (XY) for polycrystals and whole rocks, with an equal-area and upper hemisphere projection. The volume proportions of normalized bi-mineralogical assemblage of Gln + Lws are manually measured using their area proportions in optical photo-micrographs and are shown in the upper right of the figure. X: lineation, Z: foliation normal, Y: orthogonal to both X and Z.

polarization anisotropies residing at low and high angles to the foliation, respectively. In the glaucophane aggregates in both massive and foliated LBSs, the direction of fast-shear wave polarization is nearly parallel to lineation when shear-waves propagate nearly normal to foliation, but fast shear-waves tend to polarize parallel to foliation when the incident angle is low relative to foliation. The magnitude of seismic anisotropies of glaucophane aggregates is significantly larger in the foliated LBS (AV_p = 23.9–29.8%, max. AV_s = 13.84–17.95%) than in the massive LBS (AV_p = 5.4–11.6%, max. AV_s = 2.88–5.63%) in which no significant difference between the M1 and M2 types is exhibited (Table 3.2 and Fig. 3.10).

3.6.3. Lawsonite polycrystals

Because the [001] axis of lawsonite has the fastest P-wave velocity, the seismic anisotropy patterns of lawsonite aggregates are greatly affected by the preferred orientation of the [001] axis. For the M1 type LBS, the [001] axis of lawsonite is clustered close to the *Y*-direction, and thus results in the same direction of maximum V_p (Fig. 3.9b). However, the [001] axis of lawsonite and the fastest V_p of lawsonite aggregates are sub-perpendicular to foliation in the M2 type (Fig. 3.9c) and the foliated LBS (Figs. 3.9d and e). In all the lawsonite aggregates, the fast shear-wave mostly polarizes sub-perpendicularly to lineation when the incident ray propagates sub-normal to foliation. Similar to the glaucophane aggregates, the magnitudes of seismic anisotropies of lawsonite aggregates vary in a similar range for both M1 and M2 type LBSs (AV_p = 2.2–3.5%, max. AV_s = 4.34–6.90%), which are much smaller than those in the foliated LBS (AV_p = 8.8–11.7%, max. AV_s = 15.94–20.62%) (Table 3.2 and Fig. 3.10).

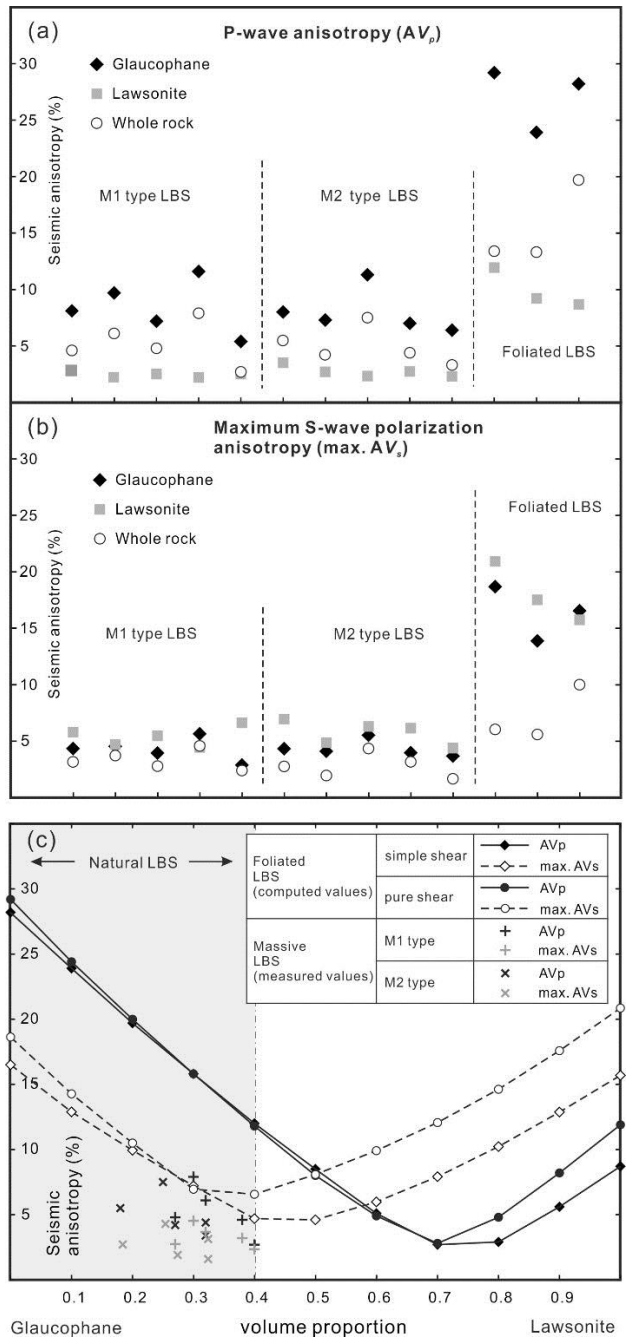

Fig. 3.10. (a) P-wave anisotropies; and (b) maximum shear waves polarization anisotropy for glaucophane and lawsonite aggregates and whole rocks; (c) seismic anisotropies vs. mineral volume proportions for M1, M2 types and foliated lawsonite blueschist (LBS). Mineral volume abundances of natural LBS are indicated as grey areas. A maximum volume proportion of about 40% lawsonite is suggested in terms of this study.

Table. 3.2. Mineral volume proportions and seismic anisotropies for massive and foliated lawsonite blueschist.

Sample	Rock type	Mineral volume proportion (%)			Gln aggregate		Lws aggregate		Whole-rock	
		Gln	Lws	Ab	AV_p (%)	Max. AV_s (%)	AV_p (%)	Max. AV_s (%)	AV_p (%)	Max. AV_s (%)
08QS-16	M1 type LBS	62	38		8.1	4.34	2.8	5.74	4.6	3.2
08QS-18-1	M1 type LBS	68	32		9.7	4.53	2.2	4.65	6.1	3.67
12JGQ-12	M1 type LBS	60	40		5.4	2.88	2.5	6.57	2.7	2.35
QL-03	M1 type LBS	73	27		7.2	3.94	2.5	5.42	4.8	2.74
QL-04	M1 type LBS	70	30		11.6	5.63	2.2	4.39	7.9	4.53
08QS-18-2	M2 type LBS	68	32		7.0	3.96	2.7	6.09	4.4	3.12
12JGQ-06	M2 type LBS	82	18		8.0	4.32	3.5	6.9	5.5	2.71
12JGQ-10	M2 type LBS	73	27		7.3	4.09	2.7	4.82	4.2	1.91
12JGQ-17	M2 type LBS	75	25		11.3	5.52	2.3	6.25	7.5	4.29
QL-02	M2 type LBS	68	32		6.4	3.67	2.3	4.34	3.4	1.6
11QL-24-1	Foliated LBS				29.8	17.95				
11QL-24-2	Foliated LBS	64	36		29.2	18.63	11.9	20.85	13.4	5.98
11QL-24-4	Foliated LBS						10.1	16.84		
2S12	Foliated LBS	48	7	45	23.9	13.84	9.2	17.45	13.3	5.54
2S30	Foliated LBS	80	20		28.2	16.50	8.7	15.69	19.7	9.94
GRL_NI-01[1]	Foliated LBS	91	9		25.3	13.9	10.7	21.3	17.2	9.19

Sample	Rock type	Mineral volume proportion (%)			Gln aggregate		Lws aggregate		Whole-rock	
		Gln	Lws	Ab	AV_p (%)	Max. AV_s (%)	AV_p (%)	Max. AV_s (%)	AV_p (%)	Max. AV_s (%)
LRL_NI-01[1]	Foliated LBS	75	25		20.2	9.9	8.8	19.4	12	5.54
QL-47[2]	Foliated EBS								15.1	11.14
QL-53[2]	Foliated EBS								13.6	8.39
QL-68[2]	Foliated EBS								13.4	6.77
QL-73[2]	Foliated EBS								24.6	14.66
GRL_Omi-03[1]	Foliated EBS								19.6	11.3
ERL_Omi-03[1]	Foliated EBS								11.8	8.43
B2010[3]	Foliated EBS								16.1	10.37

Abbreviations: lawsonite blueschist (LBS), epidote blueschist (EBS), glaucophane (Gln), lawsonite (Lws), albite (Ab).

[1] Data from Kim et al. (2013a)
[2] Data from Cao et al. (2013)
[3] Data from Bezacier et al. (2010)

3.6.4. Whole rocks

It is apparent that the seismic anisotropy pattern of whole rock is controlled by the volume proportions of each of the monomineralic aggregates and their individual seismic properties (which are governed by the seismic properties of single-crystals and their polycrystal fabrics). As shown in Figs. 3.9b-e, the overall anisotropy patterns of P-wave and shear-wave polarization resemble those of glaucophane in both massive and foliated LBSs, due to the larger volume proportions of glaucophane than lawsonite. Similar to glaucophane and lawsonite aggregates, the magnitudes of seismic anisotropies for whole rock are higher for foliated LBS (AV_P = 13.2–19.7%, max. AV_S = 5.54–9.94%) compared to both subtypes of massive LBS that have similar magnitudes of seismic anisotropy (AV_P = 2.6–7.9%, max. AV_S = 1.6–4.53%) (Table 3.2 and Fig. 3.10). Because the seismic anisotropy patterns of glaucophane and lawsonite aggregates are opposite (counteracting with each other) (Figs. 3.9b-e), the whole-rock seismic anisotropies are strongly reduced in both the massive and foliated LBSs. Specifically, the P-wave anisotropy is higher in glaucophane than lawsonite aggregates, but shows an intermediate value for whole rocks (Fig. 3.10a). In contrast, the maximum shear-wave polarization anisotropy is larger in lawsonite than glaucophane aggregates, but both are higher than that of whole rocks (Fig. 3.10b). Thus, these data suggest that the counteracting effect of the seismic anisotropy between glaucophane and lawsonite aggregates (same as "countervailing effect" in Kim et al. 2013a) is more significant in shear-wave polarization anisotropy than P-wave polarization anisotropy. Assuming that glaucophane and lawsonite have constant LPOs with their modal abundances, we calculated the variations of seismic anisotropies with mineral volume proportions for two foliated LBS, under either a simple shear or pure shear dominant deformation regime (Fig. 3.10c). This result shows that both

the whole-rock P-wave and the polarization anisotropies decrease with increasing lawsonite abundance in a similar slope, irrespective of the deformation regime, and that they reach minimum values at 70–80 vol.% (AV_p ~ 3%) and 40–50 vol.% (AV_s ~ 5%) lawsonite, respectively.

3.7. Discussions

3.7.1. Deformation mechanisms of glaucophane and lawsonite

Previous studies have proposed that natural amphiboles can be deformed by a variety of deformation mechanisms (Díaz Aspiroz *et al.*, 2007), such as cataclastic flow (Imon *et al.*, 2004, Nyman *et al.*, 1992), rigid-body rotation (Berger & Stunitz, 1996, Ildefonse *et al.*, 1990, Siegesmund *et al.*, 1994), dislocation creep (Biermann, 1981, Dollinger & Blacic, 1975, Reynard *et al.*, 1989, Skrotzki, 1992), and dissolution-precipitation creep (Imon *et al.*, 2002, Imon *et al.*, 2004, Miller, 1988, Wintsch & Yi, 2002). Several previous studies have advocated that dislocation creep can dominantly account for the deformation of natural glaucophane (Kim *et al.*, 2013b, Reynard *et al.*, 1989, Zucali *et al.*, 2002). In this study, the very fine-grained and well-oriented anhedral glaucophane grains in foliated LBS (Fig. 3.4f) clearly indicate a dynamic recrystallization process without extensive grain-boundary sliding and subsequent anisotropic growth (Poirier, 1985). The development of very pronounced glaucophane LPOs may also support the principal deformation mechanism of dislocation creep (Figs. 3.5c and d).

Kim *et al.* (2013b) studied the microstructures of naturally deformed LBS and suggested that the mechanical strength of glaucophane is weaker than that

of lawsonite. This significant viscosity contrast causes lawsonite crystal to behave as a nearly rigid body that rotates passively and deforms slightly in a soft glaucophane matrix in a non-coaxial deformation regime (Passchier & Sokoutis, 1993, Piazolo *et al.*, 2002). The euhedral morphology, lack of intra-crystalline plasticity, and dispersed long axis orientation of lawsonite grains, confirm that lawsonite has a deformation mechanism dominated by rigid-body rotation (Figs. 3.4 and 3.8). The high vorticity numbers (W_m = 0.86-0.93) estimated from the orientations of lawsonite indicate a large non-coaxial deformation component (Fig. 3.8b).

Many previous studies have proposed that rigid-body rotation is capable of developing lattice and shape-preferred orientations for the anisotropic rigid particles in a flowing matrix, which are generally characterized by a tendency for the longest and shortest axes to approach the directions of maximum extension and shortening, respectively (e.g., Gay, 1968, Masuda *et al.*, 1995, Passchier, 1987, Piazolo *et al.*, 2002, Wallis *et al.*, 1993). Employing the axis notations of lawsonite from Libowitzky and Armbruster (1995), the [100] and [001] axes are the longest and shortest axes for lawsonite single crystal, respectively (Fig. 3.11). In agreement with the prediction from previous studies above, the results of lawsonite LPO in foliated LBS show that the [001] axis is strongly aligned perpendicular to foliation (maximum shortening direction) (Figs. 3.7c and d). However, the intermediate-length [010] axis, and not the [100] axis, is preferentially oriented sub-parallel to lineation that indicates the direction of maximum extension, especially in a dominant simple shear deformation regime (Fig. 3.7c). To understand the reason for this discrepancy, we modeled the preferred orientation of a lawsonite single crystal under an incoming flow, using a finite-volume method (FVM) that is frequently applied in computational fluid dynamics (CFD). The idea of this modeling is very straightforward. Because of the complexity in modeling simple shear

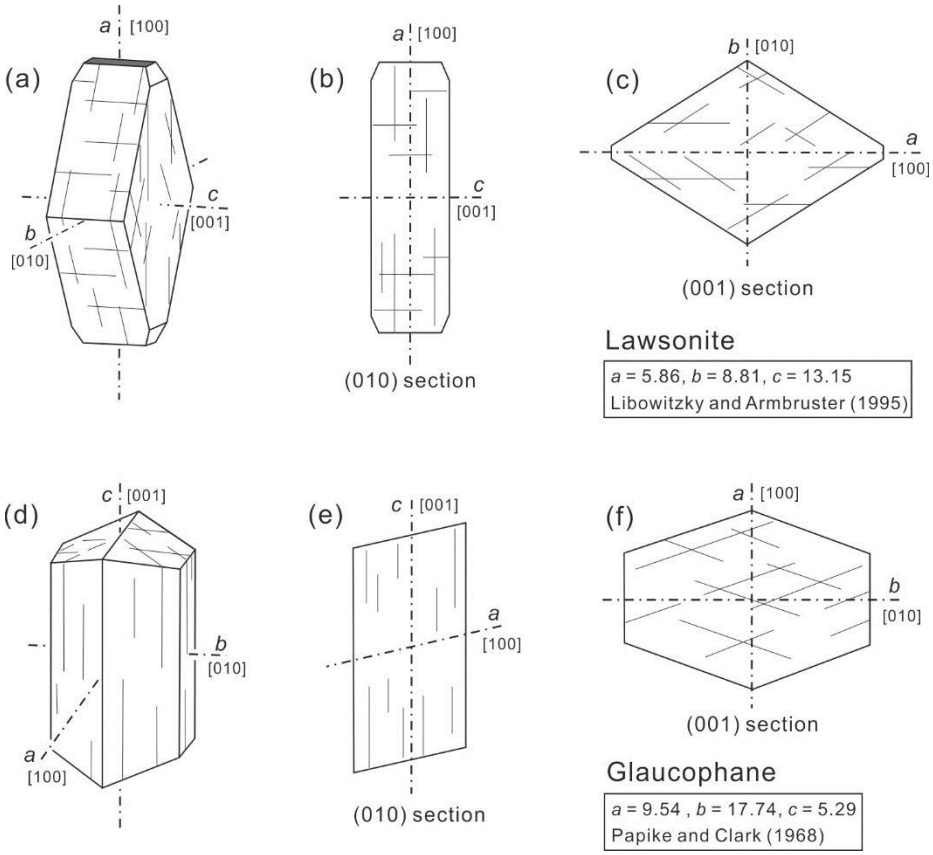

Fig. 3.11. Typical morphology of (a-c) lawsonite and (d-f) glaucophane single crystal. Modified from Nesse (2004).

deformation in a three-dimensional space, we designed two simple cases where either the [100] or [010] axis of lawsonite align sub-parallel to the flow direction in a two-dimensional space (corresponding to the foliation plane), and analyzed the stabilities of these two orientations under a small perturbation in a homogeneous incoming flow.

As shown in Fig. 3.12a, a small perturbation is imposed by deviating the [100] axis of lawsonite from the flow direction at 5 °. This small perturbation instantaneously exerts a torque on the lawsonite, which increases shortly afterwards and then decreases, until a nearly constant value is reached after some small variations (Fig. 3.12b). The sign of the torque is always negative with time in this process, indicating that lawsonite crystal will rotate clockwise and further deviate its [100] axis from the flow direction (the coefficient of moment is defined as positive when the rotation is counter-clockwise). Therefore, aligning the [100] axis of lawsonite sub-parallel to lineation may not be a stable orientation in naturally deformed LBS. In contrast, when the [010] axis of lawsonite is perturbed at 5 °with the flow direction (Fig. 3.12c), a positive torque is instantaneously created. This torque then decreases shortly afterwards, and is followed by an oscillation pattern in which the coefficient of moment varies between positive and negative values, with a positive average (Fig. 3.12d). Hence, this result suggests that although lawsonite crystal may rotate either clockwise or counter-clockwise with time, the averaged tendency is to rotate counter-clockwise. In other words, the probability of a counter-clockwise rotation is larger than that of a clockwise rotation, causing the [010] axis of lawsonite more likely to return parallel to the flow direction. It may thus be reasonable to consider that the [010] axis of lawsonite plunging sub-parallel to lineation is a more preferable orientation compared to the [100] axis in naturally deformed LBS. It should be noted that this modeling process is fairly simplified and qualitative due to two main reasons. (1) Most importantly, the

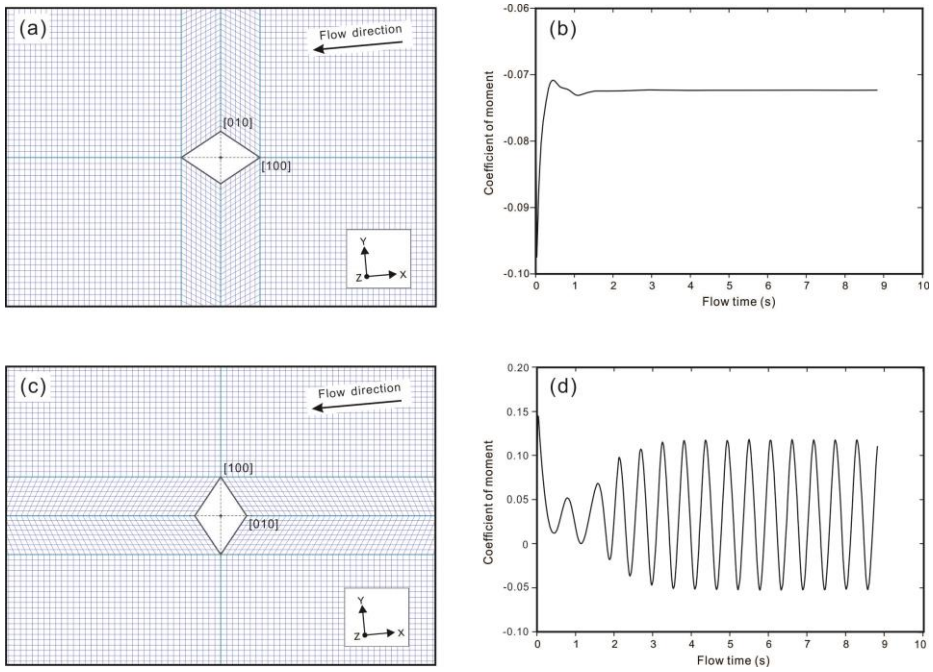

Fig. 3.12. Two-dimensional finite-volume modeling (FVM) for the shape preferred orientation of a lawsonite single crystal under a deforming glaucophane-rich matrix. The shape of a lawsonite single crystal is considered as an ideal rhombic, with a common axis ratio of 1.5, which is displayed on a (001) section as shown in Fig. 11c. Because glaucophane is significantly weaker than lawsonite and the exact viscosity values of glaucophane and lawsonite are unknown, we simplified the modeling by treating lawsonite as a rigid body emerging in a homogeneous incoming fluid with the viscosity of water. As shown in (a) and (c), the flow direction of incoming fluid is consistent with lineation (X). Two extreme cases were considered in calculation: (a, b) Case 1 - The flow direction is at 5 °with the [100] axis of lawsonite; (c, d) Case 2 - The flow direction is at 5 °with the [010] axis of lawsonite. The mesh grids in (a) and (c) were generated using ANSYS ICEM CFD meshing software; and (b) and (d) show variations of the 2D coefficient of moment with time, as calculated using ANSYS Fluent software. The coefficient of moment was calculated from the rotation of rhombic lawsonite around its center point in (a) and (c). It is defined as positive when the rotation is counter-clockwise.

assumption of homogeneous fluid flow employed in this modeling limits an effective application to a three-dimensional case, because the [001] axis of lawsonite would be expected to align in any directions perpendicular to the flow direction and the rotation of lawsonite long axis around foliation cannot be simulated if the fluid flows homogeneously in a 3D space. This pattern of fluid flow is very different from simple shearing in natural rocks which have clear shear planes, and thus a sophisticated 3D numerical simulation employing more appropriate layered flow and incorporating other factors (e.g., grain size, mineral growth) are needed. (2) The exact viscosities of lawsonite and glaucophane are unknown, which is thus incapable of describing the explicit evolution of lawsonite fabric in a geological time-scale. Despite the limitations in current simplified modeling, the consistent modeling result with the observations of the lawsonite LPOs in this study suggests that our 2D numerical simulation still has some merits in this preliminary study.

In this study, the lawsonite fabrics in foliated LBS are similar to those reported by Kim et al. (2013a,b), but are different from those found by Teyssier *et al.* (2010) ([001] axis parallel to lineation; [100] axis normal to foliation) and Fujimoto *et al.* (2010) ([100] axis parallel to lineation; [001] axis normal to foliation). It is difficult to speculate the exact reasons for these different fabrics because the textures of LBS in all these studies are very similar, which all suggest that the lawsonite fabrics were formed due to the same deformation mechanism of rigid-body rotation. Because the fabric produced by rigid-body rotation is supposed to be dominantly controlled by the geometry of the rigid particle, the similar lawsonite fabric is expected to be produced from these lawsonite blueschists. Although we currently have no clear explanation for these different lawsonite fabrics, one possibility which is particularly relevant to lawsonite fabric measurement might be noteworthy. The axis designations of the lawsonite [100] and [010] axis are not consistent in literature: two notation

systems are widely used at present (Baur, 1978; Comodi and Zanazzi, 1996 versus Libowitzky and Armbruster, 1995; Meyer et al., 2001; Pawley and Allan, 2001). If they are used in EBSD measurement, these two different notation systems can thus result in different LPOs with either the [100] or [010] axis of lawsonite aligning sub-parallel to lineation.

3.7.2. LPO variations of glaucophane and lawsonite

Many factors are considered to influence the characteristics of mineral LPO formed by deformation. As described in detail earlier, glaucophane and lawsonite in massive and foliated LBS display perceptibly different LPOs, which are manifested in both fabric type and fabric strength (Figs. 3.5-3.7). Generally, the LPOs are transformed from weak and diffused types in massive LBS, to strong and clustered types in foliated LBS, in response to an increase of deformation or strain. Deformation geometry is another factor that can affect the mineral LPO. Based on the vorticity analysis of foliated LBS, two contrasting deformation geometries – simple shear and pure shear dominant – were recognized, and secondary variations of glaucophane and lawsonite LPOs were also observed between these two deformation geometries. The pure shear dominant samples tend to have strong foliation-parallel girdle distributions of a [001] axis and a (010) pole of glaucophane (Fig. 3.5d, S-type fabric) and a [100] and [010] axis of lawsonite (Fig. 3.7d), whereas the simple shear dominant samples display more lineation-parallel concentrations of a [001] axis of glaucophane (Fig. 3.5c) and a [010] axis of lawsonite (Fig. 3.7c). This feature can be quantitatively displayed using the inverse pole figure J-index (ipfJ) of lineation (*X*) and foliation normal (*Z*) for glaucophane and lawsonite (Table 3.1 and Fig. 3.13). The sum of ipfJ(*X*) and ipfJ(*Z*) can be considered as the fabric strength of inverse pole figures and thus roughly represent the

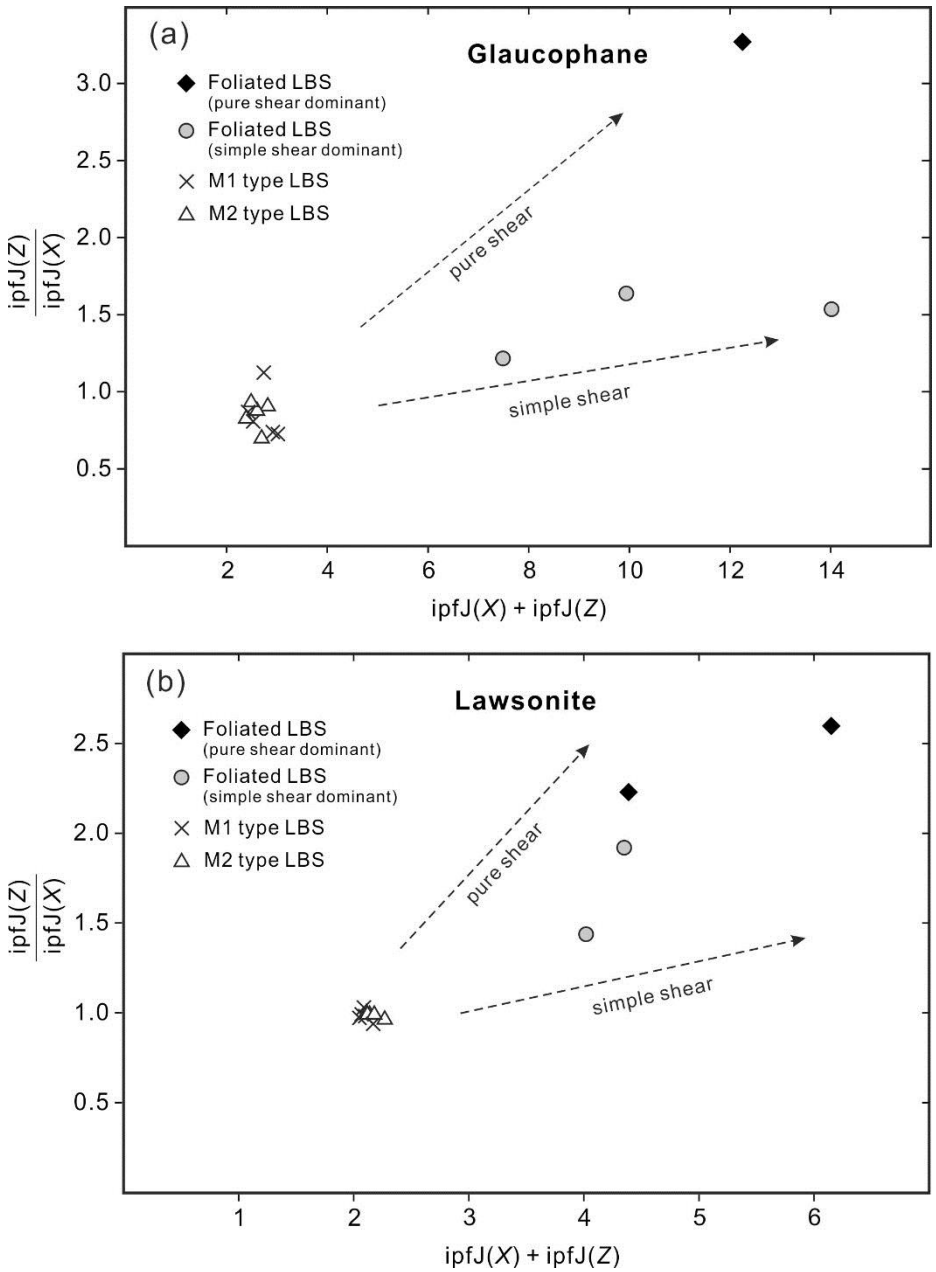

Fig. 3.13. Fabric strength variations of: (a) glaucophane; and (b) lawsonite in massive and foliated LBS. ipfJ(X) and ipfJ(Z) are inverse pole figure J-index of lineation and foliation normal, respectively. Dashed-arrow lines indicate the potential trends of simple shear and pure shear. The ratio of $\mathrm{ipfJ}(Z)/\mathrm{ipfJ}(X)$ can be reliably used to compare the samples with similar fabric strengths, because the non-uniqueness of single ipfJ-index is eliminated in a division operation.

deformation degree, and the ratio of $\mathrm{ipfJ}(Z)/\mathrm{ipfJ}(X)$ indicates the extent of the mineral crystallographic axis orienting perpendicular to foliation relative to aligning parallel to lineation. Because a value of ipfJ equivalent to 1 indicates a random fabric, it suggests a very weak fabric for massive LBS (M1 and M2 type) when the sum of ipfJ(*X*) and ipfJ(*Z*) is slightly higher than 2 for both glaucophane and lawsonite. In contrast, if the sum of ipfJ(*X*) and ipfJ(*Z*) for both glaucophane and lawsonite is very large, it thus indicates a strong fabric, such as foliated LBS. In addition, the ratios of $\mathrm{ipfJ}(Z)/\mathrm{ipfJ}(X)$ for glaucophane and lawsonite are remarkably higher in pure shear dominant samples than simple shear dominant samples, and both of them are higher than that in massive LBS. In another word, the mineral axes tend to be more concentrated perpendicularly to foliation in a coaxial deformation regime, whereas they predominantly become clustered parallel to lineation in non-coaxial deformation geometry. Because glaucophane and lawsonite show the same trend of fabric variation in spite of their different deformation mechanisms, such a variation of mineral fabrics is supposed to be principally controlled by deformation geometry and is irrespective of the deformation mechanism. Similar results have also been implied in the LPO developments of olivine and clinopyroxene due to dislocation creep under simple shear and pure shear deformation regimes, which were modeled using a viscoplastic self-consistent method (VPSC) (Bascou *et al.*, 2002, Tommasi *et al.*, 2000, Tommasi *et al.*, 1999). Therefore, this relationship between mineral LPOs and deformation geometry may provide a useful approach to qualitatively infer the deformation regime through the patterns of mineral LPOs (Fig. 3.13).

3.7.3. Seismic anisotropy of subducting oceanic crust

Subduction zones are seismologically unique areas where trench-parallel

polarization anisotropy is observed in most of the fore-arc regions (e.g., Huang *et al.*, 2011a, Long & Silver, 2008, Long & van der Hilst, 2005, Nakajima & Hasegawa, 2004, Russo & Silver, 1994, Smith *et al.*, 2001, Zhao, 2012). To explain this seismic observation, previous studies proposed that an anisotropic fore-arc mantle is the major source of trench-parallel polarization anisotropy. This anisotropic structure of the fore-arc mantle is formed by a variety of mechanisms, such as mantle flow parallel to trench associated with slab roll-back (Long & Silver, 2008, Russo & Silver, 1994), crustal foundering (Behn *et al.*, 2007) or oblique subduction (Mehl *et al.*, 2003), B-type olivine LPO induced by water (Jung & Karato, 2001a, Jung *et al.*, 2006, Karato *et al.*, 2008, Kneller *et al.*, 2008, Kneller *et al.*, 2005) or pressure (Jung *et al.*, 2009c, Ohuchi *et al.*, 2011), and the LPO of antigorite in the serpentized mantle wedge (Ji *et al.*, 2013, Jung, 2011, Katayama *et al.*, 2009). Some researchers also suggest that rather than the fore-arc mantle, the fore-arc crust is the major source of trench-parallel anisotropy (Huang *et al.*, 2011a). In addition, the subducting oceanic slab is also proposed as a potential contributor for the seismic anisotropies in the subduction zone (e.g., Healy *et al.*, 2009, Wang & Zhao, 2010).

Although it is relatively thin (~7 km), the oceanic crust in a "cold" subducting slab is mainly composed of blueschist which can be seismically very anisotropic. Hence, the contribution of the subducting oceanic crust to the seismic anisotropy in the subduction zone should not be completely ignored. In general, the anisotropic structure of deep-seated blueschist can be manifested in two forms: dehydration-induced fluid-filled cracks (Healy *et al.*, 2009), and the LPO of the constituent minerals (Bezacier *et al.*, 2010b, Cao *et al.*, 2013). In this study, we focus on the latter manifestation. Applying the seismic properties that are obtained from natural blueschists in outcrops to those deep-seated blueschists in subduting oceanic crust may not be apparently

straightforward, mainly because the exhumation-related deformation process can overprint the original deformation textures formed during subduction. Based on the microstructural observations, it is noted that blueschist was most likely plastically deformed in the blueschist facies, which suggests a deep origin, therefore their deformation textures are supposed to reflect the deformation behaviors and seismic properties in the deep subducting oceanic crust although some overprinting of the deformation of rock during exhumation is likely. Moreover, we consider that it is the deformation mechanism and geometry that dominantly control the microstructures of blueschist. Since blueschists are likely to experience the same deformation geometry (simple shear dominant) and the similar deformation mechanism during both subduction and exhumation, the subduction-related deformation is supposed to cause similar deformation texture to those formed during exhumation.

Because glaucophane and lawsonite aggregates display opposite seismic anisotropy patterns (Fig. 3.9; also see Kim et al. 2013a) and an abundance of lawsonite may weaken the fabric strength of glaucophane, a significant weakening of whole-rock seismic anisotropies, particularly polarization anisotropy, is expected to occur in lawsonite blueschist (Figs. 3.9 and 3.10). This counteracting effect between the glaucophane and lawsonite aggregates can induce a significant weaker seismic anisotropy for LBS than that of epidote blueschist, because glaucophane and epidote show similar seismic anisotropy patterns (Cao *et al.*, 2013, Fujimoto *et al.*, 2010, Kim *et al.*, 2013a). As shown in Table 3.2 (excluding one outlier of foliated epidote blueschist), the magnitude of the polarization anisotropy of foliated lawsonite blueschist (max. AV_s = 5.5–9.9%) is about 25% lower than that of foliated epidote blueschist (max. AV_s = 6.8–11.3%), whereas there is no significant difference in the P-wave anisotropy between foliated lawsonite blueschist (AV_p = 12.0–19.7%) and foliated epidote blueschist (AV_p = 11.8–19.6%). In addition, the deformation

degree can also significantly affect the magnitude of seismic anisotropy, as the massive lawsonite blueschist exhibits about 65% lower P-wave anisotropy (AV_p = 2.7–7.9%) and about 60% lower S-wave polarization anisotropy (max. AV_s = 1.6–4.5%) than those of foliated lawsonite blueschist. Cao *et al.* (2013) suggested that a trench-parallel polarization anisotropy with a moderate delay time (0.1–0.3s) in a high-angle subducting slab (> 45–60 °) can be produced, assuming that the subducting oceanic crust is dominated by strongly foliated epidote blueschist. However, this delay time would be reduced down to 0.08–0.23s (~25% lower) if the strongly deformed lawsonite blueschist dominates in the subducting oceanic crust, and it would become further smaller (down to 0.03–0.09s, ~60% lower) if the weakly deformed lawsonite blueschist is assumed to be dominant in the subducting oceanic crust. Therefore, the delay time of 0.03–0.09s and 0.1–0.3s can be considered as the lower and upper bound induced by an actual subducting oceanic crust, respectively. The contribution of deformed blueschists to the seismic anisotropy would thus be much smaller than originally thought.

In addition, it is noteworthy that Teyssier *et al.* (2010) reported a unique LPO of lawsonite, in which lawsonite aggregate aligns in a fast V_p direction ([001] axis) parallel to the fast V_p direction of the glaucophane aggregate ([001] axis), and the slow V_p direction ([100] axis) of the lawsonite aggregate is aligned consistently with the slow V_p direction of the glaucophane aggregate ([100] axis). In this case, it is possible that the seismic anisotropies of lawsonite blueschist are strengthened instead of weakened, and thus a larger delay time is expected to be generated by the subducting oceanic slab. However, before drawing this conclusion, further research on the causes of the different LPOs of lawsonite is required.

3.8. Conclusions

As generally believed, lawsontie bluschist (LBS) is an important component in the 'cold' subducting oceanic crust, and thus able to affect the rheological and seismic properties in the subducting slab. In this study, we distinguished and investigated the microstructures and petro-fabrics of two different types of lawsonite blueschists (i.e. massive and foliated lawsonite blueschist) in North Qilian suture zone, NW China. Based on the microstructures, we found that the straining of glaucophane and lawsonite crystals in foliated lawsonite blueschist were accommodated by different deformation mechanisms. Namely, glaucophane and lawsonite are dominantly formed by the deformation mechanism of dislocation creep and rigid-body rotation, respectively. Despite of the different deformation mechanisms, both glaucophane and lawsonite present pronounced LPOs. Specifically speaking, the glaucophane is mainly characterized by the [001] axis aligning parallel to lineation and the [100] axis and (110) pole plunging perpendicular to foliation; whereas the LPO of lawsonite features the maximum [010] axis concentrated close to lineation and the [001] axis strongly clustered normal to foliation.

This observed LPO of lawsonite resembles that reported by Kim *et al.* (2013a), Kim *et al.* (2013b), but diverges from the results from Fujimoto *et al.* (2010), Teyssier *et al.* (2010). To understand the reasons for these discrepancies, we tentatively conducted a two-dimensional numerical modeling of lawsonite LPO development using the finite-volume method (FVM). The results showed that the preferred orientation of [010] axis of lawsonite parallel to lineation is more stable than [100] axis aligning parallel to lineation, which is consistent with the observation in this study. In addition, we also performed a kinematic vorticity analysis based on the orientation of lawsonite crystals in the matrix. The result suggested that both pure shear dominant (W_m = 0.18–0.26) and

simple shear dominant (W_m = 0.86–0.93) deformation regimes are present in foliated LBS. These different deformation regime result in different LPO patterns of lawsonite and glaucophane. Principally, the [001] axis and (010) pole of glaucophane, and the [100] and [010] axes of lawsonite, tend to distribute in a foliation-parallel girdle in the pure shear dominant samples, but simple shear dominant samples display more lineation-parallel concentrations of a [001] axis of glaucophane and a [010] axis of lawsonite.

Because the whole-rock seismic anisotropies in foliated LBS are significantly higher than those in massive LBS (as indicated by the much stronger mineral LPOs in foliated LBS than in massive LBS), a counteracting effect on seismic anisotropies occurs between glaucophane and lawsonite is expected. This negative influences will thus lead to a much weaker seismic anisotropic properties in the subducting oceanic crust than previously estimated from strongly deformed epidote blueschist. The estimated delay time of fast S-wave polarization anisotropy induced by an actual subducting oceanic crust with a high subducting angle (> 45–60 °) is expected to range from 0.03–0.09s (lower bound for massive LBS) to 0.1–0.3s (upper bound for foliated epidote blueschist).

CHAPTER 4

Plastic deformation and seismic implications in the fore-arc mantle: Constrains from Yushigou harzburgites in North Qilian suture zone, NW China

Abstract

The fore-arc mantle above the subducting slab is a unique site where complex partial melting, melt-rock interaction, mantle deformation, dehydration and rehydration that occurred in an evolutionary subduction zone can be recorded. To constrain these geological and geodynamic processes, we analyzed the deformation microstructures, mineral crystal preferred orientations (CPOs), chemical compositions of mineral and whole rock, as well as water concentrations in the natural harzburgites which occur as exhumed massifs in the North Qilian suture zone, NW China. These harzburgites are highly refractory in mineral modal (very low content of clinopyroxene) and chemistry compositions (spinel Cr# ~ 0.6–0.7, olivine Mg# ~ 0.91–0.93), confirming their genesis as high-degree (~ 25–30%) partial melting residue at a young and warm fore-arc setting. Pronounced CPOs are observed in olivine and orthopyroxene. Detailed analysis of the mineral textures, CPOs and rotation axes distributions suggest that the plastic deformations of olivine and pyroxenes are accommodated by activating a series of dislocation systems at low-pressure (< 2–3 GPa), high-temperature (~ 1200–1350 °C), low-stress (< 4 MPa) and

dry conditions. Olivine (A/-D-type fabric) showed dominant (010)[100], secondary (001)[100] and other minor [100]-slip, {0kl}[100] and [001]-slip systems; Orthopyroxene showed dominant (100)[001] and secondary (010)[001], (100)[010], (100)[0vw] slip systems. The water contents are extremely low in orthopyroxene (38–44 wt. ppm) and equilibrated olivine (4–7 wt. ppm) and bulk-rock (9–14 wt. ppm), which is mainly credited to high degree of partial melting and consistent with the olivine dry A-/D-type CPO. Based on these observations, an improved schematic model about the olivine fabric distributions in the subduction zone is proposed. In this model, the A-/D-type olivine fabric is supposed to be prevalent in the fore-arc lithospheric mantle. The contradicting polarizing directions of A-/D-type olivine fabric with other anisotropic sources (e.g., B-type olivine fabric and oriented serpentinite layers) may weaken the contribution of trench-parallel seismic anisotropy that result from deformed fore-arc mantle, and thus provide an alternative explanation on the weak or nearly null delay times that were detected at some fore-arc regions. Additionally, the seismic properties of two end-member antigorite orientations (topotactic growth versus deformation-induced antigorite fabrics) associated with anisotropic harzburgite are also discussed. The low seismic velocities, high Vp/Vs or Poisson's ratios and large trench-parallel seismic anisotropies which are commonly observed in a hydrous fore-arc mantle might be tentatively explained by the combination of these two serpentinization processes.

4.1. Introduction

Investigating the compositions, thermal and seismic structures, and deformation characteristics of fore-arc mantle is important for constructing the

integrated formation and evolution patterns of a subduction zone. Over the past two decades, an increment of progress has been achieved in understanding the physical and chemical properties of fore-arc mantle. For instance, an abundance of seismic and geothermal observations on modern mature fore-arc mantles worldwide have revealed a suite of prominent features such as low heat flow, low seismic velocities, low seismic attenuation (high Q), low seismicity and high Vp/Vs (Poisson's) ratio. These distinctive geophysical features convergently suggest that the fore-arc mantle is conductively cooled by a underlying "cold" subducting slab and is hydrated or metasomatized (particularly serpentinized) by reacting with slab-derived silica-rich fluids (e.g., Bostock *et al.*, 2002, Brocher *et al.*, 2003, Currie & Hyndman, 2006, Davey & Ristau, 2011, DeShon & Schwartz, 2004, Hyndman & Peacock, 2003, Kamiya & Kobayashi, 2000, Kim *et al.*, 2013c, Kim *et al.*, 2012, Tibi *et al.*, 2008, Zhao, 2001). Trench-parallel fast shear wave polarization anisotropy is another commonly observed seismological phenomenon in a fore-arc region (e.g., Huang *et al.*, 2011b, Iidaka *et al.*, 2014, Kneller & van Keken, 2007, Long & Silver, 2008, Long & van der Hilst, 2005, Nakajima & Hasegawa, 2004, Park & Levin, 2002, Rabbel *et al.*, 2011, Russo & Silver, 1994, Smith *et al.*, 2001, Wölbern *et al.*, 2014, Wagner *et al.*, 2013), and one of the main sources for this anisotropy is the deformed fore-arc mantle wedge above slab: strained peridotite under corner flow (wet olivine B-type fabric) (e.g., Jung & Karato, 2001a, Kneller *et al.*, 2005, Kneller *et al.*, 2007, McCormack *et al.*, 2013, Nakajima & Hasegawa, 2004, Nakajima *et al.*, 2006, Ohuchi *et al.*, 2012) or arc-parallel flow (dry olivine A- or D-type and moderately wet olivine E-type fabrics) (e.g., Anglin & Fouch, 2005, Behn *et al.*, 2007, Kneller & van Keken, 2007, Lin & Kuo, 2013, Mehl *et al.*, 2003, Rabbel *et al.*, 2011, Smith *et al.*, 2001, Wang & Zhao, 2008), and oriented layers of antigorite, chlorite and other hydrous phases (e.g., Brownlee *et al.*, 2013, Ji *et al.*, 2013, Jung, 2011,

Katayama *et al.*, 2009, Kim & Jung, 2014, Mainprice & Ildefonse, 2009, Mookherjee & Mainprice, 2014, Morales *et al.*, 2013, Olive *et al.*, 2014, Shao *et al.*, 2014).

In comparison with these numerous data acquired by diverse geophysical methods, relatively smaller amount of geochemical constraints were obtained from examining the natural samples originated from a confirmative fore-arc mantle. For example, recent oceanic dredging and drilling at Izu-Bonin/Ogasawara-Mariana fore-arcs, southern Tore-Madeira Rise and South Sandwich fore-arcs recovered a series of serpentinized peridotites (e.g., Ishii *et al.*, 1992, Merle *et al.*, 2012, Parkinson & Pearce, 1998, Pearce *et al.*, 2000). These rocks consistently displayed highly refractory and fluid-affected geochemical features as well as complex melt/fluid-rock reaction behaviors, which are distinguishable from those abysmal peridotites (e.g., Ishii *et al.*, 1992, Merle *et al.*, 2012, Parkinson & Pearce, 1998, Pearce *et al.*, 2000). These similar results were also gathered from some modern inland fore-arc peridotite xenoliths or massifs (e.g., Ionov, 2010, Ishikawa *et al.*, 2007). However, the deformation characteristics and seismic properties of natural fore-arc peridotites, as well as their seismic implications in the fore-arc regions, were only occasionally addressed. The available data lead to a general conclusion that the deformation behaviors and mantle flow patterns could be fairly complicated in a fore-arc mantle, which are embodied by the findings of variable olivine fabrics (Harigane *et al.*, 2013, Jung, 2011, Mehl *et al.*, 2003, Michibayashi *et al.*, 2009b, Michibayashi *et al.*, 2007, Mizukami *et al.*, 2004, Soustelle & Tommasi, 2010, Soustelle *et al.*, 2013, Soustelle *et al.*, 2010, Tasaka *et al.*, 2008). Therefore, to better understand the enigmatic geodynamic processes in fore-arc mantle, more in-depth studies and concrete models that incorporate spatio-temporal variations of partial melting, dehydration-hydration, metasomatism and deformation are needed.

The main purposes of this study are attempting to unravel the deformation behaviors in the fore-arc mantle by examining the microstructures and olivine fabrics of natural peridotites (Yushigou harzburgite) which were believed to originate from an ancient fore-arc mantle. This fore-arc region was formed owing to the subduction of Qilian Ocean (an eastern branch of the Iapetus Ocean) plate beneath Alashan block (a separated Paleoproterozoic terrane from the western part of the North China Craton) at Early Paleozoic era (~520–490 Ma) (Dan *et al.*, 2012, Song *et al.*, 2013b, Song *et al.*, 2014). Later, the microstructure and fabric data obtained in this study will be combined with the measurement of water content, mineral chemistry, geochemical results from this and previous studies to formulate an improved schematic model to illustrate the spatio-temporal distributions and evolutions of olivine fabrics in a subduction zone. Lastly, the seismic implications of deformation-induced anisotropic harzburgites and associated serpentinization processes in the fore-arc mantle will be discussed.

4.2. Geological setting

The present-day manifestations of the ancient subduction of Qilian Ocean plate beneath Alashan block and following collision between Qilian-Qaidam block (an affinity with the Yangtze Craton) and Alashan block are preserved as a suite of ophiolite sequence, island-arc igneous complex, high-pressure low-temperature metamorphic rocks, as well as associated flysch formation, molasses construction and sedimentary covers in the North Qilian orogen, NW China (Fig. 4.1; reviews of Song *et al.*, 2013b, Song *et al.*, 2014, Song *et al.*, 2009a). This North Qilian orogenic belt (or North Qilian suture zone) is NW-SE elongated and currently belongs to the central part of the Central China orogenic belt. Specifically, the North Qilian orogenic belt extends

northwestward into the Tarim Craton and is structurally offset by the large left-lateral Altyn-Tagh Fault system; while its southeastern end is connected to the western limb of Qinling-Dabie orogen which separates the North China Craton on the north and the Yangtze Craton on the south (Fig. 4.1a).

Unlike most of the other ophiolite sequences which represent segments of oceanic lithosphere of the Qilian Ocean formed at seafloor spreading centers or mid-ocean ridge (MORB-type) in the North Qilian orogenic belt, the ultramafic assemblage in the Yushigou ophiolite suite stands for a remnant of a fossil wedge mantle (or referred to as supra-subduction zone type, i.e. SSZ-type) which was exhumed in response to the tectonic collision (Song *et al.*, 2009b). As shown in Fig. 4.1c, the Yushigou ophiolite occurs as various-sized nappes over-thrusting onto the Precambrian crystalline basement of the Central-Qilian block. They consist of mantle peridotites, gabbroic cumulates, pillow basalts and marine sedimentary rocks. The ultramafic nappes in the east are strongly elongated and bounded by the northern thrusting fault in parallel with the trend of orogenic belt, whereas the fault-bounded nappe in the west (with the largest size ~25 km^2) is relatively weakly stretched and oriented in the similar direction as former. Because of the intensive and pervasive serpentinization in the outcrops, as well as the tough plateau environment, the original sub-types of ultramafic rocks have not been well distinguished and mapped yet. However, the collections of fresh samples suggest that the peridotite bodies are likely dominated by harzburgite with minor dunite and pyroxenite occurring as dikes/veins within harzburgite (Song *et al.*, 2013b, Song *et al.*, 2009b). The precise age of the Yushigou peridotite is unknown. However, a SHRIMP zircon age of 550 ± 17 Ma was obtained from the spatially associated gabbros (Shi *et al.*, 2004), which is earlier than the age of high pressure metamorphism (~466 ± 10 Ma) determined from eclogites outcrops to the southeast in the regions nearby Qilian town (Song *et al.*, 2004b).

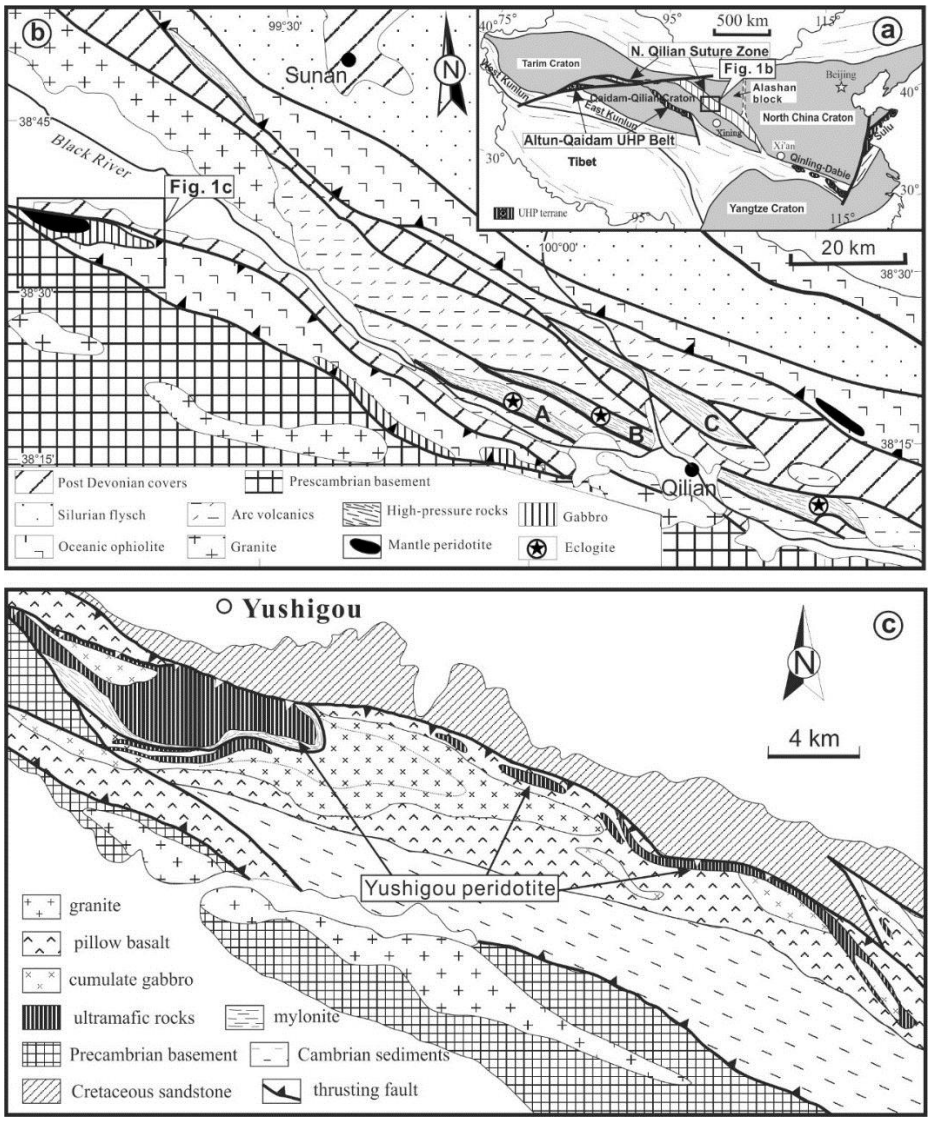

Fig. 4.1. (a) Schematic maps showing the major tectonic units of China and (b) lithological complexes in the middle part of the North Qilian suture zone. A, B and C denote three high-grade blueschist sub-belts. (c) The enlarged geological map showing the Yushigou ophiolite suite and its surrounding rock types. The sub-types of ultramafic rocks are not well distinguished yet. Modified after Song *et al.* (2006, 2009a, 2012).

4.3. Microstructures and petrology

Five of the fresh harzburgites collected from the largest ultramafic block in the west were selected in this study. They exhibit continuous gradation of coarse-grained texture from weak to clear porphyroclastic characteristics (Fig. 4.2). The analysis of mineral modal composition categorizes them as typical spinel harzburgites, which shows dominant mineral phases of olivine (Ol, 81–87 vol.%) and orthopyroxene (Opx, 11–17 vol.%), with minor clinopyroxene (Cpx, ~1–2 vol.%) and spinel (Sp, ~1.0 vol.%). The grain size of olivine and Opx varies widely in a similar range from 100 to 7000 μm. All samples present a gentle foliation defined by elongated olivine and Opx crystals which have medium to large grain-sizes and aspect ratios (> 2:1). The widely-spaced subgrain boundaries with a spacing range (50–1000 μm) are ubiquitously observed in most olivine grains (Figs. 4.2 and 4.3). In contrast, weak undulose extinctions and kink bands are occasionally found in Opx crystals (Figs. 4.3a and b). The subgrain boundaries and kink bands are preferably oriented sub-perpendicular to the long axis of crystals and foliation in all samples (Figs. 4.2 and 4.3). The most prominent textures of olivine and Opx are their xenomorphic shapes. The grain and phase boundaries between olivine and Opx are rarely straight, but prevailingly vary from curvilinear, serrated to irregular (Figs. 4.2 and 4.3). Locally, anhedral subgrain-bearing olivine crystals that show grain-scale interpenetrating texture are observed, implying intense syn-kinematic grain boundary migrations at a length scale comparable to grain size (Figs. 4.3e and f). The small polygonal-shaped olivine grains showing 120 °triple junctions are also occasionally observed in some domains (Fig. 4.3a). Clinopyroxene usually occurs as small irregular and interstitial phase (<300 μm) commonly surrounded by olivine grains and occasionally neighbored by Opx (Figs. 4.3a, b and e). Similar to most Opx crystals that contain abundant Cpx exsolution

lamellae (Fig. 4.3b and e), the Opx exsolution lamellae is also observed in most Cpx grains (Fig. 2f in Song *et al.*, 2009b). These exsolution textures of pyroxene suggest that both Opx and Cpx are primary in origin, whereas secondary pyroxenes are not explicitly recognized. The spinel is also anhedral in shape (~500 μm) and always occurs in the junctions of olivine and Opx (Fig. 4.3c). Additionally, abundant fluid inclusions rich in CH_4 + C + H_2 were also reported in olivine crystals but not in other phases (Song *et al.*, 2009b).

In agreement with the refractory nature, the mineral compositions of olivine, Opx, Cpx and spinel in Yushigou harzburgite all show very depleted characteristics that are indicative of high-degree partial melting (Fig. 4.12; Song *et al.*, 2009b). Both olivine and Opx have high magnesium number (Mg# = Mg/[Mg + Fe^{2+}]) which varies in the same range of 91–93. This value becomes even higher in Cpx (Mg# = 95–98). Besides, Opx crystals display flat distribution of low Al_2O_3 concentration from core to rim (1.02–1.84 wt.%). The Al_2O_3 content is similar to that of Cpx (1.02–1.91% wt.%). Similarly, the Al_2O_3 content is also very low in spinel, leading to a high chromium number (Cr# = Cr/[Cr + Al]) of 0.58–0.67. In addition, spinel also has very low TiO_2 content (< 0.1 wt.%). Likewise, the whole-rock compositions are also highly depleted in both major and trace elements: high MgO (~ 46 wt.%) and FeO (7.13–8.35 wt.%) and low TiO_2 (< 0.01 wt.%), Al_2O_3 (0.40–0.65 wt.%), CaO (0.30–0.54 wt.%), Na_2O (< 0.05 wt.%) contents and low HREE abundances (0.01–0.20 chondrite value).

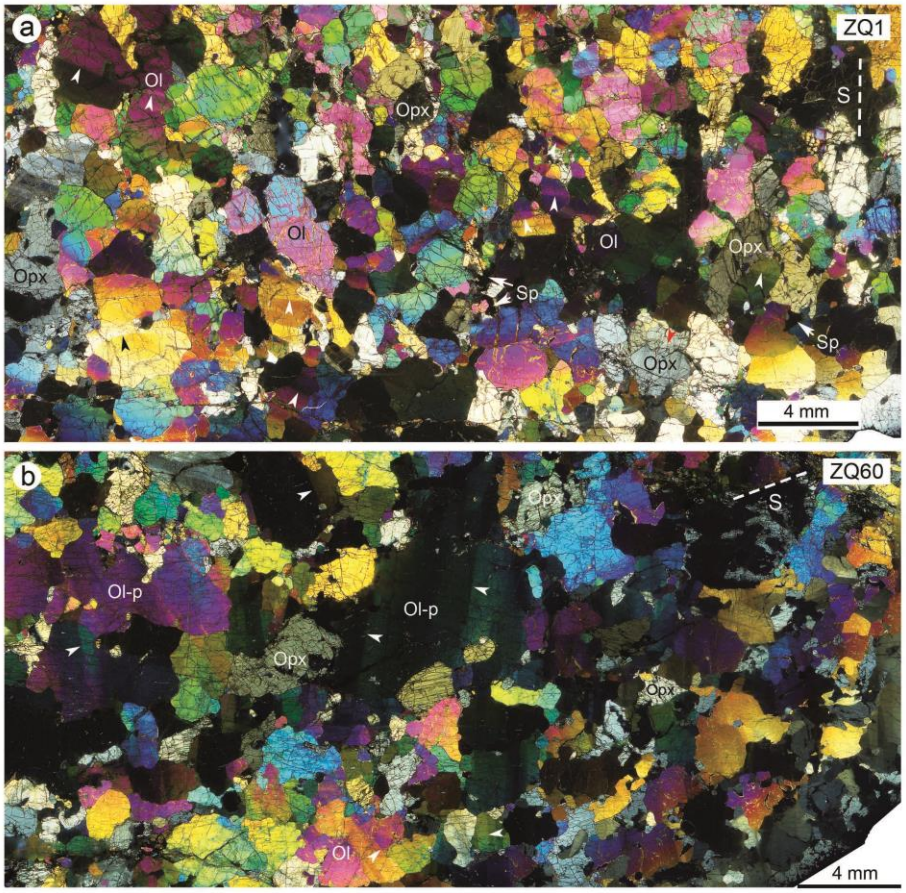

Fig. 4.2. Photomicrographs in cross-polarized light showing the (a) weak and (b) clear coarse-grained porphyroclastic textures, in which olivine porphyroclasts (Ol-p) are distinguishable from their surrounding smaller olivine and Opx grains. The trace of foliation (S) is indicated by preferred orientations of those olivine and Opx crystals with large grain size and aspect ratios, and is denoted as dashed white lines. The subgrain boundaries in olivine and kink bands in Opx are indicated by white and red arrow heads, respectively.

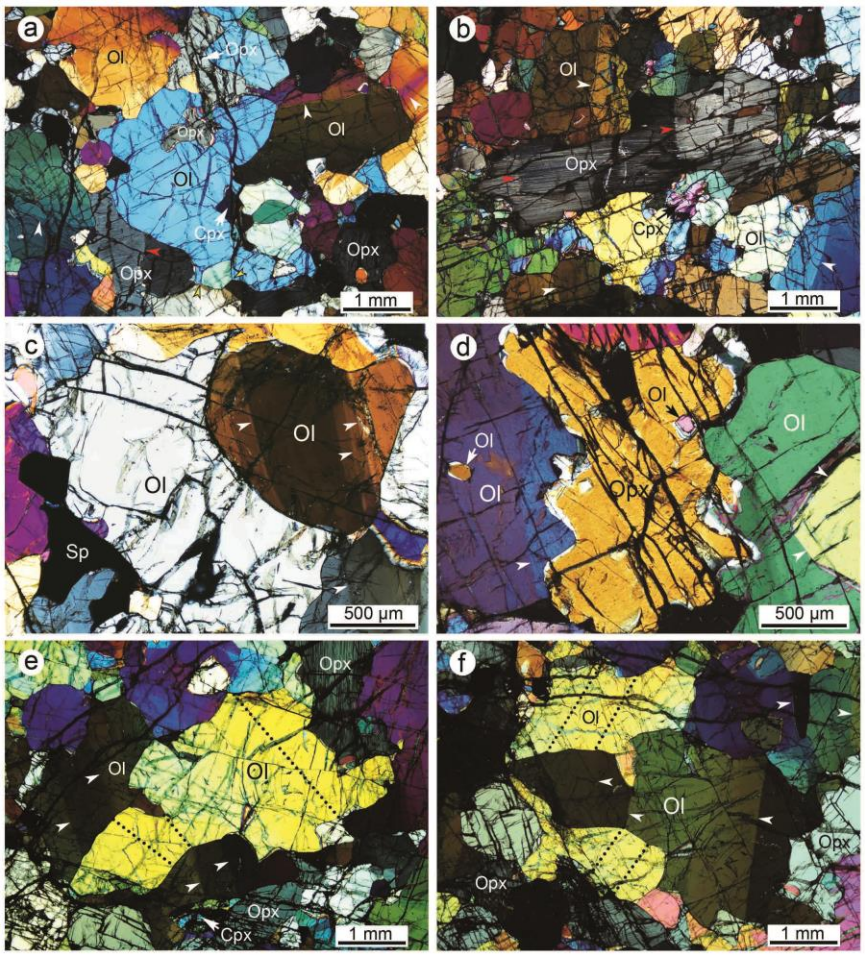

Fig. 4.3. Photomicrographs in cross-polarized light showing representative microstructures of spinel harzburgites. Subgrain boundaries in numerous olivine grains and kink bands in a few Opx grains are indicated by white and red arrow heads, respectively. (a) Interlobate texture of olivine and Opx grains. The shape of Opx crystals are quite irregular with finger-like protrusions penetrating into neighboring olivine crystals. A polygonal olivine crystal with 120 °triple junctions is denoted by yellow arrow head. (b) An elongated primary Opx crystal exhibiting dense Cpx exsolution lamellae and widely-spaced kink bands parallel and perpendicular to its long axis, respectively. The boundaries of this Opx grain is embayed with neighboring olivine crystals. (c) Anhedral olivine crystals showing curvilinear boundaries and cusps into other olivine grain. An anhedral "puppy-like" spinel crystal is also displayed in the lower left of image. (d) An Opx crystal presenting sinuous phase boundaries with two neighboring olivine grains. Small rounded olivine grains enclosed by olivine and Opx crystals are also seen. (e and f) Cross-polarized images taken from two different extinction directions at the same domain showing the grain-scale interpenetration of two coarse olivine grains. Note that one olivine grain is almost cut through by the other. The subgrain boundaries of two olivine crystals are oriented sub-parallel to the other and indicated by white arrow heads and black dotted lines.

4.4. Determination of the dislocation slip systems

4.4.1. Crystal preferred orientations

4.4.1.1. Analytical procedure

Measuring the mineral crystal preferred orientations (CPOs) from a thinsection with known structural orientation is the most conventional method to infer the activated dislocation slip systems. The precision and efficiency of CPO analysis process can be significantly increased by using an electron-backscattered diffraction (EBSD) system (Prior *et al.,* 1999). In general, the thinsection is cut in XZ plane which is parallel to the lineation and perpendicular to the foliation, so that the inference of slip system can be eased. In this case, the preferred orientations of crystallographic axes parallel to the lineation and normal to the foliation correspond to the slip direction and slip plane, respectively. In this study, we used these thinsections cut in the most probable XZ plane by analyzing the shape preferred orientation (SPO) of the clearly elongated olivine and Opx large grains in three orthogonal planes from a specimen. These thinsections were later carefully polished stepwise using 600 to 6000 mesh alumina polishing powders, 1 μm diamond paste and SYTON (0.06 μm colloidal silica) fluid until the ultimate chemical-mechanical polishing. To prevent charging and to obtain the sharpest electron diffraction patterns (Kikuchi bands) in the SEM, thinsections were moderately coated with ~3 nm thick carbon layer before the CPO analysis.

Lastly the CPO measurements were conducted using the SEM-EBSD facility at School of Earth and Environmental Sciences, Seoul National University. The system is running at a high vacuum environment with experimental conditions of 20 kV acceleration voltage, 15 mm working distance and spot size of 60. The surface of thinsection is tilted at 70 °to interact

with a vertically incident electron beam. The Kikuchi bands are generated from diffracted electrons and are captured on a phosphor screen. We manually acquired and indexed the diffraction patterns which are different between neighboring grains over most area of the whole thinsection. This procedure was conveniently done using the HKL CHANNEL 5.0 software. The CPO result obtained in this study is similar to the CPO acquired using one measurement per grain methods in an automatic EBSD mapping.

To quantify the CPO strength, both M-index (Skemer *et al.*, 2005) and J-index (Bunge, 1982) were used. The M-index describes the differences of uncorrelated misorientation angle distributions between observed fabric and theoretically random fabric. It ranges from 0 (random) to 1 (single crystal). The J-index (or texture index) is volume-averaged integral of squared orientation density. It has a value of 1 (random) to infinity (single crystal), but most natural peridotites show values between 2 and 20 (Ben Ismaïl & Mainprice, 1998, Tommasi *et al.*, 2000). The J-index of all samples in this study was calculated using the MTEX toolbox for MATLAB with a kernel half width of 10° (Bachmann *et al.*, 2010). In a similar manner, we also used pfJ-index to describe the sharpness or strength of a pole figure for each given crystallographic axis. It also has a minimum value of 1 for random distribution, whereas the maximum value is dependent on the crystal symmetry and the symmetry of the crystal direction (Michibayashi *et al.*, 2006b). In the case of olivine and Opx, the [100], [010] and [001] axes are all in two-fold rotation symmetry, thus the pfJ values can be directly compared. In addition, we performed an eigenvalue analysis to quantify the shape of the crystallographic fabrics using the point (*P*), girdle (*G*) and random (*R*) fabric indexes (Vollmer, 1990). For each principal crystallographic axis, these three fabric indexes can be calculated from three normalized eigenvalues (λ_1, λ_2, λ_3) as $P = \lambda_1 - \lambda_3$, $G = 2(\lambda_2 - \lambda_3)$ and $R = 3\lambda_3$. In a second-order analysis, we employed a shape parameter (*K*) defined by

$K = \ln(\lambda_1 - \lambda_2)/\ln(\lambda_2 - \lambda_3)$ to better constrain the difference between point and girdle fabrics, as $K > 1$ and $K < 1$ indicate more point and girdle distributions in a pole figure, respectively.

4.4.1.2. Results

As shown in Fig. 4.4, the orientations between $[100]_{Ol}$ and $[001]_{Opx}$ and between $[010]_{Ol}$ and $[100]_{Opx}$ are fairly consistent, their maximum tend to align sub-parallel to lineation and sub-perpendicular to foliation, respectively. In addition, we also observed some secondary components of $[001]_{Ol}$ and $[010]_{Opx}$ plunging at high angle to the foliations, as well as a weak foliation-parallel girdle of $[001]_{Opx}$ in some samples (Fig. 4.4). These results thus suggest that olivine was probably deformed by dominant (010)[100] and secondary (001)[100] dislocation slip systems, whereas the deformation of Opx was controlled by dominant (100)[001] and secondary (010)[001] slip systems. The further shape analysis of olivine CPO suggested that olivine [100] and [010] axes are plotted in point and girdle field, respectively; whereas [001] axis is located close to the boundary between random and girdle (Fig. 4.5). These results agree well with shape parameter (*K*) which is larger and smaller than 1 for [100] and [010] axes of olivine, respectively (Table 4.2). This type of olivine CPO was named as axial-[100] or [100]-fiber pattern or A-/D-type fabric, which has been widely observed in natural peridotites (e.g., Baptiste *et al.*, 2012, Bascou *et al.*, 2008, Falus *et al.*, 2008, Falus *et al.*, 2011, Frets *et al.*, 2014, Higgie & Tommasi, 2012, Jung *et al.*, 2009b, Kaczmarek & Tommasi, 2011, Kamei *et al.*, 2010, Le Roux *et al.*, 2008, Michibayashi *et al.*, 2006a, Michibayashi *et al.*, 2006b, Michibayashi & Oohara, 2013, Michibayashi *et al.*, 2009b, Morales & Tommasi, 2011, Palasse *et al.*, 2012, Satsukawa & Michibayashi, 2014, Satsukawa *et al.*, 2010, Soustelle *et al.*, 2013, Soustelle *et*

al., 2010, Tommasi *et al.*, 2004, Tommasi *et al.*, 2006, Vonlanthen *et al.*, 2006, Warren *et al.*, 2008, Zaffarana *et al.*, 2014) and experimental samples (e.g., Bystricky *et al.*, 2000, Carter & Ave'Lallemant, 1970, Hansen *et al.*, 2014, Zhang *et al.*, 2000). In contrast, the [001] axis of Opx fall into both point (K >1) and girdle (K <1) regions with high components of random distribution; whereas the [010] and [100] axes are distributed in random field but less random for [100] axis (Fig. 4.5), which agrees with more activation of (100)[001] than (010)[001] slip systems as inferred from pole figures. This is the most common Opx CPO pattern that has been observed in both naturally and experimentally deformed orthopyroxene (e.g., Frets *et al.*, 2012, Harigane *et al.*, 2013, Jung *et al.*, 2013, Jung *et al.*, 2010, Le Roux *et al.*, 2008, Manthilake *et al.*, 2013, Naz é*et al.*, 1987, Palasse *et al.*, 2012, Soustelle *et al.*, 2009, Soustelle *et al.*, 2013, Tommasi *et al.*, 2006, Tommasi *et al.*, 2008, Wang *et al.*, 2013b). The oblique angle between the maximum of olivine [100] and Opx [001] axes is estimated to be 18–36° (Table 4.1, Fig. 4.4), which is a common value observed in naturally deformed peridotites (e.g., Le Roux *et al.*, 2008, Soustelle *et al.*, 2010, Tommasi *et al.*, 2004, Tommasi *et al.*, 2006) and is usually attributed to the lower finite strains accommodated in stronger Opx than olivine crystals (Wenk *et al.*, 1991). Despite limited number of grains, the Cpx still exhibits a discernable CPO pattern which resembles the CPO of Opx.

As shown in Fig. 4.6 and Table 4.1, the CPO strengths of olivine and Opx vary in small ranges and olivine has relatively stronger fabric than Opx in the studied samples (M_{Ol} = 0.21–0.32, J_{Ol} = 4.19–7.01; M_{Opx} = 0.11–0.20, J_{Opx} = 4.02–5.92). Their CPO strengths seems uncorrelated as the strongest olivine and Opx CPOs are in sample ZQ48 and ZQ1, respectively. Most notably, the fabric strength orders of three principal crystallographic axes of olivine and Opx are consistent with all studied samples:

Olivine: $pfJ_{[100]} > pfJ_{[010]} > pfJ_{[001]}$ versus Opx: $pfJ_{[001]} > pfJ_{[100]} > pfJ_{[010]}$.

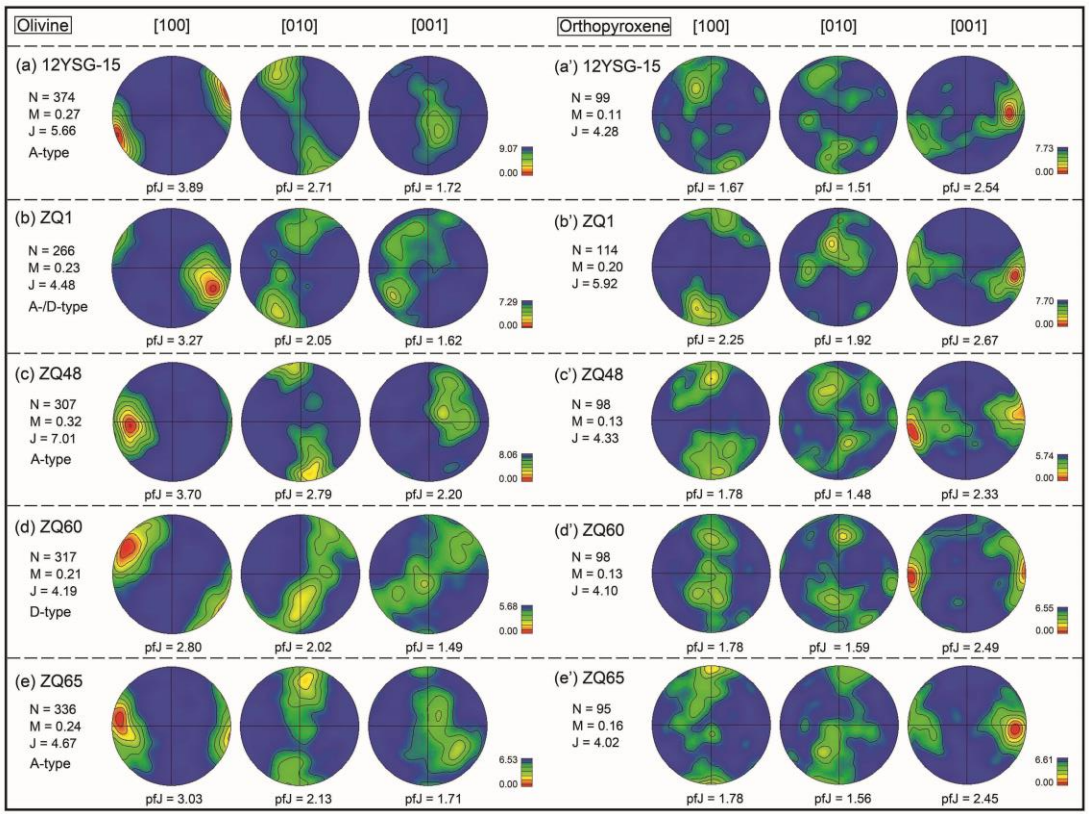

Fig. 4.4. Crystallographic preferred orientation of (a-e, left column) olivine and (a'-e', right column) orthopyroxene. Pole figures are projected on equal-area and lower-hemisphere stereonets and contoured with half width of 20 °and cluster size of 5 °. N is grain number, M is M-index, J is J-index, and pfJ is pfJ-index. E-W is lineation and N-S is foliation-normal.

Table 4.1. Summary of results

Sample	Mineral volume proportion				CPO strength[a]				$Ol_{[100]\ max.} \angle Opx_{[001]\ max.}$[b]
	Ol	Opx	Cpx	Sp	J_{Ol}	M_{Ol}	J_{Opx}	M_{Opx}	
12YSG-15	81	17	1-2	1	5.66	0.27	4.28	0.11	35 °
ZQ1	82	16	1-2	1	4.48	0.23	5.92	0.2	18 °
ZQ48	86	12	1-2	1	7.01	0.32	4.33	0.13	22 °
ZQ60	85	13	1-2	1	4.19	0.21	4.10	0.13	33 °
ZQ65	87	11	1-2	1	4.67	0.24	4.02	0.16	36 °

Sample	Water content (wt. ppm)				Olivine (μm)		Stress (MPa)[g]			Seismic anisotropy (%)[h]	
	$Ol_{meas.}$ (N)	$Ol_{calc.}$[c]	$Opx_{meas.}$ (N)	Bulk[d]	Grain size[e]	Subgrain size[f]	GSP	SGSP_1	SGSP_2	AVp	max. AVs
12YSG-15	7 ±3 (17)	4.9 ±0.5	44 ±5 (15)	11.6 ±1.3	2340 ±750	350 ±170	$4.0^{+1.4}_{-0.8}$	$1.7^{+3.4}_{-0.8}$	$0.7^{+1.3}_{-0.3}$	12.5	8.13
ZQ1	6 ±3 (17)	4.6 ±0.5	41 ±5 (19)	10.5 ±1.2	3480 ±980	320 ±150	$3.0^{+0.9}_{-0.5}$	$2.0^{+3.5}_{-0.9}$	$0.8^{+1.3}_{-0.4}$	10.9	7.74
ZQ48	17 ±9 (11)	7.3 ±0.9	66 ±9 (13)	14.2 ±1.9	3170 ±1000	250 ±120	$3.2^{+1.1}_{-0.6}$	$2.9^{+5.5}_{-1.4}$	$1.2^{+2.0}_{-0.5}$	12.7	8.52
ZQ60	7 ±1 (6)	4.2 ±0.4	38 ±4 (6)	8.7 ±0.9	3540 ±1370	360 ±200	$3.0^{+1.3}_{-0.6}$	$1.6^{+4.9}_{-0.8}$	$0.7^{+1.8}_{-0.3}$	10.5	7.26
ZQ65	6 ±4 (25)	4.6 ±0.7	42 ±7 (31)	8.6 ±1.4	2930 ±900	330 ±140	$3.4^{+1.1}_{-0.6}$	$1.9^{+2.9}_{-0.8}$	$0.8^{+1.1}_{-0.3}$	11.3	7.85

a. J is J-index; M is M-index.
b. Angle between the maximum [100] axis direction of olivine and maximum [001] axis direction of orthopyroxene.
c. Equilibrium olivine water concentration calculated using measured water content in Opx and water partition coefficient $D^{Ol/Opx}$ of 0.11.
d. Equilibrium bulk-rock water concentration calculated using water contents and modal proportions of Ol and Opx.
e. Converted grain size corresponding to that of linear-intercept method. Because the olivine grain boundaries are irregular, the grain-size was calculated by the following steps: (1) calculating the diameters of circle of equivalent areas to those measured grains, and weighted by grain numbers; (2) converting number-weighted grain-size by multiplying a factor of 1.12, into the grain-size estimated by linear-intercept method (LIM), based on the relations established by Berger *et al*. (2011); (3) converting 2D into 3D grain-size by multiplying a factor of 1.5. The same olivine grains which have well-developed

subgrain boundaries were also used for subgrain size measurement.

f. The sub-grain size was estimated by measuring the spacing of neighboring sub-grain boundaries in high magnification images under optical microscope.

g. Stress estimated using different method: recrystallized grain size piezometer (GSP) (Van der Wal *et al.*, 1993), subgrain size piezometer_1 (SGSP_1, Ross *et al.*, 1980) and subgrain size piezometer_2 (SGSP_2, Karato *et al.*, 1980).

h. AVp is P-wave anisotropy; max. AVs is maximum shear wave polarization anisotropy.

Table 4.2. Eigenvalue analysis of olivine and orthopyroxene fabrics.

Sample	Mineral / Axis	pfJ	λ_1	λ_2	λ_3	Point	Girdle	Random	ln (λ_1/λ_2)	ln (λ_2/λ_3)	Shape parameter (K)
12YSG-15	Ol / [100]-axis	3.89	0.76	0.16	0.09	0.62	0.12	0.27	1.56	0.58	2.71
ZQ1		3.27	0.74	0.17	0.09	0.58	0.15	0.28	1.47	0.64	2.31
ZQ48		3.70	0.78	0.12	0.11	0.66	0.02	0.32	1.87	0.09	21.51
ZQ60		2.80	0.72	0.16	0.12	0.57	0.07	0.36	1.50	0.29	5.23
ZQ65		3.03	0.73	0.18	0.10	0.55	0.16	0.30	1.40	0.59	2.38
12YSG-15	Ol / [010]-axis	2.71	0.62	0.33	0.04	0.29	0.57	0.13	0.63	2.11	0.30
ZQ1		2.05	0.54	0.37	0.09	0.17	0.57	0.26	0.38	1.41	0.27
ZQ48		2.79	0.64	0.31	0.06	0.33	0.50	0.17	0.72	1.64	0.44
ZQ60		2.02	0.50	0.42	0.08	0.08	0.68	0.24	0.17	1.66	0.11
ZQ65		2.13	0.57	0.34	0.08	0.23	0.52	0.25	0.52	1.45	0.36
12YSG-15	Ol / [001]-axis	1.72	0.54	0.28	0.18	0.25	0.21	0.54	0.66	0.44	1.49
ZQ1		1.62	0.48	0.36	0.16	0.12	0.41	0.47	0.29	0.81	0.35
ZQ48		2.20	0.62	0.25	0.13	0.38	0.24	0.38	0.91	0.65	1.39
ZQ60		1.49	0.44	0.41	0.15	0.02	0.53	0.45	0.07	1.01	0.07
ZQ65		1.71	0.54	0.31	0.15	0.23	0.31	0.46	0.55	0.73	0.76
12YSG-15	Opx / [100]-axis	1.67	0.50	0.31	0.20	0.19	0.22	0.59	0.48	0.44	1.09

Sample	Mineral / Axis	pfJ	λ_1	λ_2	λ_3	Point	Girdle	Random	ln (λ_1/λ_2)	ln (λ_2/λ_3)	Shape parameter (K)
ZQ1		2.25	0.63	0.22	0.15	0.40	0.15	0.45	1.05	0.38	2.75
ZQ48		1.78	0.54	0.31	0.15	0.24	0.31	0.46	0.55	0.73	0.76
ZQ60		1.78	0.50	0.37	0.14	0.13	0.47	0.41	0.30	0.97	0.31
ZQ65		1.78	0.52	0.33	0.15	0.20	0.36	0.44	0.45	0.79	0.58
12YSG-15		1.51	0.42	0.36	0.22	0.06	0.29	0.65	0.15	0.49	0.31
ZQ1		1.92	0.55	0.25	0.20	0.30	0.10	0.60	0.79	0.22	3.53
ZQ48	Opx / [010]-axis	1.48	0.43	0.32	0.24	0.11	0.16	0.73	0.30	0.29	1.03
ZQ60		1.59	0.43	0.34	0.24	0.09	0.20	0.71	0.23	0.35	0.67
ZQ65		1.56	0.48	0.34	0.19	0.14	0.30	0.56	0.34	0.58	0.59
12YSG-15		2.54	0.59	0.32	0.09	0.27	0.45	0.28	0.61	1.27	0.48
ZQ1		2.67	0.63	0.30	0.07	0.33	0.47	0.20	0.74	1.46	0.51
ZQ48	Opx / [001]-axis	2.33	0.60	0.31	0.09	0.29	0.43	0.28	0.66	1.24	0.53
ZQ60		2.49	0.63	0.25	0.12	0.37	0.27	0.36	0.92	0.73	1.26
ZQ65		2.45	0.64	0.24	0.12	0.40	0.26	0.35	0.98	0.69	1.42

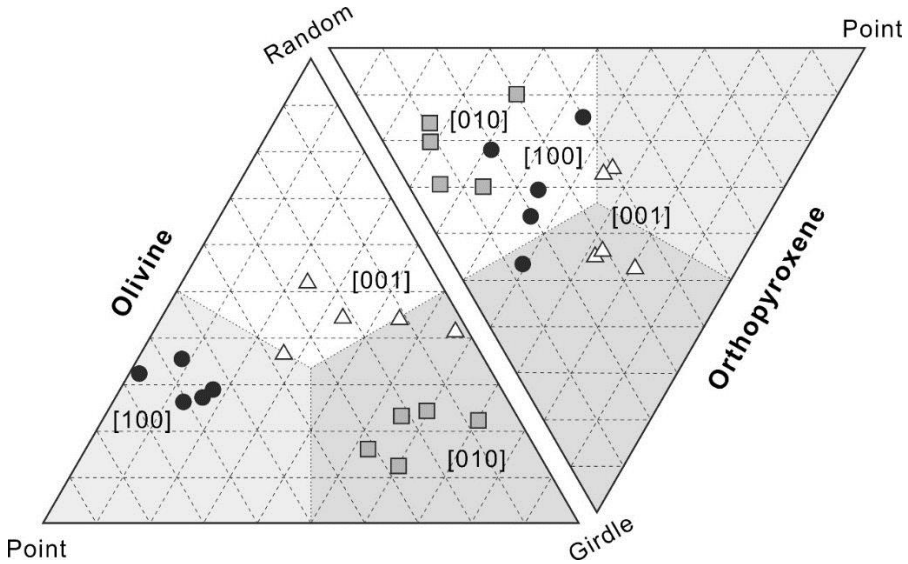

Fig. 4.5. Ternary diagrams showing Point–Girdle–Random components of the [100] (black circle), [010] (grey square) and [001] (white triangle) axes distributions of olivine (lower left) and Opx (upper right) fabrics.

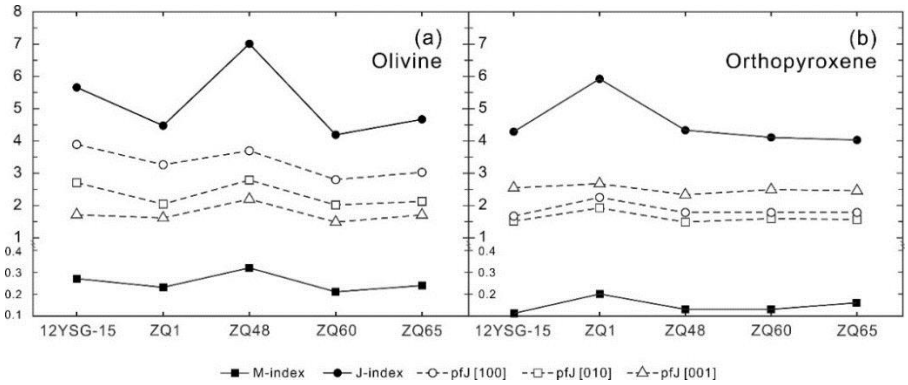

Fig. 4.6. Intensity of olivine and orthopyroxene CPOs in studied samples.

According to the modeling results of CPO evolution in a deforming polycrystalline aggregate (Tommasi *et al.*, 2000, Tommasi *et al.*, 1999), crystallographic axes corresponding to the slip direction and the pole of the slip plane tend to orient faster than the remaining axes, these two axes would thus have higher fabric strength than the others. Therefore, combing with the known slip systems of olivine and Opx, the fabric strength orders of three principal axes suggest that the (010)[100] and (100)[001] are the dominant dislocation slip systems for olivine and Opx, respectively. Moreover, the larger strength of $[100]_{Ol}$ and $[001]_{Opx}$ compared with the respective $[010]_{Ol}$ and $[100]_{Opx}$, indicates larger component of simple shear than axial shorting.

4.4.2. Subgrain boundaries and rotation axes

The dislocation slip system of a mineral can also be inferred using either the distributions of rotation axes (also referred to as misorientation axes) or geometrical relationship between subgrain boundaries and rotation axes based on EBSD mapping (Prior *et al.*, 1999). The basis of the former method is that the rotation axes can accommodate low-angle misorientations (< 10 °) mostly across a subgrain boundary within a crystal, they thus contain the information of dislocation slip systems – the two orthogonal axes that are perpendicular to rotation axis indicate either slip direction or the pole of slip plane (Fig. 4.7f and 4.9e). This method has the most striking advantages, because of its great convenience and ability to know the bulk-rock slip system when combined with large-area EBSD mapping. Hence, it has been applied to identify the olivine dislocation systems in a variety of studies on both natural peridotites (Falus *et al.*, 2011, Hansen *et al.*, 2013, Higgie & Tommasi, 2012, Kaczmarek & Tommasi, 2011, Kaczmarek & Reddy, 2013, Soustelle *et al.*, 2010, Tommasi *et al.*, 2008, Zaffarana *et al.*, 2014) and experimental samples (Demouchy *et al.*, 2014, Hansen *et al.*, 2014, Hansen *et al.*, 2011, Hansen *et al.*, 2012). However,

an obvious pitfall of this method is that the slip direction and slip plane cannot be specified, and that the inference of slip system strictly relies on the known slip systems of a specific mineral. For example, the rotation axes close to [010] axis of olivine indicate that three independent dislocation slip systems (two tilt-wall-associated edge dislocations of (001)[100] and (100)[001], and one set of twist-wall associated screw dislocations of (010)[100] and (010)[001]) could be equally activated (Fig. 4.7f). By contrast, a single-crystal based EBSD mapping method which further takes into account of the geometrical relationships between rotation axes and subgrain boundaries can result in a more direct and precise inference of slip systems, because either slip direction or slip plane can be determined from indexing the subgrain boundaries. This analytical approach has mostly been used to identify the slip systems of porphyroclasts in natural peridotites (e.g., Kaczmarek & Reddy, 2013, Katayama *et al.*, 2011, Palasse *et al.*, 2012, Précigout & Hirth, 2014). In contrast to the previous approach, a potential problem of employing this method is that a large number of grains showing subgrain textures may need to be measured, in order to give a statistically meaningful estimation of bulk-rock dislocation slip systems. However, this method is in many cases difficult to apply, owing to the limited number of grains with clear subgrain textures and its time-consumingness.

Because of the ubiquitous subgrain textures in our specimen, we used the second method by selecting those olivine grains which show clear multiple sub-parallel subgrain boundaries and by applying EBSD-scan along directions at high angle to the subgrain boundaries, so that more rotation axes (misorientation angle = 2–10°) can be sampled. The step size was set in the range of 1–15 μm which is about 100 times smaller than the size of analyzed grains. About 20 olivine grains were analyzed for each sample and their representative results are shown in Fig. 4.7. The olivine subgrain boundaries

are predominantly parallel to (100) plane (Figs. 4.7a-e) with a minority parallel to (001) plane (Fig. 4.7e) and rarely parallel (010) plane, indicating that [100] is the dominant slip direction and [001] is minor slip direction, and that (010) twist wall is rarely activated. Combining with the distributions of rotation axes, the slip planes could be inferred and slip systems of olivine were determined accordingly (Figs. 4.7a-e). After summarizing the measurement of about 100 olivine grains in 5 samples (Fig. 4.7g), we found that about 74% olivine grains show the dominant and equally activated slip systems of (010)[100] and (001)[100] (Figs. 4.7a-c), and ~46% olivine grains contain the other [100]-slip systems (Fig. 4.7e). Only ~20% and ~22% olivine grains display multiple {0kl}[100] slip systems and [001]-slip or other unspecified slip systems, respectively (Figs. 4.7d and e). These statistics and distributions of rotation axes also suggest that multiple slip systems are commonly activated in a single olivine crystal (Figs. 4.7c-e and g). However, one drawback in this statistic is that only the frequencies but not the intensities of different slip systems are considered. Therefore, we plotted the rotation axes from all measurements for each sample and their synthesized sample (Fig. 4.8). Similar to the results shown in the frequency histogram (Fig. 4.7g), olivine slip systems are composed of dominant (010)[100] and (001)[100], secondary other [100]-slip and minor [001]-slip systems (Figs. 4.8a-e), based on the slip system identification diagram (Fig. 4.7f). In the synthesized sample (Fig. 4.8f), (001)[100] slip system, however, is more activated than others. It is noteworthy that the equal activations of (010)[100] and (001)[100] slip systems or even more dominant (001)[100] slip system were also observed in olivines from other natural peridotites (Falus *et al.*, 2011, Kaczmarek & Tommasi, 2011, Soustelle *et al.*, 2010, Zaffarana *et al.*, 2014), and these results seem not consistent with the dominant (010)[100] slip system inferred from olivine CPO and fabric strength orders of principal axes. This discrepancy is likely due to

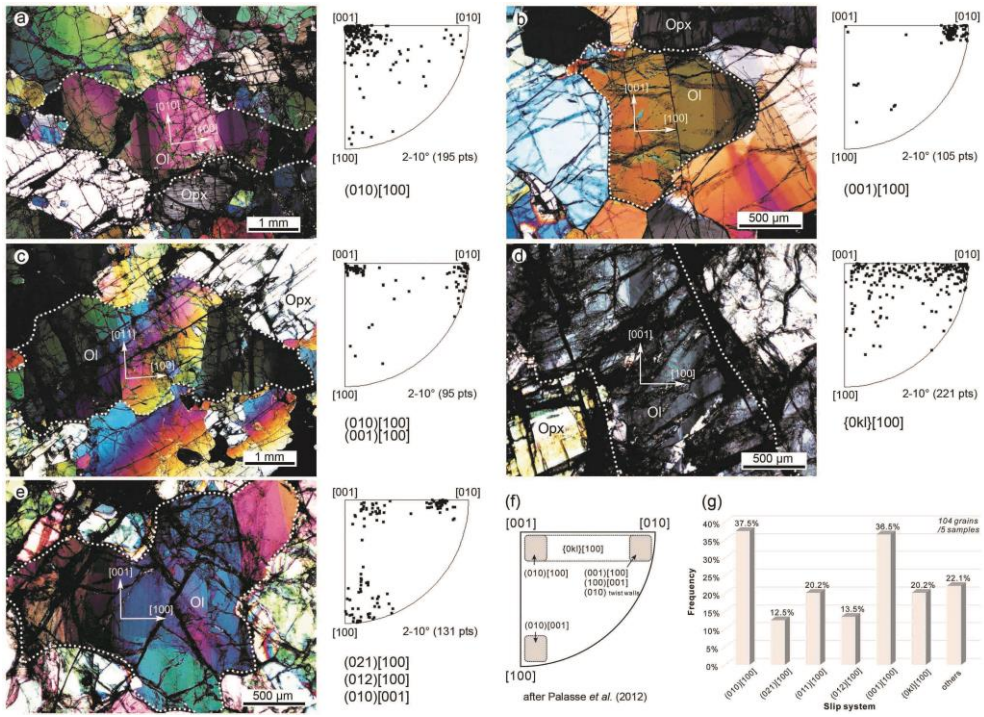

Fig. 4.7. (a-e) The representative olivine crystals (dotted outline) showing subgrain boundaries (left photomicrographs) and their rotation axes distributions (right inverse pole figures). Misorientation angle of 2–10° for the rotation axes between neighbor-pair are plotted. Below the inverse pole figures are the inferred dominant slip systems of olivine activated. (f) A diagram showing the distribution of rotation axes and slip systems of olivine. (g) Histogram showing the percentage of identified slip systems of olivine in the studied samples. The [100]-slip dislocations are approximately categorized into six groups – (010)[100], (021)[100], (011)[100], (012)[100], (001)[100] and {0kl}[100], and the last group named as "others" represents both [001]-slip and other non-specified slip systems.

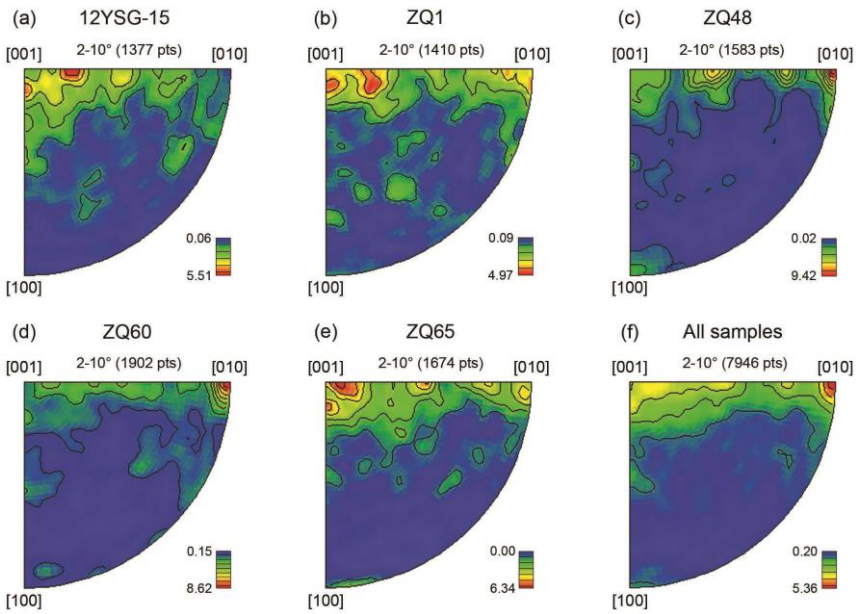

Fig. 4.8. Distributions of olivine rotation axes in (a-e) studied samples and (f) their synthesized sample. Rotation axes from ~20 analyzed olivine grains were plotted for each sample, while rotation axes from ~100 olivine grains in 5 studied samples were plotted for the synthesized sample. Data are for neighbor-pair rotation axes with misorientation angle of 2–10°, and are contoured with half width of 5 °in equal-area and lower-hemisphere inverse pole figures.

the faster or more extensive recovery for the relatively more mobile (010)[100] than (001)[100] slip systems at a geological time-scale, as this difference has never been observed in experimentally deformed samples that quenched rapidly (Demouchy *et al.*, 2014, Hansen *et al.*, 2014, Hansen *et al.*, 2011, Hansen *et al.*, 2012).

The slip systems of orthopyroxene were also determined by a similar manner. Because most Opx grains show weaked undulose extinctions, only 8 Opx crystals having clear kind bands whereby either slip direction or plane can be unambiguously inferred, were selected for analysis (Fig. 4.9). The observed kink bands are mostly parallel to (001) plane, indicating [001]-slip systems such as dominant (100)[001] (Fig. 4.9a), secondary (010)[001] and minor {210}[001] (Fig. 4.9b). However, some Opx grains also display (0vw) kind bands, implying the secondary [0vw]-slip systems such as (100)[012] and (100)[0vw] (Fig. 4.9c). These slip systems and their intensities can also be inferred from the synthesized sample in which the rotation axes of all measurements were plotted (Fig. 4.9d), based on the slip system identification diagram of orthopyroxene (Fig. 4.9e). The higher density of (100)[001] than (010)[001] agrees with the higher concentrations (larger pfJ-index) of [100] than [010] axes aligning perpendicular to foliation (Figs. 4.4a'-e'). More noticeably, the secondary activations of (100)[010] and (100)[0vw] slip systems can also explain the girdle distributions of [001] axis and the deviation of [010] axis from foliation-normal to more random dispersion (Figs. 4.4a'-e' and 4.5). Unlike olivine, the rotation axes distributions of Opx faithfully reflect the characteristics of their CPOs, which is also observed in other similar studies (Kaczmarek & Tommasi, 2011, Soustelle *et al.*, 2010).

In summary, the detailed analysis of CPOs and geometrical relationships between rotation axes and subgrain boundaries suggested that a series of dislocation slip systems are activated in both olivine and orthopyroxene. The

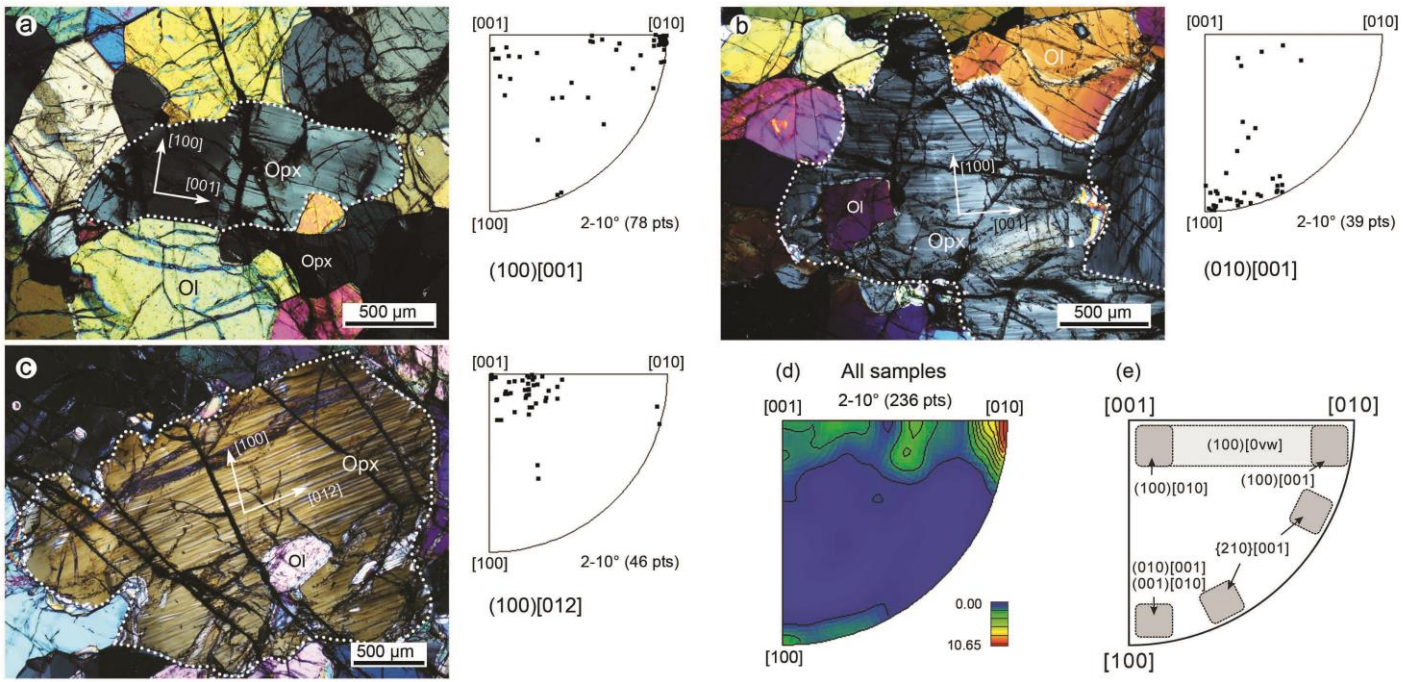

Fig. 4.9. (a-c) The representative orthopyroxene crystals (dotted outline) showing subgrain boundaries (left photomicrographs) and their rotation axes distributions (right inverse pole figures). Below the inverse pole figures are the inferred dominant slip system activated in each orthopyroxene grain. (d) The synthesized sample containing the rotation axes of all measurements. Data are contoured with half width of 5 °in equal-area and lower-hemisphere inverse pole figures. Misorientation angle of 2–10° for the rotation axes between neighbor-pair are plotted. (e) The orthopyroxene slip system identification diagram, which is based on the distribution of rotation axes and known slip systems in Opx. The dislocation slip systems shown in (e) are on the basis of the TEM observations of Opx crystals (e.g., Manthilake *et al.*, 2013; Naz é*et al.*, 1987; Ohuchi *et al.*, 2011).

plastic deformation of olivine was accommodated by dominant (010)[100], secondary (001)[100] and other minor [100]-slip, {0kl}[100] and [001]-slip systems, whereas orthopyroxene was deformed by dominant (100)[001] and secondary (010)[001], (100)[010], (100)[0vw] slip systems.

4.5. Water contents in olivine and orthopyroxene

4.5.1. Analytical procedure

As the most conventional method, unpolarized Fourier Transformation Infrared (FTIR) absorption spectra were used to measure the water contents in olivine and orthopyroxene on doubly polished slice with a thickness of 150–350 μm. The slices were carefully polished following the same procedure as those thinsections prepared for EBSD analysis. The slices were later bathed in acetone for over 24 hours and were gently wiped on double surface using acetone-moistened cotton swab to remove any residual adhesive. Then, the slices were dried in oven at 120 ℃ for more than 24 hours to remove the free water residing on slice surfaces and grain-boundaries. The measurements were performed at room temperature and pressure using a Nicolet 6700 spectrometer with a Continuum IR Microscope at Tectonophysics Laboratory in Seoul National University. An unpolarized light source, a KBr beam splitter and an MCT detector cooled by liquid nitrogen were used. Throughout the IR measurement, dry and pure nitrogen gas was flushed into the system and the chamber which hosts the stage of microscope to avoid the disturbance of moisture in the atmosphere. The IR spectrum was yielded from an average of a series of 128 scans with a resolution of 4 cm^{-1}. Because cracks and inclusions are ubiquitously developed, we carefully selected the optically inclusion- and crack-free areas without specifying the locations of core or rim, and analyzed using various-sized square or rectangular apertures (40–100 μm in edge length)

depending on the shape and size of the clean regions. The infrared spectra and water content in Cpx grains were not measured, owing to their small and sporadic occurrence.

The water content in the analyzed minerals was calculated using a modified form of Beer-Lambert law (e.g, Xia *et al.*, 2010):

$$c = \Delta / \left(I \times t \times \gamma \right)$$

where c is the hydroxyl concentration (weight ppm H_2O), Δ is the unpolarized integrated area (cm^{-1}) of absorption bands in the region of interest, I is the integral specific absorption coefficient (ppm^{-1} cm^{-2}), t is the thickness (cm), and γ is the orientation factor accounting for the anisotropy of the crystal as discussed by Paterson (1982). Baseline corrections were carried out by drawing a straight line from 3900 to 3100 cm^{-1}, and the range of calculating OH integral absorbance for olivine and orthopyroxene was 3600–3400 cm^{-1} and 3700–3100 cm^{-1}, respectively. The integral specific coefficient of 5.32 ppm^{-1} cm^{-2} for olivine (Bell *et al.*, 2003) and 14.84 ppm^{-1} cm^{-2} for orthopyroxene (Bell *et al.*, 1995), as well as an orientation factor of 1/3 for olivine and Opx were used in unpolarized measurements. To increase the precision of water calculation, we used the discrete thickness at the position of each infrared analysis over the whole slice to account for the small thickness heterogeneity. To minimize the difference between unpolarized average integrated absorbance $\left(3 \times \int A_{\text{unpol,avg}} \right)$ from randomly-oriented anisotropic minerals and polarized total integrated absorbance $\left(\int A_{\text{tot}} \right)$, 10–30 different grains of olivine or Opx were analyzed in each sample, except for sample ZQ60 in which only 6 measurements for each olivine and Opx were made. This approximation assumes that the water content is homogeneous among different grains, and their averaged value was thus taken as the water content of that mineral in that sample (e.g., Asimow *et al.*,

2006, Kovács *et al.*, 2008, Sambridge *et al.*, 2008). However, Withers (2013) recently pointed out that a non-ignorable systematic underestimation of water content may still exist, unless $\left(\int A_{\mathrm{tot}}\right)$ can be calculated from unpolarized transmittance and averaged from at least 10 unpolarized spectra which have weak anisotropy (the maximum linear absorbance does not exceed 0.3 absorbance units), rather than estimated from unpolarized absorbance (Equation 17 in Withers (2013)). This systematic error is thickness or maximum linear absorbance dependent. Because the maximum linear absorbances of both olivine and Opx are fairly small (Fig. 4.10, less than 0.1 absorbance units), we consider that the water content calculated using the method in this study would be underestimated less than ~20–30% (Fig. 4 in Withers (2013)). For comparisons with other studies, this calculated water content in olivine can be converted, by approximately multiplying by a factor of 1/3 to the calibration of Paterson (1982) (e.g., Bell *et al.*, 2003, Mosenfelder *et al.*, 2006). More recently, Withers *et al.* (2012) recalibrated the absorption coefficient of olivine and suggested that the real water content would be ~35% lower than the calibration of Bell *et al.* (2003). The conversion relations between three olivine IR calibrations were presented for necessary comparisons with other studies.

4.5.2. IR spectra and water content

Despite of the careful sample preparations, noise with nearly constant amplitude was still observed in the whole wavenumber range of most spectra, except for sample 12YSG-15 which has the lowest level of noise (Fig. 4.10). The cause of this noise is unclear but probably due to the different systematic instability of FTIR system at each run, because one sample was measured at one run and the level of noise is similar in one sample but varies from sample to sample (cf. IR spectra between olivine and Opx in the same sample, and IR

spectra of olivine or Opx between different samples). This unfavorable noise thus impede the precise recognition of the weak OH peak signals in a spectrum, and result in an overestimate of water content by mistakenly integrating the fake absorption bands that are induced by noise, such as the case of olivine in this study (Fig. 4.10). Accordingly, the water content calculation using the calibration of Bell *et al.* (2003) yield low average water concentrations of 6–17 ppm with moderate standard deviations of 1–9 ppm in olivine grains (Table 4.1), However, based on the least noise-disturbed spectra from sample 12YSG-15, it seems that no significant hydroxyl absorption bands can be observed in olivine. These measured water contents need to be corrected to even lower values to remove noise-induced overestimation.

In contrast, because orthopyroxene displays much higher IR absorbance than the amplitude of noise, the major OH absorption bands in their spectra can be identified. Besides, the troughs and crests of noise that are overlapped with the OH absorption bands can offset each other when integrating the absorbance, the noise would thus have a negligible effect in the calculation of water content. As shown in Fig. 4.10, the Opx grains from different samples consistently show a broad peak containing three major OH absorption bands with decreasing absorbance at 3414–3425, 3516–3518 and 3556–3563 cm^{-1}. This group of OH bands belongs to the high-energy Group I bands of Opx termed by Ingrin and Skogby (2000) and has also been frequently observed in other natural orthopyroxenes (e.g., Gose *et al.*, 2009, Grant *et al.*, 2007a, Mosenfelder & Rossman, 2013, Skogby, 2006, Skogby *et al.*, 1990, Xia *et al.*, 2010, Yang *et al.*, 2012). These OH bands above 3400 cm^{-1} are commonly related to the incorporation of trivalent cations (e.g., Al, Cr and Fe^{3+}) by coupled substitution of $R^{3+} + H^{+}$ for Si^{4+} or $2Mg^{2+}$ (e.g., Kohn *et al.*, 2005, Mierdel *et al.*, 2007, Rauch & Keppler, 2002, Stalder, 2004, Stalder & Skogby, 2002, Zhang *et al.*, 2013). In this study, the average water content of Opx is estimated to be in a

narrow range of 38–44 ppm, except for sample ZQ48 that presents a contrastingly higher value of 66 ppm (Table 4.1). The variations of Opx water content are relatively small with standard deviations of 4–9 ppm in the studied samples (Table 4.1). These measured Opx water contents fall into the lower end of water concentration distribution of natural Opx in mantle peridotites (10–460 ppm, see summary of Opx water content by Warren and Hauri (2014) and references therein), suggesting a very dry mantle condition.

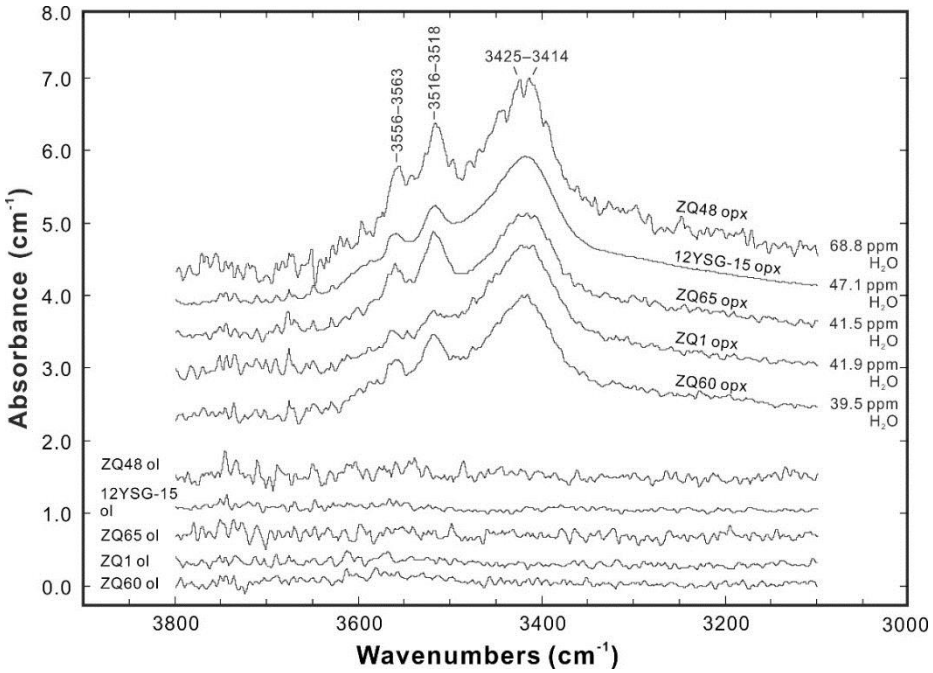

Fig. 4.10. Representative unpolarized infrared spectra without baseline corrections for olivine and orthopyroxene. The selected spectra have approximate average water contents of olivine and Opx in that sample. The spectra are normalized by sample thickness to 1 cm^{-1}. Note that noise is prevailing in all infrared spectra, except for sample 12YSG-15, probably leading to the overestimates of water content in olivine.

4.6. Seismic properties

4.6.1. Analytical method

The rock seismic velocities and anisotropies can be quantitatively calculated by solving the Christoffel equation in which the macroscopic elastic stiffness tensor < C_{ij} > and bulk density are required. The < C_{ij} > can be estimated by averaging the single-crystal elastic stiffnesses tensor (C_{ij}) of all mineral grains over all orientations that are acquired from EBSD analysis; and the bulk density is a weighted average of single-crystal density and mineral volume proportions (Mainprice & Humbert, 1994). The entire calculation procedure can be conveniently processed using an updated petro-physical software which is originally developed by Mainprice (1990). In the approximate calculations of seismic properties of harzburgite, we used a normalized mineral assemblage of olivine + orthopyroxene, neglecting the contributions from minor clinopyroxene and spinel. This approximation may lead to slightly higher estimate of seismic anisotropies owing to weaker Cpx fabric and quasi-isotropic spinel crystal (Michibayashi *et al.*, 2012, Morales & Tommasi, 2011, Satsukawa *et al.*, 2011, Soustelle & Tommasi, 2010, Soustelle *et al.*, 2013, Zaffarana *et al.*, 2014), and nearly unchanged seismic velocities due to lower velocity of Cpx and higher velocity of spinel. The single-crystal elastic stiffness tensors at ambient conditions for olivine (Abramson *et al.*, 1997) and orthopyroxene (Chai *et al.*, 1997), and Vogit-Reuss-Hill averaging scheme were applied. Besides, the seismic properties of an averaged sample from 5 harzburgites were also calculated in this study. This averaged sample was treated consisting of 10 mineral aggregates (2 mineral aggregates (olivine and Opx) × 5 samples) with normalized volume proportions (volume proportions

of olivine and Opx in each sample divided by 5 samples). In this treatment, the contributions from each sample are equal and the effects of different points of CPO measurement between samples are eliminated.

One noteworthy aspect is that the seismic velocities and anisotropies are bulk-rock properties, a CPO thus obtained by one measurement per pixel using automatic EBSD mapping over the whole thinsection area would be the most appropriate. The main difference of CPOs between one measurement per pixel and one measurement per grain is that the fabric strength (e.g., J-index) is lower in the latter due to dispersion of fabric that results from recrystallized fine grains whereas the symmetry of CPO is only slightly modified (Falus *et al.*, 2011, Soustelle *et al.*, 2010, Tommasi *et al.*, 2008). The extent of this fabric weakening depends on the degree of grain-size refinement which is apparently related to fabric strength, in that higher fabric strength is associated with larger strain and more recrystallization. The CPOs in this study were obtained using one measurement per grain method and showed a moderate CPO strength of olivine (J = 4.19–7.01, Fig. 4.4). This range of fabric strength is about ~ 20% lower than the fabric strength estimated using one measurement per pixel method (Soustelle & Tommasi, 2010, Tommasi *et al.*, 2008), and may thus imply an underestimate of seismic anisotropies of similar percentage. By contrast, the isotropic seismic velocities are not controlled by the CPO strength, but more sensitive to the mineral modal compositions.

4.6.2. Seismic anisotropies and velocities

The seismic properties of averaged harzburgite sample were calculated at ambient *P-T* conditions and presented in the XZ structural frames (Fig. 4.11). In the analyzed samples, the P-wave and slow shear wave (S2) are the fastest when propagating parallel to the lineation (the maximum direction of olivine [100] axis) and form slow velocity girdles when travelling perpendicular to the

lineation with the minimum P-wave velocity normal to the foliation (the maximum direction of olivine [010] axis). The fast shear wave (S1) velocity exhibits bimodal maximum bisecting the lineation and the direction perpendicular to lineation on the foliation, and minimum direction normal to the foliation. These P-wave and S-wave velocity patterns thus yield axial and orthorhombic distribution patterns of Vp/Vs1 and Vp/Vs2 ratios, respectively. Similar to the P-wave and slow shear wave, both Vp/Vs1 and Vp/Vs2 contain the maximum ratios at low angle to lineation and minimum ratios at high angle to foliation. In contrast, shear wave splitting induced shear velocity difference (dVs = Vs1 – Vs2) and birefringence (AVs) are the lowest when shear wave is propagating at low angle to the lineation, and form high value girdles with maximum parallel to the foliation when shear wave travels perpendicular to the lineation. The polarization directions of the fast shear wave are always parallel to the lineation that is sub-parallel to the olivine [100] maximum. The intensities of seismic anisotropies have no significant variations among the studied samples and are overall correlated with CPO fabric strengths of olivine (Table 4.1). Their averaged sample shows P-wave anisotropy, fast and slow shear wave azimuthal anisotropies, and maximum shear wave polarization anisotropy of 11.5%, 2.8%, 6.5% and 7.42%, respectively.

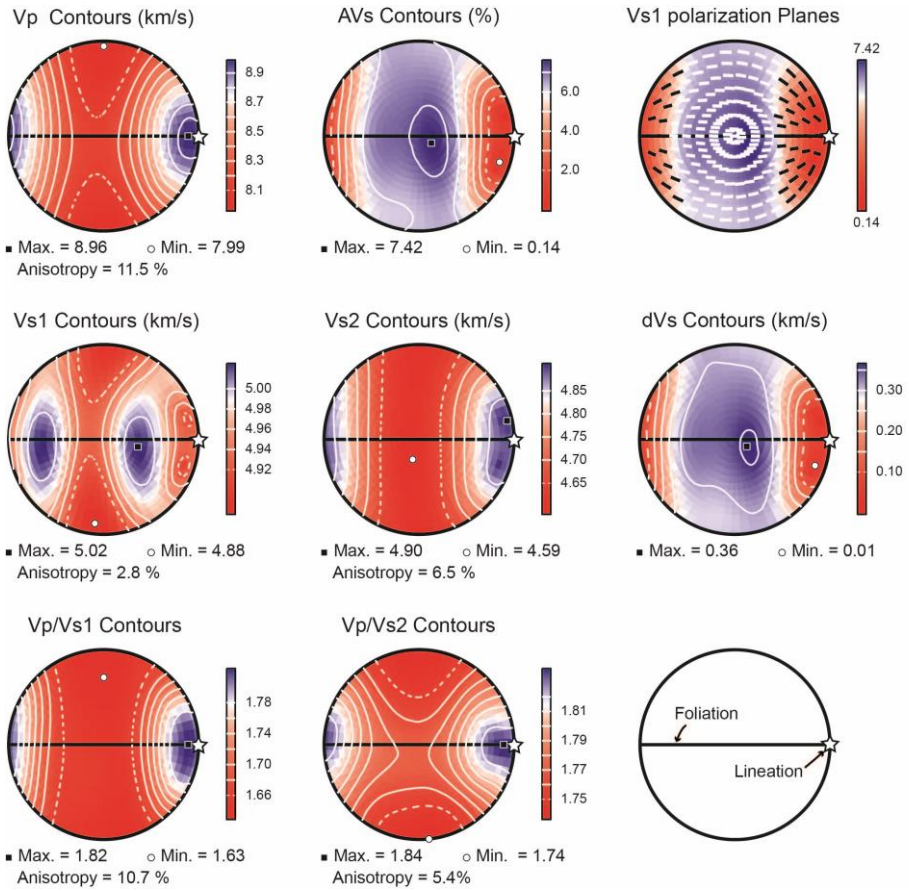

Fig. 4.11. Seismic properties of an averaged sample which takes into the account of olivine and Opx polycrystals of the 5 harzburgite samples in this study. Pole figures are presented in a plane parallel to lineation and perpendicular to foliation using equal area and lower hemisphere projection.

4.7. Discussions

4.7.1. Relations between petrological and deformational processes

4.7.1.1. Partial melting and melt/fluid-rock reaction

The previous study proposed that the Yushigou harzburgite body represent a remnant of a Paleozoic mantle wedge, based on the highly refractory mineral and whole-rock compositions, enrichments of fluid-mobile elements, crustal origin isotopic compositions of CH_4-rich fluid inclusions, and oxidized nature of harzburgite (Song *et al.*, 2009b). However, more detailed analysis of their mineral compositions can further specify this petro-genetic setting as a fore-arc mantle which developed at early and warm subduction zone. As shown in Fig. 4.12, the compositions of olivine, spinel, Cpx and Opx all have signatures of melting residue and indicate that the Yushigou harzburgites have experienced a high-degree partial melting (~ 25–30% fractional melting) and constituted the refractory fore-arc lithospheric mantle later. The similar melting degree can also be inferred from very low Cpx modal abundance (< 2 vol.%) which corresponds to a melting degree above 25% at a wet spinel facies condition, because Cpx is the phase consumed most rapidly during partial melting of a spinel peridotite (e.g., Gaetani & Grove, 1998, Jaques & Green, 1980, Niu, 1997). Besides, the low whole-rock HREE concentrations (Fig. 4.13a, see also Song *et al.* (2009b)) also agree with a high partial melting degree of ~21–27% at spinel facies (Piccardo *et al.*, 2007), because these elements are negatively correlated to the degree of partial melting and generally resistant to later metasomatic and melt-rock reaction processes (Hellebrand *et al.*, 2001, Parkinson *et al.*, 1992).

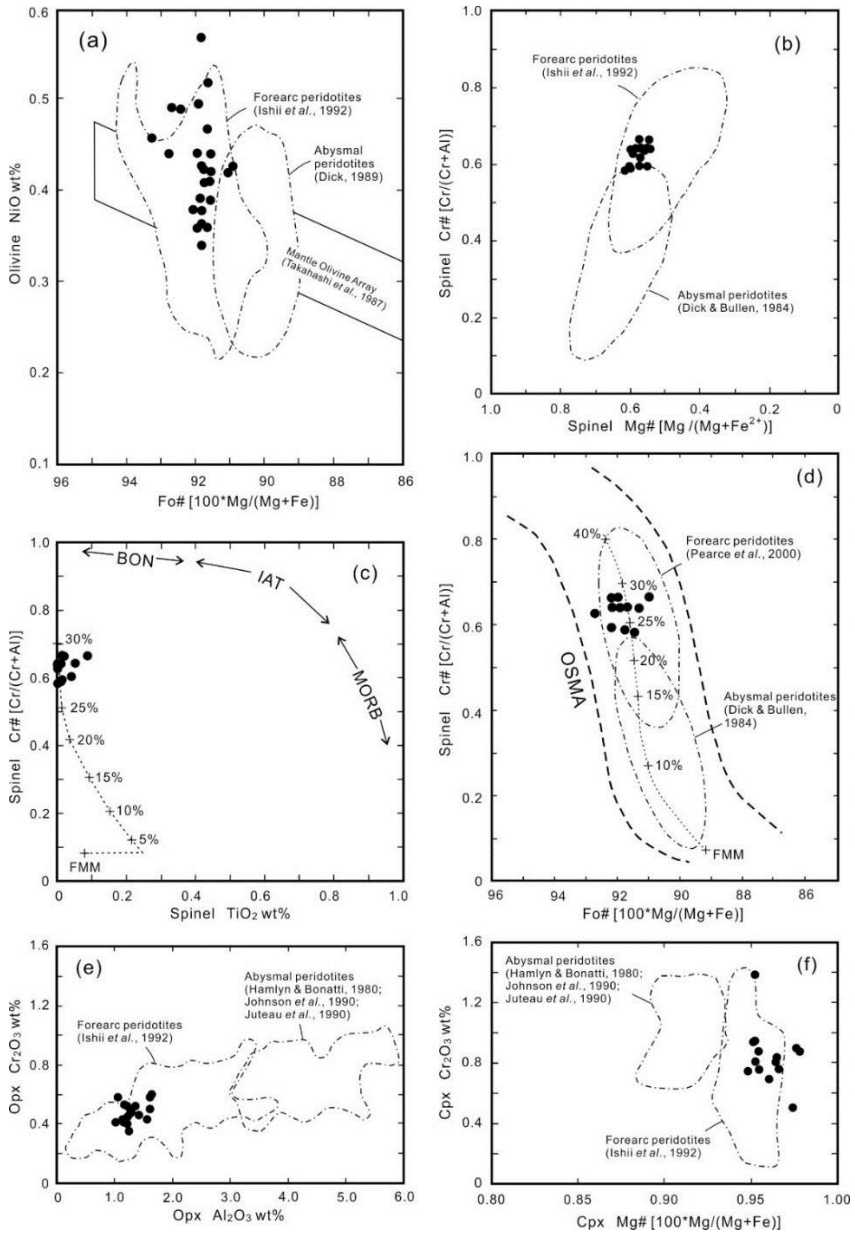

Fig. 4.12. Mineral compositions of olivine, spinel, Opx and Cpx in Yushigou harzburgites (solid circle). Data from Song *et al.* (2009b) were re-plotted in figures. All data consistently indicate their forearc mantle provenance after a high-degree partial melting of fertile MORB mantle (FMM) source. (a) Olivine NiO vs. Fo# relationship. (b) Spinel Cr# vs. Mg# relationship. (c) Spinel TiO_2 vs. Cr# relationship. Dash line showing the variations of spinel compositions with incremental fractional melting degree of a FMM, as well as the spinel compositions in boninite (BON), island arc tholeiite (IAT) and mid-ocean ridge basalt (MORB) were from Pearce *et al.* (2000). (d) Olivine Fo# vs. spinel Cr# relationship. Olivine-spinel mantle array (OSMA) and mineral composition variations with incremental melting of a FMM were from Arai (1994). (e) Opx Al_2O_3 vs. Cr_2O_3 relationship. (f) Cpx Mg# vs. Cr_2O_3 relationship.

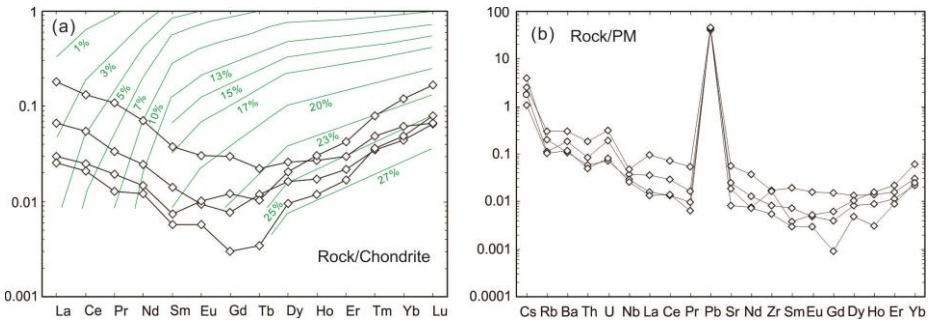

Fig. 4.13. (a) Chondrite normalized whole-rock REE patterns; and (b) primitive mantle normalized trace element diagram of the Yushigou harzburgites. Modified after Song *et al.* (2009b). Green lines are modeled chondrite-normalized REE of refractory peridotites after variable degrees of fractional melting (as labeled) of depleted spinel-facies MORB mantle (Piccardo *et al.*, 2007).

The intensely molten residual characteristic can also be reflected by the very low water concentrations in minerals and whole rock. As commonly observed, the estimated water content in natural olivine seldom retained their original values in the deep mantle as a result of water loss due to extremely fast hydroxyl diffusion rate at high temperature, decreasing solubility of water with decreasing pressure and slow emplacement rate (e.g., Demouchy *et al.*, 2006, Denis *et al.*, 2013, Li *et al.*, 2008, Peslier & Luhr, 2006), whereas Opx can preserve the original mantle hydration state owing to sluggish water diffusion in Opx (e.g., Peslier *et al.*, 2002, Peslier *et al.*, 2012, Warren & Hauri, 2014). This conclusion can be manifested in Fig. 4.14a, in which measured water contents of olivine and Opx in the peridotites from different subduction zone settings were summarized (Falus *et al.*, 2008, Peslier & Luhr, 2006, Peslier *et al.*, 2002, Soustelle *et al.*, 2013, Soustelle *et al.*, 2010, Warren & Hauri, 2014). Excluding several outliers, the data are located above the water content equilibrium line of olivine and Opx and form a fairly good linear relationship with a slope obviously larger than the experimentally determined Opx-Ol water partition coefficients. This fact likely indicates that significant amounts of water have been lost in olivine compared to Opx during the emplacement. Alternatively, the Opx-Ol partition coefficient could be larger if more amount of Al_2O_3 was contained in Opx (Kohn & Grant, 2006, Peslier, 2010). In this study, the precise water content of olivine was not well determined due to their low water concentration levels and high noise signal ratio, the apparent nearly equilibrium of water contents between olivine and Opx is thus probably an artifact (Fig. 4.14a). The real water concentrations in olivine are likely lower than 1 wt ppm, based on the measured water content of Opx and the relationship between olivine and Opx.

Although the water contents in the core and rim of a single Opx grain were not measured, the relatively small standard deviations of water content (4–9

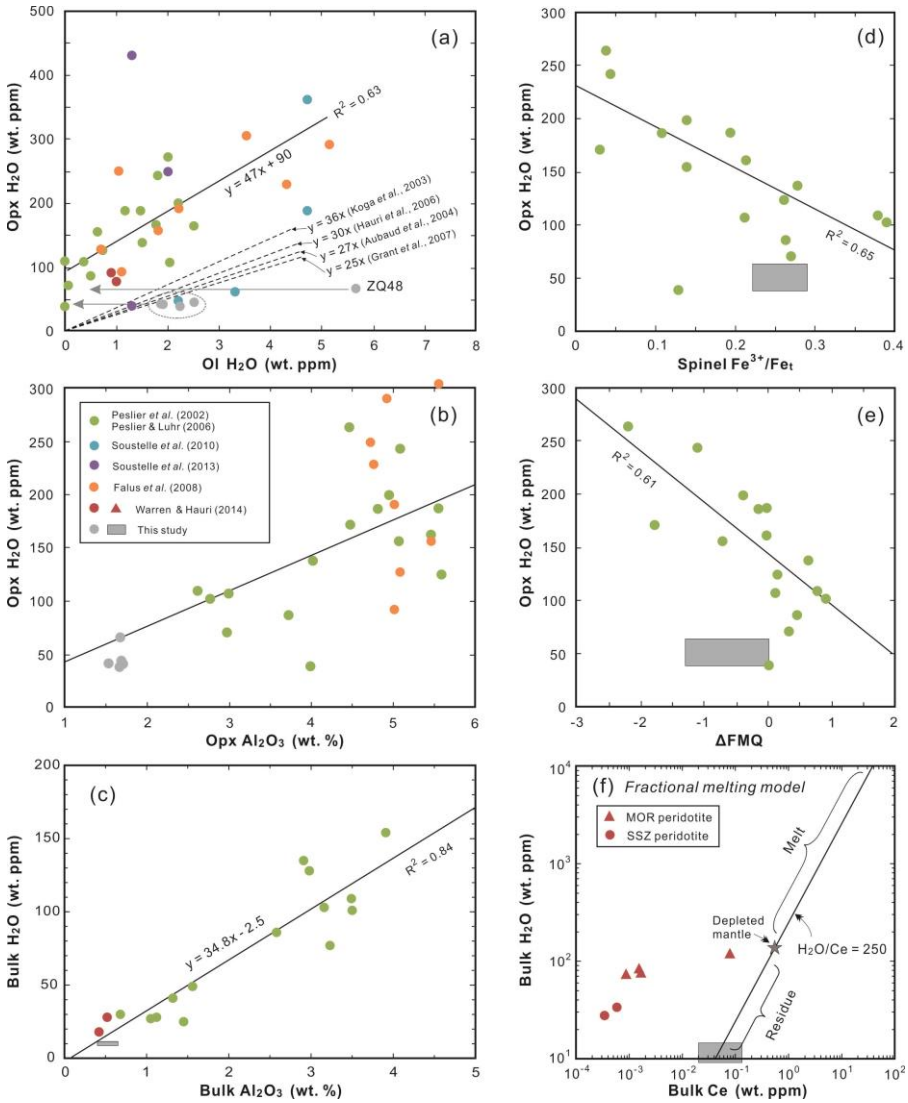

Fig. 4.14. (a) Measured water contents of olivine and Opx in Yushigou harzburgites and the peridotites originated from other different subduction zone settings. The water concentrations of olivine are converted to the calibration of Paterson (1982) for comparison between data in this study (grey symbols) and literature (color symbols). Different experimentally determined equilibrium relations of water contents between olivine and Opx (dashed lines) are also modified based on the calibration of Paterson (1982). Grey arrows suggested that the measured water concentrations of olivine were probably overestimated due to noise and need to be reduced to very low values corresponding to the olivine-Opx trend derived from literature data. (b, c) Relations between water and Al_2O_3 contents in Opx (b) and whole rock (c). (d, e) Relations between Opx water content and spinel Fe^{3+} ratio (d) and oxygen fugacity (ΔFMQ) (e) of peridotites. (f) Relations between whole-rock water and Ce concentrations. The ranges of water and Ce contents in melt and residue were calculated after variable degree of fractional melting of a depleted mantle by Warren & Hauri (2014), and are well consistent with H_2O/Ce ratio of ~250.

ppm) of Opx in the studied samples may still imply the minimum loss of water in Opx. Consequently, the original amount of water in olivine can be recalculated from the Opx water concentration using the known Opx-Ol partition coefficients, and effects of spectra noise in disturbing the olivine water estimation can be ignored. By applying the experimentally determined average Opx-Ol partition coefficient $D_{H_2O}^{Ol/Opx}$ of 0.11 ± 0.03 obtained from low-pressure (< 2 GPa) alumina-bearing experiments (Aubaud *et al.*, 2004, Grant *et al.*, 2007b, Hauri *et al.*, 2006, Koga *et al.*, 2003) which is similar to the depleted nature of spinel harzburgites in this study, we obtained average water concentrations of 4–7 wt ppm for olivine and 9–14 wt ppm for bulk-rock using the approximate olivine and Opx modal proportions (Table 4.1). The extremely low water concentrations in Opx and whole rock are well-correlated with the very low Al_2O_3 contents in Opx and whole rock, respectively (Figs. 4.14b and c). This result can be explained by the highly incompatible behavior of water during partial melting (e.g., Hirschmann, 2006, Michael, 1995), as well as the low solubility of water in Al_2O_3-depleted Opx because coupled substitution of $Al^{3+} + H^+$ is a main water incorporation mechanism in Opx (e.g., Keppler & Bolfan-Casanova, 2006, Mierdel *et al.*, 2007, Rauch & Keppler, 2002). Both of these processes are strongly dependent on the degree of partial melting, indicating that the extremely low water contents are consistent with their extremely refractory residual origin (e.g., Hao *et al.*, 2014). On the other hand, the good correlations between water and Al_2O_3 concentrations in Opx and whole rock, imply that no significant water loss has occurred in Opx during emplacement. This feature of low water concentration, however, is less controlled by the redox state of the peridotite, because the Opx shows remarkably lower water content at measured spinel Fe^{3+} content and calculated oxygen fugacity (Figs. 4.14d and e), although the rocks are fairly oxidized

corresponding to a fore-arc mantle setting.

The extremely depleted mineral and whole rock compositions and low water contents not only characterize a residual nature of harzburgites after high-degree partial melting, but also imply that no significant melt/fluid-rock reactions have occurred simultaneously or subsequently. Conformably, prominent whole rock trace element compositions such as elevated LREE pattern (U-shaped REE pattern) and large ion lithophile elements (LILEs) enrichments (Fig. 4.13, see also Song *et al.* (2009b)) suggest that melt-rock reaction have most likely occurred following the termination of partial melting but in a mild extent, because (1) the observed mineral modal abundances are similar to the residue purely results from high-degree partial melting; and (2) only a small amount of reacting melt (less than a few percent) could be enough to modify the incompatible elements concentration of the very depleted nature of harzburgites (Parkinson & Pearce, 1998, Parkinson *et al.*, 1992). To maintain the depleted natures of mineral compositions, the reactive melt needs to be highly depleted and Mg-rich (e.g., boninite) so that it can dissolve pyroxenes to form high Fo# olivine and/or high Cr# spinel (e.g., Parkinson & Pearce, 1998, Pearce *et al.*, 2000, Zhou *et al.*, 1996). Because water behaves highly incompatibly with the great similarity to Ce during partial melting (e.g., Hirschmann, 2006, Michael, 1995), both the melt and residue would have a similar H_2O/Ce ratio (Fig. 4.14f). Unlike the peridotites displaying much higher water content at extremely depleted bulk Ce content, which is probably owing to a late-stage melt infiltration at relatively low temperature (e.g., T = 1000 ℃) during which only hydrogen can diffuse fast enough to attain re-equilibration (Warren & Hauri, 2014), the similar H_2O/Ce ratio of refertilized Yushigou harzburgites to those melt and residue (Fig. 4.14f) corroborates that the reacting melt probably has a very high temperature which most likely corresponds to boninitic magma (T > 1100 ℃) that is generated at an early and warm fore-arc

mantle setting (Crawford, 1989, Kim & Jacobi, 2002). In contrast, the relatively low-temperature Mg-rich melt reacting with harzburgites is indicated by replacive dunitic veins which have lower olivine Fo# (~ 90) and spinel Cr# (0.41–0.50) (Song *et al.*, 2009b), whose genesis is likely linked with residual melt of boninite – more tholeiitic in composition – after its high-temperature reaction with harzburgites. In this context, the reaction between olivine and Si-rich melt to form pyroxenes at relatively low temperatures is thus unreasonable for Yushigou harzburgites. The observed textures of anhedral and interstitial Opx and Cpx which are often taken as secondary crystallizing phases to evidence the Si-rich fluid/melt infiltration and its reactions with solid rock can also indicate the dissolution of pyroxenes due to intense partial melting and/or reaction with Mg-rich melt.

4.7.1.2. Plastic deformation

The plastic deformation processes of Yushigou harzburgites are clearly documented by the strained olivine and Opx grains which show intense intracrystalline plasticity features (e.g., subgrain boundaries, kink bands and undulose extinctions, see Figs. 4.2, 4.3, 4.7 and 4.9), and the pronounced mineral CPOs (Fig. 4.4). It is reasonable to believe that this plastic deformation probably occurred after and/or simultaneously with partial melting, because (1) the intensive static partial melting (~25–30% degree, as this case) and associated crystalized new olivine grains may be expected to weaken, if there is, any strong pre-existing mineral fabrics, in a similar manner to those intense magma-rock interaction processes (e.g., Morales & Tommasi, 2011, Tommasi *et al.*, 2004), and (2) axial-[100] or dry A-/D-type olivine fabric requires a water-poor harzburgite which is most likely dried out by intense partial melting (e.g., Bystricky *et al.*, 2000, Jung *et al.*, 2006). Provided that the plastic deformation was concurrent with partial melting, the observed strong olivine

and Opx as well as the discernable Cpx fabrics likely suggest the presence of a low instantaneous melt fraction which in turn requires efficient melt extraction during partial melting, because large amounts of accumulated melt can favor melt-enhanced diffusional creep and lead to a decrease in mineral fabric intensity (e.g., Frets *et al.*, 2014, Higgie & Tommasi, 2012, Hirth & Kohlstedt, 1995b, Holtzman *et al.*, 2003, Holtzman & Kohlstedt, 2007, Le Roux *et al.*, 2008). As discussed above, the mild high-temperature melt-rock interaction probably occurred simultaneously with partial melting or shortly after following the cessation of partial melting when the harzburgite is still hot enough, which also implies a post- or syn-kinematic Mg-rich melt percolation process. In the post-kinematic case, because of the observed remarkable mineral fabrics and the inferred small amount of infiltrating melt, the CPO strength and pattern of olivine and pyroxene are only expected to be slightly affected by melt-rock reactions (e.g., Tommasi *et al.*, 2008, Zaffarana *et al.*, 2014). In contrast, when a small instantaneous melt fraction, either derived from partial melting or melt percolation, is present as triple junctions or less interconnected bands in the system synchronously with plastic deformation, a local increase in stress due to reduced solid contact area between grains and a local enhance in grain boundary sliding (GBS) process would be expected (e.g., Hirth & Kohlstedt, 1995a, Holtzman & Kohlstedt, 2007, Kohlstedt & Holtzman, 2009, Rosenberg & Handy, 2001, Scott & Kohlstedt, 2006). These outcomes may further lead to decrease in viscosity, and promote mineral fabric developments by the mechanisms of dislocation creep and/or dislocation-accommodated GBS (DisGBS) process during plastic deformation.

The plastic deformation accommodated by the slip of dislocation are explicitly responsible for the CPO developments of olivine, Opx and Cpx in our samples. The observed axial-[100] or A-/D-type olivine fabric dominated by (010)[100] slip system and dominant (100)[001] slip system of Opx are

essentially similar to those reported in literature (see references in previous section). In the second-order context, previous laboratory experiments, numerical simulations and natural rock investigations proposed that three different sub-mechanisms involving dislocation slip can explain the formation of D-type olivine CPO under dry and low-pressure conditions, including low-temperature and high-stress conditions relative to A-type or orthorhombic olivine CPO (Bystricky *et al.*, 2000, Carter & Ave'Lallemant, 1970, Jung *et al.*, 2006, Zhang *et al.*, 2000), transtensional deformation regime (Tommasi *et al.*, 1999), high-temperature and low-stress dislocation creep with strain compatibility constraints relaxed by grain-to-grain interactions (Tommasi *et al.*, 2000) or GBS (Hansen *et al.*, 2012, Warren *et al.*, 2008) under moderate transient strain condition (Hansen *et al.*, 2014). The above discussed relations between partial melting, melt-rock reaction and plastic deformation, as well as the interpenetrating subgrain-bearing olivine grains indicative of syn-kinematic intense grain boundary migration (GBM) process (Figs. 4.3e and f), together suggest that the slip of dislocation and development of the subgrain textures mainly occurred at near solidus high temperature (T ~ 1200–1350 °C) and dry conditions. The absence of garnet in spinel harzburgites indicates that the equilibrium pressure was likely less than 2–3 GPa at a hot fore-arc mantle setting, since high Cr content of spinel can increase its stability to higher pressure condition (~3 GPa at bulk-rock Cr# of ~0.6, based on Klemme (2004)). The average differential stress of harzburgites was in the low ranges of 3–4 and 1–3 MPa which were estimated by using dry olivine recrystallized grain size piezometer of Van der Wal *et al.* (1993) and dry olivine subgrain size piezometers of Karato *et al.* (1980) and Ross *et al.* (1980), respectively (Table 4.1). Because the same olivine grains having remarkable subgrain textures were used for the measurement of the recrystallized grain size and subgrain size, the slight difference between the stress values estimated from recrystallized grain

size and subgrain size piezometers suggests that an approximate stress equilibrium between subgrains and their hosting grains might have been obtained in the specimen.

These estimated high-temperature and low-stress values of axial-[100] or A-/D-type olivine CPO in Yushigou harzburgites as well as the peridotites in other studies, represent a typical lower lithospheric to asthenospheric condition; and these temperature and stress values seem indistinguishable from many other natural peridotites which have clear orthorhombic A-type olivine CPO (e.g., Falus *et al.*, 2011, Higgie & Tommasi, 2014, Zaffarana *et al.*, 2014). Besides, the inferred olivine dislocation slip systems in Yushigou harzburgites are dominated by (010)[100] and less (001)[100], whereas other [100]-slip, {0kl}[100] and [001]-slip systems are minor in proportions (Figs. 4.7 and 4.8). This result seems different from D-type olivine CPO in which the {0kl}[100] slip system is considered as dominantly activated at the high-stress conditions (Bystricky *et al.*, 2000, Jung *et al.*, 2006, Zhang *et al.*, 2000). In contrast, (010)[100] and (001)[100] are the dominant slip systems to form A- and E-type olivine CPOs which are both favored at low-stress conditions (Jung *et al.*, 2006, Katayama *et al.*, 2004, Zhang & Karato, 1995, Zhang *et al.*, 2000). Even though one sample (ZQ60) showed a D-type fabric (Fig. 4.4d), the stress of the sample appears to be similar level to the other samples (Table 4.1). The relatively weak development of foliation may favor a transtensional deformation regime, however, the fabric strength order of different principal axes of olivine and Opx and weak girdle distribution of Opx [001] axis parallel to foliation indicate that the deformation is dominated by simple shear. Besides, the transtensional deformation most commonly occur in an extensional continental rifting region (e.g., Vauchez *et al.*, 2000), and is less likely observed in a convergent setting such as subduction zone.

The D-type olivine CPO is also likely caused by the DisGBS process,

which is an important mechanism to relax strain compatibility constraints and Von Mises condition, so that the olivine aggregate can be deformed homogeneously with the activations of limited independent easiest dislocation slip systems of (010)[100] and (001)[100] (Hansen *et al.*, 2012, Hirth & Kohlstedt, 1995a, Warren *et al.*, 2008). Although DisGBS process has been confirmed by the deformation experiments (Hansen *et al.*, 2011), it is necessary to note that this interpretation may not be definitive as for our natural samples, because no clear textural evidence of GBS was observed, and ubiquitous syn-kinematic interlocking olivine grains resulted from intense GBM (Figs. 4.3e and f) may restrict the activation of GBS and thus question the efficacy of DisGBS process. The similar issue questioning the reasonability of GBS has also recently been raised by Cordier *et al.* (2014), they instead proposed that the motion of grain-boundary rotational crystallographic defects (i.e. disclinations) could be an alternative mechanism to accommodate homogeneous plastic deformation of olivine-rich rocks in the mantle. If this argument is reasonable, we speculate that the disclinations based GBM might be another possible mechanism to produce D-type olivine CPO in Yushigou harzburgites, where GBM process was intensely activated. To test this hypothesis, more detailed examinations on the crystallographic sub-microstructures of migrated grain boundaries would be needed.

Although the number of studied sample is limited in this study, it is still interesting to note that sample ZQ48 shows consistently higher olivine fabric strength (M- and J-index, Fig. 4.6), water contents of Opx and whole rock (Figs. 4.10, 4.14 and Table 4.1), and stress (estimated from sub-grain size piezometer, Table 4.1) than the other four samples. These positive correlations may imply that stress and strain might have been localized in the sample which contains relatively more water and thus has a weaker mechanical strength. Besides, it is also noted that sample ZQ48 exhibits the largest shape parameters of both

olivine [100] and [010] axes, suggesting larger component of (010)[100] slip system (or A-type CPO) than the other samples (Table 4.2). The relation between larger activation of (010)[100] slip system and higher strain is consistent with the experimental result by Hansen *et al.* (2014), and likely supports the protracted evolution of A- and D-type olivine fabrics. However, to further confirm this argument, more comparisons of olivine CPOs between different strained samples are obviously necessary.

4.7.2. Distributions of olivine fabrics in subduction zone

The distributions of olivine fabrics in an evolutionary subduction zone is an open and complicated issue that has been addressed in some previous studies, but has not been systematically organized in details yet. It is no doubt that understanding how the olivine fabric distributes in a subduction zone would be beneficial for the further interpretations of variable seismological observations which will also be briefly discussed in the next section. In this section, we attempt to present an improved schematic model to describe how the olivine fabrics are distributed in two end-member cases – young & warm and mature & cold subduction zones – with the emphasis in the mantle wedge, based on the results from this research and a number of previous studies.

As discussed in the previous sections, the mineral and rock chemical compositions and the estimates of pressure, temperature, water content and stress together indicate that the Yushigou harzburgite was probably generated and deformed in a shallow and hot lower lithospheric to asthenospheric mantle wedge beneath fore-arc region at an early evolutionary stage of subduction zone (Fig. 4.15a). In this context, the Yushigou harzburgite can be regarded as the relict of high-degree melting residue which was produced above the subducting oceanic slab by addition of H_2O-rich fluid or silicate melt from the slab. Because the melting residue has lower density than the surrounding unmolten

mantle, it rose as a diapir and later constituted the fore-arc lithospheric mantle with ongoing cooling. The plastic deformation of Yushigou harzburgite was driven by the mantle flow and occurred simultaneously or after partial melting when the temperature was high enough before the rock and its mineral fabrics was ultimately fossilized into the cold lithosphere. The conditions of high-temperature, low-stress and water-depleted nature of Yushigou harzburgite thus yielded A-/D-type olivine fabrics which is expected to be prevailing in the fore-arc lithospheric mantle. By contrast, the primordial peridotites in unmolten region immediately overlying the subducting oceanic slab would expect to contain E- or C-type olivine fabrics which can be formed in a wet, high-temperature and low-stress condition under simple shear (Jung *et al.*, 2006, Katayama *et al.*, 2004, Katayama & Karato, 2006) (Fig. 4.15a). However, the primordial fore-arc peridotite having E- or C-type olivine fabrics has actually not been reported in nature yet. Rather, the natural E-type olivine fabric was occasionally found in some highly refractory fore-arc peridotites (Harigane *et al.*, 2013, Mehl *et al.*, 2003). The explanations for this observations could be multifold. However, based on the speculated schematic model above, one suggested likelihood is that the E- or C-type olivine fabrics could be developed, if some refractory peridotites were eroded or pinched off the base of the overriding fore-arc lithosphere and returned into the wet interface between downgoing slab and mantle wedge, owing to the corner-flow induced convective erosion or the Raleigh-Taylor instabilities induced small-scale convective destabilization (e.g., Arcay *et al.*, 2005, Le Voci *et al.*, 2014a, van Keken, 2003).

The incremental accumulation of refractory diapirs due to sustained partial melting and conductive cooling of fore-arc mantle by continuous subduction of cold oceanic lithosphere would gradually thicken and chill down the fore-arc lithosphere, as well as deepen the melting region towards the core of mantle

wedge. Under this situation, A-/ D-type olivine fabrics would be expected to occur in both fore-arc and back-arc lithospheric mantle in a mature and cold subduction zone (Fig. 4.15b). This speculation may be corroborated by the frequent observations of A-/D-type olivine CPO in natural peridotites derived from fore-arc and back-arc mantle lithosphere (Falus *et al.*, 2008, Jung *et al.*, 2009b, Michibayashi *et al.*, 2006a, Michibayashi *et al.*, 2009a, Michibayashi *et al.*, 2009b, Michibayashi *et al.*, 2007, Morales & Tommasi, 2011, Satsukawa & Michibayashi, 2014, Soustelle & Tommasi, 2010, Soustelle *et al.*, 2013, Soustelle *et al.*, 2010, Tommasi *et al.*, 2006). In the shallow vicinity of subducting slab, the fore-arc lithospheric mantle is supposed to be partially hydrated or metasomatized (dominantly serpentinization) by the silicate and water rich fluids released from the underlying slab. As depth increases in the fore-arc mantle, the olivine fabric is considered to be changed from A-/D-type CPO in the lithosphere into a wet B-type CPO owing to simple shearing under wet, low-temperature and high-stress conditions (Jung & Karato, 2001a, Jung *et al.*, 2006, Ohuchi *et al.*, 2012) or partly due to the topotactic grow of olivine after the oriented antigorite (Nagaya *et al.*, 2014) in the lithosphere-asthenosphere boundary (LAB) region near the descending slab (Kneller *et al.*, 2005, McCormack *et al.*, 2013) (B-type region in Fig. 4.15b). In a similar mechanism with the wet E- or C-type olivine fabric occurring in the warm subduction zone, the B-type olivine fabric can be formed in either primordial or refractory peridotites in a cold subduction zone, which has been evidenced by several natural observations (e.g., Jung, 2009, Jung *et al.*, 2014, Kim & Jung, 2014, Mizukami *et al.*, 2004, Nagaya *et al.*, 2014, Skemer *et al.*, 2006, Tasaka *et al.*, 2008, Wang *et al.*, 2013a). In comparison, the E- or C-type olivine fabrics would preferably occur in the deeper arc to back-arc mantle above descending slab where the temperature is higher for the formation of these fabrics (Karato *et al.*, 2008, Kneller *et al.*, 2005, Terada *et al.*, 2013). This inference is also

consistent with the available observations of natural C-type olivine fabrics in the high-pressure garnet peridotites originated from cold subduction zones (Frese *et al.*, 2003, Jung *et al.*, 2013, Katayama *et al.*, 2005, Wang *et al.*, 2013a, Wang *et al.*, 2013b, Xu *et al.*, 2005), although the effects of pressure on forming C-type fabric is still debated.

Compared with the olivine fabrics inside mantle wedge, the olivine fabric in the subducting oceanic lithosphere and asthenosphere is much less understood yet. It is generally regarded that the dry olivine CPOs (i.e. A- and D-type) would be the most dominant fabric types residing in the oceanic lithosphere owing to the extensive water depletion by partial melting at the mid-oceanic ridge regions, whereas the relatively damp asthenosphere might bear wet E- or C-type fabrics (reviews of Karato *et al.*, 2008). Besides, some high-pressure experiments implied that C- or B-type CPO of olivine may also be present in the deep oceanic lithosphere or asthenosphere due to high pressure (> 3–7 GPa) (e.g., Couvy *et al.*, 2004, Jung *et al.*, 2009c, Mainprice *et al.*, 2005, Ohuchi *et al.*, 2011, Raterron *et al.*, 2007). More recently, some studies based on the seismic evidences and natural samples also suggested that AG-type olivine fabric – [010] axis clustering normal to foliation, while [100] and [001] axes dispersing on foliation-parallel girdles – may also exist in the oceanic lithosphere and asthenosphere (e.g., Bascou *et al.*, 2008, Harigane *et al.*, 2011, Song & Kawakatsu, 2012). Therefore, the olivine fabric distributions in the subduction zone, especially in the oceanic lithosphere and sub-slab mantle, are actually more complicated than previously considered. More analysis of the natural peridotite samples and seismic observations in the arc and oceanic mantle would greatly benefit to understand the characteristics of mantle deformation in the subduction zone setting.

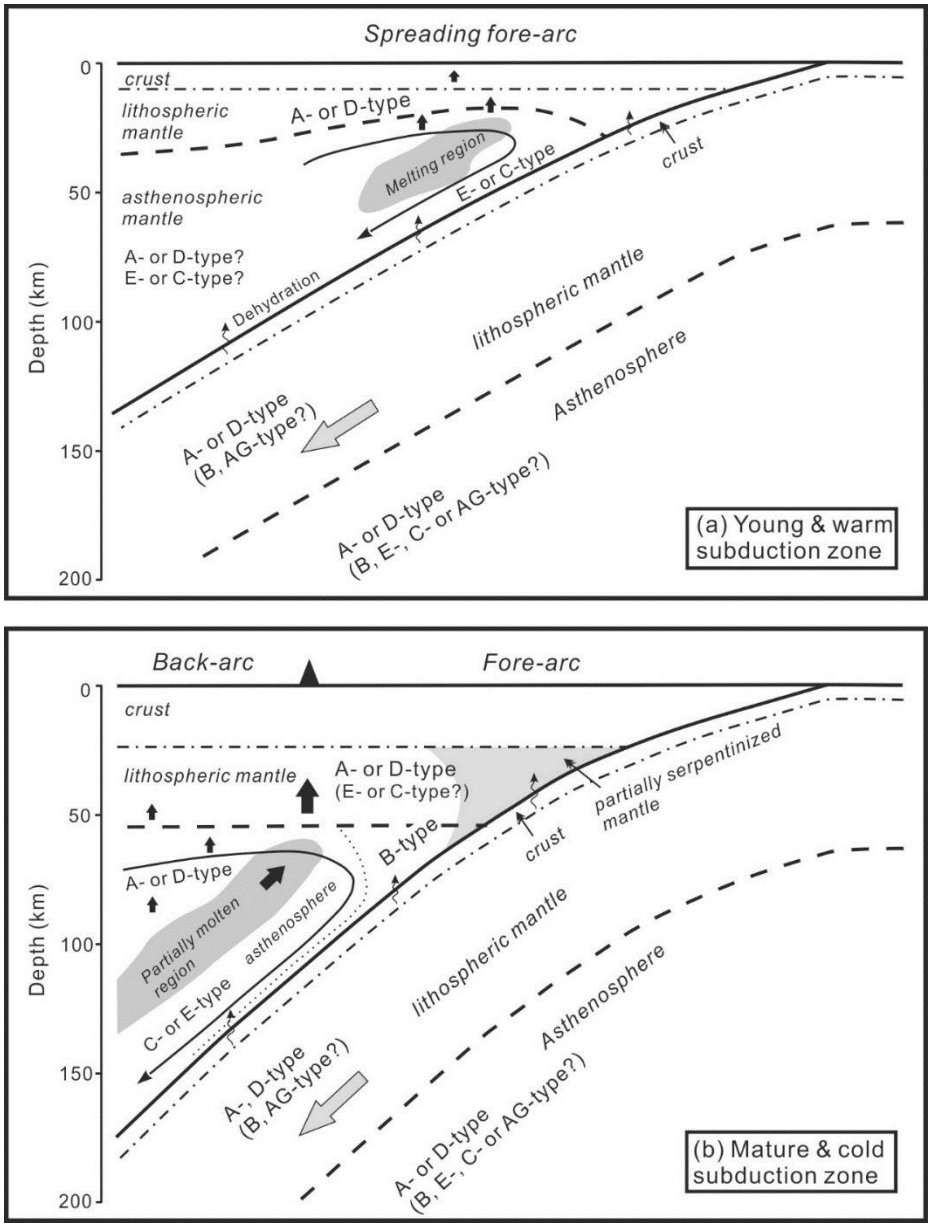

Fig. 4.15. Schematic illustrations showing the olivine fabric distributions in (a) young & warm and (b) mature & cold subduction zones under two-dimensional corner flow. The depths of LAB are denoted as thick dashed lines. Diapiric upwelling of melting residue and corner flow are indicated by thick and thin solid arrows, respectively. Dotted line in (b) denotes the boundary between olivine B-type and C- or E-type fabrics. Refer to the main text for the detailed explanations of olivine fabric occurrences and references therein for the structures of subduction zone.

4.7.3. Seismic implications in the fore-arc mantle

As discussed in the previous section, it is reasonable to consider that both fore-arc and back-arc mantle lithospheres are plastically deformed and mainly contain A-/D-type olivine fabrics, based on frequent observations in natural peridotites which are originated from arc lithospheric mantle (this and previous studies as shown above). The anisotropic layer of mantle lithosphere will thus undoubtedly affect the seismic anisotropies observed in both fore-arc and back-arc regions, although the degree of impact can be variable depending on a set of parameters such as the thickness of anisotropic layer, extent of plastic deformation, olivine fabric, and olivine modal composition, as well as the flow geometry inside mantle wedge. The fore-arc region of a mature subduction zone, is a unique tectonic area where the upward travelling fast shear waves commonly polarize sub-parallel to the trench or the strike of subduction zone. Unlike this convergent seismic phenomenon, the formation mechanisms are however highly divergent and at least four major anisotropic sources can contribute significantly to this trench-parallel seismic anisotropy, including the overriding crust (e.g., Huang *et al.*, 2011b, Iidaka *et al.*, 2014, Wölbern *et al.*, 2014), mantle wedge (e.g., Jung & Karato, 2001a, Jung *et al.*, 2006, Kim & Jung, 2014, Nakajima & Hasegawa, 2004, Nakajima *et al.*, 2006, Rabbel *et al.*, 2011, Russo & Silver, 1994, Smith *et al.*, 2001), subducting oceanic slab (e.g., Cao *et al.*, 2013, Faccenda *et al.*, 2008, Healy *et al.*, 2009) and sub-slab mantle (e.g., Di Leo *et al.*, 2014, Faccenda & Capitanio, 2012, Jung *et al.*, 2009c, Long & Silver, 2008).

Among these sources, the mantle wedge is the most complicated one, because the trench-parallel fast velocity directions can be caused by B-type olivine fabric under corner flow, A-, D- or E-type olivine fabrics under arc-parallel flow, as well as the oriented layers of hydrous phases above descending

slab (refer to the references in the introduction section). Moreover, the anisotropic sources of lithospheric and asthenospheric mantle inside mantle wedge were often not well separated, which may in turn limit the interpretation of the olivine fabrics and mantle flow patterns on the basis of seismic anisotropy observations. If as depicted in Fig. 4.15b, the A-/D-type and B-type olivine fabrics were formed under a two-dimensional corner flow and dominated in the lithospheric and asthenospheric mantle beneath the mature fore-arc region, respectively, the overall contribution of seismic anisotropy that results from the deformed mantle wedge is expect to be reduced, owing to the contradictory polarizing directions of fast shear wave between olivine A-/D-type (trench-normal) and B-type (trench-parallel) fabrics. Likewise, this counteracting effect also exists between A-/D-type olivine fabric and other trench-parallel seismic anisotropic sources such as oriented serpentinite layer, aligned cracks in the overriding crust and subducting slab. This counteracting effect between different anisotropic layers may thus offer an alternative mechanism to explain the weak or nearly null delay time (i.e. $\delta t < 0.3$s) observed in some cold fore-arc regions especially where thin layers of strong trench-parallel seismic anisotropy (e.g., oriented serpentine or chlorite) are supposed to be stable immediately above the slab-wedge interface, such as northeast Japan (e.g., Nakajima & Hasegawa, 2004, Tsuji *et al.*, 2008). This argument may, on the other hand, weaken the importance of B-type olivine fabric and highlight other mechanisms in explaining the observed trench-parallel polarization anisotropy, especially those showing large delay times (i.e. $\delta t > 1$s). This conclusion may not be significantly different from that in the three-dimensional mantle flow, if the lithospheric and asthenospheric mantle can be assumed to flow successively in a conformable pattern.

Additionally, the olivine fabric in the mantle wedge can also significantly influence the fabric of antigorite which is formed in the uppermost region of

the serpentinized fore-arc lithospheric mantle, and in turn affect its seismic velocities and anisotropies (case 1 in Fig. 4.16d). Previous microstructures analysis (e.g., EBSD and TEM) have clearly demonstrated that antigorite fabric can grow topotactically after olivine crystal with a predominant topotatic relationship as $[001]_{atg} // [100]_{ol}$ and $[010]_{atg} // [001]_{ol}$ (e.g., Boudier *et al.*, 2010, Brownlee *et al.*, 2013, Morales *et al.*, 2013). Among the reported antigorite fabrics, the most commonly observed one shows that [001] axis clusters perpendicularly to the antigorite foliation whereas [100] and [010] axes form a girdle with a maximum of [010] axis aligning sub-parallel to the lineation (e.g., Brownlee *et al.*, 2013, Hirauchi *et al.*, 2010, Jung, 2011, Morales *et al.*, 2013, Nishii *et al.*, 2011, Shao *et al.*, 2014, Soda & Takagi, 2010). Based on the predominant topotatic relationship between olivine and antigorite, the consistent clustering between $[001]_{atg}$ and $[100]_{ol}$ and girdles between $[100]_{atg}$, $[010]_{atg}$ and $[010]_{ol}$, $[001]_{ol}$ thus indicate that the A-/D-type olivine fabric could be a likely precursor of this antigorite fabric which develops in the partially serpentinized fore-arc lithospheric mantle of serpentinization that is dominantly controlled by topotatic growth (case 1 in Fig. 4.16d). Because (1) antigorite is a plate-like mineral which is nearly transversely isotropic in seismic velocities, and (2) the seismic rays emanated from intra-slab earthquakes tend to propagate vertically more than horizontally when propagating through the uppermost fore-arc mantle (Fig. 4.16d), the seismic velocities, P to S wave velocity ratios and seismic anisotropies which are observed in the fore-arc region would be closely affected by the orientations of serpentinite foliation in the serpentinized mantle wedge (e.g., Bezacier *et al.*, 2010a, Hacker & Abers, 2012, Jung, 2011). If the lineation of A- or D-type olivine fabric is nearly horizontal due to early horizontal corner flow at the LAB, a steep foliation of antigorite would thus expect to form by topotactically replacing the pre-existing A-/D-type olivine

crystals. In this case, the low angle geometry between steep antigorite foliation and seismic ray paths will therefore generate relatively high velocities (Vp ~ 7.0–8.1 km/s, Vs ~ 3.8–4.8 km/s), relatively low Vp/Vs1 ratios (~ 1.63–1.72) and variable shear wave polarization anisotropies (AVs ~ 1–30%), depending on the fractions of antigorite or the degrees of serpentinization (Figs. 4.16a-c). Both P-wave and S-wave velocities decrease steadily with incremental fractions of antigorite (Fig. 4.16a). The Vp/Vs1 ratios are the lowest when seismic rays propagate at high-angle to the foliations of fresh harzburgite, but increase slightly and remain constant with increasing serpentinization degrees (Fig. 4.16b). The variations of fast shear wave polarization anisotropy are more complex (Fig. 4.16c). The polarization directions change gradually from trench-normal which is controlled by the mineral fabrics in harzburgite to trench-parallel which is determined by oriented antigorite with the increasing fractions of antigorite. This trend of transition in polarization direction is also accompanied by the intensity variation of seismic anisotropy which decreases initially and increases rapidly at an inflection point of approximately ~20% antigorite fraction (Fig. 4.16c) (see also Boudier *et al.*, 2010, Brownlee *et al.*, 2013). However, these calculated relatively high Vp and Vs values in Fig. 4.16a seem not very well matching with the low seismic velocities (Vp ~ 6.4–7.7 km/s, Vs ~ 3.0–4.4 km/s) that are frequently observed in a typical hydrous fore-arc mantle (e.g., Bohm *et al.*, 2002, Bostock *et al.*, 2002, Brocher *et al.*, 2003, DeShon & Schwartz, 2004, Hyndman & Peacock, 2003, Kamiya & Kobayashi, 2000, Matsubara *et al.*, 2009, Nakajima *et al.*, 2009a, Ramachandran *et al.*, 2006, Tibi *et al.*, 2008, Tsuji *et al.*, 2008). The calculated Vp/Vs1 ratios in Fig. 4.16b also appear too low to match the high Vp/Vs ratios (~ 1.76–1.85) in fore-arc mantle, but agree well with the unusually low Vp/Vs ratios (~ 1.60–1.72) in the deeper mantle wedge (50–100 km) (e.g., Eberhart-Phillips *et al.*, 2006, Hacker & Abers, 2012, Rossi *et al.*, 2006, Wagner *et al.*, 2008). Nevertheless,

this topotactic growth of antigorite after A-/D-type olivine fabric can result in trench-parallel fast shear wave polarization anisotropy with large delay times from local and teleseismic events.

By contrast, the low velocities and high Vp/Vs ratios indicative of typical hydrous fore-arc mantle can be well explained by the oriented antigorite layers replacing strained harzburgite immediately atop the subducting slab (Vp ~ 5.9–8.1 km/s, Vs ~ 3.3–4.8 km/s, Vp/Vs1 ~ 1.55–1.85; see case 2 in Figs. 4.16a, b and d). The antigorite fabric having (001) plane sub-parallel to the olivine [100] axis and slab surface most likely results from intense shearing at the slab-wedge interface. The deformation-induced antigorite fabric presents (001) plane parallel to shear plane, and [010] axis aligning sub-parallel to shear direction or lineation (e.g., Hirauchi & Katayama, 2013, Jung, 2011, Katayama *et al.*, 2009, Soda & Takagi, 2010, Soda & Wenk, 2014), which essentially resembles the topotactic antigorite fabric grown after A-/D-type olivine fabric. The relations between shear wave polarization anisotropy and fraction of antigorite follow similar trend as those in the case 1, however, the intensities of trench-parallel seismic anisotropy (AVs ~ 2–13%) are significantly lower than the case 1 from intra-slab seismic events (Fig. 4.16c).

However, it is noteworthy that these two serpentinization cases are extremely idealized as end-member cases. The core of the serpentinized fore-arc mantle may thus be regarded as the intermediate case between the case 1 and 2, in which the antigorite fabric is caused by both topotactic growth and plastic deformation. Therefore, the observed seismic properties should be more appropriately taken as the average of these different anisotropic layers, if the depth resolution of seismic wave is not available. This concept may, on the other hand, imply that the proportions of these different serpentinization layers and degrees of serpentinization might be estimated based on the observed seismic velocities, Vp/Vs ratios and intensities of seismic anisotropies.

However, before drawing this implication, the influences of other factors (e.g., other hydrous phases, fluids, orientations of different anisotropic layers) have to be constrained in priority. Besides that, it is also necessary to point out the notion proposed above is probably over-simplified, since the vertical flow of serpentinite as diapirs is obviously not considered. This diapiric flow process may tremendously increase the structural complexities inside hydrous fore-arc mantle and limit the implications based on the current interpretations. Nevertheless, it is still worthwhile to raise these details about the potential seismic effects of anisotropic harzburgite and associated serpentinization processes in an enigmatic fore-arc setting.

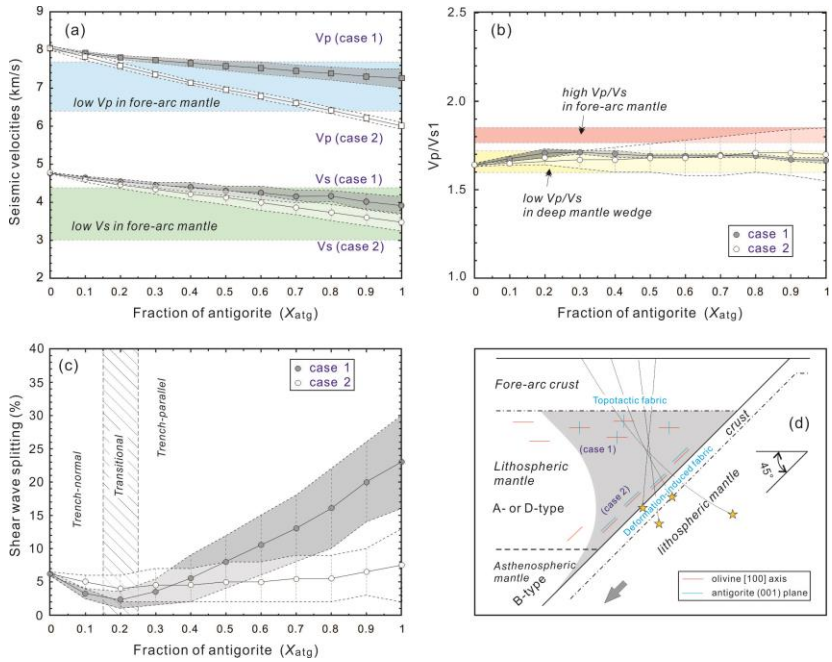

Fig. 4.16. The relationships of (a) seismic velocities, (b) Vp/Vs1 ratios and (c) intensities of shear wave splitting with fractions of antigorite for two end-member serpentinization cases in fore-arc lithospheric mantle as shown in (d). Serpentinization case 1 is located in the uppermost fore-arc mantle where topotactic growth of antigorite was assumed after anisotropic peridotite, Serpentinization case 2 is located immediately atop the descending slab where deformation-induced antigorite fabric was assumed. The orientations of olivine [100] axis and traces of antigorite (001) plane in 2D cross-section of subduction zone are marked as red and blue lines in (d), respectively. The orientation of olivine [100] axis was presumably formed due to prior corner flow which is fossilized in the present-day lithospheric mantle. The representative seismic rays emanated from intra-slab earthquake events (yellow star in (d)) are also presented to show the sampling path of anisotropic medium in the fore-arc mantle. The seismic velocities and anisotropies of serpentinized harzburgite are calculated using the ambient densities and rock elasticity stiffness tensors of averaged Yushigou harzburgite in this study and a deformed antigorite aggregate from Jung (2011) (Table 3). Because the seismic rays from intra-slab earthquake events tend to propagate at high angles to the rock foliations in both cases 1 and 2, the calculated seismic velocities, Vp/Vs1 ratios and intensities of shear wave splitting within about 30 °to the pole of foliation are presented with their variation ranges filled in grey and white colors and outlined by thin dash lines. The ranges of variation reflect the spatial clustering of seismic velocities and anisotropies: wider variation range implies stronger spatial concentration, and vice versa. See main text for the references of low Vp and Vs values and high Vp/Vs ratios in fore-arc mantle, as well as the low Vp/Vs ratios in deep mantle wedge in (a) and (b). Additionally, because most local shear wave arrival times are based on picks of the first arriving signal, only the calculated Vp/Vs1 ratio was applied to represent the seismologically measured Vp/Vs ratio (Hacker & Abers, 2012).

4.8. Conclusions

Examining the chemical composition, deformation and seismic properties of natural peridotites originated from fore-arc mantle provides a rare opportunity to directly understand the geological and geodynamic processes that occurred in the history of fore-arc and subduction zone evolution. The Yushigou harzburgite from the North Qilian suture zone is such a case. The detailed mineral and whole rock composition analysis suggest that these harburgites are highly refractory after experiencing a high-degree partial melting (~ 25–30% fractional melting) and mild high-temperature melt-rock reaction, and thus represent a remnant of a fossil fore-arc lithospheric mantle in a young and warm subduction zone setting. The elaborative analysis on olivine, Opx and Cpx CPOs and subgrain rotation axes distributions suggest that both olivine and pyroxenes have typical mineral fabrics that result from the activation of a series of dislocation slip systems. Olivine (A-/D-type fabric) showed dominant (010)[100], secondary (001)[100] and other minor [100]-slip, {0kl}[100] and [001]-slip systems. Opx showed dominant (100)[001] and secondary (010)[001], (100)[010], (100)[0vw] slip systems. In consistency with the extremely refractory nature and dry olivine fabric, the measured water concentrations using unpolarized FTIR spectrometer are extremely low in Opx (38–44 wt. ppm) and equilibrated olivine (4–7 wt. ppm) and whole rock (9–14 wt. ppm). On the basis of deformation texture, fabrics, and stress estimation, the plastic deformation and mineral fabrics are expected to mainly occur at near solidus high-temperature (~ 1200–1350 °C), low-stress (< 4 MPa) and low pressure (< 2–3 GPa) conditions corresponding to the lithosphere-asthenosphere boundary.

Taken them together, we proposed that the Yushigou harzburgite was initially deformed simultaneously or immediately after partial melting at a LAB

depth owing to the mantle flow at a young fore-arc setting; then the harzburgite and olivine A-/D-type fabric were gradually accumulated and ultimately fossilized into the cold fore-arc mantle lithosphere, which resulted from the on-going cooling of subduction zone. Based on previous and this studies, an improved schematic model about the olivine fabric distribution at an evolutionary subduction zone was proposed. The prevalence of A-/D-type olivine fabric in the fore-arc lithospheric mantle may have several important seismic implications at the fore-arc setting. Firstly, because olivine A-/D-type and olivine B-type or antigorite fabrics have contradictory polarizing directions of fast shear wave, the contribution of the trench-parallel seismic anisotropy credited to deformed mantle wedge would be reduced. This counteracting effect may thus provide an alternative explanation on the weak or nearly null delay times that were detected at some fore-arc regions, such as northeast Japan. Secondarily, we considered two end-member serpentinization cases which are associated with topotactic growth or shear-induced fabrics in the fore-arc mantle. The A-/D-type olivine fabric controlled antigorite fabric in the uppermost fore-arc mantle due to topotactic growth can induce large trench-parallel seismic anisotropy, however, it cannot explain the low velocities and high Vp/Vs ratios that are commonly observed in hydrous fore-arc mantle. In contrast, the deformation-induced oriented antigorite layers atop the subducting slab boundary may account for these distinctive seismic signatures, but have relatively smaller trench-parallel seismic anisotropy or delay times that are produced by intra-slab earthquake events in the fore-arc region. Therefore, we tentatively suggest that a combination of these two serpentinization processes as well as the different olivine fabrics might have the advantage to interpret the universal and special seismic properties in the fore-arc regions. More detailed investigations on deformation textures and fabrics of fore-arc mantle derived natural peridotites with variable textures and degrees of serpentinization will

surely benefit our understandings on the complex geodynamic processes and the origins of their unique seismic properties in the fore-arc mantle.

CHAPTER 5

Partial melting, melt-rock interaction and plastic deformation in a fore-arc mantle: Constraints from Songshugou peridotites in Qinling orogenic belt, central China

Abstract

The Songshugou ultramafic massif is located in the eastern part of the Qinling orogenic belt. It is a large spinel peridotite body dominated by coarse- and fine-grained dunite with minor harzburgite, olivine clinopyroxenite and chromitite. The highly depleted modal and whole-rock compositions indicate that dunites and harzburgites were refractory residues after a high degree of partial melting (25–33% for batch melting or 23–27% for fractional melting). Dissolved orthopyroxene grains, euhedral spinel crystals, enrichment of light rare earth elements (LREEs) and high field strength elements (HFSEs), and high Fo# (91–93) in olivine and high Cr# (76–83) in primary spinel suggest that extensive melt-rock interaction postdated early partial melting. Both partial melting and melt-rock interaction are considered to occur in a sub-fore-arc lithospheric mantle. Increasing Fe^{2+}, Fe^{3+}, and TiO_2 contents in spinel, as well as the estimated oxygen fugacity ($\Delta \log fO_2$(FMQ) = 2.6–4.9) from harzburgites and coarse-grained dunites to fine-grained dunites further imply a two-stage interaction between residue and magma (boninite followed by island arc tholeiite) and/or mineral re-equilibrium that were controlled by plastic

deformation during subduction zone cooling. The final exhumation associated retrograde metamorphism overprinted the volatile-depleted peridotite mineral assemblage as evidenced by ubiquitously occurring amphibole, Cr-chlorite and dolomite.

Additionally, the co-occurrence of B- and C-type lattice preferred orientations (LPO) of olivine were found in fine- and coarse-grained dunites, respectively. Consistent with previous experimental results on the B- and C-type fabric transition in wet condition and a pressure of ~2.0 GPa, our study suggests that fine-grained dunite experienced a higher stress and a lower deformation temperature (σ = 70−83 MPa, T = 710−830 ℃) than coarse-grained dunite (σ = 30−39 MPa, T = 820–1060 ℃). The rare occurrence of olivine C-type LPO in low-pressure spinel peridotite potentially suggests an association with a hot fore-arc mantle setting, whereas the olivine B-type LPO might be produced in a cooling fore-arc mantle during exhumation to the lower continental crust. The transition of olivine fabrics from C- to B-type may reflect the cooling process of subduction zone and/or subsequent exhumation. On the basis of olivine B- and C-type LPOs and their associated tectonic setting, it is implied that (1) the polarization direction of the fast shear wave in the fore-arc regions would change from trench-normal to trench-parallel due to the cooling of fore-arc mantle, and (2) olivine B-type LPO formed in thrust-dominant shear zones during exhumation can also contribute to the orogen-parallel fast shear wave polarization anisotropy.

5.1. Introduction

The “tectonically emplaced” mantle rocks refer to those ultramafic peridotites that were tectonically exhumed from the upper mantle, such as sub-

continental, sub-oceanic and sub-arc settings. They mainly occur as (1) dispersed ultramafic bodies in suture zones and orogenic belts (Alpine-type or orogenic peridotite with sub-continental provenance), (2) lower ultramafic sections of ophiolite or island arc complexes obducted onto continental or oceanic crusts (sub-oceanic and sub-arc provenance), and (3) ultramafic rocks exhumed on the seafloor (e.g., abysmal peridotite) or above sea level by normal faults (sub-oceanic provenance) (see the review of Bodinier & Godard, 2007, and references therein). Because the primary rock lithologies, mineral textures and compositions of these tectonically emplaced peridotites may be obscured by subsequent deformation and retrograde metamorphism during exhumation, or by their intrinsic complex evolution histories, it is often complicated to unravel the original geodynamic setting of these peridotites, in particular those occurring in ancient orogenic belts. Nevertheless, this complexity also provides a valuable opportunity to investigate the diverse mantle processes, including partial melting, melt extraction, melt-rock interaction, metasomatism and plastic deformation (e.g., Abily & Ceuleneer, 2013, Bonatti, 1990, Choi *et al.*, 2008, Dai *et al.*, 2011, Dare *et al.*, 2009, Dijkstra *et al.*, 2004, Eyuboglu *et al.*, 2010, Ishikawa *et al.*, 2007, Kelemen *et al.*, 1992, Kelemen *et al.*, 1995, Mehl *et al.*, 2003, Niu, 1997, Pal, 2011, Parkinson & Pearce, 1998, Song *et al.*, 2007a, Song *et al.*, 2009b, Song *et al.*, 2004a, Soustelle *et al.*, 2010, Tasaka *et al.*, 2008, Zhou *et al.*, 2005, Zhou *et al.*, 1996).

The Songshugou peridotite is a large ultramafic massif tectonically emplaced into the Qinling orogenic belt, central China. Over the past three decades, a number of studies have been conducted on this peridotite body and its surrounding rocks, attempting to reveal their formation mechanisms and associated tectonic settings (e.g., Dong *et al.*, 2008, Lee *et al.*, 2010, Liu *et al.*, 2007, Liu *et al.*, 1995, Song *et al.*, 1998, Song *et al.*, 2005, Wang *et al.*, 2005b, Zhang, 1995). However, the results of these massive studies are significantly

divergent and still hotly debated. For example, some proposed that it is a tectonically emplaced Alpine-type (Li *et al.*, 1991) or cumulate body (Song *et al.*, 1998, Wang *et al.*, 2005b), or a segment of a mid-ocean ridge (MOR) ophiolitic mantle (either as residue or cumulate or both) (e.g., Lee *et al.*, 2010, Zhang, 1995). Others claim that it represents a melt-rock interaction product associated with mantle plume activity without an explicit tectonic setting (Liu *et al.*, 2007, Song *et al.*, 2005). In this study, we will present new petrological data for texturally and lithologically different Songshugou perdotites. Then we will integrate these data with recently reported geochemical results and olivine fabrics to confirm their provance as a fore-arc mantle. The integration of data from different aspects could therefore place useful constraints on the petrogenesis of this peridotite body.

5.2. Geological setting

The Qinling orogen is a major orogenic belt trending WNW-ESE separating the North China Craton to the north and the Yangzi Craton to the south in central China (Fig. 5.1a). It can be subdivided into the north Qinling belt and the south Qinling belt, which are separated by the Shangdan Fault zone (e.g., Meng & Zhang, 2000, Ratschbacher *et al.*, 2003). The Songshugou ultramafic massif is situated within the core region of the Qinling Complex, which is a tectonic slice of Precambrian crystalline basement and is located in the southernmost margin of the North Qinling belt (Fig. 5.1b). It is a large (~ 20 km^2) fault-bounded, lentoid spinel peridotite block trending NW-SE, with a maximum width of 2 km and a length of 20 km within the high-grade metamorphic complex consisting of garnet-amphibolite, garnet-pyroxenite and high-pressure granulite

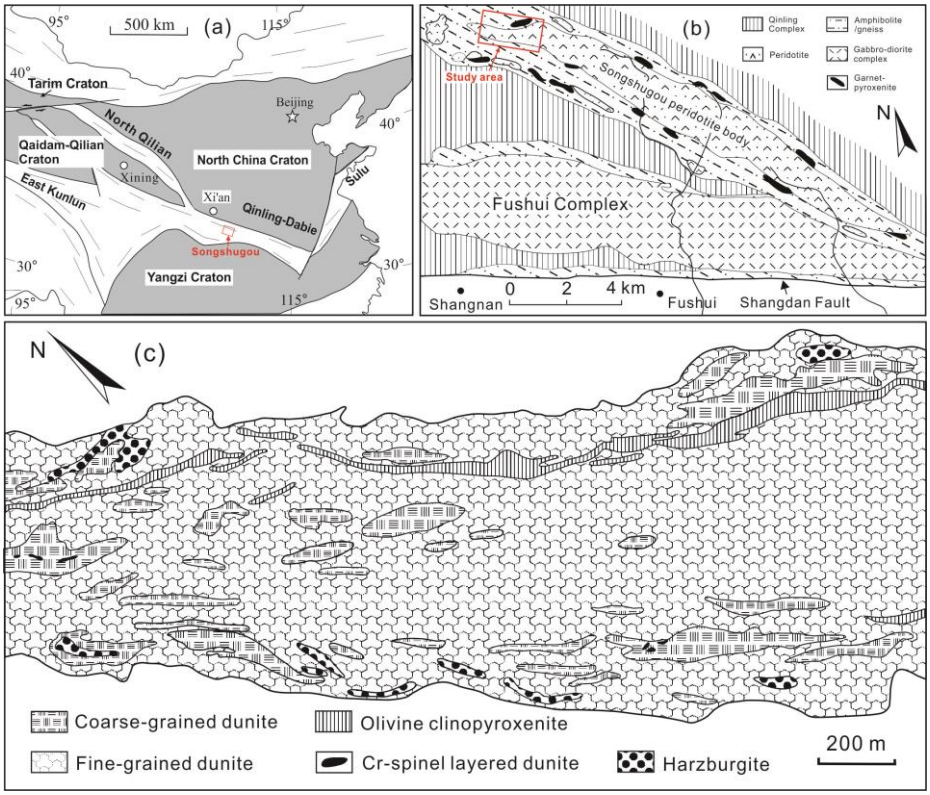

Fig. 5.1. (a) Geological map showing the major tectonic units in China and location of Songshugou area in Qinling orogenic belt, central China. (b) Enlargement of Songshugou area showing peridotite body and its surrounding rock complexes and major tectonic fault. (c) Enlargement of study area in Songshugou peridotite body and major types of rock are presented Modified after Su *et a*l., (2005).

(e.g., Liu *et al.*, 1995) (Fig. 5.1b). These surrounding meta-mafic rocks are considered as decompressed eclogite on the basis of retrograde symplectite of omphacite and estimated *P-T* conditions (Bader *et al.*, 2012, Liu *et al.*, 1995).

The formation ages of the Songshugou peridotite is poorly constrained. However, a number of metamorphic ages of its surrounding rocks are reported. Recent U-Pb dating of zircons in high-pressure granulites and garnet pyroxenites yields consistent ages of 480–510 Ma, which are possibly contemporary with the emplacement of the peridotite massif (e.g., Chen *et al.*, 2004, Li *et al.*, 2009, Liu *et al.*, 2009, Su *et al.*, 2004). These ages thus indicate that the uplift of this peridotite massif is caused by continental collision during the Early Paleozoic.

5.3. Lithology and petrography

The Songshugou ultramafic massif is mainly comprised of well-preserved dunite with minor harzburgite, olivine clinopyroxenite and podiform chromitite (Fig. 5.1c). Later amphibolization is widely observed in most of these rocks. On the basis of field and petrographic observations, four rock types were distinguished within this peridotite massif (e.g., Song *et al.*, 1998, Song *et al.*, 2005).

5.3.1. Fine-grained and porphyroclastic dunite

The fine-grained and porphyroclastic dunites are the predominant rock types and occupy up to 85 vol.% of the massif. It consists of a large modal content of fine-grained olivine (~90%) with minor amphibole, talc and spinel and is strongly deformed and foliated. The foliation is clearly defined by well-oriented olivine and needle-shaped amphibole crystals (Fig. 5.2a). Occasionally,

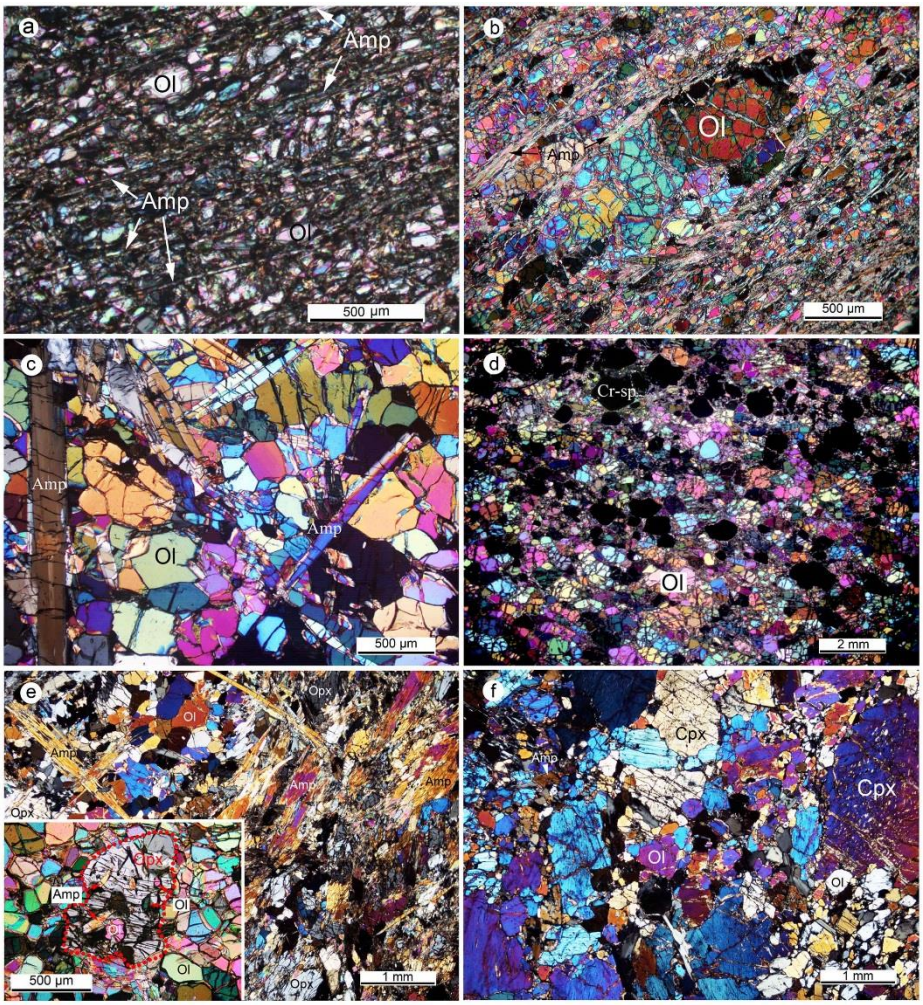

Fig. 5.2. Optical micro-photographs showing the textures of dunites (a-d), harzburgite (e) and olivine clinopyroxenite (f). (a) Well oriented fine-grained olivine and strongly elongated amphibole (anthophyllite) forming well-developed foliation in fine-grained dunite. (b) Large lentoid olivine relic in fine-grained, well-foliated olivine matrix in porphyroclastic dunite. (c) Coarse-grained dunite shows large columnar amphibole crosscutting large olivine grains. (d) Coarse-grained dunite shows elongated olivine grains and spinel layers. (e) Coarse-grained harzburgite shows amphibole randomly cross-cutting the Ol + Opx assemblage (upper left) and orienting parallel to foliation in the amphibole-rich layer (lower right). Inset in (e) is a weakly amphibolized region: Opx crystal (as outlined in red dots) showing irregular grain boundaries and inclusion of Amp and Ol. (f) Cpx megacrysts occur in the fine-grained matrix of olivine and amphibole in olivine clinopyroxenite.

single olivine porphyroclasts or aggregates occur as relic lenses within the fine-grained and foliated matrix, which is composed of olivine, amphibole or talc (Fig. 5.2b). Remarkable undulatory extinction and tilt walls are observed in coarse-grained olivines, but are deficient in the fine-grained equi-granular olivines. The spinel is generally strongly deformed and fractured with a preferred orientation that is sub-parallel to the foliation (Fig. 5.3a). The field observations suggest that the stretching lineation mainly plunges sub-perpendicular to the trending of peridotite body (Song *et al.*, 1998).

5.3.2. Coarse-grained dunite

This type of rock crops out as lentoid blocks of various size and occupies ~10 vol.% of the peridotite massif (Fig. 5.1c). Similar to fine-grained dunite, many coarse-grained dunites are deformed or foliated as shown by elongated olivine crystals (Figs. 5.2c and d). Some coarse-grained dunite specimens contain spinel layers that are sub-parallel to the elongation direction of olivine which shows remarkable undulatory extinctions or tilt boundaries (Fig. 5.2d). Euhedral amphibole crystals commonly randomly crosscut the olivine grains (Fig. 5.2c), but are occasionally aggregated and oriented sub-parallel to the foliation. The modal proportion of amphibole is largely variable among different samples ranging from nearly amphibole-free up to 15 vol.%. The spinel occurs dominantly as euhedral or subhedral crystals with homogenous (Fig. 5.3b) or patchy composition patterns (Fig. 5.3c) in the core and mantle, but is occasionally observed as anhedral crystals (Fig. 5.3d).

5.3.3. Harzburgite

Similar to coarse-grained dunite, harzburgite crops out as lenses or boudins within fine-grained dunite (Fig. 5.1c). Both coarse- and fine-grained

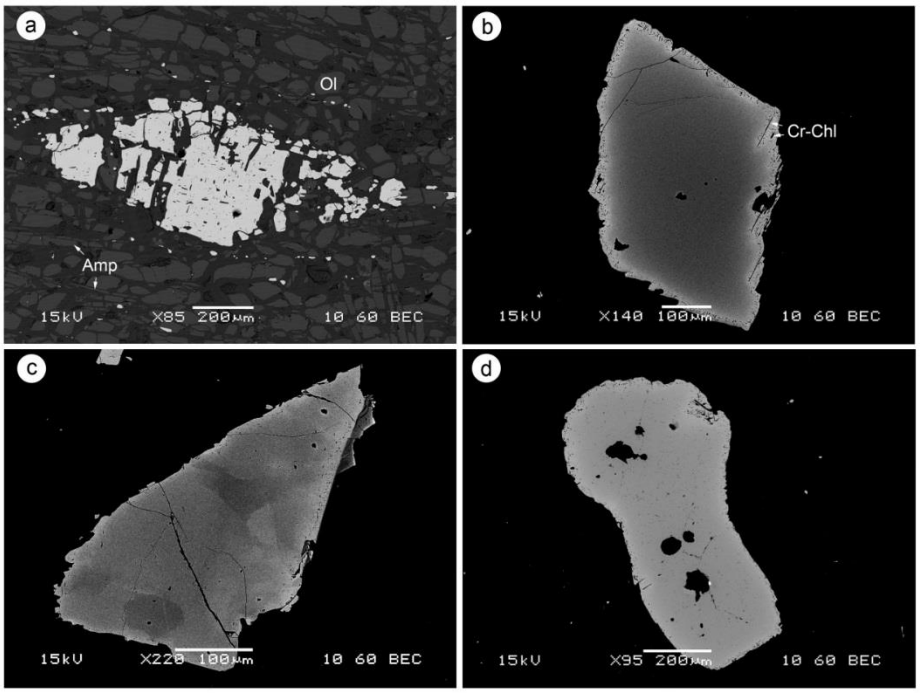

Fig. 5.3. Electron backscatter images showing the textures of matrix spinel. (a) Deformed and extensively fractured spinel (ferri-chromite) occurring in fine-grained dunite. The spinel is fairly homogeneous in composition and oriented in conformity with the overall foliation. (b) Euhedral rhomb-shaped spinel in coarse-grained dunite. The spinel shows higher and relatively homogeneous Cr, Al and Mg content (chromite) in the core and mantle but higher Fe content (ferri-chromite) in the rim. An abundant of voids and cleavages filled with Cr-chlorite are also displayed in the rim. (c) Subhedral spinel occurring in harzburgite shows patchy composition pattern. (d) Anhedral spinel in coarse-grained dunite. It is characterized by irregular shape and corroded grain boundaries.

harzburgites were reported in previous studies (Chen, 2004, Lee *et al.*, 2010, Liu *et al.*, 2007, Song *et al.*, 2005, Wang *et al.*, 2005b). The mineral assemblage is olivine + orthopyroxene (Opx) + amphibole with minor spinel. The modal proportion of Opx is variable and can reach up to ~80 vol.% in some samples. The shape and occurrence of spinel are very similar to those in the coarse-grained dunite. In this study, only one coarse-grained sample was examined. Large amounts of amphibole (~ 40 vol.%) occur as retrograde phase, randomly cross-cutting olivine and Opx crystals in the olivine and Opx rich domains, or forming oriented amphibole-rich layers (Fig. 5.2e). In the weakly amphibolized regions, the primary texture of Opx is well preserved and characterized by irregular grain boundaries and a few Amp and Ol inclusions (inset of Fig. 5.2e). This texture clearly suggests that Opx was dissolved or incongruently melted to form olivine, and mildly modified by amphibole during later retrograde metamorphism.

5.3.4. Olivine clinopyroxenite

Olivine clinopyroxenite occurs as 1-5 meter-wide dykes within the northern part of the fine-grained dunite (Fig. 5.1c). The rock is mostly weakly deformed and shows a mosaic texture dominated by clinopyroxene (Cpx), amphibole (mostly tremolite) and olivine, plus minor spinel. Cpx usually occurs as megacryst (up to 1 cm) in the fine-grained matrix of olivine, amphibole and spinel (Fig. 5.2f).

5.3.5. Mineral inclusions

A number of mineral inclusions is found in both olivine and spinel crystals. The representative types of inclusions are shown in Fig. 5.4. Orthopyroxene occurs as rounded inclusions in olivine and spinel, implying the dissolution or incongruent melting of Opx to form olivine (Fig. 5.4a). Tremolite and dolomite

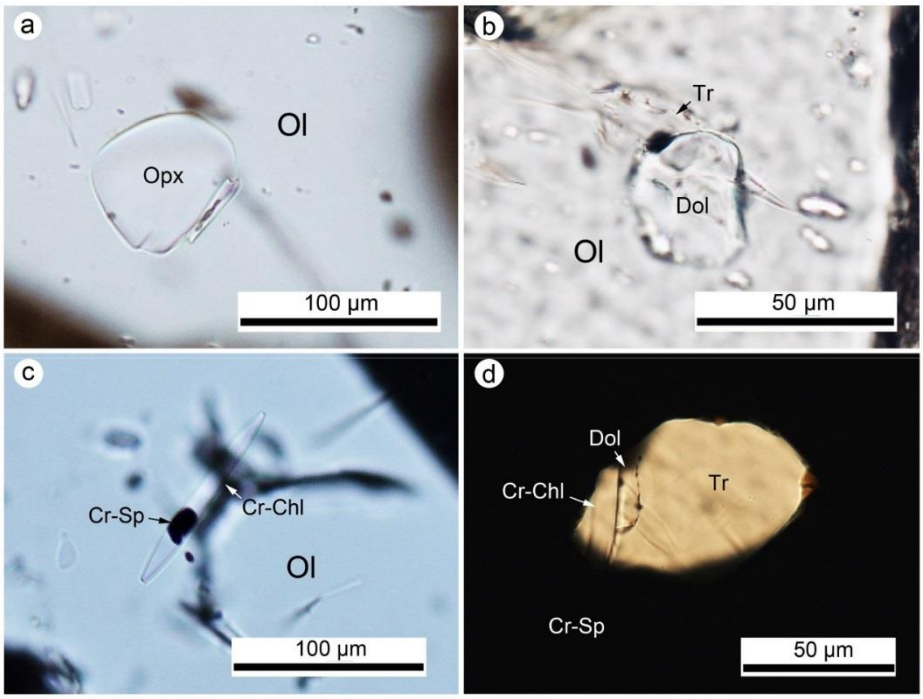

Fig. 5.4. Representative optical micro-photographs showing a variety of inclusions contained in olivine and spinel. (a) Rounded orthopyroxene crystal occurs as inclusion in coarse-grained olivine. (b) Granular dolomite crystal and columnar tremolite inclusions in olivine. (c) Cr-spinel-bearing Cr-chlorite occurs as a spindle-like inclusion in olivine crystal. (d) A composite mineral inclusion of tremolite, dolomite and chromium chlorite in spinel crystal.

frequently occur as inclusions in olivine and spinel (Figs. 5.4b and d). The shape of chromium chlorite inclusions in olivine are variable and commonly encloses fine-grained anhedral spinel grains (Fig. 5.4c). In contrast, the Cr-chlorite inclusion occurring in the spinel contains no spinel (Fig. 5.4d). These textures thus imply that Cr-chlorite was probably formed by alteration of spinel (see below).

5.4. Mineral compositions and estimates of temperature and stress

Electron microprobe analyses of minerals were performed on a JEOL JXA-8100 electron probe micro-analyzer (EPMA) at Peking University. The measurement was operated at a 15 kV acceleration voltage, with a 10 nA beam current, 1 μm beam spot and 20s counting time with relevant standard minerals (from SPI corp. US) being used for calibration. Final results were corrected using the PRZ method. The chemical compositions of major constituent minerals and inclusions were all measured in the core region of grains. The formulae of minerals were calculated using the AX 2.0 program. Additional data of olivine and spinel in 5 harzburgite and 4 olivine clinopyroxenite samples were compiled from Wang *et al.* (2005b).

5.4.1. Mineral compositions

5.4.1.1. Olivine

Olivine shows a narrow compositional variation with a Fo# of 91-93 in coarse- and fine-grained dunites, and harzburgites, whereas the NiO content ranges from 0.2 to 0.4 wt.% (Fig. 5.5a and b) . In contrast, coarse-grained

dunites with spinel layers (indicating a large modal abundance of spinel) have a higher Fo# of 93–95 and a wider variation of NiO ranging from 0.15 to 0.5 wt.%. Their significantly higher Fo# in olivine and Mg# in spinel (Fig. 5.5d), compared to spinel-layer-free dunites, can most likely be attributed to the strong Fe-depletion effect of spinel on olivine and a less pervasive effect of later re-equilibration between spinel and olivine (Barnes & Roger, 2001). Olivine in the olivine clinopyroxenites shows distinctly lower Fo# (84-90) and NiO contents (mean 0.22 wt.%) than those above.

5.4.1.2. Spinel

Spinel is chromium rich and varies in a wide range of chemical compositions among samples. The composition of spinel is fairly homogenous in the core and mantle areas of most grains in coarse-grained dunites, whereas the rims show conspicuously higher Fe and lower Cr, Al and Mg contents (Fig. 5.3b, Lee *et al.*, 2010) due to the alteration by Cr-chlorite in the rim (see below). As for spinel in fine-grained dunites, its composition is homogeneous and similar to the altered rim area of their counterparts in coarse-grained dunites (Fig. 5.3a). Fe^{3+}-Cr-Al, and $Fe^{3+}/(Fe^{3+}+Cr+Al)$ vs. $Fe^{2+}/(Fe^{2+}+Mg)$ diagrams (Figs. 5c and d) show that it follows the Fe-Ti trend that indicates an increasing $Fe^{2+}/(Fe^{2+}+Mg)$ and Fe^{3+} towards magnetite (Barnes & Roger, 2001). This transition takes place from coarse-grained dunites and harzburgites through porphyroclastic dunites to fine-grained dunite and olivine clinopyroxenite. In terms of chemical composition, spinel mostly belongs to chromite in the coarse-grained dunite and harzburgite, but transforms to ferri-chromite in the fine-grained dunite and olivine clinopyroxenite. The average Cr# [100*Cr/(Cr+Al)] of spinel increases from ~80 in coarse-grained dunites, through ~84 in porphyroclastic dunites, to ~90 in fine-grained dunites and olivine clinopyroxenite. Spinel's Cr# in the harzburgites (~78) and olivine

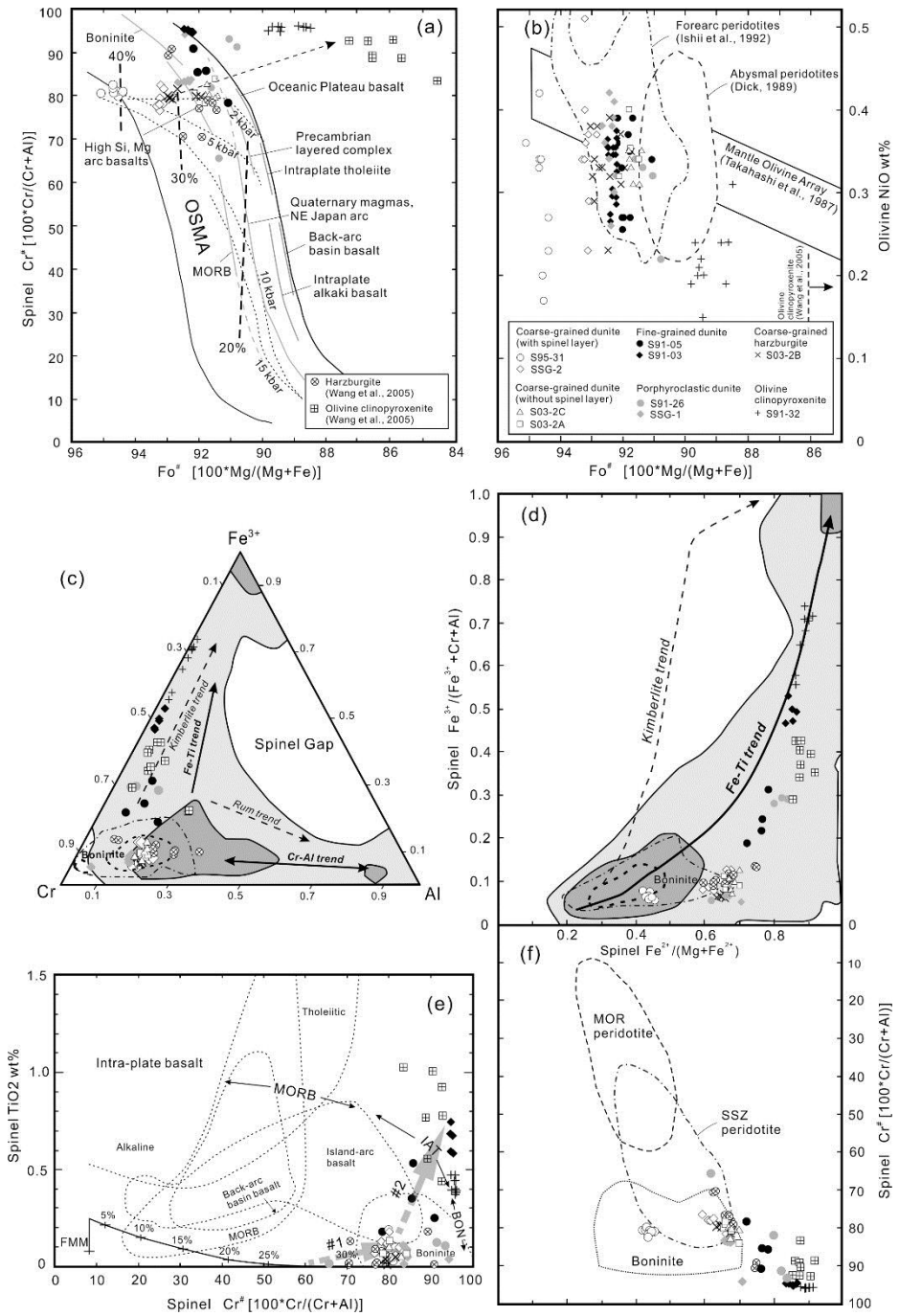

Fig. 5.5. (a) Olivine Fo# vs spinel Cr# relationship showing studied samples, dash arrow line indicates the trend of increasing Cr# and decreasing Fo#. OSMA: olivine-spinel mantle array from Arai (1994). (b) Olivine NiO vs. Fo# relationship showing studied samples. Dash line enclosed area is for abysmal peridotite. Fields for olivine in abysmal and forearc peridotite were from Dick (1989) and Ishiii *et al.* (1992), respectively. Olivine of Fo# range (84.5-87.3, as indicated by right arrow) without given NiO data (as indicated by dash line) in olivine clinopyroxenites were taken from Wang *et al.* (2005). (c) Fe^{3+}-Cr-Al

relationship showing studied sample. Light and dark shading represent enclosed most densely packed 90% and 50% of the source data points in Barnes & Roger (2001), respectively. (d) $Fe^{3+}/(Fe^{3+}+Cr+Al)$ vs. $Fe^{2+}/(Fe^{2+}+Mg)$ (inverse of Mg#) relationship in spinel. Light dash-dotted line and heavy dotted line are contours of 90% and 50% of enclosed spinel data points in boninite, respectively. (e) Compositional variation of TiO_2 vs Cr# in spinel. Dash lines denote the fields for spinels in Mg-rich magmas derived from different tectonic settings (Arai, 1992). Partial melting degree of a fertile MORB (FMM) source (fractional melting, 5-30%) are shown in the labeled curve; double arrowed lines denote the ranges of interaction between mantle and various types of magma - boninite (BON), island arc tholeiite (IAT) and mid-ocean ridge basalt (MORB) (Pearce et al., 2000). Large grey arrows are melt-mantle reaction trends with BON (#1) and IAT (#2). (f) Cr# vs. $Fe^{2+}/(Fe^{2+}+Mg)$ (inverse of Mg#) relationship in spinel. Fields for spinel in mid-ocean ridge (MOR) peridotite, supra-subduction zone (SSZ) peridotite and boninite were from Dick & Bullen (1984), Ishii *et al.* (1992) and Van der Laan et al. (1992), respectively. Sample symbols are shown in (a) and (b). Extra data points of olivine and spinel in harzburgites and olivine clinopyroxenites were taken from Wang *et al.* (2005b)

clinopyroxenites (~90) are similar with those of coarse- and fine-grained dunites, respectively (Figs. 5.5a,e and f). The TiO_2 concentration in spinel is higher in fine-grained dunite and olivine clinopyroxenite (0.2-1.0 wt.%) than in harzburgite and coarse-grained and porphyroclastic dunite (< 0.2 wt.%) (Fig.5.5e).

5.4.1.3. Orthopyroxene

Only chemical compositions of a few Opx grains were analyzed. The Opx in harzburgite is highly depleted with a very low Al_2O_3 (0.19−0.26 wt.%) and a high Mg# (~ 92). Opx inclusions in olivine and spinel show similar Al_2O_3 contents (0.09–0.11 wt.%) and Mg# (91.2–91.6).

5.4.1.4. Clinopyroxene

The clinopyroxene in olivine clinopyroxenite belongs to diopside and shows a high Mg# (0.94–0.99 wt.%) and high Cr_2O_3 contents (0.34–0.40 wt.%), but low Al_2O_3 (0.8–1.0 wt.%), TiO_2 (< 0.01 wt.%), Na_2O (0.1–0.3 wt.%) and K_2O (< 0.01 wt.%) contents.

5.4.1.5. Amphibole

Both ortho-amphibole and clino-amphibole were recognized in the studied samples. The ortho-amphibole is characterized by Mg-anthophyllite (Mg# ~ 0.9), which is the dominant amphibole phase in the Songshugou peridotite. The secondary clino-amphibole is Ca-rich and belongs to tremolite, this is the dominant amphibole phase in the Ca-rich olivine clinopyroxenite. The texture that large columnar tremolite crystals are peripherally altered to fibrous anthophyllite is also often observed.

5.4.1.6. Chlorite

The chlorite inclusions occurring in olivine and spinel display high Cr_2O_3 (1.6–3.3 wt.%) and relatively low Al_2O_3 (12.0–16.8 wt.%) contents, which yields a Cr# [100*Cr/(Cr + Al)] of 6-12 hence it is a chromium chlorite. In addition, chlorite also contains high MgO (32.1–34.6 wt.%) and low FeO (2.0–4.3 wt.%) contents yielding a very high Mg# of 0.93–0.97.

5.4.1.7. Carbonate

The carbonate inclusions in olivine and spinel are close to the end-member dolomite with a nearly unit atomic ratio of Ca/Mg, as CaO and MgO contents are ~32 and 24–25 wt.%, respectively.

5.4.2. Temperature estimates

Because Opx and Cpx are absent in nearly all dunites and harzburgites, the equilibrium temperature of the Songshugou peridotites was estimated using the olivine-spinel Mg-Fe^{2+} exchange geothermometer (Ballhaus *et al.*, 1991b). This temperature was calculated at an arbitrary pressure of 1.5 GPa and was also employed in the calculation of the oxygen fugacity (see below). Because the diffusion of Mg and Fe^{2+} between spinel and olivine might be enhanced by deformation and is fairly fast at a relatively low temperature (~ 650 ℃) (Fabriès, 1979, Henry & Medaris, 1980), fine-grained dunites yield remarkably lower temperature results than coarse-grained dunites, and most estimated temperatures are far below the solidus of peridotite. (spinel rich coarse-grained dunite: 955 ± 107 ℃; spinel poor coarse-grained dunites: 826 ± 13 ℃; porphyroclastic dunite: 802 ± 23 ℃; fine-grained dunite: 757 ± 52 ℃; harzburgite: 822 ± 24 ℃; olivine clinopyroxenite: 686 ± 46 ℃)

5.4.3. Stress estimates

The differential stress in the fine- and coarse-grained dunites was estimated using the olivine grain size piezometer under wet conditions (Jung & Karato, 2001b). The results suggest that fine-grained dunites had experienced a significantly higher stress (70–83 MPa) than coarse-grained dunites (30–39 MPa) (Fig. 5.13), which is consistent with a higher dislocation density in fine-grained olivine compared with coarse-grained olivine (Fig. 5.6).

5.5. Whole-rock major and trace element compositions

The major and trace element compositions of the Songshugou peridotites (without spinel-layered dunites) summarized from previous studies (Chen, 2004, Lee *et al.*, 2010, Liu *et al.*, 2007, Song *et al.*, 2005). The compositions were measured using X-ray fluorescence (XRF) and inductively coupled plasma mass spectrometry (ICP-MS). In this study, these original data were recalculated on a volatile-free basis, to correct for the dilution effect caused by later metasomatism or retrograde metamorphism (e.g., amphibolization) (Parkinson & Pearce, 1998, Parkinson *et al.*, 1992).

5.5.1. Major elements characteristics

Most of the dunites and harzburgites fall within the harzburgite field in the reconstructed low-pressure (e.g., stable in the spinel peridotite field) modes (Niu, 1997) from their whole-rock compositions (Fig. 5.7a). This result thus implies that an amount of original Opx in the original harzburgites should have been consumed during later retrograde metamorphism, resulting in the currently observed harzburgites and dunites (see below). Modal proportions of clinopyroxene are very low (< 2.3%) in most recalculated dunite and

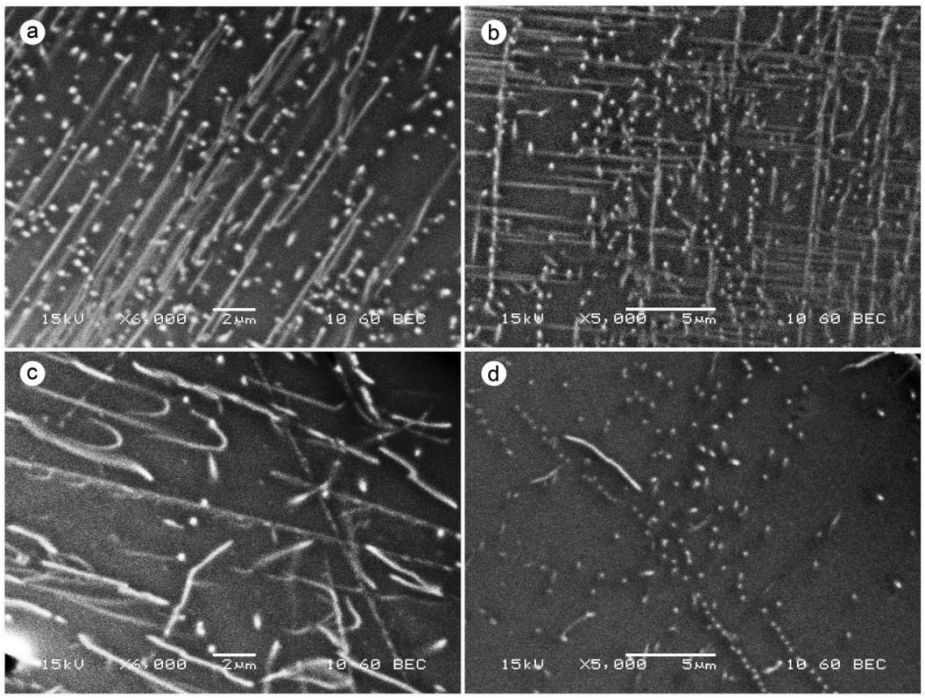

Fig. 5.6. Back-scattered electron (BSE) images showing representative dislocation microstructures in olivine after oxygen decoration of (a,b) fine-grained (c,d) and coarse-grained dunite (Karato, 1987, Kohlstedt *et al.*, 1976). Dislocations mostly occur as white straight lines and dots (some arrays to form sub-grain boundaries), occasionally as curves or loops, which are consistent with previous experimental results in the specimen showing water-rich fabrics (Jung *et al.*, 2006). The fine-grained dunites show significantly higher dislocation density than coarse-grained dunites.

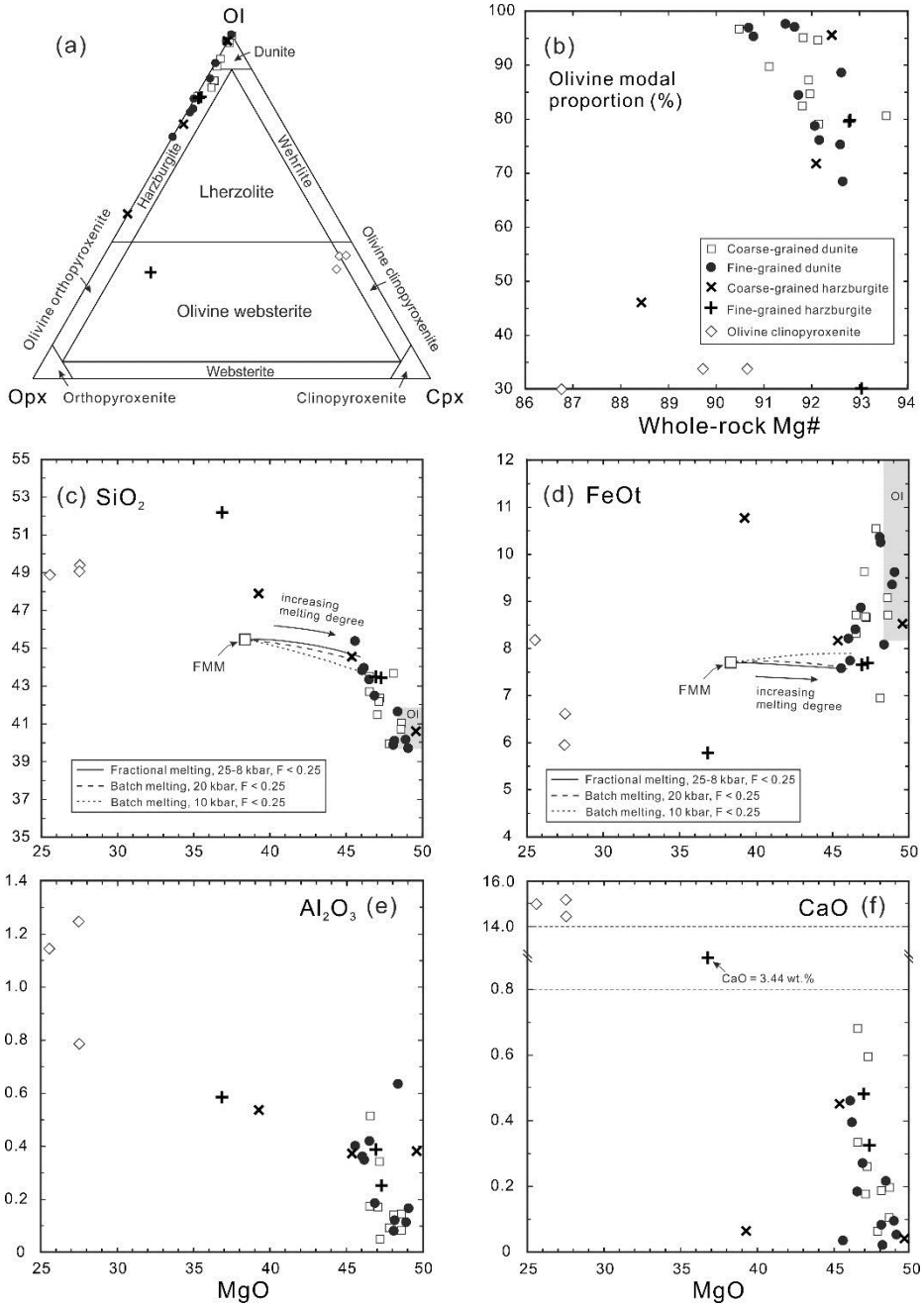

Fig. 5.7. (a) Recalculated normative Ol-Opx-Cpx modal proportions of peridotites using their whole-rock major element compositions and CIPW norm. (b) Relationship between recalculated modal proportion of olivine and whole-rock Mg number. (c-f) Diagrams showing the plots of MgO vs. other oxides (wt.%): (c) MgO vs. SiO_2, (d) MgO vs. FeOt, (e) MgO vs. Al_2O_3, and (f) MgO vs. CaO. The variations of SiO_2, FeOt and MgO contents in the residues melted from a fertile MORB mantle (FMM) source are plotted for comparison in (c) and (d) (modified after Niu 1997), in which three different melting models are shown (near-fractional decompression melting from 28-8 kbar and isobaric

batch melting at 10 and 20 kbar). Shaded area in (c) and (d) indicates the composition range of olivine in Songshugou peridotites. Deviations of two harzburgite samples from the main trends in (e-f) could be due to large mineral modal variations. (f) One harzburgite sample contains significantly higher CaO content (3.44 wt.%) than the other harzburgites and dunites, possibly due to the presence of secondary carbonate.

harzburgite samples, except for one plotted in the olivine websterite field. Excluding two harzburgite samples that are plotted far away from the concentration area, harzburgites and dunites show a discernible trend of a decreasing olivine modal proportion with an increasing whole-rock magnesium number (Fig. 5.7b). In comparison, all the olivine clinopyroxenite samples are close or well within the field of recalculated olivine clinopyroxenite. Besides, the olivine clinopyroxenites display contrastingly lower olivine modal abundances and whole-rock Mg# than most of the harzburgites and dunites, implying their possible origin from an evolved magma (see below).

As shown in Figs. 5.7e and f, the concentrations of Al_2O_3 and CaO are very low (< 0.7 wt.%) in most harzburgites and dunites. More importantly, negative relationships between MgO and SiO_2, MgO and Al_2O_3, and MgO and CaO, as well as a positive relationship between MgO and FeOt can be readily recognized after removing two off-trend harzburgite samples (Figs. 5.7c-f). It is noteworthy that the plots of MgO-SiO_2 and MgO-FeOt differ remarkably from the melting curves and link the end of the melting curves (high degree of partial melting) with a region of olivine composition (also see Niu, 1997, Song *et al.*, 2004a). In addition, it is also observed that olivine clinopyroxenites are clearly displaced to much lower MgO contents aside from the above trends, which might suggests their different genesis from those of harzburgites and dunites.

5.5.2. Trace element characteristics

We first examined the extent to which later retrograde metamorphism affected the whole-rock trace element compositions. As shown in Fig. 5.8, the concentration ratios of fluid mobile elements (e.g., Rb, Sr, U and La) and other high field strength elements (HFSEs; e.g., Zr and Hf) over more compatible element (Yb) were plotted against loss on ignition (LOI). Most elements ratios

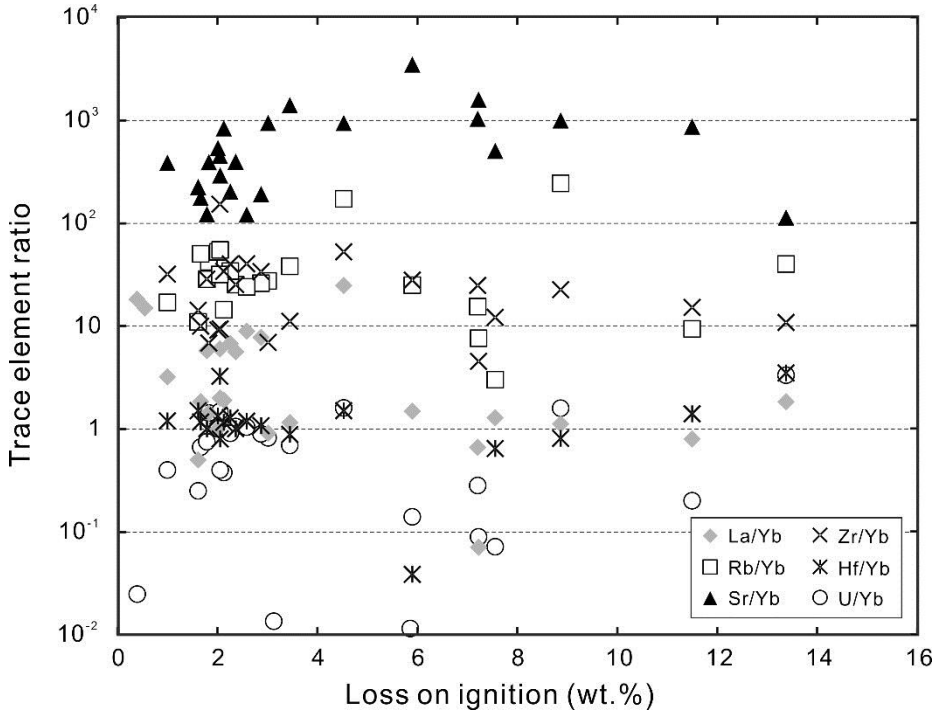

Fig. 5.8. Trace element ratios vs. loss on ignition for harzburgites and dunites.

are overall constant with respect to the LOI, despite of large variations. However, across the LOI of 4 wt.%, Sr/Yb and La/Yb ratios increase and decrease by a magnitude, respectively. These data thus suggest that later retrograde metamorphism might have not significantly modified the whole rock trace-elements compositions, although some fluid mobile elements (e.g., Sr) and light rare earth elements (LREEs) (e.g., La) can still be moderately introduced or extracted.

The chondrite-normalized REE patterns of the Songshugou peridotites are presented in Figs. 5.9a-d and i. Two groups of coarse-grained dunites can be recognized on the basis of their REE patterns: Group 1 shows very low REE abundances (REE concentration < 0.1 times chondrite), gentle U-shaped REE patterns and a positive Eu anomaly; whereas Group 2 displays significantly higher REE concentrations (> 0.1 times chondrite), remarkably elevated LREE and flat MREE-HREE patterns, and a weak to moderate negative Eu anomaly (Fig. 5.9a). Fine-grained dunites are similar to Group 1 coarse-grained dunites in their REE patterns but with a positive, negative or without a Eu anomaly (Fig. 5.9b). The REE patterns of coarse-grained harzburgites resemble those of Group 2 coarse-grained dunites, but without a discernible Eu anomaly (Fig. 5.9c). In contrast, REE defines pronounced U shapes in fine-grained harzburgites without a Eu anomaly (Fig. 5.9d). On the whole, the HREE concentrations of dunites and harzburgites are generally lower than 0.1 times chondrite, and are indicative of their highly depleted nature (Piccardo *et al.*, 2007). The significant enrichments of LREE and MREE clearly indicate subsequent refertilization due to melt-rock interaction. Olivine clinopyroxenites exhibit distinct REE patterns with respect to those of dunites and harzburgites, such as depletion in LREE, flattening MREE-HREE trends without a Eu anomaly, and elevated REE concentrations between 0.1 and 1 times chondrite (Fig. 5.9i).

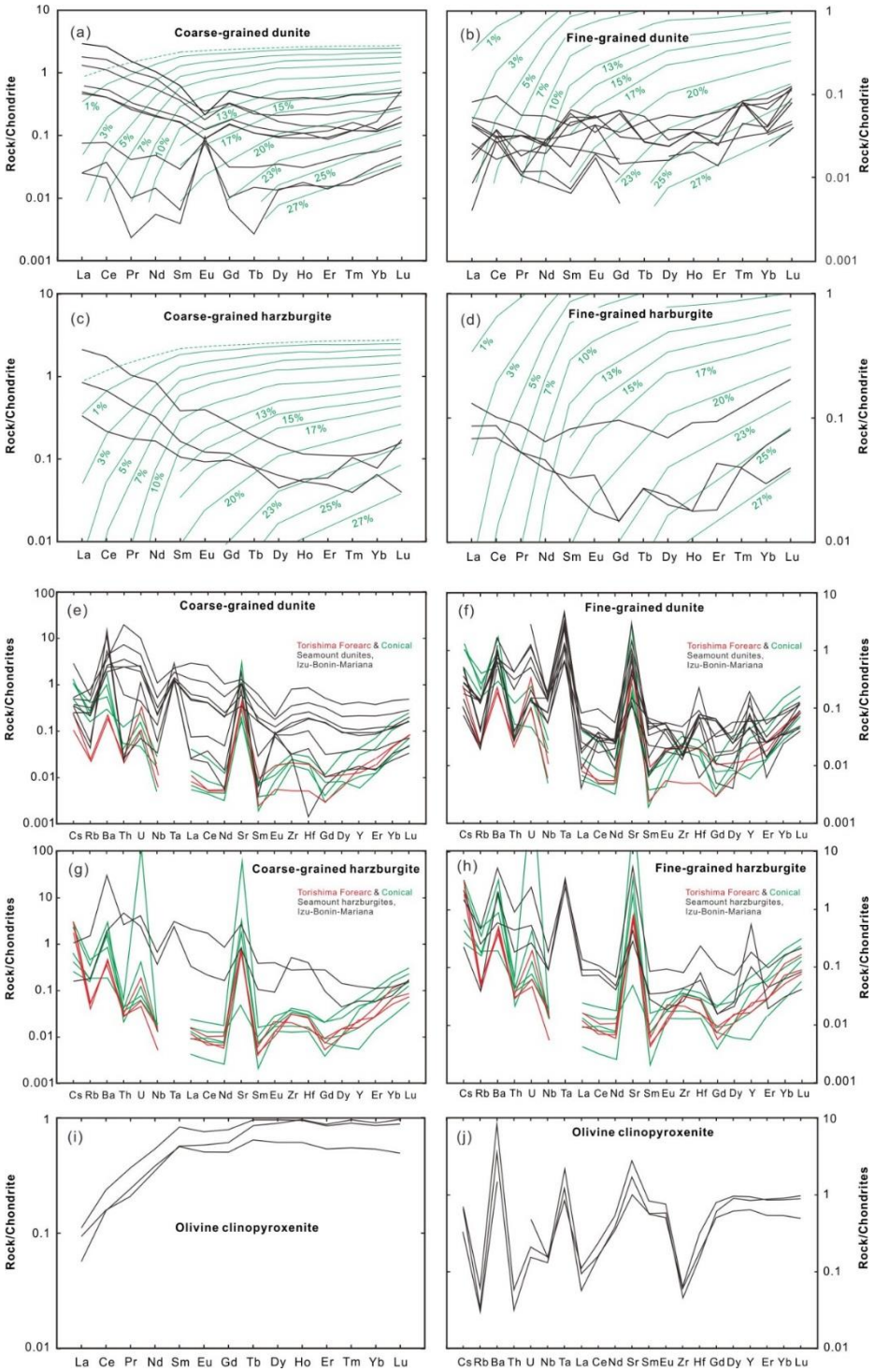

Fig. 5.9. Chondrite-normalized whole-rock REE patterns: (a) coarse-grained dunite, (b) fine-grained dunite, (c) coarse-grained harzburgite, (d) fine-grained harzburgite, and (e) olivine clinopyroxenite. Green solid lines indicating

chondrite-normalized REE patterns calculated for refractory peridotites after variable degrees (as labeled) of fractional melting of spinel facies depleted MOR mantle (DMM, as green dash line) are plotted for comparisons in (a-d) (modified after Piccardo *et al.* 2007). Chondrite-normalized whole-rock extended REE patterns: (e) coarse-grained dunite, (f) fine-grained dunite, (g) coarse-grained harzburgite, (h) fine-grained harzburgite, and (j) olivine clinopyroxenite. (e-h) Red and Green extended REE patterns of dunites and harzburgite were from Torishima Forearc and Conical Seamount of Izu-Bonin-Mariana zone, respectively (Parkinson & Pearce, 1998).

Because the order of incompatibility for trace elements is dependent on the fertility of the mantle residue, we plotted the extended REE patterns for the depleted peridotite using the element order suggested by Parkinson *et al.* (1992) (Figs. 5.9e-h and j). As a whole, all peridotite samples exhibit spiked patterns on the left side of diagram in which Cs, Ba, U and Ta are enriched relative to Rb, Th and Nb. However, the most conspicuous exception is that thorium is not depleted but enriched in most coarse-grained dunites and harzburgites. Pronounced positive strontium anomalies and weak to moderate enrichments of Zr and Hf are also observed in most harzburgites and dunites. However, Zr and Hf are strongly depleted in the olivine clinopyroxenites. Strong Nb-Ta fractionation is also present in many dunites and harzburgites (e.g., Nb/Ta < 1), which might suggest their extremely depleted origin (Niu & Hékinian, 1997). In addition, yttrium displays enrichment in fine-grained dunites and harzburgites, but shows no anomaly in coarse-grained dunites, harzburgites and olivine clinopyroxenites. Overall, the extended REE patterns of dunites and harzburgites resemble those as have been reported from the Torishima Forearc and Conical Seamount of the Izu-Bonin-Mariana zone, which are interpreted as a highly depleted mantle residue that subsequently interacted with magmas in a supra-subduction zone setting (Parkinson & Pearce, 1998).

5.6. Lattice preferred orientations of olivine

Four fine-grained and four coarse-grained dunites were selected for olivine LPO measurement under XZ thin-sections (X: lineation; Z: normal to foliation) using an electron back-scattered diffraction (EBSD) system. Both foliation and lineation were determined by analyzing the orientation of ~ 200 grains in thin-sections from different facets of a cubic sample (see Table 5.1 for more

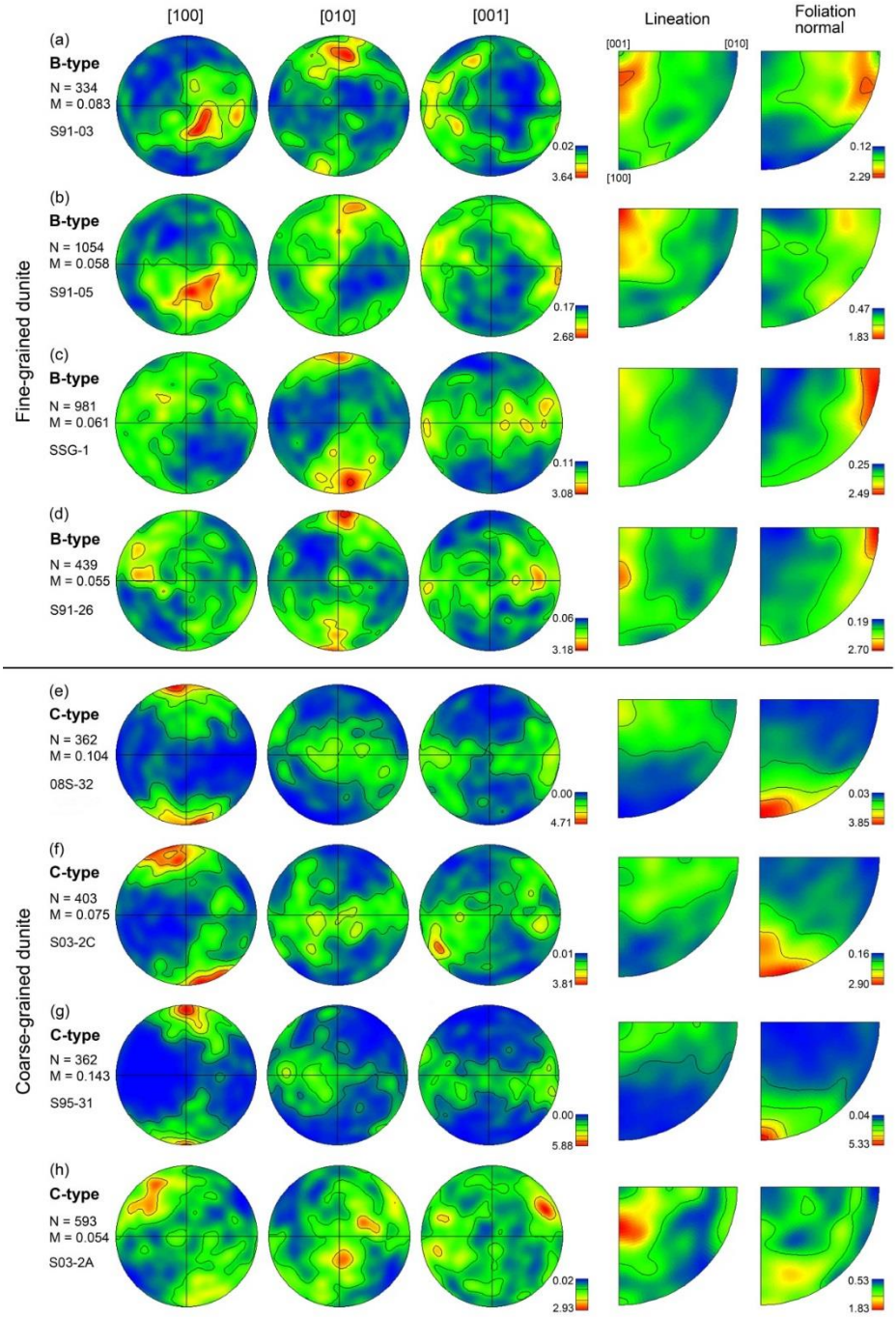

Fig. 5.10. Pole figures (left column) and inverse pole figures (right column) showing the LPO of olivine. N is the number of grains measured, M is M-index. The pole figures are presented in the upper hemisphere using equal area projection. In the inverse pole figures, lineation and foliation normal orientation correspond to east-west and north-south directions in the pole figures, respectively. Both pole figure and inverse pole figure were drawn using a half width of 15 ° and cluster size of 5 °, and contoured in terms of density of data

points by multiples of uniform distribution. (a-d) B-type dominated LPO of olivine, with a minor component of A-type LPO ([100] axis tending to be sub-parallel to lineation) shown in (c) and (d), which suggests that plastic deformation might also occur after water diffused out of olivine grains. (e-h) C-type dominated LPO of olivine. (e-g) Concentrations of [100] axis are strongly perpendicular to foliation, whereas [001] and [010] axis are distributed as a girdle sub-parallel to foliation (Z-direction), with their [001] axis maxima aligned sub-parallel to lineation (X-direction) and [010] axis aligned subnormal to both X and Z direction, except for (g) that the maxima of [010] also tends to cluster to lineation.

details). The EBSD patterns were manually indexed for every grain whose Kikuchi pattern was obviously different from that of its neighboring grains, to avoid repetition of data. Fine-grained dunites mainly show a B-type LPO which is characterized as [001] maxima that are sub-parallel to lineation, while [010] axes align sub-normal to the foliation, suggesting a dominant dislocation slip system of [001](010) (Fig. 5.10a-d). This slip system is more clearly shown in the inverse pole figure in which lineation tends to concentrate sub-parallel to the [001] axis, while foliation aligns sub-parallel to the (010) plane (Fig. 5.10a-d). It is, however, noteworthy that the typical B-type LPO shows [100] maxima that are almost normal to lineation and parallel to foliation, whereas our samples show [100] maxima that are moderately oblique to both foliation and lineation (Fig, 5.10a-d). Coarse-grained dunites display a C-type LPO in which the [001] maxima are sub-parallel to lineation, while the [100] axes are almost perpendicular to foliation (dominant dislocation slip system of [001](100)) (Fig. 5.10e-h). The strength of olivine LPO (quantified by the misorientation index, M-index, Skemer *et al.*, 2005) in coarse-grained dunites (M = 0.05−0.14) covers that in their fine-grained counterparts (M = 0.06−0.08). See Table 5.1 for a summary of data.

5.7. Discussions

5.7.1. Highly refractory partial melting residue

There are several lines of evidence suggest that Songshugou harzburgites and dunites probably represent a mantle residue which had experienced high degrees of partial melting. The nature of residue can be inferred from anhedral spinel, whereas euhedral spinel is crystalized from a reactive melt (e.g., Dare *et al.*, 2009). In some harzburgites and dunites, both euhedral and anhedral

Table 5.1. Sample descriptions and results.

Sample	Type of rock	Olivine LPO type*	Mean grain size (μm)†	Estimated stress (MPa) §	Dislocation density (10^{12} m^{-2})	Estimated stress (MPa)#	M-index of olivine**	Deformation temperature (℃) ††
S91-03	Fine-grained or porphyroclastic dunite	B	163 (±15)	83 (±4)	0.95 (±0.26)	120 (±28)	0.083	709 (±17)
S91-05		B	219 (±22)	70 (±4)	0.72 (±0.18)	98 (±21)	0.058	815 (±17)
SSG-1		B	183 (±13)	77 (±3)	0.88 (±0.44)	110 (±50)	0.061	825 (±17)
S91-26		B	164 (±15)	82 (±4)	0.94 (±0.34)	117 (±37)	0.055	767 (±16)
S03-2A	Coarse-grained dunite	C	638 (±64)	38 (±2)	0.57 (±0.17)	83 (±21)	0.054	820 (±14)
S03-2C		C	964 (±111)	30 (±2)	n.a	n.a.	0.075	831 (±13)
08S-32		C	617 (±61)	39 (±2)	0.46 (±0.15)	71 (±19)	0.104	n.a.
S95-31 §§		C	893 (±130)	32 (±3)	n.a.	n.a.	0.143	1056 (±29)##

n.a., not analyzed

* LPO of minerals were measured in XZ thin-section with 70 ° tilt to the incident beam using an electron back-scattered diffraction (EBSD) system (JEOL JSM6380 with HKL channel 5). The system is running at the experimental environment of 20 kV acceleration voltage, 15 mm working distance and spot size of 60. For some coarse-grained samples without clear foliation and lineation, the XZ thin-sections were prepared in the procedures as below: (1) cutting a cubic sample (3-5 cm in each length); (2) making two or three thin-sections from the orthogonal facies; (3) measuring the shape preferred orientations (SPOs) of olivine in these thin-sections to determine the foliation (XY); (4) cutting and making thin-section parallel to foliation (XY thin-section); (5) measuring the shape SPO of olivine in XY thin-section to determine lineation (X); (6) cutting and making thinsection parallel to lineation and normal to foliation (XZ thin-section). The preferred orientations of olivine are also double-checked using the trails of elongated spinel if available.

† The three-dimensional grain size is estimated from two-dimensional images, using the linear intercept method with a stereographic correction factor of 1.5 (Gifkins, 1970).

§ Stress estimated based on relationship between stress and dynamically recrystallized grain size under wet condition (Jung & Karato, 2001b).

Stress estimated based on relationship between dislocation density and stress (Karato & Jung, 2003). The calculated stresses are larger than those obtained from recrystallized grain size, probably due to heterogeneous dislocation distribution and low density of dislocation were not included in calculation.

** M-index, misorientation index characterizes the fabric strength of olivine (Skemer *et al.*, 2005).

†† Temperature was estimated assuming 1.5 GPa using olivine-spinel Mg-Fe^{2+} exchange geothermometer (Ballhaus *et al.*, 1991a).

§§This sample contains distinct spinel-rich layer and olivine-rich layer.

The compositions of olivine and spinel were determined from olivine- and spinel-rich layers in the same thin-section, respectively. This texture impedes prevailing Mg-Fe re-equilibrium between olivine and spinel in both olivine- and spinel-rich layers during cooling, and thus olivine and spinel could preserve their primary compositions which were equilibrated at high temperatures.

spinels can be observed in a single sample (Figs. 5.3b and d). On the other hand, because the olivine shows a narrow Fo# range (~91–93) for all the spinel-layer-free harzburgites and dunites as presented in this study, and the absence of lower Fo# olivine suite in harzburgite or lherzolite in the field (Figs. 5.5a and b; also see Wang *et al.*, 2005b), it is difficult to interpret that these rocks were formed by continuous fractional crystallization. In addition, the inverse relationship between olivine modal proportion and whole-rock Mg# might either not favor a simple fractional crystallization or a solely cumulate origin for harzburgites and dunites (Fig. 5.7b).

The supporting arguments for their high-degree melting nature include as below: (1) Very low Cpx modal abundance (< 2.3%) in the recalculated Ol-Opx-Cpx mineral assemblage. The modal amount of clinopyroxene is good measure of degree of melting (e.g., Dick & Fisher, 1984, Niu, 1997), because Cpx is the phase consumed most rapidly during anhydrous partial melting in the spinel facies (Jaques & Green, 1980). A peridotite containing 15% and 0% Cpx thus represents approximately no melting and above ~25% (batch melting mode), respectively. However, a minor amount of Cpx may persist to above ~25% melting if the water is participated into melting of a spinel peridotite (Gaetani & Grove, 1998). Therefore, most of the harzburgites or dunites showing a very low recalculated modal abundance of Cpx may suggest that they have undergone a melting degree above 25%.

(2) Very low whole-rock CaO, Al_2O_3 and TiO_2 contents. The whole-rock CaO, Al_2O_3 and TiO_2 are progressively depleted as melting proceeds, which enables their concentrations to be a calibrator for melting degree (Ishiwatari, 1985, Pearce *et al.*, 1992). In most Songshugou harzburgites and dunites, the very low concentrations of whole-rock Al_2O_3 (< 0.7 wt.%) and CaO (< 0.7 wt.%), thus suggest a melting degree of 30–33% (batch melting), whereas TiO_2 (< 0.01 wt.%) corresponds to >20% melting (fractional melting). Because

concentrations of TiO_2 are under the detection limit of XRF measurement and precise determination from ICPMS is not available, the TiO_2 content summarized in this study can only be considered as upper-bound value and a fractional melting degree of 20% could be under-estimated.

(3) The plots of whole-rock MgO-SiO_2 and MgO-FeOt bridge between melting curves at high degree melting end (~ 25% partial melting in both batch and fractional melting modes) and compositions of olivine (Figs. 5.7c and d). This characteristic might imply that these harzburgites and dunites had been partially melted to an extent of about 25%, and then enriched by olivine due to olivine crystallization and/or dissolution of pyroxene (mostly Opx) during melt-rock interactions (e.g., Kelemen *et al.*, 1995, Niu, 1997).

(4) Depleted whole-rock HREE pattern (Figs.5.9a-d). The extent of partial melting in mantle peridotite can be better inferred from the abundance of whole-rock HREE, because these elements are considered to be slightly affected by metasomatic processes (Hellebrand *et al.*, 2001). In comparison with the chondrite-normalized REE patterns of variable melting degree (Piccardo *et al.*, 2007), the Songshugou harzburgites and dunites exhibit a melting degree of 23–27% (fractional melting), except for Group 2 coarse-grained dunite. The exact reasons accounting for the distinctive feature of Group 2 coarse-grained dunites are unknown, as one of the possible explanations, however, their elevated LREE-HREE concentrations might be attributed to their relatively larger porosities which could cause both LREE and HREE to be retained during melting.

Consequently, we concluded that Songshugou harzburgites and dunites are highly depleted mantle residues which are resulted from a melting degree of 25-33% for batch melting mode or 23-27% for fractional melting mode. Because fractional melting is more efficient in depleting the incompatible components than batch melting does, a relatively higher melting degree for

batch melting compared to fractional melting is required for obtaining the same extent of depletion.

5.7.2. Melt-rock interactions

It is a well-known fact that the refractory mantle composition after extensive melting can be modified subsequently by interacting with percolating melt. This melt-rock interaction process has also believed to occur in Songshugou harzburgites and dunites and its signature can be manifested in following aspects. (1) First direct evidence comes from well-preserved textures of anhedral Opx in matrix (Fig. 5.2e) and rounded Opx inclusions in olivine and spinel (Fig. 5.4a). Both irregular grain boundaries of Opx in contact with fresh olivine and rounded Opx inclusion in olivine are indicative of the dissolution of Opx to form olivine by reactive melt (e.g., Bédard *et al.*, 2009, Dai *et al.*, 2011, Edwards & Malpas, 1995, Zhou *et al.*, 2005). In addition, the euhedral spinel is indicative of its crystallization from reacting melt (Fig. 5.3b), and some subhderal spinels showing patchy composition pattern may suggest the mixing of old anhedral spinel remnants with a newly crystalized subhedral spinel (Fig. 5.3c).

(2) Significant enrichments of LREEs and HFSEs (e.g, Nb, Ta, Zr, Hf and Ti) are useful indicators of melt infiltration and melt-residue interaction (e.g., Dai *et al.*, 2011, Parkinson *et al.*, 1992, Song *et al.*, 2004a). Therefore, the observed high LREE/MREE ratios, U-shaped REE patterns, as well as elevated Ta, Zr and Hf concentrations in most Songshugou harzburgites and dunites (Fig. 5.9a-h) clearly suggest that these rocks were not solely originated from partial melting of primitive mantle, but also pervasively modified due to the following melt-rock interaction. The pronounced spikes of fluid-mobile large ion lithophile elements (LILEs, Cs, Ba, U and Sr) could also be interpreted as resulting from enrichment by interaction between a fluid-rich component (e.g.,

fluid or hydrous melt) and residue.

(3) It is generally accepted that the high Fo# in olivine and Cr# in spinel are indicators of the highly refractory mantle character (Arai, 1994, Dick & Fisher, 1984, Matsukage & Kubo, 2003). However, very high Fo content of olivine (>91) and Cr# of spinel (>70) in dunites could more likely be produced by melt-rock interaction, rather than by high degree of melting (Zhou *et al.*, 2005, Zhou *et al.*, 1996). As shown in Fig. 5.5a, almost all Songshugou harzburgites and dunites fall within the high Fo# and Cr# region of olivine-spinel mantle array (OSMA) of Arai (1994). Excluding the spinel-layered dunites, the compositions of olivine (Fo# ~ 91–93) and spinel (Cr# ~ 76–83) in coarse-grained dunites and harzburgites show a residue origin after 25–33% partial melting (batch melting) at ~2 kbar. This melting degree seems consistent with the estimated value as inferred from other methods (see above), however, two critical issues may stand against this inference. (1) It is almost impossible to reach such a high extent of melting at only 2 kbar (depth of ~6 km), which requires a temperature above 1300 ℃ (Jaques & Green, 1980). (2) The dominant range of Cr# (76–83) in primary spinels from harzburgites, coarse-grained and porphyroclastic dunites corresponds to a fractional melting degree of over 30% (Fig. 5.5e), if the spinels are simply remnant after high degree partial melting. This melting degree is obviously inconsistent with previously estimated value (25–33% in batch melting). One of the reasonable interpretations for this inconsistence is that those primary spinels were not formed by partial melting, but through melt-rock interaction, and this explanation is supported by dominant occurrence of euhedral spinels in the harzburgites and coarse-grained dunites (crystalizing from infiltrating melts). In addition, as shown in Fig. 5.5a, because Fo# in olivine is dominantly controlled by melting degree but less affected by melting pressure, olivine Fo# of 91–93 can also be formed by 25–33% of batch melting degree at pressure >

2 kbar, and this melting degree agrees well with that suggested above. In most dunites and harzburgites, olivine shows a very narrow variation of Fo#, the later melt-rock interaction is thus supposed to form new olivine grains of similar Fo# as partial melting. In another word, olivines containing Fo# of 91–93 were produced by both partial melting and melt-rock interaction. This could be the most reasonable interpretation, since it is difficult to accept that such a huge dunite body and its volumetric dominant phase olivine are the solely products by dissolution of Opx and/or crystallization of olivine during melt-rock interactions. Integrated with the characteristic of very low TiO_2 content (0.01–0.2 wt.%) in primary spinels (Fig. 5.5e), the harzburgites and coarse-grained dunites thus represent a residue after interacting with TiO_2-depleted but Cr_2O_3 and MgO rich magma (e.g., boninite).

(4) It is well-known that the Ti concentration in spinel/chromites is strongly controlled by the composition of their equilibrium magmas (Arai, 1992, Kamenetsky *et al.*, 2001). Hence the concentration variation of TiO_2 in spinels can also be considered as a typical result from melt-rock interaction (Pearce *et al.*, 2000). The spinels from Songshugou peridotites present contrastingly higher TiO_2 in fine-grained dunites than coarse-grained dunites and harzburgites (Fig. 5.5e), thus implying a reaction between TiO_2-depleted residue and a TiO_2-rich magma. Combined with argument (3), the contrasting TiO_2 concentration in spinels between coarse-grained dunites, harzburgites and fine-grained dunites may suggest two stages of melt-rock interactions.

(5) The podiform chromitite in mantle assemblage is generally believed to be originated from melt-rock interaction process, during which infiltrating melt dissolves pyroxene and precipitates olivine and chromite (e.g., Melcher *et al.*, 1997, Zhou *et al.*, 1994, Zhou *et al.*, 1996). A sporadic occurrence of high-Cr podiform chromitite (e.g., spinel/chromite layered dunites) in the Songshugou ultramafic body (Fig. 5.1c and 5.2d), therefore provides another important

evidence for melt-rock interaction.

(6) Same as the argument for highly refractory nature, the plots of whole-rock MgO-SiO_2 and MgO-FeOt of Songshugou harzburgites and dunites are mostly located linearly between end of melting curve and region of olivine. This feature may also indicate the enrichment of olivine from infiltrating melt.

Based on above evidence, we therefore conclude that the Songshugou harzburgites and dunites are a mantle residue that not only derived from large extent of melting, but also contain excess olivine and fertile components which could be introduced by crystallization of olivine from percolating melts and/or by dissolution of pyroxene (mostly Opx) to form olivine during melt-rock interactions.

5.7.3. Tectonic setting

Unraveling the tectonic setting from which Songshugou peridotites originated is a key issue for reconstructing the evolution history of Qinling orogenic belt, it is however, still not well constrained so far. In this study, a couple of evidence can point out that fore-arc region in a supra-subduction zone setting is the most likely provenance. The compositions of olivine and spinel are powerful petrogenetic indicators and can thus be used for the tectonic discrimination of peridotites (e.g., Arai, 1994, Dick & Bullen, 1984, Kamenetsky *et al.*, 2001, Pearce *et al.*, 2000). In the olivine Fo# vs. NiO diagram, almost all harzburgites, coarse- and fine-grained dunites fall within the field of modern fore-arc peridotites (Fig. 5.5b; Ishii *et al.*, 1992), except for a few olivines plotted in the near-boundary field of abysmal peridotites (Dick, 1989) and olivines in spinel-layered dunites showing apparently higher off-field Fo#. In the diagrams of spinel Cr# vs. olivine Fo# (Fig. 5.5a), spinel Cr# vs. spinel TiO_2 (Fig. 5.5e) and spinel Cr# vs. spinel Mg# (Fig. 5.5f) , almost all harzburgites and coarse-grained dunites show close relationships with supra-

subduction zone (SSZ) peridotes, high-Mg arc magma or boninites. This boninite affinity of harzburgites and coarse-grained dunites are also presented in Figs. 5.5c and d, as spinels clustering in the boninite fields. These results thus imply that the Songshugou peridotites were most likely formed at a SSZ environment, because the only unequivocal tectonic setting in which modern boninites had been recognized is a fore-arc region (Crawford, 1989, Kim & Jacobi, 2002). The enrichments of fluid-mobile LILEs and similar whole-rock extended REE patterns with those dunites and harzburgites from Torishima Forearc & Conical Seamount in Izu-Bonin-Mariana (Figs. 5.9e-h), might also agree with a supra-subduction zone setting (Parkinson & Pearce, 1998, Spandler & Pirard, 2013). One the other hand, because the ocean island basalt (OIB) component commonly exhibit marked enrichments of MREEs and Nb, the relative depletion of MREEs with respect to HREEs and strong depletion of Nb in harzburgites and dunites may indicate that the enriched materials were not derived from hot mantle plume source and disfavor an intra-plate setting.

Additional evidence supporting for the fore-arc setting is from the estimated oxygen fugacity in peridotites. The oxygen fugacity was calculated using conventional olivine-orthopyroxene-spinel thermobarometer, based on the reaction:

$$6\,Fe_2SiO_4 + O_2 = 3\,Fe_2Si_2O_6 + 2\,Fe_3O_4 \quad (1)$$

olivine *orthopyroxene* *spinel*

Because most dunite samples do not contain Opx and precise pressure is unknown in most peridotites, we calculated the equilibrium temperature and fO_2 at an arbitrary pressure of 1.5 GPa, employing the experimentally calibrated spinel-olivine oxygen barometer by Ballhaus *et al*. (1991b). To calculate oxygen fugacity, the stoichiometric Fe^{3+} values obtained from EMPA were applied. The ratio of $Fe^{3+}/(Fe^{2+}+Fe^{3+})$ is about 0.26 ±0.08 among all harzburgites and dunites, which corresponds to a propagated error of ~0.3 $\Delta \log fO_2$(FMQ)

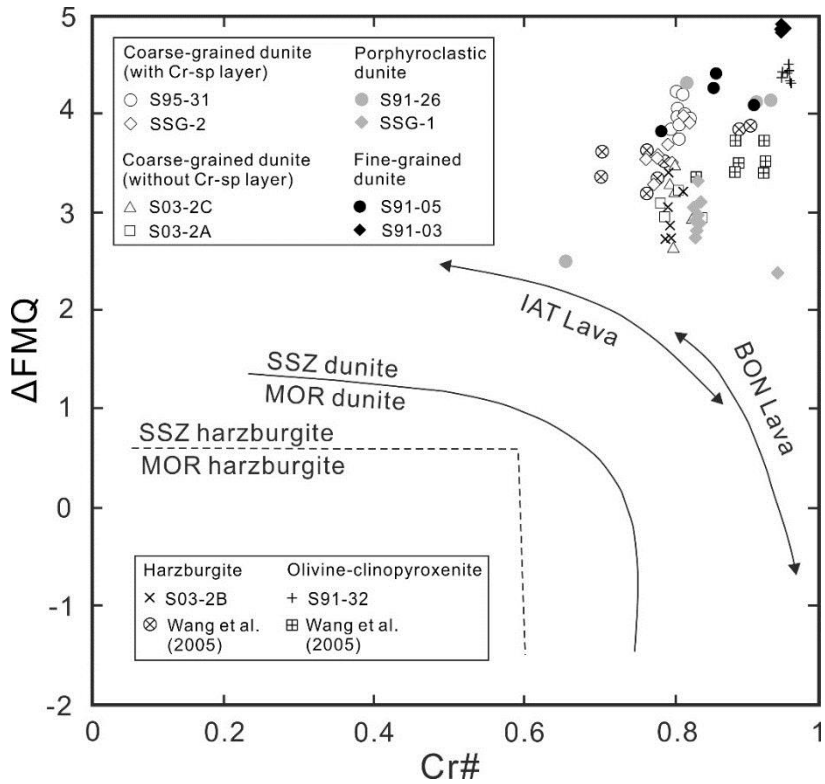

Fig. 5.11. Plots of oxygen fugacity vs. spinel Cr# for studied peridotite samples. The boundaries between SSZ and MOR harzburgite/dunite, as well as the ranges of island arc tholeiitic (IAT) and boninnic (BON) lava (double-arrowed line) are taken from Dare *et al.* (2009).

caused by 1.5% uncertainty in R_2O_3 content of spinels on calculated fO_2 (Parkinson & Arculus, 1999). These obtained fO_2 values are better considered as maximum values, due to absence of Opx. As shown in Fig. 5.11, all peridotite samples exhibit $\Delta\log fO_2$(FMQ) level of 2.4–4.9, and fine-grained dunites show distinctly higher oxygen fugacity than those harzburgites and coarse-grained dunites ($\Delta\log fO_2$(FMQ) = 3.8–4.9 vs. 2.6–4.2). These estimated fO_2 values for Songshugou harzburgites and dunites fall into the region of SSZ peridotites and are higher than most of reported fO_2 values for SSZ peridotites (e.g., Arai *et al.*, 2007, Dare *et al.*, 2009, Pal, 2011, Parkinson & Arculus, 1999, Pearce *et al.*, 2000). Although the equilibrium temperatures used in fO_2 estimation were determined by Mg-Fe exchange reaction between olivine and spinel, which are significantly lower than the melting or melt-rock interaction temperatures and could thus affect the real fO_2 at high temperature, the recalculated compositions for volumetrically minor spinel in equilibrium with olivine at high temperature will only yield slightly decrease of oxygen fugacity (< 0.1 $\Delta\log fO_2$(FMQ) per 100 ℃) (Melcher *et al.*, 1997). This highly oxidized state most likely corresponds to an oxidized sub-arc/sub-fore-arc mantle condition, where a substantial amount of oxidizing agent (ferric iron and water) can be brought back into mantle by fluid/melt derived from hydrous subducting slab (Evans *et al.*, 2012, Mungall, 2002, Parkinson & Arculus, 1999).

The fore-arc setting for Songshugou peridotites can also be inferred from the olivine fabrics. The C- and B-type olivine fabrics observed in respective coarse- and fine-grained dunites are generally considered to be formed under wet conditions that are most likely achieved in a subduction zone setting and are supported by many studies on natural peridotites from convergent settings (see Karato *et al.*, 2008 and references therein). In particular, B-type olivine fabric has been considered as a typical product of plastic deformation along the cold and stress-concentrated layer between fore-arc mantle and fore-arc crust

or subducting slab (Kneller *et al.*, 2005). B-type olivine fabric is also proposed as one of the major factors contributing to the trench-parallel fast shear wave polarization anisotropy commonly observed in the fore-arc regions (e.g., Jung & Karato, 2001a, Kneller *et al.*, 2008, Kneller *et al.*, 2005).

However, it is important to point out that all above-mentioned indicators of tectonic setting are actually closely associated with melt-rock interaction and later plastic deformation process, because (1) primary spinels in harzburgites and coarse-grained dunites were derived dominantly from infiltrating melt, and (2) plastic deformation should have taken place at a solid-state condition postdating or accompanying melt-rock interaction, otherwise the deformation structures could be readily eradicated by partial melting or melt-rock interaction process. Hence, the inferred fore-arc region should better be regarded as the place in which melt-rock interaction and later sub-solidus evolution occurred. Then what is the tectonic setting for partial melting? Probably the most useful information is from the chemical compositions of remnant olivine and spinel formed by partial melting. As shown in Fig. 5.5 and discussed above, olivines of Fo# ~91–93 are likely formed during both partial melting and melt-rock interaction, and a few anhedral spinels (melting remnant) of lower Cr# (65-70) were also found. These mineral compositions are well matched with the estimated melting degree and also related to a SSZ setting. In addition, the harzburgites and dunites have undergone a melting degree of 25–33% (batch melting) or 23–27% (fractional melting). Such an extensive melting seems unlikely to achieved in any mid-ocean ridges including those fast-spreading ones, as indicated through vast studies on abysmal peridotites (Niu & Hékinian, 1997, Song *et al.*, 2004a), however, it is very likely to be realized in a boninite associated fore-arc region (Crawford, 1989). The highly refractory nature and boninitic affinity also suggest that anomalously high temperature (>1100 ℃) and introduction of subduction zone fluids are especially required (Crawford,

1989, Fallon & Danyushevsky, 2000). Consequently, we considered that Songshugou peridotite probably represents a sub-fore-arc lithospheric mantle (or pre-existing oceanic mantle lithosphere) that has undergone both extensive partial melting and subsequent melt-rock interactions in a hot fore-arc setting.

5.7.4. Tectonic evolutions

Based on the discussions above, a tectonic evolution consisting of partial melting and following melt-rock reactions in a sub-fore-arc lithospheric mantle was outlined. However, more details in this tectonic evolution can be provided from the texturally distinct peridotites (coarse-grained, fine-grained, porphyroclastic dunites, harzburgites, and olivine clinopyroxenites). The different deformation microstructures between coarse- and fine-grained dunites suggested that (1) due to dynamic recrystallization, coarse-grained dunites transform into fine-grained dunites, with porphyroclastic dunites as the intermediate products, and (2) coarse-grained dunites (C-type olivine fabric, 30−39 MPa, T = 820–1060 ℃) were deformed at lower stress but higher temperature conditions than those fine-grained dunites (B-type olivine fabric, σ = 70−83 MPa, T = 710−830 ℃) (see below section). These results thus imply that a two-stage deformation process during the cooling of subduction zone. As discussed above, fine-grained dunites show significantly higher TiO_2 concentration in spinels than coarse-grained dunites and harzburgites, which suggest two-stage interaction processes of melting residues with TiO_2-enriched and TiO_2-depleted melt. The TiO_2-depleted melt could be relevant to a boninite, whereas TiO_2-enriched melt could be associated with an island arc tholeiite (Fig. 5.5e). The two-stage deformation is considered to be well correlated with the two-stage melt-rock interaction due to two reasons: (1) High-temperature boninite accords with high-temperature deformation in coarse-grained dunites,

which is supposed to occur at the initiation of subduction zone, whereas low-temperature island arc tholeiite agrees with low-temperature deformation in fine-grained dunites, which is expected to take place in an evolved or cooled subduction zone. (2) Increasing Fe^{2+}, Fe^{3+} and TiO_2 contents in spinels (Figs. 5.5c and d), as well as corresponding elevating oxygen fugacity levels (Fig. 5.11) from coarse-grained, through or not through porphyroclastic, to fine-grained dunites may indicate a melt/fluid enhanced melt-rock interaction and/or mineral re-equilibrium that were controlled by plastic deformation. The longer and stronger plastic deformation experienced, the more facilitated melt/fluid infiltration and reaction, and easier spinel composition can be modified.

Olivine clinopyroxenite is a typical crystallization product from evolving magma, as indicated by high modal abundance of clinopyroxene megacryst (Fig. 5.2f) and dyke-like occurrence in field (Fig. 5.1c). The high concentration of flat MREE-HREEs pattern (0.5-1 times chondrite) and depleted LREEs pattern with positive slope in olivine clinopyroxenites (Fig. 5.9i) are clearly different from those dunites and harzburgites, disagreeing with their origin as melting reside and/or melt-rock interactions. In addition, the olivine Fo# of olivine clinopyroxenite varies in a continuous range of 84-90 and is remarkably lower than olivines in dunites and harzburgites (Fig. 5.5a,b), whereas the contents of Fe^{2+}, Fe^{3+} and TiO_2 in spinel (following Fe-Ti trend which can be attributed to fractional crystallization) are similar with those fine-grained dunites (Fig. 5.5c-f). These above features thus suggest that olivine clinopyroxenite is probably a fractional crystallization product from a boninitic - island arc tholeiitic magma.

The subsolidus evolution of Songshugou harzburgites and dunites can be indicated by the ubiquitous occurrence of hydrous or carbonate minerals (e.g., amphibole, Cr-chlorite, dolomite) (Figs. 5.2 and 5.4) due to metasomatism or retrograde metamorphism. Their olivine-penetrating texture and/or occurrence

as undeformed inclusions in olivines and spinels clearly indicate that the retrograde metamorphism postdated plastic deformation during exhumation. As shown in the P-T pseudosection for a representative coarse-grained dunite (Fig. 5.12a), the P-T stability field of dominant hydrous phase anthophyllite is <1 GPa and 600-700 ℃ (also see Yang & Powell, 2008). This temperature range is well below the plastic deformation temperature (T = 710-1060 ℃), and pressure condition corresponds to crust level (less than brittle-ductile transition depth). This P-T condition inhibits the prevalence of plastic deformation, but favors brittle fracturing which can account for the texture of amphiboles cross-cutting olivines. More detailed phase diagram analysis suggests that ortho-amphibole (anthophyllite dominant) was majorly formed by the following hydration reaction:

$$9\ (Mg,Fe)_2SiO_6 + 2\ H_2O = 2\ (Mg,Fe)_7Si_8O_{22}(OH)_2 + 2\ (Mg,Fe)_2SiO_4 \quad (2)$$

orthopyroxene *ortho-amphibole* *olivine*

Namely, 2 moles of ortho-amphibole and 2 moles of olivine can be produced by reacting 9 moles of Opx with water. In Songshugou dunites, the volume proportion of amphibole (ortho-amphibole dominant) is 0–15 vol.%, and thus corresponds to similar volume percentage of Opx (0–15 vol.%) in an anhydrous mineral assemblage, considering the molar volume difference between ortho-amphibole and Opx at ambient condition ($V_{ortho\text{-}amphibole}$ is about 4 times V_{Opx}). This result is consistent with the fact that many Songshugou dunites actually fall into the harzburgites field in the recalculated Ol-Opx-Cpx modal proportion diagram (Fig. 5.7a), due to the consumption of Opx during retrograde metamorphism. In terms of near-fractional melting model of Niu (1997) at 1–3 GPa and anhydrous condition, 23–27% of melting consumes Opx and Cpx and results in ~25 ± 5 vol.% (similar value in wt.% due to similar density between Ol, Opx and Cpx) of Opx in a Ol-Opx-Cpx assemblage. If this approximate value is accepted, we estimated that a minimum of ~5–15 vol.% of Opx might

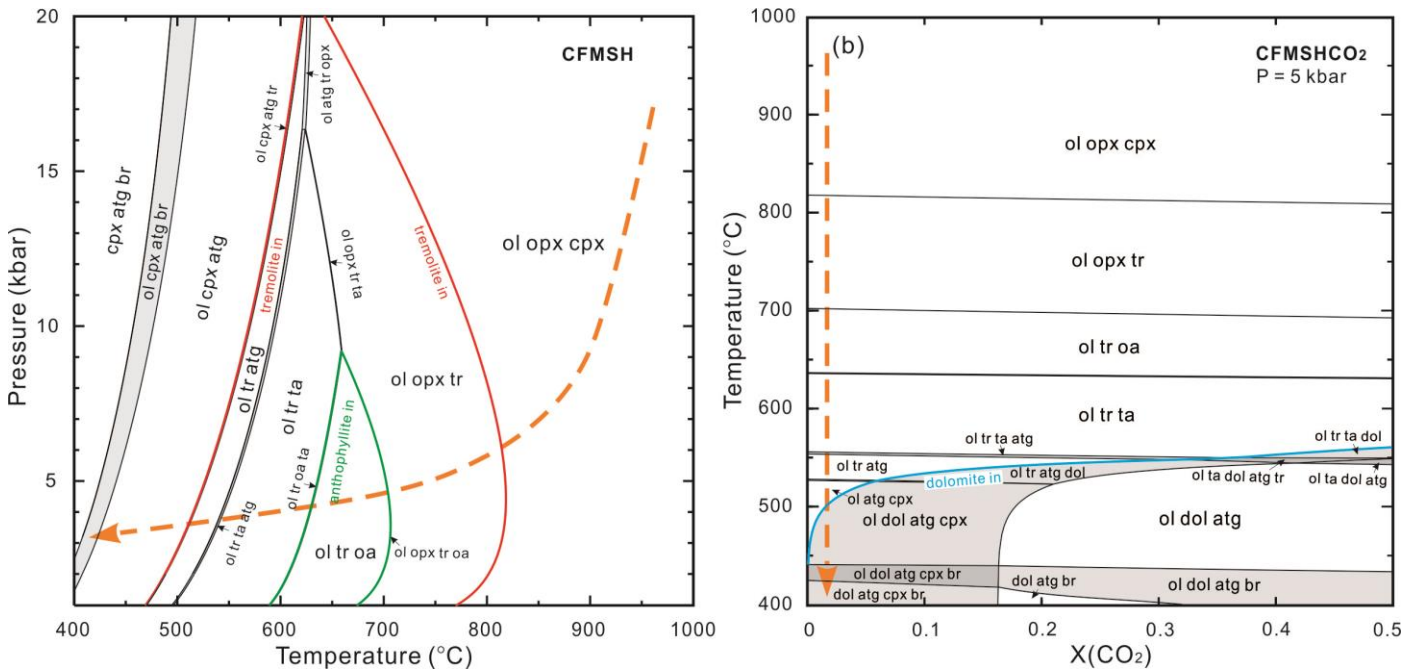

Fig. 5.12. (a) *P-T* pseudosection for representative coarse-grained dunite in the system of CaO-FeO-MgO-SiO_2-H_2O (CFMSH) (modal proportions of oxides: CaO = 0.60, FeO = 6.49, MgO = 57.25, SiO_2 = 35.25, H_2O in excess), calculated using THERMOCALC v3.33 (Powell & Holland, 1998). Green and red lines indicate the stability field of ortho-amphibole and tremolite, respectively. Yellow dash arrow line denotes the possible exhumation *P-T* path. (b) Isobaric *T-X*(CO_2) pseudosection at 0.5 GPa for the same representative coarse-grained dunite in CaO-FeO-MgO-SiO_2-H_2O-CO_2 (CFMSHCO_2) system, with H_2O-CO_2 fluid in excess. Blue line indicates the stability field of dolomite. Yellow dash arrow line denotes an arbitrary cooling path with a very low and constant *X*(CO_2). Mineral abbreviation: antigorite (atg), brucite (br), clinopyroxene (cpx), dolomite (dol), ortho-amphibole (oa), olivine (ol), ortho-amphibole (oa), orthopyroxene (opx), talc (ta), tremolite (tr).

had been dissolved by infiltrating melt during melt-rock interaction. Because the Mg# in Opx is ~91–92, the newly formed olivine may inherit the Opx Mg# and show Fo# similar with that formed by partial melting and/or melt-rock interaction (91–93).

Secondary amphibole phase tremolite was also recognized in dunite samples (Figs. 5.4b and d), however, tremolite is the dominant hydrous phase in olivine clinopyroxenites (Fig. 5.2f). As shown in Figs. 5.12a and b, tremolite has a much wider P-T stability field than ortho-amphibole, and appears at temperature less than about 800 ℃ during cooling, at the expense of Opx and Cpx through the reaction:

$$5\,(Mg,Fe)_2Si_2O_6 + 4\,Ca(Mg,Fe)Si_2O_6 + 2\,H_2O = 2\,Ca_2(Mg,Fe)_5Si_8O_{22}(OH)_2 + 2\,(Mg,Fe)_2SiO_4 \quad (3)$$

Orthopyroxene *clinopyroxene* *tremolite* *olivine*

The infrequent occurrence of tremolite in dunites compared with anthophyllite is consistent with nearly complete consumption of Cpx during partial melting and/or melt-rock interaction, whereas abundant tremolite is in agreement with high modal proportion of Cpx in olivine clinopyroxenites. Integrated with the discussions above, we can conclude that the Opx and Cpx were consumed, while olivine was produced in successive processes of partial melting, melt-rock interactions and retrograde metamorphism.

Cr-chlorite is another ubiquitous hydrous phase that is often observed in ultramafic rocks (Merlini *et al.*, 2009). Because the thermodynamic models for Cr-bearing minerals are still unavailable, we cannot calculate the precise P-T stability field of Cr-chlorite using phase diagram. However, a few recent experiments suggested that Cr-chlorite is more stable than common chlorite and it can persist up to 900 ℃ at 3.5 GPa (Fischer *et al.*, 2008). The frequent co-occurrences of Cr-spinel and Cr-rich spinel in Songshugou dunites and

harzburgites (Figs. 5.3b, 5.4c and d) imply that the following hydration reaction is very likely (modified from Kimball, 1990):

$$Mg(Al,Cr)_2O_4 + 4MgO + 3SiO_2 + 4H_2O = Mg_5(Al,Cr)_2Si_3O_{10}(OH)_8 \quad (4)$$

spinel *melt/fluid* *chlorite*

through which the Mg, Al and Cr in spinel can be transferred into chlorite. Because the Cr# is much higher in spinel than chlorite, the formation of chlorite will deplete Al and enrich Cr contents in spinel. Therefore, the spinel Cr# that is significantly higher in fine-grained duintes than harzburgite and coarse-grained dunite, can be interpreted by their different extents of retrograde metamorphism controlled by plastic deformation. The weakly deformed olivine clinopyroxenites have similar Cr# and TiO_2 content in spinel with fine-grained dunites, their high spinel Cr# and TiO_2 concentration might be explained by extensive hydration reactions associated with crystallization from hydrous magma with island arc tholeiitic component.

Besides hydrous minerals, carbonate can also be formed by reaction with H_2O-CO_2 fluid. Dolomite commonly occurs below 450–600 ℃ depending on the specific CO_2 fraction in H_2O-CO_2 fluid (Fig. 5.12b). Because the appearance temperature of dolomite is obviously lower than that of tremolite, the co-occurrence of dolomite, tremolite and/or Cr-chlorite in olivine and spinel (Figs. 5.4b and d) can be interpreted as sequential retrograde metamorphisms - carbonation following hydration during exhumation process.

5.7.5. Olivine fabric transition and tectonic evolution

The texture, mineral compositions and geochemistry of coarse- and fine-grained dunites and harzburgites suggest that the Songshugou peridotite represents a refractory residue that was formed by a high-degree of partial melting and modified subsequently by melt-rock interaction in a fore-arc lithospheric mantle setting (Figs. 5.5 and 5.9). The systematic variations of

spinel composition (increasing Fe^{2+}, Fe^{3+} and TiO_2 contents from coarse-grained to fine-grained dunite) suggest a two-stage interaction between residue and magma (boninite followed by island arc tholeiite) and/or mineral re-equilibrium that were controlled by plastic deformation during the cooling of subduction zone (Figs. 5.5d,e). Namely, coarse-grained dunites were linked with early high-temperature deformation and reaction with boninite, whereas fine-grained dunites were associated with later low-temperature deformation and reaction with island arc tholeiite. This two stage plastic deformation history of the Songshugou peridotite can also be well manifested in multiple aspects:

(1) The macroscopic texture that various-sized coarse-grained lentoid dunites crops out in the fine-grained dunite (Fig. 5.1c), as well as the microscopic texture that large olivine lentoid grains occur in fine-grained olivine matrix in a porphyroclastic dunite (Fig. 5.2b) indicate that coarse-grained dunite is probably the remnant after plastic deformation and represents precursor of their fine-grained counterparts.

(2) The olivine LPOs are linked with the grain sizes of dunite. Namely, C- and B-type LPOs occur in coarse- and fine-grained dunites, respectively. Typical B-type LPO shows [100] axis aligning perpendicular to lineation and residing on foliation, whereas C-type LPO display [100] axis normal to the foliation. Within the fine grained B-type dunites, however, the [100] maxima are oriented oblique to foliation and sub-perpendicular to lineation (Fig 5.10a-c), might indicate the incomplete transition from the C- to B-type LPO.

(3) The higher M-index of olivine in some coarse-grained dunites than that in fine-grained ones, might suggest that strain partitioning during a single stage of deformation in a localized shear zone is not the mechanism that causes the strain of both coarse- and fine-grained dunite. It instead indicates that the coarse-grained dunites were formed earlier than fine-grained dunites.

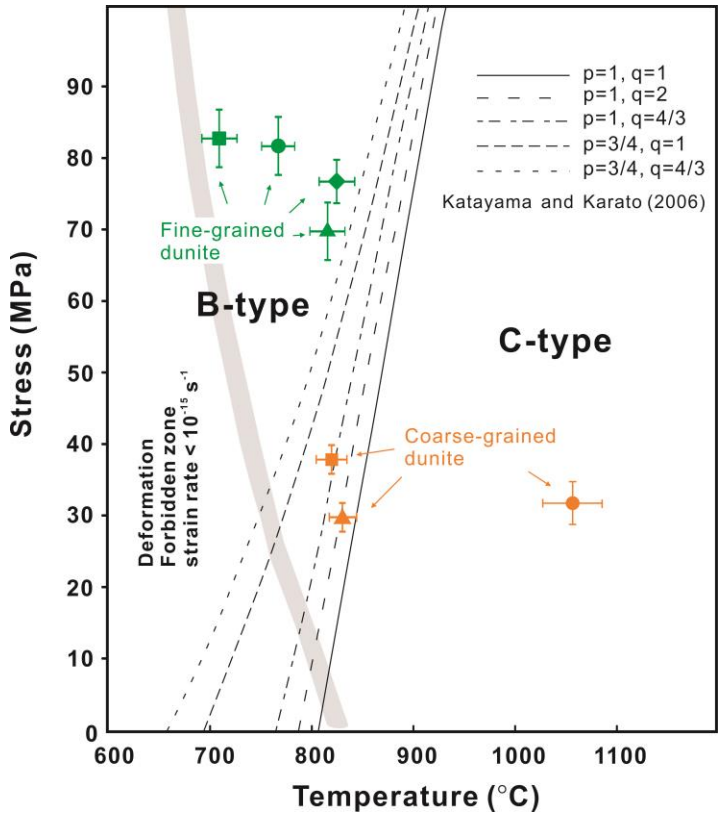

Fig. 5.13. Stress-temperature diagram showing the calculated temperature and stress conditions for deformation in fine-grained and coarse-grained dunites. Boundaries between B-type and C-type LPO of olivine (water saturated, P = 2.0 GPa) are from Katayama & Karato (2006). p and q are the non-dimensional parameters in flow law for Peierls mechanism. Gray area indicates the boundaries of strain rate of 10^{-15} s^{-1} below which no appreciable strain can be observed in geological time-scale.

(4) Consistent with previous experimental results of Katayama and Karato (2006), coarse-grained dunites bearing an olivine C-type LPO shows a significantly higher temperature and lower stress than fine-grained dunites showing an olivine B-type LPO (Fig. 5.13). These stress and temperature differences might thus imply distinct deformation conditions for coarse- and fine-grained dunites.

Consequently, it is reasonable at least partly to conclude that (1) coarse-grained olivine and its C-type LPO are indicative of an early deformation event, whereas fine-grained olivine and its B-type LPO are the product of a later deformation process by modifying the original coarse-grained texture and C-type fabric; (2) coarse- and fine-grained dunites were deformed at different specific tectonic conditions to create C- and B-type LPO independently.

The temperature calculated using the olivine-spinel Mg-Fe^{2+} exchange geothermometer (Ballhaus *et al.*, 1991a) may provide a minimum estimate for the temperature of main deformation event for two reasons: (1) deformation can facilitate the equilibrium of Mg and Fe^{2+} between olivine and spinel. The temperature of the latest deformation event has most likely been recorded, even if the rock had experienced a higher temperature stage of plastic deformation. (2) The diffusion of Mg and Fe^{2+} between spinel and olivine would be fairly fast and continues during cooling to relatively low temperatures (~ 650 ℃) (e.g., Henry & Medaris, 1980). Therefore, the deformation temperature for coarse-grained dunites showing a C-type fabric (T = 820–1060 ℃) could be underestimated. The experiments by Katayama and Karato (2006) suggest that an olivine C-type LPO can be formed at wet and very high temperature conditions in the dislocation creep regime. The maximum temperature for dislocation creep could be approximately considered as the solidus for the peridotite (~1300 ℃), because diffusional creep (e.g., Coble creep) might be prevalent if a significant amount of melt is present in the rock (Kohlstedt, 2002).

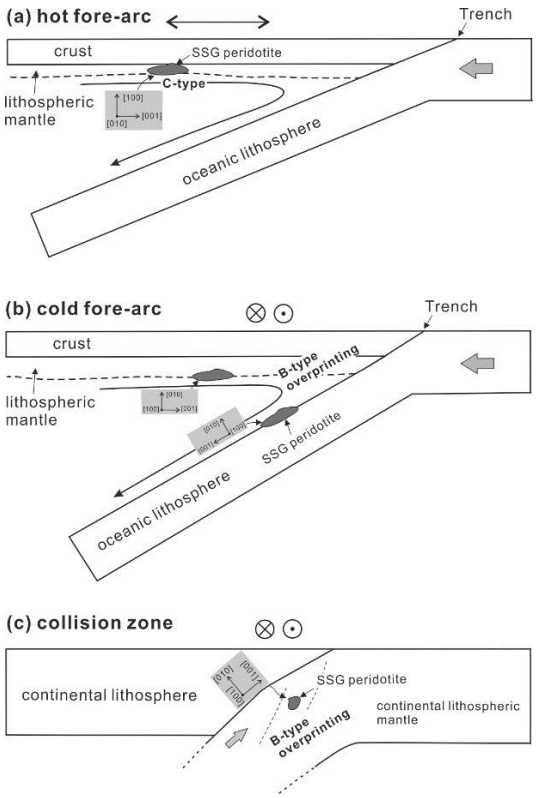

Fig. 5.14. Schematic tectonic settings showing the possible occurrence and evolution of olivine fabrics (B- and C-type LPOs) of Songshugou (SSG) peridotite, Polarization direction of fast S-wave is shown as double arrow and in-and-out symbol. (a) Hot fore-arc which represents the early stage of oceanic subduction zone. The SSG peridotite was probably a rather infertile mantle residue residing at the lithosphere-asthenosphere boundaries (LAB), and underwent the shearing caused by hot convecting fore-arc mantle. The coarse-grained texture and C-type LPO of olivine, as well as the resulting trench-normal polarization direction are due to plastic deformation at high temperature and low stress conditions. (b) Cold fore-arc as a later stage of subduction zone, probably due to the on-going cooling by cold subducted slab. Because of the decreasing temperature of mantle which might result in a more viscous flow, SSG peridotite might be scraped off from LAB by convecting mantle and later deformed in a cold and stress-concentrated fore-arc crust-mantle interface and/or layer above subducting slab. Texture of fine-grained olivine showing B-type LPO, and associated trench-parallel seismic anisotropy might thus be formed by partly modifying the original coarse-grained olivine bearing C-type fabric. (c) The latest stage that two continents collide, in which the SSG peridotite experienced large extent of thrust-shearing during exhumation (the trending-normal dominant plunge direction of stretching lineation in the fine-grained dunite might suggest that the exhumation process was mainly governed by thrusting (Song *et al.*, 1998)). Fine-grained olivine and B-type fabric would be subsequently formed by deforming their original coarse-grained and C-type counterparts, leading to fast shear wave polarizing sub-parallel to the mountain-belts.

In this case, the occurrence of a C-type olivine fabric in a low pressure peridotite most likely possesses a potential association with a hot fore-arc mantle (Katayama & Karato, 2006) (Fig. 5.14a), because the high temperature required for forming C-type LPOs can otherwise only be reached at a deeper slab-mantle interface where garnet peridotite becomes stable in a cool subduction zone (most of natural C-type LPO were found in high-pressure garnet peridotite in subduction zone prior to this study).

In contrast, the experimentally-determined temperature conditions for olivine B-type fabric indicate that the calculated deformation temperatures of 710–830 ℃ for fine-grained dunites showing a B-type olivine LPO might be more reasonable estimates with a possible slight underestimation (Fig. 5.13). This range of deformation temperatures and olivine B-type fabrics are most likely realized in two different tectonic settings where the stress can be concentrated: (1) in a fore-arc crust-mantle interface and/or a slab-wedge interface in a cold fore-arc mantle (Kneller *et al.*, 2005) (Fig. 5.14b); and (2) in an exhumation related shear zone in the lower continental crust (Fig. 5.14c), where water is available.

Therefore, the C-type to B-type LPO transition in olivine accompanied with grain size reduction in the low pressure peridotite might be associated with the continuous cooling of a subduction zone as well as later exhumation (Fig. 5.14). In this process, the hydrous subducting slab ensures the source of water required to form both olivine B- and C-type LPO. This interpretation of subduction zone setting is in good agreement with previous studies. Assuming a two-dimensional corner flow model, the seismic anisotropy in a fore-arc region can be explained by using olivine fabrics, B- and C-type LPOs of olivine can induce trench-parallel and trench-normal polarization directions of fast shear waves, respectively (Jung *et al.*, 2006, Katayama & Karato, 2006, Kneller *et al.*, 2005; also see Fig. 5.15). In this case, it is expected that the seismic anisotropy as

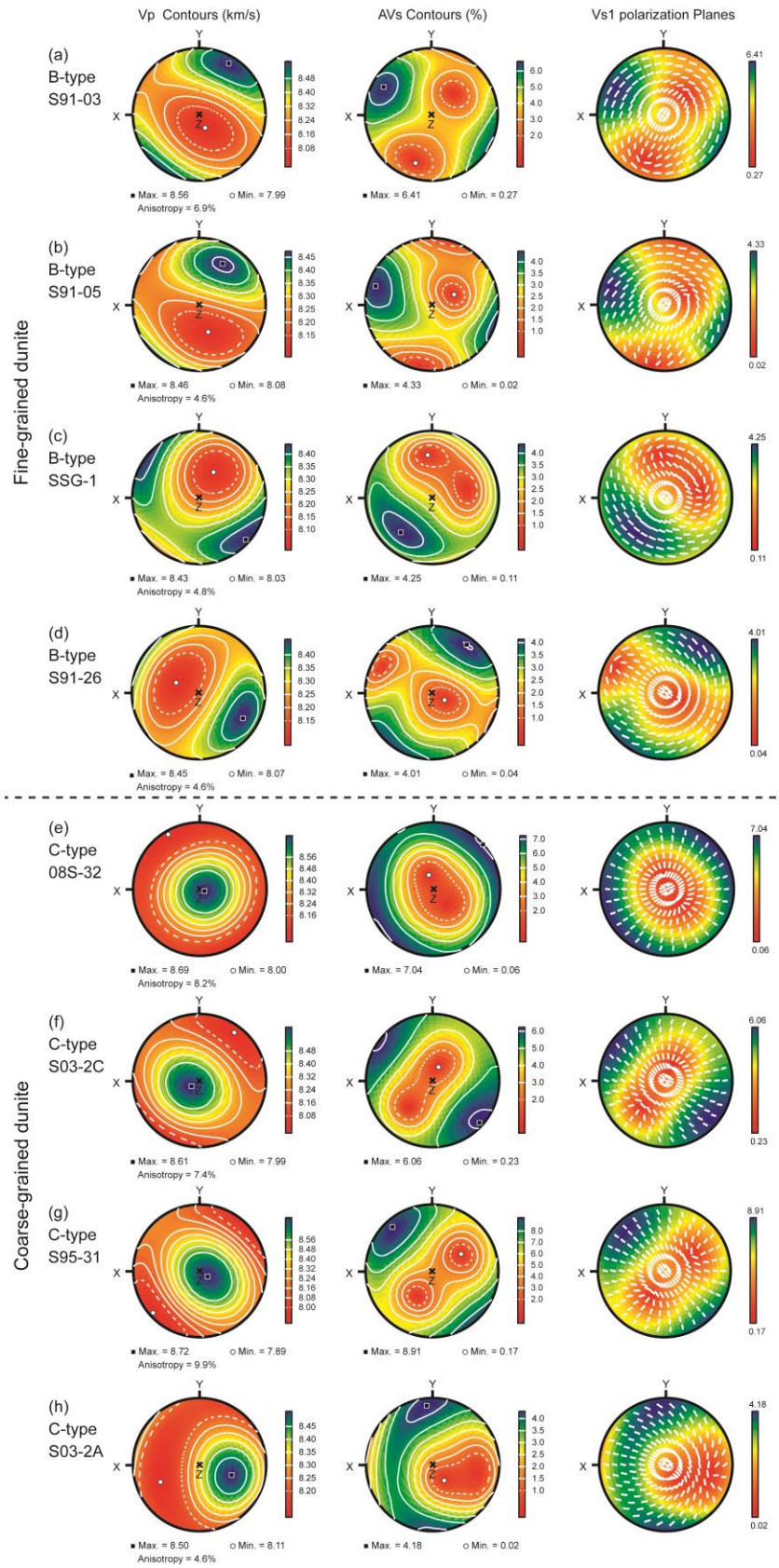
Vp Contours (km/s)
AVs Contours (%)
Vs1 polarization Planes
Fine-grained dunite
Coarse-grained dunite
(a)
B-type
S91-03
Max. = 8.56
Min. = 7.99
Anisotropy = 6.9%
Max. = 6.41
Min. = 0.27
(b)
B-type
S91-05
Max. = 8.46
Min. = 8.08
Anisotropy = 4.6%
Max. = 4.33
Min. = 0.02
(c)
B-type
SSG-1
Max. = 8.43
Min. = 8.03
Anisotropy = 4.8%
Max. = 4.25
Min. = 0.11
(d)
B-type
S91-26
Max. = 8.45
Min. = 8.07
Anisotropy = 4.6%
Max. = 4.01
Min. = 0.04
(e)
C-type
08S-32
Max. = 8.69
Min. = 8.00
Anisotropy = 8.2%
Max. = 7.04
Min. = 0.06
(f)
C-type
S03-2C
Max. = 8.61
Min. = 7.99
Anisotropy = 7.4%
Max. = 6.06
Min. = 0.23
(g)
C-type
S95-31
Max. = 8.72
Min. = 7.89
Anisotropy = 9.9%
Max. = 8.91
Min. = 0.17
(h)
C-type
S03-2A
Max. = 8.50
Min. = 8.11
Anisotropy = 4.6%
Max. = 4.18
Min. = 0.02

Fig. 5.15. Seismic anisotropy of olivine polycrystals in (a-d) fine-grained and (e-g) coarse-grained dunite as shown in the foliation plane. X, Z and Y represent lineation, foliation normal, and direction perpendicular to X and Z. Seismic anisotropy and velocities were calculated based on the single-crystal elastic constants, crystal density, orientations of olivine polycrytals (LPO) using the Voigt-Reuss-Hill (VRH) averaging scheme (Mainprice, 1990). The densities and elastic constants of single crystal olivine (Abramson *et al.*, 1997) at equilibrium condition (1.5 GPa and 850 ℃) were used in calculations. Methods for estimating single crystal density and elasticity at various P-T conditions are described by Mainprice (2007). Assuming a horizontal flow, the polarization direction of fast shear wave is sub-normal to the lineation (flow direction) due to B-type LPO (a,b), however, it becomes at moderate angle to lineation, due to minor component of A-type LPO (c,d). In contrast, the fast shear wave polarizes nearly parallel to lineation for C-type LPO (e,f,h), except for (g) which shows oblique polarization of fast shear wave to lineation.

observed in the fore-arc region would transform from trench-normal to trench-parallel due to on-going cooling of the fore-arc mantle. Because the lineations of fine-grained dunites showing B-type LPO tend to plunge subnormal to the trend of peridotite body or mountain belt (Song *et al.*, 1998), a contribution of fast shear waves polarizing sub-parallel to the orogenic belt would also be expected.

5.8. Conclusions

In this study, we conducted a comprehensive petrographical, mineral and whole-rock geochemical analysis on a suite of orogenic peridotites from Songshugou ultramafic massif, Qinling orogenic belt, central China. Based on the discussions, several important findings are summarized as below:

(1) Very low modal abundance of Cpx, low whole-rock CaO, Al_2O_3 and TiO_2 content, and highly depleted HREE patterns suggest that Songshugou dunites and harzburgites were a highly refractory residue, which was caused by high degree of partial melting (25–33% for batch melting mode or 23–27% for fractional melting mode).

(2) Melt-rock interaction had also been prevalent in dunites and harzburgites, as indicated by evidence including dissolution texture of Opx, dominant euhderal primary spinels, enrichment of LREEs and HFSEs, U-shaped REE patterns, high Fo# in olivine (91–93) and high Cr# in primary spinel (76–83), TiO_2 content in spinel, and occurrence of podiform chromitites.

(3) The partial melting and melt-rock interaction processes are considered to occur in a hot sub-fore-arc lithospheric mantle which can be inferred from high degree of partial melting, spinel and olivine composition, enrichment of fluid-mobile LILEs, high oxygen fugacity ($\Delta \log fO_2$(FMQ) = 2.6–4.9),

water-induced olivine B- and C-type fabrics in dunites and harzburgites.

(4) Harzburgites and coarse-grained dunites exhibit low TiO_2, Fe^{2+} and Fe^{3+} contents in spinel, whereas fine-grained dunites show high TiO_2, Fe^{2+} and Fe^{3+} contents in spinel. These results might indicate a two-stage melt/fluid enhanced melt-mantle interaction and/or mineral re-equilibrium that were controlled by plastic deformation.

(5) Olivine clinopyroxenites exhibit low Fo# in olivine and high Fe^{2+}, Fe^{3+} and TiO_2 in spinel, thus probably represent a fractional crystallization product derived from a boninitic - island arc tholeiitic magma.

(6) The occurrences of amphibole (anthophyllite with minor tremolite), Cr-chlorite and dolomite reflect sequential retrograde metamorphic reactions (hydration followed by carbonation) during exhumation.

(7) A reasonable evolution of Songshugou peridotites can be depicted as following sequences: (a) The sub-fore-arc lithospheric mantle (or pre-existing oceanic mantle lithosphere in fore-arc setting) was extensively melted at initiation of subduction zone; (b) The highly refractory residue was plastically deformed and interacted successively with magmas containing boninitic and island arc tholeiitic components during on-going cooling of subduction zone; (c) The peridotite body was exhumed accompanying with pervasive retrograde metamorphisms.

(8) The occurrence of olivine C-type LPO in low-pressure spinel peridotite potentially suggests an association with a hot fore-arc mantle setting, whereas the olivine B-type LPO might be produced in a cooling fore-arc mantle during exhumation to the lower continental crust. The transition of olivine fabrics from C- to B-type may reflect the cooling process of subduction zone and/or subsequent exhumation.

(9) On the basis of olivine B- and C-type LPOs and their associated tectonic setting, it is implied that (a) the polarization direction of the fast shear wave

in the fore-arc regions would change from trench-normal to trench-parallel due to the cooling of fore-arc mantle, and (b) olivine B-type LPO formed in thrust-dominant shear zones during exhumation can also contribute to the orogen-parallel fast shear wave polarization anisotropy.

CHAPTER 6

Summary

This thesis presents detailed analysis of deformation microstructures, petro-fabrics, mineral and whole-rock compositions on the natural blueschists, eclogites (Chapter 2 and 3) and peridotites (Chapter 4 and 5) which are derived from two ancient subduction zones in China. On the analogy of modern subduction zones, these obtained results may provide useful constraints on the observed seismic velocities and anisotropies in the present-day subducting oceanic crust and overriding mantle wedge.

In Chapter 2, the lithologically and texturally different epidote blueschists and eclogites show different seismic velocities and anisotropies. Specifically, the massive and porphyroclastic (glaucophane-poor) eclogite display the highest P-wave and S-wave velocities, which are close to those of mantle peridotite. In contrast, the mafic blueschist and foliated eclogite (glaucophane-rich) show lower and similar P-wave and S-wave velocities which are approximately 3-12% lower than adjacent mantle and thus able to explain the low velocity upper layer in subducting slab. The seismic anisotropies also decrease from blueschist (AV_p = 13–25%; max. AV_s = 7–15%), through foliated eclogite (AV_p = 5–10%; max. AV_s = 4–8%), to massive or porphyroclastic eclogite (AV_p = 1–3%; max. AVs = 1–2%), in response to the increasing subducting depth. The relatively high shear wave splitting intensities in blueschist and foliated eclogite suggest that a trench-parallel fast anisotropy with a moderate delay time (0.1–0.3 s) can be effectively induced by deformed oceanic crust in a high-angle (>45–60 °) subducting slab. The calculated reflection coefficients at the lithologic interfaces between eclogite and

blueschist are fairly large (R_c = 0.04–0.20) and thus imply that large eclogite bodies could be detected in the shallow accretion wedge by using the high-resolution seismic reflection tecniques.

In Chapter 3, the microstructure and mineral fabric analysis on two texturally different lawsonite blueschists suggest that different dominant deformation mechanisms for glaucophane and lawsonite (i.e. dislociation creep for glaucophane versus rigid-body rotation for lawsonite). Both glaucophane and lawsonite develop pronounced mineral fabrics in spite of their different deformation mechanisms. The fabric of lawsonite shows maximum [010] axis concentrated close to lineation and the [001] axis strongly clustered normal to foliation, which is consistent with the result of two-dimensional fabric modeling using finite-volume method (FVM). The kinematic vorticity analysis suggests that both pure shear dominant (W_m = 0.18–0.26) and simple shear dominant (W_m = 0.86–0.93) deformation regimes are present in foliated LBS, which controls the secondary fabric developments in glaucophane and lawsonite. Additionally, the calculated seismic properties indicate that a counteracting effect of seismic anisotropies exist between glaucophane and lawsonite, and thus lead to a much weaker seismic anisotropy in the subducting oceanic crust than previously estimated based on strongly deformed epidote blueschists (Chapter 2). Therefore, the delay time of fast shear wave polarization anisotropy induced by an actual subducting oceanic crust with a high subducting angle (> 45–60 °) is estimated. It is expected to range from 0.03 to 0.09s (lower bound for massive LBS) and from 0.1 to 0.3s (upper bound for foliated epidote blueschist).

In Chapter 4, the mineral and whole rock composition analysis of the harzburgite samples suggest that these harburgites are highly refractory and water-depleted after experiencing a high-degree partial melting (~ 25–30% fractional melting) and mild high-temperature melt-rock reaction, and thus

represent a remnant of a fossil fore-arc lithospheric mantle in an early and warm subduction zone setting. Mineral fabric examinations indicate that the olivine has a A-/D-type fabric which is credited to the activation of dominant (010)[100], secondary (001)[100] and other minor [100]-slip, {0kl}[100] and [001]-slip systems at low-stress and high-temperature conditions. This A-/D-type olivine fabric is supposed to be prevalent in the fore-arc lithospheric mantle, and thus has weakening effects on the trench-parallel seismic anisotropy in a corner-flow mantle wedge. The topotactic growth of antigorite after A-/D-type olivine fabric in the uppermost fore-arc mantle can induce large trench-parallel seismic anisotropy, however, it cannot explain the low velocities and high Vp/Vs ratios that are commonly observed in hydrous fore-arc mantle. In contrast, the deformation-induced oriented antigorite layers immediately above the subducting slab boundary may account for these distinctive seismic signatures, but have relatively smaller trench-parallel seismic anisotropy or delay times that are produced by intra-slab earthquake events in the fore-arc region. It is thus tentatively suggested that a combination of these two serpentinization processes as well as the different olivine fabrics might have the advantage to interpret the universal and special seismic properties in the fore-arc regions.

In Chapter 5 which is analogous to Chapter 4, the petrographic, mineral and whole-rock composition analysis indicate that the Songshugou peridotite also represent a highly refractory residue (23–27% fractional melting) after intensive partial melting at fore-arc lithospheric mantle. In addition, two stages of melt/fluid enhanced melt-mantle interactions and/or mineral re-equilibrium were inferred. These two melt-rock interaction processes were presumably affected by two stages of plastic deformation which produced C- and B-type olivine fabrics in high-temperature & coarse-grained and low-temperature & fine-grained dunites, respectively. The transition of olivine fabrics from C- to

B-type may reflect the cooling process and imply the incidental transition of fast shear wave polarization anisotropy from trench-normal to trench-parallel directions in subduction zone evolution and/or subsequent exhumation process. Additionally, the sequential post-kinematic retrograde metamorphisms (hydration followed by carbonation) are widely preserved in the peridotites and corroborated by the result of the phase diagram modelling. These conclusions apparently sound reasonable in the context of this study, it is nevertheless necessary to point out several points that could be ambiguous to reconcile with the conclusion in Chapter 4. The wet C- and B-type olivine fabrics are different from the dry A-/D-type olivine fabric in Chapter 4, while both peridotites are highly refractory and supposed to agree with an extremely dry condition. The wet condition required by the developments of C- and B-type olivine fabric thus implies an ambiguous hydration of process and likely imply a pre-existing dry A- or D-type olivine fabric which however has not been observed. In addition, the transition of olivine fabric from C- to B-type may not be definitive, because alternative explanation of activating C- and B-type olivine fabric simultaneously at different mantle conditions cannot be totally excluded. Therefore, even though some significant results have been obtained at this moment, more in-depth researches are still needed for solving these discrepancies prior to final submission.

REFERENCES

Abalos, B., Fountain, D. M., Ibarguchi, J. I. G., Puelles, P. (2011). Eclogite as a seismic marker in subduction channels: Seismic velocities, anisotropy, and petrofabric of Cabo Ortegal eclogite tectonites (Spain). *Geological Society of America Bulletin* **123**, 439-U477.

Abers, G. A. (2000). Hydrated subducted crust at 100–250 km depth. *Earth and Planetary Science Letters* **176**, 323-330.

Abily, B. & Ceuleneer, G. (2013). The dunitic mantle-crust transition zone in the Oman ophiolite: Residue of melt-rock interaction, cumulates from high-MgO melts, or both? *Geology* **41**, 67-70.

Abramson, E. H., Brown, J. M., Slutsky, L. J., Zaug, J. (1997). The elastic constants of San Carlos olivine to 17 GPa. *Journal of Geophysical Research: Solid Earth* **102**, 12253-12263.

Aleksandrov, K. S., Alchikov, U. V., Belikov, B. P., Zaslavskii, B. I., Krupnyi, A. I. (1974). Velocites of elastic waves in minerals at atmospheric pressure and increasing precision of elastic constants by mean of EVM. *Bulletin of the Academy of Sciences of the USSR, Geol. Ser.* **10**, 15-24.

Aleksandrov, K. S., Ryzhova, T. V., Belikov, B. P. (1964). The elastic properties of pyroxenes. *Soviet physics, crystallography* **8**, 589-591.

Angiboust, S., Agard, P., Jolivet, L., Beyssac, O. (2009). The Zermatt-Saas ophiolite: the largest (60-km wide) and deepest (c. 70–80 km) continuous slice of oceanic lithosphere detached from a subduction zone? *Terra Nova* **21**, 171-180.

Anglin, D. K. & Fouch, M. J. (2005). Seismic anisotropy in the Izu-Bonin subduction system. *Geophysical Research Letters* **32**, 1-4.

Arai, S. (1992). Chemistry of chromian spinel in volcanic-rocks as a potential guide to magma chemistry. *Mineralogical Magazine* **56**, 173-184.

Arai, S. (1994). Characterization of spinel peridotites by olivine-spinel compositional relationships: Review and interpretation. *Chemical Geology* **113**, 191-204.

Arai, S., Abe, N., Ishimaru, S. (2007). Mantle peridotites from the Western Pacific. *Gondwana Research* **11**, 180-199.

Arcay, D., Tric, E., Doin, M. P. (2005). Numerical simulations of subduction zones - Effect of slab dehydration on the mantle wedge dynamics. *Physics of the Earth and Planetary Interiors* **149**, 133-153.

Asimow, P. D., Stein, L. C., Mosenfelder, J. L., Rossman, G. R. (2006). Quantitative polarized infrared analysis of trace OH in populations of randomly oriented mineral grains. *American Mineralogist* **91**, 278-284.

Aubaud, C., Hauri, E. H., Hirschmann, M. M. (2004). Hydrogen partition coefficients between nominally anhydrous minerals and basaltic melts. *Geophysical Research Letters* **31**, 1-4.

Bédard, É., Hébert, R., Guilmette, C., Lesage, G., Wang, C. S., Dostal, J. (2009). Petrology and geochemistry of the Saga and Sangsang ophiolitic massifs, Yarlung Zangbo Suture Zone, Southern Tibet: Evidence for an arc–back-arc origin. *Lithos* **113**, 48-67.

Bachmann, F., Hielscher, R., Schaeben, H. (2010). Texture Analysis with MTEX – Free and Open Source Software Toolbox. *Solid State Phenomena* **160**, 63-68.

Bader, T., Zhang, L. F., Franz, L., Ratschbacher, L., de Capitani, C. (2012). The enigmatic Songshugou complex (Qinling orogen, central China): mélange of high-pressure and (ultra) high-temperature metamorphic rocks? *10th Swiss Geoscience Meeting*. Bern, 109-110.

Ballevre, M., Pitra, P., Bohn, M. (2003). Lawsonite growth in the epidote blueschists from the Ile de Groix (Armorican Massif, France): a potential geobarometer. *Journal of Metamorphic Geology* **21**, 723-735.

Ballhaus, C., Berry, R., Green, D. (1991a). High pressure experimental calibration of the olivine-orthopyroxene-spinel oxygen geobarometer: Implications for the oxidation state of the upper mantle. *Contributions to Mineralogy and Petrology* **107**, 27-40.

Ballhaus, C., Berry, R. F., Green, D. H. (1991b). High pressure experimental calibration of the olivine-orthopyroxene-spinel oxygen geobarometer: Implications for the oxidation state of the upper mantle. *Contributions to Mineralogy and Petrology* **107**, 27-40.

Baptiste, V., Tommasi, A., Demouchy, S. (2012). Deformation and hydration of the lithospheric mantle beneath the Kaapvaal craton, South Africa. *Lithos* **149**, 31-50.

Barnes, S. J. & Roger, P. L. (2001). The range of spinel compositions in terrestrial mafic and ultramafic rocks. *Journal of Petrology* **42**, 2279-2302.

Bascou, J., Barruol, G., Vauchez, A., Mainprice, D., Egydio-Silva, M. (2001). EBSD-measured lattice-preferred orientations and seismic properties of eclogites. *Tectonophysics* **342**, 61-80.

Bascou, J., Delpech, G., Vauchez, A., Moine, B. N., Cottin, J. Y., Barruol, G. (2008). An integrated study of microstructural, geochemical, and seismic properties of the lithospheric mantle above the Kerguelen plume (Indian Ocean). *Geochemistry Geophysics Geosystems* **9**, 1-26.

Bascou, J., Tommasi, A., Mainprice, D. (2002). Plastic deformation and development of clinopyroxene lattice preferred orientations in eclogites. *Journal of Structural Geology* **24**, 1357-1368.

Bass, J. D. (1989). Elasticity of grossular and spessartite garnets by Brillouin spectroscopy. *Journal of Geophysical Research: Solid Earth* **94**, 7621-7628.

Baur, W. H. (1978). Crystal structure refinement of lawsonite. *American Mineralogist* **63**, 311-315.

Behn, M. D., Hirth, G., Kelemen, P. B. (2007). Trench-parallel anisotropy produced by foundering of arc lower crust. *Science* **317**, 108-111.

Bell, D. R., Ihinger, P. D., Rossman, G. R. (1995). Quantitative analysis of trace OH in garnet and pyroxenes. *American Mineralogist* **80**, 465-474.

Bell, D. R., Rossman, G. R., Maldener, J., Endisch, D., Rauch, F. (2003). Hydroxide in olivine: A quantitative determination of the absolute amount and calibration of the IR spectrum. *Journal of Geophysical Research: Solid Earth* **108**, 1-9.

Ben Ismaïl, W. & Mainprice, D. (1998). An olivine fabric database: An overview of upper mantle fabrics and seismic anisotropy. *Tectonophysics* **296**, 145-157.

Berger, A. & Stunitz, H. (1996). Deformation mechanisms and reaction of hornblende: Examples from the Bergell tonalite (Central Alps). *Tectonophysics* **257**, 149-174.

Bezacier, L., Reynard, B., Bass, J. D., Sanchez-Valle, C., Van de Moortèle, B. (2010a). Elasticity of antigorite, seismic detection of serpentinites, and anisotropy in subduction zones. *Earth and Planetary Science Letters* **289**, 198-208.

Bezacier, L., Reynard, B., Bass, J. D., Wang, J., Mainprice, D. (2010b). Elasticity of glaucophane, seismic velocities and anisotropy of the subducted oceanic crust. *Tectonophysics* **494**, 201-210.

Bhagat, S. S., Bass, J. D., Smyth, J. R. (1992). Single-crystal elastic properties of omphacite-C2/c by Brillouin spectroscopy. *Journal of Geophysical Research: Solid Earth* **97**, 6843-6848.

Biermann, C. (1981). (100) Deformation twins in naturally deformed amphiboles. *Nature* **292**, 821-823.

Biermann, C. & Vanroermund, H. L. M. (1983). Defect structures in naturally deformed clinoamphiboles - a TEM study. *Tectonophysics* **95**, 267-278.

Bodinier, J. L. & Godard, M. (2007). 2.04 - Orogenic, Ophiolitic, and Abyssal Peridotites. In: Editors-in-Chief: Heinrich, D. H. & Karl, K. T. (eds.) *Treatise on Geochemistry*. Oxford: Pergamon, 1-73.

Bohm, M., Lüth, S., Echtler, H., Asch, G., Bataille, K., Bruhn, C., Rietbrock, A., Wigger, P. (2002). The Southern Andes between 36° and 40°S latitude: seismicity and average seismic velocities. *Tectonophysics* **356**, 275-289.

Bonatti, E. (1990). Subcontinental mantle exposed in the Atlantic Ocean on St Peter-Paul islets. *Nature* **345**, 800-802.

Bostock, M. G., Hyndman, R. D., Rondenay, S., Peacock, S. M. (2002). An inverted continental Moho and serpentinization of the forearc mantle. *Nature* **417**, 536-538.

Boudier, F., Baronnet, A., Mainprice, D. (2010). Serpentine mineral replacements of

natural olivine and their seismic implications: oceanic lizardite versus subduction-related antigorite. *Journal of Petrology* **51**, 495-512.

Brocher, T. M., Parsons, T., Tréhu, A. M., Snelson, C. M., Fisher, M. A. (2003). Seismic evidence for widespread serpentinized forearc upper mantle along the Cascadia margin. *Geology* **31**, 267-270.

Brownlee, S. J., Hacker, B. R., Harlow, G. E., Seward, G. (2013). Seismic signatures of a hydrated mantle wedge from antigorite crystal-preferred orientation (CPO). *Earth and Planetary Science Letters* **375**, 395-407.

Bunge, H. (1982). *Texture Analysis in Materials Science: Mathematical Models.* London: Butterworths.

Bystricky, M., Kunze, K., Burlini, L., Burg, J.-P. (2000). High shear strain of olivine aggregates: rheological and seismic consequences. *Science* **290**, 1564-1567.

Calvert, A. J. (2011). The seismic structure of island arc crust. *Arc-Continent Collision*: Springer Berlin Heidelberg, 87-119.

Cao, S. Y., Liu, J. L., Leiss, B. (2010). Orientation-related deformation mechanisms of naturally deformed amphibole in amphibolite mylonites from the Diancang Shan, SW Yunnan, China. *Journal of Structural Geology* **32**, 606-622.

Cao, Y., Jung, H., Song, S. (2014). Microstructures and petro-fabrics of lawsonite blueschist in the North Qilian suture zone, NW China: Implications for seismic anisotropy of subducting oceanic crust. *Tectonophysics* **628**, 140-157.

Cao, Y., Jung, H., Song, S. G. (2013). Petro-fabrics and seismic properties of blueschist and eclogite in the North Qilian suture zone, NW China: Implications for the low-velocity upper layer in subducting slab, trench-parallel seismic anisotropy, and eclogite detectability in the subduction zone. *Journal of Geophysical Research: Solid Earth* **118**, 3037-3058.

Cao, Y., Song, S. G., Niu, Y. L., Jung, H., Jin, Z. M. (2011). Variation of mineral composition, fabric and oxygen fugacity from massive to foliated eclogites during exhumation of subducted ocean crust in the North Qilian suture zone, NW China. *Journal of Metamorphic Geology* **29**, 699-720.

Carter, N. L. & Ave'Lallemant, H. G. (1970). High temperature flow of dunite and peridotite. *Geological Society of America Bulletin* **81**, 2181-2202.

Chai, M., Brown, J. M., Slutsky, L. J. (1997). The elastic constants of an aluminous orthopyroxene to 12.5 GPa. *Journal of Geophysical Research: Solid Earth* **102**, 14779-14785.

Chantel, J., Mookherjee, M., Frost, D. J. (2012). The elasticity of lawsonite at high pressure and the origin of low velocity layers in subduction zones. *Earth and Planetary Science Letters* **349–350**, 116-125.

Chen, D., Liu, L., Sun, Y., Zhang, A., Liu, X., Luo, J. (2004). LA-ICP-MS zircon U-Pb dating for high-pressure basic granulite from North Qinling and its geological

significance. *Chinese Science Bulletin* **49**, 2296-2304.

Chen, Z. H. (2004). The neoproterozoic tectono-thermal events in the Qinling orogen, and their geo-tectonic significances. Beijing: Chinese Academy of Geological Sciences.

Choi, S., Shervais, J., Mukasa, S. (2008). Supra-subduction and abyssal mantle peridotites of the Coast Range ophiolite, California. *Contributions to Mineralogy and Petrology* **156**, 551-576.

Christensen, N. I. & Mooney, W. D. (1995). Seismic velocity structure and composition of the continental crust: A global view. *Journal of Geophysical Research: Solid Earth* **100**, 9761-9788.

Clarke, G. L., Aitchison, J. C., Cluzel, D. (1997). Eclogites and blueschists of the Pam Peninsula, NE New Caledonia: a reappraisal. *Journal of Petrology* **38**, 843-876.

Collins, M. D. & Brown, J. M. (1998). Elasticity of an upper mantle clinopyroxene. *Physics and Chemistry of Minerals* **26**, 7-13.

Comodi, P. & Zanazzi, P. F. (1996). Effects of temperature and pressure on the structure of lawsonite. *American Mineralogist* **81**, 833-841.

Connolly, J. A. D. & Kerrick, D. M. (2002). Metamorphic controls on seismic velocity of subducted oceanic crust at 100–250 km depth. *Earth and Planetary Science Letters* **204**, 61-74.

Cordier, P., Demouchy, S., Beausir, B., Taupin, V., Barou, F., Fressengeas, C. (2014). Disclinations provide the missing mechanism for deforming olivine-rich rocks in the mantle. *Nature* **507**, 51-56.

Couvy, H., Frost, D. J., Heidelbach, F., Nyilas, K., Ungár, T., Mackwell, S., Cordier, P. (2004). Shear deformation experiments of forsterite at 11 GPa - 1400 °C in the multianvil apparatus. *European Journal of Mineralogy* **16**, 877-889.

Crawford, A. J. (1989). *Boninites*. London: Unwin Hyman.

Currie, C. A. & Hyndman, R. D. (2006). The thermal structure of subduction zone back arcs. *Journal of Geophysical Research: Solid Earth* **111**, B08404.

Díaz Aspiroz, M., Lloyd, G. E., Fernández, C. (2007). Development of lattice preferred orientation in clinoamphiboles deformed under low-pressure metamorphic conditions. A SEM/EBSD study of metabasites from the Aracena metamorphic belt (SW Spain). *Journal of Structural Geology* **29**, 629-645.

Dai, J.-G., Wang, C.-S., Hébert, R., Santosh, M., Li, Y.-L., Xu, J.-Y. (2011). Petrology and geochemistry of peridotites in the Zhongba ophiolite, Yarlung Zangbo Suture Zone: Implications for the Early Cretaceous intra-oceanic subduction zone within the Neo-Tethys. *Chemical Geology* **288**, 133-148.

Dan, W., Li, X.-H., Guo, J., Liu, Y., Wang, X.-C. (2012). Paleoproterozoic evolution of the eastern Alxa Block, westernmost North China: Evidence from in situ zircon

U–Pb dating and Hf–O isotopes. *Gondwana Research* **21**, 838-864.

Dare, S. A. S., Pearce, J. A., McDonald, I., Styles, M. T. (2009). Tectonic discrimination of peridotites using fO2–Cr# and Ga–Ti–FeIII systematics in chrome–spinel. *Chemical Geology* **261**, 199-216.

Davey, F. J. & Ristau, J. (2011). Fore-arc mantle wedge seismicity under northeast New Zealand. *Tectonophysics* **509**, 272-279.

Davis, P. B. & Whitney, D. L. (2006). Petrogenesis of lawsonite and epidote eclogite and blueschist, Sivrihisar Massif, Turkey. *Journal of Metamorphic Geology* **24**, 823-849.

Deer, W. A., Howie, R. A., Zussman, J. (1966). *An Introduction to the Rock-Forming Minerals*. London: Longmans.

Demouchy, S., Jacobsen, S. D., Gaillard, F., Stern, C. R. (2006). Rapid magma ascent recorded by water diffusion profiles in mantle olivine. *Geology* **34**, 429-432.

Demouchy, S., Mussi, A., Barou, F., Tommasi, A., Cordier, P. (2014). Viscoplasticity of polycrystalline olivine experimentally deformed at high pressure and 900 ℃. *Tectonophysics* **623**, 123-135.

Denis, C. M. M., Demouchy, S., Shaw, C. S. J. (2013). Evidence of dehydration in peridotites from Eifel Volcanic Field and estimates of the rate of magma ascent. *Journal of Volcanology and Geothermal Research* **258**, 85-99.

DeShon, H. R. & Schwartz, S. Y. (2004). Evidence for serpentinization of the forearc mantle wedge along the Nicoya Peninsula, Costa Rica. *Geophysical Research Letters* **31**, L21611.

Di Leo, J. F., Walker, A. M., Li, Z. H., Wookey, J., Ribe, N. M., Kendall, J. M., Tommasi, A. (2014). Development of texture and seismic anisotropy during the onset of subduction. *Geochemistry, Geophysics, Geosystems* **15**, 192-212.

Dick, H. B. & Bullen, T. (1984). Chromian spinel as a petrogenetic indicator in abyssal and alpine-type peridotites and spatially associated lavas. *Contributions to Mineralogy and Petrology* **86**, 54-76.

Dick, H. J. B. (1989). Abyssal peridotites, very slow spreading ridges and ocean ridge magmatism. *Journal of Geological Society, London, Special Publications* **42**, 71-105.

Dick, H. J. B. & Fisher, R. L. (1984). Mineralogic studies of the residues of mantle melting: Abyssal and alpine-type peridotites. In: Kornprobst, J. (ed.) *Kimberlites II. The Mantle and Crust-Mantle Relationships*. Amsterdam: Elsevier, 298-308.

Dijkstra, A. H., Drury, M. R., Vissers, R. L. M., Newman, J., Van Roermund, H. L. M. (2004). Shear zones in the upper mantle: evidence from alpine- and ophiolite-type peridotite massifs. *Geological Society, London, Special Publications* **224**, 11-24.

Dollinger, G. & Blacic, J. D. (1975). Deformation mechanisms in experimentally and

naturally deformed amphiboles. *Earth and Planetary Science Letters* **26**, 409-416.

Dong, Y.-P., Zhou, M.-F., Zhang, G.-W., Zhou, D.-W., Liu, L., Zhang, Q. (2008). The Grenvillian Songshugou ophiolite in the Qinling Mountains, Central China: Implications for the tectonic evolution of the Qinling orogenic belt. *Journal of Asian Earth Sciences* **32**, 325-335.

Eberhart-Phillips, D., Christensen, D. H., Brocher, T. M., Hansen, R., Ruppert, N. A., Haeussler, P. J., Abers, G. A. (2006). Imaging the transition from Aleutian subduction to Yakutat collision in central Alaska, with local earthquakes and active source data. *Journal of Geophysical Research: Solid Earth* **111**, B11303.

Edwards, S. J. & Malpas, J. (1995). Multiple origins for mantle harzburgites: examples from the Lewis Hills, Bay of Islands ophiolite, Newfoundland. *Canadian Journal of Earth Sciences* **32**, 1046-1057.

Evans, B. W. (1990). Phase relations of epidote-blueschists. *Lithos* **25**, 3-23.

Evans, K. A., Elburg, M. A., Kamenetsky, V. S. (2012). Oxidation state of subarc mantle. *Geology* **40**, 783-786.

Eyuboglu, Y., Dilek, Y., Bozkurt, E., Bektas, O., Rojay, B., Sen, C. (2010). Structure and geochemistry of an Alaskan-type ultramafic–mafic complex in the Eastern Pontides, NE Turkey. *Gondwana Research* **18**, 230-252.

Fabriès, J. (1979). Spinel-olivine geothermometry in peridotites from ultramafic complexes. *Contributions to Mineralogy and Petrology* **69**, 329-336.

Faccenda, M., Burlini, L., Gerya, T. V., Mainprice, D. (2008). Fault-induced seismic anisotropy by hydration in subducting oceanic plates. *Nature* **455**, 1097-U1098.

Faccenda, M. & Capitanio, F. A. (2012). Development of mantle seismic anisotropy during subduction-induced 3-D flow. *Geophysical Research Letters* **39**, L11305.

Fallon, T. J. & Danyushevsky, L. V. (2000). Melting of refractory mantle at 1.5, 2 and 2.5 GPa under anhydrous and H_2O-undersaturated conditions: Implications for the petrogenesis of high-Ca boninites and the influence of subduction components on mantle melting. *Journal of Petrology* **41**, 257-283.

Falus, G., Tommasi, A., Ingrin, J., Szabo, C. (2008). Deformation and seismic anisotropy of the lithospheric mantle in the southeastern Carpathians inferred from the study of mantle xenoliths. *Earth and Planetary Science Letters* **272**, 50-64.

Falus, G., Tommasi, A., Soustelle, V. (2011). The effect of dynamic recrystallization on olivine crystal preferred orientations in mantle xenoliths deformed under varied stress conditions. *Journal of Structural Geology* **33**, 1528-1540.

Fischer, J. K., Poli, S., Fumagalli, P. (2008). The effects of Cr solubility in chlorites and its implications for Cr-clinochlore stability. *12th International Conference on Experimental Mineralogy, Petrology and Geochemistry September 7th - 10th 2008*. Innsbruck: Innsbruck University Press, 23 - 23.

Forbes, R. B., Evans, B. W., Thurston, S. P. (1984). Regional progressive high-pressure metamorphism, Seward Peninsula, Alaska. *Journal of Metamorphic Geology* **2**, 43-54.

Forneris, J. F. & Holloway, J. R. (2003). Phase equilibria in subducting basaltic crust: implications for H(2)O release from the slab. *Earth and Planetary Science Letters* **214**, 187-201.

Fountain, D. M., Boundy, T. M., Austrheim, H., Rey, P. (1994). Eclogite-facies shear zones--deep crustal reflectors? *Tectonophysics* **232**, 411-424.

Frese, K., Trommsdorff, V., Kunze, K. (2003). Olivine [100] normal to foliation: lattice preferred orientation in prograde garnet peridotite formed at high H2O activity, Cima di Gagnone (Central Alps). *Contributions to Mineralogy and Petrology* **145**, 75-86.

Frets, E., Tommasi, A., Garrido, C. J., Padron-Navarta, J. A., Amri, I., Targuisti, K. (2012). Deformation processes and rheology of pyroxenites under lithospheric mantle conditions. *Journal of Structural Geology* **39**, 138-157.

Frets, E. C., Tommasi, A., Garrido, C. J., Vauchez, A., Mainprice, D., Targuisti, K., Amri, I. (2014). The Beni Bousera peridotite (Rif Belt, Morocco): an oblique-slip low-angle shear zone thinning the subcontinental mantle lithosphere. *Journal of Petrology* **55**, 283-313.

Fujie, G., Kodaira, S., Yamashita, M., Sato, T., Takahashi, T., Takahashi, N. (2013). Systematic changes in the incoming plate structure at the Kuril trench. *Geophysical Research Letters* **40**, 88-93.

Fujimoto, Y., Kono, Y., Hirajima, T., Kanagawa, K., Ishikawa, M., Arima, M. (2010). P-wave velocity and anisotropy of lawsonite and epidote blueschists: Constraints on water transportation along subducting oceanic crust. *Physics of the Earth and Planetary Interiors* **183**, 219-228.

Gaetani, G. A. & Grove, T. L. (1998). The influence of water on melting of mantle peridotite. *Contributions to Mineralogy and Petrology* **131**, 323-346.

Gao, Klemd, Zhang, Wang, Xiao. (1999). P–T path of high-pressure/low-temperature rocks and tectonic implications in the western Tianshan Mountains, NW China. *Journal of Metamorphic Geology* **17**, 621-636.

Gay, N. C. (1968). Pure shear and simple shear deformation of inhomogeneous viscous fluids. 1. Theory. *Tectonophysics* **5**, 211-234.

Ghent, E. D., Stout, M. Z., Erdmer, P. (1993). Pressure–temperature evolution of lawsonite-bearing eclogites, Pinchi Lake, British Columbia. *Journal of Metamorphic Geology* **11**, 279-290.

Gifkins, R. C. (1970). *Optical Microscopy of Metals*. New York: Elsevier.

Gose, J., Schmädicke, E., Beran, A. (2009). Water in enstatite from Mid-Atlantic Ridge peridotite: Evidence for the water content of suboceanic mantle? *Geology* **37**, 543-

546.

Grant, K., Ingrin, J., Lorand, J., Dumas, P. (2007a). Water partitioning between mantle minerals from peridotite xenoliths. *Contributions to Mineralogy and Petrology* **154**, 15-34.

Grant, K. J., Kohn, S. C., Brooker, R. A. (2007b). The partitioning of water between olivine, orthopyroxene and melt synthesised in the system albite-forsterite-H2O. *Earth and Planetary Science Letters* **260**, 227-241.

Hacker, B. R. & Abers, G. A. (2012). Subduction Factory 5: Unusually low Poisson's ratios in subduction zones from elastic anisotropy of peridotite. *Journal of Geophysical Research: Solid Earth* **117**.

Hacker, B. R., Abers, G. A., Peacock, S. M. (2003a). Subduction factory - 1. Theoretical mineralogy, densities, seismic wave speeds, and H2O contents. *Journal of Geophysical Research: Solid Earth* **108**, 1-26.

Hacker, B. R., Peacock, S. M., Abers, G. A., Holloway, S. D. (2003b). Subduction factory 2: Are intermediate-depth earthquakes in subducting slabs linked to metamorphic dehydration reactions? *Journal of Geophysical Research: Solid Earth* **108**, 1-16.

Hansen, L. N., Cheadle, M. J., John, B. E., Swapp, S. M., Dick, H. J. B., Tucholke, B. E., Tivey, M. A. (2013). Mylonitic deformation at the Kane oceanic core complex: Implications for the rheological behavior of oceanic detachment faults. *Geochemistry Geophysics Geosystems* **14**, 3085-3108.

Hansen, L. N., Zhao, Y. H., Zimmerman, M. E., Kohlstedt, D. L. (2014). Protracted fabric evolution in olivine: Implications for the relationship among strain, crystallographic fabric, and seismic anisotropy. *Earth and Planetary Science Letters* **387**, 157-168.

Hansen, L. N., Zimmerman, M. E., Kohlstedt, D. L. (2011). Grain boundary sliding in San Carlos olivine: Flow law parameters and crystallographic-preferred orientation. *Journal of Geophysical Research: Solid Earth* **116**, B08201.

Hansen, L. N., Zimmerman, M. E., Kohlstedt, D. L. (2012). The influence of microstructure on deformation of olivine in the grain-boundary sliding regime. *Journal of Geophysical Research: Solid Earth* **117**, B09201.

Hao, Y., Xia, Q., Li, Q., Chen, H., Feng, M. (2014). Partial melting control of water contents in the Cenozoic lithospheric mantle of the Cathaysia block of South China. *Chemical Geology*.

Harigane, Y., Michibayashi, K., Morishita, T., Tani, K., Dick, H. J. B., Ishizuka, O. (2013). The earliest mantle fabrics formed during subduction zone infancy. *Earth and Planetary Science Letters* **377**, 106-113.

Harigane, Y., Mizukami, T., Morishita, T., Michibayashi, K., Abe, N., Hirano, N. (2011). Direct evidence for upper mantle structure in the NW Pacific Plate: Microstructural analysis of a petit-spot peridotite xenolith. *Earth and Planetary*

Science Letters **302**, 194-202.

Hasegawa, A., Horiuchi, S., Umino, N. (1994). Seismic structure of the northeastern Japan convergent margin: A synthesis. *Journal of Geophysical Research: Solid Earth* **99**, 22295-22311.

Hauri, E. H., Gaetani, G. A., Green, T. H. (2006). Partitioning of water during melting of the Earth's upper mantle at H2O-undersaturated conditions. *Earth and Planetary Science Letters* **248**, 715-734.

Healy, D., Reddy, S. M., Timms, N. E., Gray, E. M., Brovarone, A. V. (2009). Trench-parallel fast axes of seismic anisotropy due to fluid-filled cracks in subducting slabs. *Earth and Planetary Science Letters* **283**, 75-86.

Hellebrand, E., Snow, J. E., Dick, H. J. B., Hofmann, A. W. (2001). Coupled major and trace elements as indicators of the extent of melting in mid-ocean-ridge peridotites. *Nature* **410**, 677-681.

Helmstaedt, H., Anderson, O. L., Gavasci, A. T. (1972). Petrofabric studies of eclogite, spinel-websterite, and spinel-herzolite xenoliths from kimberlite-bearing breccia pipes in southeastern Utah and northeastern Arizona. *Journal of Geophysical Research* **77**, 4350-4365.

Henry, D. J. & Medaris, L. G. (1980). Application of pyroxene and olivine-spinel geothermometers to spinel peridotites in southwestern Oregon. *American Journal of Science* **280**, 211-231.

Higgie, K. & Tommasi, A. (2012). Feedbacks between deformation and melt distribution in the crust–mantle transition zone of the Oman ophiolite. *Earth and Planetary Science Letters* **359-360**, 61-72.

Higgie, K. & Tommasi, A. (2014). Deformation in a partially molten mantle: Constraints from plagioclase lherzolites from Lanzo, western Alps. *Tectonophysics* **615-616**, 167-181.

Hilairet, N., Reynard, B., Wang, Y., Daniel, I., Merkel, S., Nishiyama, N., Petitgirard, S. (2007). High-pressure creep of serpentine, interseismic deformation, and initiation of subduction. *Science* **318**, 1910-1913.

Hirauchi, K.-i. & Katayama, I. (2013). Rheological contrast between serpentine species and implications for slab–mantle wedge decoupling. *Tectonophysics* **608**, 545-551.

Hirauchi, K., Michibayashi, K., Ueda, H., Katayama, I. (2010). Spatial variations in antigorite fabric across a serpentinite subduction channel: Insights from the Ohmachi Seamount, Izu-Bonin frontal arc. *Earth and Planetary Science Letters* **299**, 196-206.

Hirschmann, M. M. (2006). Water, melting, and the deep Earth H_2O cycle. *Annual Review of Earth and Planetary Sciences* **34**, 629-653.

Hirth, G. & Kohlstedt, D. L. (1995a). Experimental constraints on the dynamics of the partially molten upper mantle: 2. Deformation in the dislocation creep regime.

Journal of Geophysical Research: Solid Earth **100**, 15441-15449.

Hirth, G. & Kohlstedt, D. L. (1995b). Experimental constraints on the dynamics of the partially molten upper mantle: Deformation in the diffusion creep regime. *Journal of Geophysical Research: Solid Earth* **100**, 1981-2001.

Holland, T. J. B. & Powell, R. (1998). An internally consistent thermodynamic data set for phases of petrological interest. *Journal of Metamorphic Geology* **16**, 309-343.

Holtzman, B. K., Groebner, N. J., Zimmerman, M. E., Ginsberg, S. B., Kohlstedt, D. L. (2003). Stress-driven melt segregation in partially molten rocks. *Geochemistry Geophysics Geosystems* **4**, 1-26.

Holtzman, B. K. & Kohlstedt, D. L. (2007). Stress-driven melt segregation and strain partitioning in partially molten rocks: Effects of stress and strain. *Journal of Petrology* **48**, 2379-2406.

Horine, R. L., Moore, G. F., Taylor, B. (1990). 5. Structure of the outer Izu-Bonin forearc from seismic-reflection profiling and modeling. *Proceedings of the Ocean Drilling Program, Initial Reports* **125**, 81-94.

Huang, Z., Zhao, D., Wang, L. (2011a). Shear wave anisotropy in the crust, mantle wedge, and subducting Pacific slab under northeast Japan. *Geochemistry Geophysics Geosystems* **12**, Q01002.

Huang, Z., Zhao, D., Wang, L. (2011b). Shear wave anisotropy in the crust, mantle wedge, and subducting Pacific slab under northeast Japan. *Geochemistry Geophysics Geosystems* **12**, Q01002.

Hyndman, R. D. & Peacock, S. M. (2003). Serpentinization of the forearc mantle. *Earth and Planetary Science Letters* **212**, 417-432.

Iidaka, T., Muto, J., Obara, K., Igarashi, T., Shibazaki, B. (2014). Trench-parallel crustal anisotropy along the trench in the fore-arc region of Japan. *Geophysical Research Letters* **41**, 1957-1963.

Ildefonse, B., Lardeaux, J.-M., Caron, J.-M. (1990). The behavior of shape preferred orientations in metamorphic rocks: amphiboles and jadeites from the Monte Mucrone area (Sesia-Lanzo zone, Italian Western Alps). *Journal of Structural Geology* **12**, 1005-1011.

Imon, R., Okudaira, T., Fujimoto, A. (2002). Dissolution and precipitation processes in deformed amphibolites: an example from the ductile shear zone of the Ryoke metamorphic belt, SW Japan. *Journal of Metamorphic Geology* **20**, 297-308.

Imon, R., Okudaira, T., Kanagawa, K. (2004). Development of shape- and lattice-preferred orientations of amphibole grains during initial cataclastic deformation and subsequent deformation by dissolution–precipitation creep in amphibolites from the Ryoke metamorphic belt, SW Japan. *Journal of Structural Geology* **26**, 793-805.

Ingrin, J. & Skogby, H. (2000). Hydrogen in nominally anhydrous upper-mantle

minerals: concentration levels and implications. *European Journal of Mineralogy* **12**, 543-570.

Ionov, D. A. (2010). Petrology of mantle wedge lithosphere: new data on supra-subduction zone peridotite xenoliths from the andesitic Avacha Volcano, Kamchatka. *Journal of Petrology* **51**, 327-361.

Ishii, T., Robinson, P. T., H., M., Fiske, R. (1992). 27. Petrological studies of peridotites from diapiric serpentinite seamounts in the Izu-Ogasawara-Mariana forearc, Leg 125. *Proceedings of the Ocean Drilling Program, Scientific Results* **125**, 445-485.

Ishikawa, A., Kaneko, Y., Kadarusman, A., Ota, T. (2007). Multiple generations of forearc mafic–ultramafic rocks in the Timor–Tanimbar ophiolite, eastern Indonesia. *Gondwana Research* **11**, 200-217.

Ishiwatari, A. (1985). Igneous petrogenesis of the Yakuno ophiolite (Japan) in the context of the diversity of ophiolites. *Contributions to Mineralogy and Petrology* **89**, 155-167.

Jaques, A. L. & Green, D. H. (1980). Anhydrous melting of peridotite at 0–15 Kb pressure and the genesis of tholeiitic basalts. *Contributions to Mineralogy and Petrology* **73**, 287-310.

Ji, S., Li, A., Wang, Q., Long, C., Wang, H., Marcotte, D., Salisbury, M. (2013). Seismic velocities, anisotropy, and shear-wave splitting of antigorite serpentinites and tectonic implications for subduction zones. *Journal of Geophysical Research: Solid Earth* **118**, 1015-1037.

Ji, S., Salisbury, M. H., Hanmer, S. (1993). Petrofabric, P-wave anisotropy and seismic reflectivity of high-grade tectonites. *Tectonophysics* **222**, 195-226.

Johnson, S. E., Lenferink, H. J., Price, N. A., Marsh, J. H., Koons, P. O., West Jr, D. P., Beane, R. (2009). Clast-based kinematic vorticity gauges: The effects of slip at matrix/clast interfaces. *Journal of Structural Geology* **31**, 1322-1339.

Jung, H. (2009). Deformation fabrics of olivine in Val Malenco peridotite found in Italy and implications for the seismic anisotropy in the upper mantle. *Lithos* **109**, 341-349.

Jung, H. (2011). Seismic anisotropy produced by serpentine in mantle wedge. *Earth and Planetary Science Letters* **307**, 535-543.

Jung, H., Fei, Y., Silver, P. G., Green Ii, H. W. (2009a). Frictional sliding in serpentine at very high pressure. *Earth and Planetary Science Letters* **277**, 273-279.

Jung, H., Green II, H. W., Dobrzhinetskaya, L. F. (2004). Intermediate-depth earthquake faulting by dehydration embrittlement with negative volume change. *Nature* **428**, 545-549.

Jung, H. & Karato, S. (2001a). Water-induced fabric transitions in olivine. *Science* **293**, 1460-1463.

Jung, H. & Karato, S. I. (2001b). Effects of water on dynamically recrystallized grain-size of olivine. *Journal of Structural Geology* **23**, 1337-1344.

Jung, H., Katayama, I., Jiang, Z., Hiraga, I., Karato, S. (2006). Effect of water and stress on the lattice-preferred orientation of olivine. *Tectonophysics* **421**, 1-22.

Jung, H., Lee, J., Ko, B., Jung, S., Park, M., Cao, Y., Song, S. G. (2013). Natural type-C olivine fabrics in garnet peridotites in North Qaidam UHP collision belt, NW China. *Tectonophysics* **594**, 91-102.

Jung, H., Mo, W., Choi, S. H. (2009b). Deformation microstructures of olivine in peridotite from Spitsbergen, Svalbard and implications for seismic anisotropy. *Journal of Metamorphic Geology* **27**, 707-720.

Jung, H., Mo, W., Green, H. W. (2009c). Upper mantle seismic anisotropy resulting from pressure-induced slip transition in olivine. *Nature Geoscience* **2**, 73-77.

Jung, H., Park, M., Jung, S., Lee, J. (2010). Lattice preferred orientation, water content, and seismic anisotropy of orthopyroxene. *Journal of Earth Science* **21**, 555-568.

Jung, S., Jung, H., Austrheim, H. (2014). Characterization of olivine fabrics and mylonite in the presence of fluid and implications for seismic anisotropy and shear localization. *Earth, Planets and Space* **66**, 46.

Kaczmarek, M.-A. & Tommasi, A. (2011). Anatomy of an extensional shear zone in the mantle, Lanzo massif, Italy. *Geochemistry Geophysics Geosystems* **12**, Q0AG06.

Kaczmarek, M. A. & Reddy, S. M. (2013). Mantle deformation during rifting: Constraints from quantitative microstructural analysis of olivine from the East African Rift (Marsabit, Kenya). *Tectonophysics* **608**, 1122-1137.

Kamei, A., Obata, M., Michibayashi, K., Hirajima, T., Svojtka, M. (2010). Two contrasting fabric patterns of olivine observed in garnet and spinel peridotite from a mantle-derived ultramafic mass enclosed in felsic granulite, the Moldanubian zone, Czech Republic. *Journal of Petrology* **51**, 101-123.

Kamenetsky, V. S., Crawford, A. J., Meffre, S. (2001). Factors controlling chemistry of magmatic spinel: An empirical study of associated olivine, Cr-spinel and melt Inclusions from primitive rocks. *Journal of Petrology* **42**, 655-671.

Kamiya, S. i. & Kobayashi, Y. (2000). Seismological evidence for the existence of serpentinized wedge mantle. *Geophysical Research Letters* **27**, 819-822.

Kandelin, J. & Weidner, D. J. (1988). The single-crystal elastic properties of jadeite. *Physics of the Earth and Planetary Interiors* **50**, 251-260.

Karato, S.-i., Toriumi, M., Fujii, T. (1980). Dynamic recrystallization of olivine single crystals during high-temperature creep. *Geophysical Research Letters* **7**, 649-652.

Karato, S. (1987). Scanning electron microscope observation of dislocations in olivine. *Physics and Chemistry of Minerals* **14**, 245-248.

Karato, S. & Jung, H. (2003). Effects of pressure on high-temperature dislocation creep in olivine. *Philosophical Magazine* **83**, 401-414.

Karato, S., Jung, H., Katayama, I., Skemer, P. (2008). Geodynamic significance of seismic anisotropy of the upper mantle: New insights from laboratory studies. *Annual Review of Earth and Planetary Sciences* **36**, 59-95.

Katayama, I., Hirauchi, K., Michibayashi, K., Ando, J. (2009). Trench-parallel anisotropy produced by serpentine deformation in the hydrated mantle wedge. *Nature* **461**, 1114-1117.

Katayama, I., Jung, H., Karato, S. I. (2004). New type of olivine fabric from deformation experiments at modest water content and low stress. *Geology* **32**, 1045-1048.

Katayama, I. & Karato, S. (2006). Effect of temperature on the B- to C-type olivine fabric transition and implication for flow pattern in subduction zones. *Physics of the Earth and Planetary Interiors* **157**, 33-45.

Katayama, I., Karato, S. I., Brandon, M. (2005). Evidence of high water content in the deep upper mantle inferred from deformation microstructures. *Geology* **33**, 613-616.

Katayama, I., Michibayashi, K., Terao, R., Ando, J. I., Komiya, T. (2011). Water content of the mantle xenoliths from Kimberley and implications for explaining textural variations in cratonic roots. *Geological Journal* **46**, 173-182.

Kelemen, P. B., Dick, H. J. B., Quick, J. E. (1992). Formation of harzburgite by pervasive melt/rock reaction in the upper mantle. *Nature* **358**, 635-641.

Kelemen, P. B., Shimizu, N., Salters, V. J. M. (1995). Extraction of mid-ocean-ridge basalt from the upwelling mantle by focused flow of melt in dunite channels. *Nature* **375**, 747-753.

Keppler, H. & Bolfan-Casanova, N. (2006). Thermodynamics of water solubility and partitioning. *Water in Nominally Anhydrous Minerals*, 193-230.

Kern, H., Gao, S., Jin, Z. M., Popp, T., Jin, S. Y. (1999). Petrophysical studies on rocks from the Dabie ultrahigh-pressure (UHP) metamorphic belt, Central China: implications for the composition and delamination of the lower crust. *Tectonophysics* **301**, 191-215.

Kern, H., Jin, Z., Gao, S., Popp, T., Xu, Z. (2002). Physical properties of ultrahigh-pressure metamorphic rocks from the Sulu terrain, eastern central China: implications for the seismic structure at the Donghai (CCSD) drilling site. *Tectonophysics* **354**, 315-330.

Kim, D. & Jung, H. (2014). Deformation microstructures of olivine and chlorite in chlorite peridotites from Almklovdalen in the Western Gneiss Region, SW Norway and implications for seismic anisotropy. *International Geology Review* **in press**.

Kim, D., Katayama, I., Michibayashi, K., Tsujimori, T. (2013a). Deformation fabrics

of natural blueschists and implications for seismic anisotropy in subducting oceanic crust. *Physics of the Earth and Planetary Interiors* **222**, 8-21.

Kim, D., Katayama, I., Michibayashi, K., Tsujimori, T. (2013b). Rheological contrast between glaucophane and lawsonite in naturally deformed blueschist from Diablo Range, California. *Island Arc* **22**, 63-73.

Kim, J. & Jacobi, R. D. (2002). Boninites: characteristics and tectonic constraints, northeastern Appalachians. *Physics and Chemistry of the Earth* **27**, 109-147.

Kim, Y., Clayton, R. W., Asimow, P. D., Jackson, J. M. (2013c). Generation of talc in the mantle wedge and its role in subduction dynamics in central Mexico. *Earth and Planetary Science Letters* **384**, 81-87.

Kim, Y., Clayton, R. W., Jackson, J. M. (2012). Distribution of hydrous minerals in the subduction system beneath Mexico. *Earth and Planetary Science Letters* **341**, 58-67.

Kimball, K. (1990). Effects of hydrothermal alteration on the compositions of chromian spinels. *Contributions to Mineralogy and Petrology* **105**, 337-346.

Kirby, S., Engdahl, R. E., Denlinger, R. (1996). Intermediate-depth intraslab earthquakes and arc volcanism as physical expressions of crustal and uppermost mantle metamorphism in subducting slabs. *Subduction Top to Bottom*. Washington, DC: AGU, 195-214.

Klemme, S. (2004). The influence of Cr on the garnet–spinel transition in the Earth's mantle: experiments in the system $MgO–Cr_2O_3–SiO_2$ and thermodynamic modelling. *Lithos* **77**, 639-646.

Kneller, E. A., Long, M. D., van Keken, P. E. (2008). Olivine fabric transitions and shear wave anisotropy in the Ryukyu subduction system. *Earth and Planetary Science Letters* **268**, 268-282.

Kneller, E. A. & van Keken, P. E. (2007). Trench-parallel flow and seismic anisotropy in the Mariana and Andean subduction systems. *Nature* **450**, 1222-1225.

Kneller, E. A., van Keken, P. E., Karato, S., Park, J. (2005). B-type olivine fabric in the mantle wedge: Insights from high-resolution non-Newtonian subduction zone models. *Earth and Planetary Science Letters* **237**, 781-797.

Kneller, E. A., van Keken, P. E., Katayama, I., Karato, S. (2007). Stress, strain, and B-type olivine fabric in the fore-arc mantle: Sensitivity tests using high-resolution steady-state subduction zone models. *Journal of Geophysical Research: Solid Earth* **112**.

Koga, K., Hauri, E., Hirschmann, M., Bell, D. (2003). Hydrogen concentration analyses using SIMS and FTIR: Comparison and calibration for nominally anhydrous minerals. *Geochemistry Geophysics Geosystems* **4**, 1-20.

Kohlstedt, D. L. (2002). Partial melting and deformation. *Plastic Deformation of Minerals and Rocks* **51**, 121-135.

Kohlstedt, D. L., Goetze, C., Durham, W. B., Sande, J. V. (1976). New technique for decorating dislocations in olivine. *Science* **191**, 1045-1046.

Kohlstedt, D. L. & Holtzman, B. K. (2009). Shearing melt out of the Earth: An experimentalist's perspective on the influence of deformation on melt extraction. *Annual Review of Earth and Planetary Sciences* **37**, 561-593.

Kohn, S. C. & Grant, K. J. (2006). The partitioning of water between nominally anhydrous minerals and silicate melts. *Reviews in Mineralogy and Geochemistry* **62**, 231-241.

Kohn, S. C., Roome, B. M., Smith, M. E., Howes, A. P. (2005). Testing a potential mantle geohygrometer: the effect of dissolved water on the intracrystalline partitioning of Al in orthopyroxene. *Earth and Planetary Science Letters* **238**, 342-350.

Kovács, I., Hermann, J., O'Neill, H. S. C., Gerald, J. F., Sambridge, M., Horváth, G. (2008). Quantitative absorbance spectroscopy with unpolarized light: Part II. Experimental evaluation and development of a protocol for quantitative analysis of mineral IR spectra. *American Mineralogist* **93**, 765-778.

Law, R. D., Searle, M. P., Simpson, R. L. (2004). Strain, deformation temperatures and vorticity of flow at the top of the Greater Himalayan Slab, Everest Massif, Tibet. *Journal of the Geological Society* **161**, 305-320.

Le Roux, V., Tommasi, A., Vauchez, A. (2008). Feedback between melt percolation and deformation in an exhumed lithosphere–asthenosphere boundary. *Earth and Planetary Science Letters* **274**, 401-413.

Le Voci, G., Davies, D. R., Goes, S., Kramer, S. C., Wilson, C. R. (2014a). A systematic 2-D investigation into the mantle wedge's transient flow regime and thermal structure: Complexities arising from a hydrated rheology and thermal buoyancy. *Geochemistry, Geophysics, Geosystems* **15**, 28-51.

Le Voci, G., Davies, D. R., Goes, S., Kramer, S. C., Wilson, C. R. (2014b). A systematic 2-D investigation into the mantle wedge's transient flow regime and thermal structure: Complexities arising from a hydrated rheology and thermal buoyancy. *Geochemistry Geophysics Geosystems* **15**, 28-51.

Lee, B., Zhu, L. M., Gong, H. J., Guo, B., Yang, T., Wang, F., Wang, W., Xu, A. (2010). Genetic relationship between peridotites and chromite deposit from Songshugou area of North Qinling. *Acta Petrologica Sinica* **26**, 1487-1502.

Levien, L., Weidner, D., Prewitt, C. (1979). Elasticity of diopside. *Physics and Chemistry of Minerals* **4**, 105-113.

Li, H. Y., Liu, J. F., Yang, L. (2009). Characteristics of zircons from a metamorphic contact zone of the Songshugou ultramafic pluton in North Qinling and their geological significance. *Acta Petrologica Sinica* **28**, 225-234.

Li, S. G., Chen, Y. Z., Zhang, G. W., Zhang, Z. Q. (1991). A 1 Ga B.P. Alpine peridotite body emplaced into the Qinling group: Evidence for the existence of the late

proterozoic plate tectonics in the north Qinling area. *Geological Review* **37**, 235-242.

Li, Y. J. (2010). Transition between blueschist and low-T eclogite facies from the North Qilian Orogen, NW China. *Department of Geology*: Peking University, 72.

Li, Z.-H., Di Leo, J. F., Ribe, N. M. (2014). Subduction-induced mantle flow, finite strain and seismic anisotropy: Numerical modeling. *Journal of Geophysical Research: Solid Earth*, 2014JB010996.

Li, Z.-X. A., Lee, C.-T. A., Peslier, A. H., Lenardic, A., Mackwell, S. J. (2008). Water contents in mantle xenoliths from the Colorado Plateau and vicinity: Implications for the mantle rheology and hydration-induced thinning of continental lithosphere. *Journal of Geophysical Research: Solid Earth* **113**, B09210.

Libowitzky, E. & Armbruster, T. (1995). Low-temperature phase transitions and role of hydrogen bonds in lawsonite. *American Mineralogist* **80**, 1277-1285.

Lin, C.-H., Huang, B.-S., Rau, R.-J. (1999). Seismological evidence for a low-velocity layer within the subducted slab of southern Taiwan. *Earth and Planetary Science Letters* **174**, 231-240.

Lin, S.-C. & Kuo, B.-Y. (2013). Trench-parallel flow in the southern Ryukyu subduction system: Effects of progressive rifting of the overriding plate. *Journal of Geophysical Research: Solid Earth* **118**, 302-315.

Liou, J. G., Wang, X. M., Coleman, R. G., Zhang, Z. M., Maruyama, S. (1989). Blueschists in major suture zones of China. *Tectonics* **8**, 609-619.

Liou, J. G., Zhang, R. Y., Ernst, W. G., Rumble, D., Maruyama, S. (1998). High-pressure minerals from deeply subducted metamorphic rocks. *Reviews in Mineralogy and Geochemistry* **37**, 33-96.

Liu, J. F., Sun, W. D., Sun, Y., Sun, Y. L., Liu, F. J. (2007). Geochemistry and platinum-group elements of ultramafic rocks from the Songshugou area in the Eastern Qinling: Constraints on petrogenesis. *Geological Review* **53**, 1-8.

Liu, J. F., Sun, Y., Tong, L. X., Sun, W. D. (2009). Emplacement age of the Songshugou ultramafic massif in the Qinling orogenic belt, and geologic implications. *International Geology Review* **51**, 58-76.

Liu, L., Zhou, D. W., Dong, Y. P., Zhang, H. F., Liu, Y. J., Zhang, Z. J. (1995). High pressure metabasites and their retrograde metamorphic P-T-t path from Songshugou area, Eastern Qinling Mountain. *Acta Petrologica Sinica* **11**, 127-136.

Liu, Y. J., Neubauer, F., Genser, J., Takasu, A., Ge, X. H., Handler, R. (2006). $^{40}Ar/^{39}Ar$ ages of blueschist facies pelitic schists from Qingshuigou in the Northern Qilian Mountains, western China. *Island Arc* **15**, 187-198.

Long, M. D. & Silver, P. G. (2008). The subduction zone flow field from seismic anisotropy: a global view. *Science* **319**, 315-318.

Long, M. D. & van der Hilst, R. D. (2005). Upper mantle anisotropy beneath Japan from shear wave splitting. *Physics of the Earth and Planetary Interiors* **151**, 206-222.

Long, M. D. & van der Hilst, R. D. (2006). Shear wave splitting from local events beneath the Ryukyu arc: Trench-parallel anisotropy in the mantle wedge. *Physics of the Earth and Planetary Interiors* **155**, 300-312.

MacDougall, J. G., Kincaid, C., Szwaja, S., Fischer, K. M. (2014). The impact of slab dip variations, gaps and rollback on mantle wedge flow: insights from fluids experiments. *Geophysical Journal International* **197**, 705-730.

MacLeod, C. J. (1994). 20. Structure of the outer Tonga forearc at site 841. *Proceedings of the Ocean Drilling Program, Initial Reports* **135**, 313-329.

Mainprice, D. (1990). A FORTRAN program to calculate seismic anisotropy from the lattice preferred orientation of minerals. *Computers & Geosciences* **16**, 385-393.

Mainprice, D. (2007). Seismic anisotropy of the deep Earth from a mineral and rock physics perspective. In: Schubert, G. (ed.) *Treatise on Geophysics*. Oxford: Elsevier Ltd., 437-492.

Mainprice, D. & Humbert, M. (1994). Methods of calculating petrophysical properties from lattice preferred orientation data. *Surveys in Geophysics* **15**, 575-592.

Mainprice, D. & Ildefonse, B. (2009). Seismic anisotropy of subduction zone minerals–Contribution of hydrous phases. In: Lallemand, S. & Funiciello, F. (eds.) *Subduction Zone Geodynamics*: Springer Berlin Heidelberg, 63-84.

Mainprice, D., Tommasi, A., Couvy, H., Cordier, P., Frost, D. J. (2005). Pressure sensitivity of olivine slip systems and seismic anisotropy of Earth's upper mantle. *Nature* **433**, 731-733.

Manthilake, M. A. G. M., Miyajima, N., Heidelbach, F., Soustelle, V., Frost, D. J. (2013). The effect of aluminum and water on the development of deformation fabrics of orthopyroxene. *Contributions to Mineralogy and Petrology* **165**, 495-505.

Marques, F. O., Schmid, D. W., Andersen, T. B. (2007). Applications of inclusion behaviour models to a major shear zone system: The Nordfjord-Sogn Detachment Zone in western Norway. *Journal of Structural Geology* **29**, 1622-1631.

Maruyama, S., Banno, S., Matsuda, T., Nakajima, T. (1984). Kurosegawa zone and its bearing on the development of the Japanese Islands. *Tectonophysics* **110**, 47-60.

Maruyama, S. & Liou, J. G. (1988). Petrology of Franciscan metabasites along the jadeite-glaucophane type facies series, Cazadero, California. *Journal of Petrology* **29**, 1-37.

Masuda, T., Michibayashi, K., Ohta, H. (1995). Shape preferred orientation of rigid particles in a viscous matrix: reevaluation to determine kinematic parameters of ductile deformation. *Journal of Structural Geology* **17**, 115-129.

Matsubara, M., Obara, K., Kasahara, K. (2009). High-VP/VS zone accompanying non-volcanic tremors and slow-slip events beneath southwestern Japan. *Tectonophysics* **472**, 6-17.

Matsukage, K. N. & Kubo, K. (2003). Chromian spinel during melting experiments of dry peridotite (KLB-1) at 1.0-2.5 GPa. *American Mineralogist* **88**, 1271-1278.

Mauler, A., Burlini, L., Kunze, K., Philippot, P., Burg, J. P. (2000). P-wave anisotropy in eclogites and relationship to the omphacite crystallographic fabric. *Physics and Chemistry of the Earth Part A-Solid Earth and Geodesy* **25**, 119-126.

McCormack, K., Wirth, E. A., Long, M. D. (2013). B-type olivine fabric and mantle wedge serpentinization beneath the Ryukyu arc. *Geophysical Research Letters* **40**, 1697-1702.

McSkimin, H. J., Andreatch, P., Thurston, R. N. (1965). Elastic moduli of quartz versus hydrostatic pressure at 25 °and 195.8 °. *Journal Of Applied Physics* **36**, 1624-1632.

Means, W. D., Hobbs, B. E., Lister, G. S., Williams, P. F. (1980). Vorticity and non-coaxiality in progressive deformations. *Journal of Structural Geology* **2**, 371-378.

Mehl, L., Hacker, B. R., Hirth, G., Kelemen, P. B. (2003). Arc-parallel flow within the mantle wedge: Evidence from the accreted Talkeetna arc, south central Alaska. *Journal of Geophysical Research: Solid Earth* **108**, 1-18.

Melcher, F., Grum, W., Simon, G., Thalhammer, T. V., Stumpfl, E. F. (1997). Petrogenesis of the ophiolitic giant chromite deposits of Kempirsai, Kazakhstan: a study of solid and fluid inclusions in chromite. *Journal of Petrology* **38**, 1419-1458.

Meng, Q.-R. & Zhang, G.-W. (2000). Geologic framework and tectonic evolution of the Qinling orogen, central China. *Tectonophysics* **323**, 183-196.

Merle, R., Kaczmarek, M.-A., Tronche, E., Girardeau, J. (2012). Occurrence of inherited supra-subduction zone mantle in the oceanic lithosphere as inferred from mantle xenoliths from Dragon Seamount (southern Tore–Madeira Rise). *Journal of the Geological Society* **169**, 251-267.

Merlini, A., Grieco, G., Diella, V. (2009). Ferritchromite and Cr-chlorite formation in Kalkan serpentinitic melange (Southern Urals, Russia). *American Mineralogist* **94**, 1459 - 1467.

Meyer, H.-W., Marion, S., Sondergeld, P., Carpenter, M. A., Knight, K. S., Redfern, S. A. T., Dove, M. T. (2001). Displacive components of the low-temperature phase transitions in lawsonite. *American Mineralogist* **86**, 566-577.

Michael, P. (1995). Regionally distinctive sources of depleted MORB: Evidence from trace elements and H2O. *Earth and Planetary Science Letters* **131**, 301-320.

Michibayashi, K., Abe, N., Okamoto, A., Satsukawa, T., Michikura, K. (2006a). Seismic anisotropy in the uppermost mantle, back-arc region of the northeast Japan arc: Petrophysical analyses of Ichinomegata peridotite xenoliths. *Geophysical*

Research Letters **33**, L10312.

Michibayashi, K., Ina, T., Kanagawa, K. (2006b). The effect of dynamic recrystallization on olivine fabric and seismic anisotropy: Insight from a ductile shear zone, Oman ophiolite. *Earth and Planetary Science Letters* **244**, 695-708.

Michibayashi, K., Kusafuka, Y., Satsukawa, T., Nasir, S. J. (2012). Seismic properties of peridotite xenoliths as a clue to imaging the lithospheric mantle beneath NE Tasmania, Australia. *Tectonophysics* **522–523**, 218-223.

Michibayashi, K., Ohara, Y., Stern, R. J., Fryer, P., Kimura, J. I., Tasaka, M., Ishii, T. (2009a). Peridotites from a ductile shear zone within back-arc lithospheric mantle, southern Mariana Trench: Results of a Shinkai 6500 dive. *Geochemistry Geophysics Geosystems* **10**, 17.

Michibayashi, K. & Oohara, T. (2013). Olivine fabric evolution in a hydrated ductile shear zone at the Moho Transition Zone, Oman Ophiolite. *Earth and Planetary Science Letters* **377**, 299-310.

Michibayashi, K., Oohara, T., Satsukawa, T., Ishimaru, S., Arai, S., Okrugin, V. M. (2009b). Rock seismic anisotropy of the low-velocity zone beneath the volcanic front in the mantle wedge. *Geophysical Research Letters* **36**, L12305.

Michibayashi, K., Tasaka, M., Ohara, Y., Ishii, T., Okamoto, A., Fryer, P. (2007). Variable microstructure of peridotite samples from the southern Mariana Trench: Evidence of a complex tectonic evolution. *Tectonophysics* **444**, 111-118.

Mierdel, K., Keppler, H., Smyth, J. R., Langenhorst, F. (2007). Water solubility in aluminous orthopyroxene and the origin of Earth's asthenosphere. *Science* **315**, 364-368.

Miller, R. B. (1988). Fluid flow, metasomatism and amphibole deformation in an imbricated ophiolite, North Cascades, Washington. *Journal of Structural Geology* **10**, 283-296.

Mizukami, T., Wallis, S. R., Yamamoto, J. (2004). Natural examples of olivine lattice preferred orientation patterns with a flow normal a-axis maximum. *Nature* **427**, 432-436.

Mookherjee, M. & Bezacier, L. (2012). The low velocity layer in subduction zone: Structure and elasticity of glaucophane at high pressures. *Physics of the Earth and Planetary Interiors* **208–209**, 50-58.

Mookherjee, M. & Mainprice, D. (2014). Unusually large shear wave anisotropy for chlorite in subduction zone settings. *Geophysical Research Letters* **41**, 1506-1513.

Morales, L. F. G., Mainprice, D., Boudier, F. (2013). The influence of hydrous phases on the microstructure and seismic properties of a hydrated mantle rock. *Tectonophysics* **594**, 103-117.

Morales, L. F. G. & Tommasi, A. (2011). Composition, textures, seismic and thermal anisotropies of xenoliths from a thin and hot lithospheric mantle (Summit Lake,

southern Canadian Cordillera). *Tectonophysics* **507**, 1-15.

Morrison-Smith, D. J. (1976). Transmission electron microscopy of experimentally deformed hornblende. *American Mineralogist* **61**, 272-280.

Mosenfelder, J. L., Deligne, N. I., Asimow, P. D., Rossman, G. R. (2006). Hydrogen incorporation in olivine from 2-12 GPa. *American Mineralogist* **91**, 285-294.

Mosenfelder, J. L. & Rossman, G. R. (2013). Analysis of hydrogen and fluorine in pyroxenes: I. Orthopyroxene. *American Mineralogist* **98**, 1026-1041.

Mungall, J. E. (2002). Roasting the mantle: Slab melting and the genesis of major Au and Au-rich Cu deposits. *Geology* **30**, 915-918.

Nagaya, T., Wallis, S. R., Kobayashi, H., Michibayashi, K., Mizukami, T., Seto, Y., Miyake, A., Matsumoto, M. (2014). Dehydration breakdown of antigorite and the formation of B-type olivine CPO. *Earth and Planetary Science Letters* **387**, 67-76.

Nakajima, J. & Hasegawa, A. (2004). Shear-wave polarization anisotropy and subduction-induced flow in the mantle wedge of northeastern Japan. *Earth and Planetary Science Letters* **225**, 365-377.

Nakajima, J., Shimizu, J., Hori, S., Hasegawa, A. (2006). Shear-wave splitting beneath the southwestern Kurile arc and northeastern Japan arc: A new insight into mantle return flow. *Geophysical Research Letters* **33**.

Nakajima, J., Tsuji, Y., Hasegawa, A. (2009a). Seismic evidence for thermally-controlled dehydration reaction in subducting oceanic crust. *Geophysical Research Letters* **36**, L03303.

Nakajima, J., Tsuji, Y., Hasegawa, A., Kita, S., Okada, T., Matsuzawa, T. (2009b). Tomographic imaging of hydrated crust and mantle in the subducting Pacific slab beneath Hokkaido, Japan: Evidence for dehydration embrittlement as a cause of intraslab earthquakes. *Gondwana Research* **16**, 470-481.

Nazé, L., Doukhan, N., Doukhan, J. C., Latrous, K. (1987). TEM study of lattice defects in naturally and experimentally deformed orthopyroxene. *Bull. Mineral.* **110**, 497-512.

Nesse, W. D. (2004). *Introduction to Optical Mineralogy*. New York: Oxford University Press.

Nishii, A., Wallis, S. R., Mizukami, T., Michibayashi, K. (2011). Subduction related antigorite CPO patterns from forearc mantle in the Sanbagawa belt, southwest Japan. *Journal of Structural Geology* **33**, 1436-1445.

Niu, Y. (1997). Mantle melting and melt extraction processes beneath ocean ridges: Evidence from abyssal peridotites. *Journal of Petrology* **38**, 1047-1074.

Niu, Y. & Hékinian, R. (1997). Basaltic liquids and harzburgitic residues in the Garrett Transform: a case study at fast-spreading ridges. *Earth and Planetary Science Letters* **146**, 243-258.

Nyman, M. W., Law, R. D., Smelik, E. A. (1992). Cataclastic deformation mechanism for the development of core-mantle structures in amphibole. *Geology* **20**, 455-458.

O'Neill, B., Bass, J. D., Rossman, G. R., Geiger, C. A., Langer, K. (1991). Elastic properties of pyrope. *Physics and Chemistry of Minerals* **17**, 617-621.

Oh, C. W. & Liou, J. G. (1998). A petrogenetic grid for eclogite and related facies under high-pressure metamorphism. *Island Arc* **7**, 36-51.

Ohuchi, T., Kawazoe, T., Nishihara, Y., Irifune, T. (2012). Change of olivine a-axis alignment induced by water: Origin of seismic anisotropy in subduction zones. *Earth and Planetary Science Letters* **317**, 111-119.

Ohuchi, T., Kawazoe, T., Nishihara, Y., Nishiyama, N., Irifune, T. (2011). High pressure and temperature fabric transitions in olivine and variations in upper mantle seismic anisotropy. *Earth and Planetary Science Letters* **304**, 55-63.

Okay, A. I. (1984). Distribution and characteristics of the north-west Turkish blueschists. *Geological Society London Special Publications* **17**, 455-466.

Olive, J.-A., Pearce, F., Rondenay, S., Behn, M. D. (2014). Pronounced zonation of seismic anisotropy in the Western Hellenic subduction zone and its geodynamic significance. *Earth and Planetary Science Letters* **391**, 100-109.

Pal, T. (2011). Petrology and geochemistry of the Andaman ophiolite: melt–rock interaction in a suprasubduction-zone setting. *Journal of the Geological Society* **168**, 1031-1045.

Palasse, L. N., Vissers, R. L. M., Paulssen, H., Basu, A. R., Drury, M. R. (2012). Microstructural and seismic properties of the upper mantle underneath a rifted continental terrane (Baja California): An example of sub-crustal mechanical asthenosphere? *Earth and Planetary Science Letters* **345-348**, 60-71.

Park, J. & Levin, V. (2002). Seismic anisotropy: Tracing plate dynamics in the mantle. *Science* **296**, 485-489.

Parkinson, I. J. & Arculus, R. J. (1999). The redox state of subduction zones: insights from arc-peridotites. *Chemical Geology* **160**, 409-423.

Parkinson, I. J. & Pearce, J. A. (1998). Peridotites from the Izu–Bonin–Mariana Forearc (ODP Leg 125): Evidence for Mantle Melting and Melt–Mantle Interaction in a Supra-Subduction Zone Setting. *Journal of Petrology* **39**, 1577-1618.

Parkinson, I. J., Pearce, J. A., Thirlwall, M. F., Johnson, K. T. M., Ingram, G. (1992). 28. Trace element geochemistry of peridotites from the Izu-Bonin-Mariana forearc, Leg 125. *Proceedings of the Ocean Drilling Program, Scientific Results* **125**, 487-506.

Passchier, C. W. (1987). Stable positions of rigid objects in non-coaxial flow—a study in vorticity analysis. *Journal of Structural Geology* **9**, 679-690.

Passchier, C. W. (1988). Analysis of deformation paths in shear zones. *Geologische*

Rundschau **77**, 309-318.

Passchier, C. W. & Sokoutis, D. (1993). Experimental modelling of mantled porphyroclasts. *Journal of Structural Geology* **15**, 895-909.

Paterson, M. S. (1982). The determination of hydroxyl by infrared absorption in quartz, silicate glasses and similar materials. *Bulletin De Mineralogie* **105**, 20-29.

Pawley, A. R. & Allan, D. R. (2001). A high-pressure structural study of lawsonite using angle-dispersive powder-diffraction methods with synchrotron radiation. *Mineralogical Magazine* **65**, 41-58.

Peacock, S. M. (1993). The importance of blueschist → eclogite dehydration reactions in subducting oceanic crust. *Geological Society Of America Bulletin* **105**, 684-694.

Peacock, S. M. & Hyndman, R. D. (1999). Hydrous minerals in the mantle wedge and the maximum depth of subduction thrust earthquakes. *Geophysical Research Letters* **26**, 2517-2520.

Peacock, S. M. & Wang, K. (1999). Seismic consequences of warm versus cool subduction metamorphism: Examples from Southwest and Northeast Japan. *Science* **286**, 937-939.

Pearce, J. A., Barker, P. F., Edwards, S. J., Parkinson, I. J., Leat, P. T. (2000). Geochemistry and tectonic significance of peridotites from the South Sandwich arc–basin system, South Atlantic. *Contributions to Mineralogy and Petrology* **139**, 36-53.

Pearce, J. A., van der Laan, S. R., Arculus, R. J., Murton, B. J., Ishii, T., Peate, D. W., Parkinson, I. J. (1992). 38. Boninite and harzburgite from Leg 125 (Bonin-Mariana Forearc): A case study of magma genesis during the initial stages of subduction. *Proceedings of the Ocean Drilling Program, Scientific Result* **125**, 623-659.

Peslier, A. H. (2010). A review of water contents of nominally anhydrous natural minerals in the mantles of Earth, Mars and the Moon. *Journal of Volcanology and Geothermal Research* **197**, 239-258.

Peslier, A. H. & Luhr, J. F. (2006). Hydrogen loss from olivines in mantle xenoliths from Simcoe (USA) and Mexico: Mafic alkalic magma ascent rates and water budget of the sub-continental lithosphere. *Earth and Planetary Science Letters* **242**, 302-319.

Peslier, A. H., Luhr, J. F., Post, J. (2002). Low water contents in pyroxenes from spinel-peridotites of the oxidized, sub-arc mantle wedge. *Earth and Planetary Science Letters* **201**, 69-86.

Peslier, A. H., Woodland, A. B., Bell, D. R., Lazarov, M., Lapen, T. J. (2012). Metasomatic control of water contents in the Kaapvaal cratonic mantle. *Geochimica et Cosmochimica Acta* **97**, 213-246.

Philippon, M., Gueydan, F., Pitra, P., Brun, J. P. (2013). Preservation of subduction-related prograde deformation in lawsonite pseudomorph-bearing rocks. *Journal of*

Metamorphic Geology **31**, 571-583.

Piazolo, S., Bons, P. D., Passchier, C. W. (2002). The influence of matrix rheology and vorticity on fabric development of populations of rigid objects during plane strain deformation. *Tectonophysics* **351**, 315-329.

Piccardo, G. B., Zanetti, A., Muntener, O. (2007). Melt/peridotite interaction in the Southern Lanzo peridotite: Field, textural and geochemical evidence. *Lithos* **94**, 181-209.

Pognante, U. (1989). Lawsonite, blueschist and eclogite formation in the southern Sesia zone (Western Alps, Italy). *European Journal Of Mineralogy* **1**, 89-104.

Poirier, J. P. (1985). *Creep of crystals : high-temperature deformation processes in metals, ceramics, and minerals* Cambridge, New York: Cambridge University Press.

Poli, S. & Schmidt, M. W. (2002). Petrology of subducted slabs. *Annual Review of Earth and Planetary Sciences* **30**, 207-235.

Powell, R., Holland, T., Worley, B. (1998). Calculating phase diagrams involving solid solutions via non-linear equations, with examples using THERMOCALC. *Journal of Metamorphic Geology* **16**, 577-588.

Précigout, J. & Hirth, G. (2014). B-type olivine fabric induced by grain boundary sliding. *Earth and Planetary Science Letters* **395**, 231-240.

Prior, D. J., Boyle, A. P., Brenker, F., Cheadle, M. C., Day, A., Lopez, G., Peruzzo, L., Potts, G. J., Reddy, S., Spiess, R., Timms, N. E., Trimby, P., Wheeler, J., Zetterstrom, L. (1999). The application of electron backscatter diffraction and orientation contrast imaging in the SEM to textural problems in rocks. *American Mineralogist* **84**, 1741-1759.

Rabbel, W., Koulakov, I., Dinc, A. N., Jakovlev, A. (2011). Arc-parallel shear deformation and escape flow in the mantle wedge of the Central America subduction zone: Evidence from P wave anisotropy. *Geochemistry Geophysics Geosystems* **12**.

Ramachandran, K., Hyndman, R. D., Brocher, T. M. (2006). Regional P wave velocity structure of the Northern Cascadia Subduction Zone. *Journal of Geophysical Research: Solid Earth* **111**, B12301.

Raterron, P., Chen, J., Li, L., Weidner, D., Cordier, P. (2007). Pressure-induced slip-system transition in forsterite: Single-crystal rheological properties at mantle pressure and temperature. *American Mineralogist* **92**, 1436-1445.

Ratschbacher, L., Hacker, B. R., Calvert, A., Webb, L. E., Grimmer, J. C., McWilliams, M. O., Ireland, T., Dong, S., Hu, J. (2003). Tectonics of the Qinling (Central China): Tectonostratigraphy, geochronology, and deformation history. *Tectonophysics* **366**, 1-53.

Rauch, M. & Keppler, H. (2002). Water solubility in orthopyroxene. *Contributions to*

Mineralogy and Petrology **143**, 525-536.

Ravna, E. J. K. & Terry, M. P. (2004). Geothermobarometry of UHP and HP eclogites and schists - an evaluation of equilibria among garnet-clinopyroxene-kyanite-phengite-coesite/quartz. *Journal of Metamorphic Geology* **22**, 579-592.

Reynard, B. & Bass, J. D. (2014). Elasticity of lawsonite and seismological signature of metamorphism and water cycling in the subducting oceanic crust. *Journal of Metamorphic Geology*, 1-9.

Reynard, B., Gillet, P., Willaime, C. (1989). Deformation mechanisms in naturally deformed glaucophanes - a TEM and HREM Study. *European Journal of Mineralogy* **1**, 611-624.

Rondenay, S., Abers, G. A., Van Keken, P. E. (2008). Seismic imaging of subduction zone metamorphism. *Geology* **36**, 275-278.

Rosenberg, C. L. & Handy, M. R. (2001). Mechanisms and orientation of melt segregation paths during pure shearing of a partially molten rock analog (norcamphor–benzamide). *Journal of Structural Geology* **23**, 1917-1932.

Ross, J. V., Avelallemant, H. G., Carter, N. L. (1980). Stress dependence of recrystallized-grain and subgrain size in olivine. *Tectonophysics* **70**, 39-61.

Rossi, G., Abers, G. A., Rondenay, S., Christensen, D. H. (2006). Unusual mantle Poisson's ratio, subduction, and crustal structure in central Alaska. *Journal of Geophysical Research: Solid Earth* **111**, B09311.

Rudnick, R. L. & Fountain, D. M. (1995). Nature and composition of the continental crust: A lower crustal perspective. *Review of Geophysics* **33**, 267-309.

Russo, R. M. & Silver, P. G. (1994). Trench-parallel flow beneath the Nazca Plate from seismic anisotropy. *Science* **263**, 1105-1111.

Ryzhova, T. V., Aleksandrov, K. S., Korobkova, V. M. (1966). The elastic properties of rock-forming minerals V. Additional data on silicates. *Izv. Earth Phys.* **2**, 63-65.

Sambridge, M., Gerald, J. F., Kovács, I., O'Neill, H. S. C., Hermann, J. (2008). Quantitative absorbance spectroscopy with unpolarized light: Part I. Physical and mathematical development. *American Mineralogist* **93**, 751-764.

Satsukawa, T. & Michibayashi, K. (2014). Flow in the uppermost mantle during back-arc spreading revealed by Ichinomegata peridotite xenoliths, NE Japan. *Lithos* **189**, 89-104.

Satsukawa, T., Michibayashi, K., Anthony, E. Y., Stern, R. J., Gao, S. S., Liu, K. H. (2011). Seismic anisotropy of the uppermost mantle beneath the Rio Grande rift: Evidence from Kilbourne Hole peridotite xenoliths, New Mexico. *Earth and Planetary Science Letters* **311**, 172-181.

Satsukawa, T., Michibayashi, K., Raye, U., Anthony, E. Y., Pulliam, J., Stern, R. (2010). Uppermost mantle anisotropy beneath the southern Laurentian margin: Evidence

from Knippa peridotite xenoliths, Texas. *Geophysical Research Letters* **37**, L20312.

Schmidt, M. W. & Poli, S. (1998). Experimentally based water budgets for dehydrating slabs and consequences for arc magma generation. *Earth And Planetary Science Letters* **163**, 361-379.

Scott, T. & Kohlstedt, D. L. (2006). The effect of large melt fraction on the deformation behavior of peridotite. *Earth and Planetary Science Letters* **246**, 177-187.

Shao, T., Ji, S., Kondo, Y., Michibayashi, K., Wang, Q., Xu, Z., Sun, S., Marcotte, D., Salisbury, M. H. (2014). Antigorite-induced seismic anisotropy and implications for deformation in subduction zones and the Tibetan Plateau. *Journal of Geophysical Research: Solid Earth* **119**, 2068-2099.

Shi, R. D., Yang, J. S., Wu, C. L. (2004). First SHRIMP dating for the formation of the Late Sinian Yushigou ophiolite, North Qilian Mountains. *Acta Geologica Sinica* **78**, 649-657.

Siegesmund, S., Helming, K., Kruse, R. (1994). Complete texture analysis of a deformed amphibolite: comparison between neutron diffraction and U-stage data. *Journal of Structural Geology* **16**, 131-142.

Sinogeikin, S. V., Schilling, F. R., Bass, J. D. (2000). Single crystal elasticity of lawsonite. *American Mineralogist* **85**, 1834-1837.

Skemer, P., Katayama, B., Jiang, Z. T., Karato, S. (2005). The misorientation index: Development of a new method for calculating the strength of lattice-preferred orientation. *Tectonophysics* **411**, 157-167.

Skemer, P., Katayama, I., Karato, S. I. (2006). Deformation fabrics of the Cima di Gagnone peridotite massif, Central Alps, Switzerland: evidence of deformation at low temperatures in the presence of water. *Contributions to Mineralogy and Petrology* **152**, 43-51.

Skogby, H. (2006). Water in Natural Mantle Minerals I: Pyroxenes. *Reviews in Mineralogy and Geochemistry* **62**, 155-167.

Skogby, H., Bell, D. R., Rossman, G. R. (1990). Hydroxide in pyroxene: Variations in the natural environment. *American Mineralogist* **75**, 764-774.

Skrotzki, W. (1992). Defect structure and deformation mechanisms in naturally deformed hornblende. *physica status solidi (a)* **131**, 605-624.

Smith, G. P., Wiens, D. A., Fischer, K. M., Dorman, L. M., Webb, S. C., Hildebrand, J. A. (2001). A complex pattern of mantle flow in the Lau backarc. *Science* **292**, 713-716.

Soda, Y. & Takagi, H. (2010). Sequential deformation from serpentinite mylonite to metasomatic rocks along the Sashu Fault, SW Japan. *Journal of Structural Geology* **32**, 792-802.

Soda, Y. & Wenk, H.-R. (2014). Antigorite crystallographic preferred orientations in serpentinites from Japan. *Tectonophysics* **615-616**, 199-212.

Song, S., Niu, Y., Su, L., Xia, X. (2013a). Tectonics of the North Qilian orogen, NW China. *Gondwana Research* **23**, 1378-1401.

Song, S., Su, L., Niu, Y., Zhang, L., Zhang, G. (2007a). Petrological and geochemical constraints on the origin of garnet peridotite in the North Qaidam ultrahigh-pressure metamorphic belt, northwestern China. *Lithos* **96**, 243-265.

Song, S. G., Niu, Y. L., Su, L., Xia, X. H. (2013b). Tectonics of the North Qilian orogen, NW China. *Gondwana Research* **23**, 1378-1401.

Song, S. G., Niu, Y. L., Su, L., Zhang, C., Zhang, L. F. (2014). Continental orogenesis from ocean subduction, continent collision/subduction, to orogen collapse, and orogen recycling: The example of the North Qaidam UHPM belt, NW China. *Earth-science Reviews* **129**, 59-84.

Song, S. G., Niu, Y. L., Zhang, L. F., Wei, C. J., Liou, J. G., Su, L. (2009a). Tectonic evolution of early Paleozoic HP metamorphic rocks in the North Qilian Mountains, NW China: New perspectives. *Journal of Asian Earth Sciences* **35**, 334-353.

Song, S. G., Su, L., Niu, Y. L., Lai, Y., Zhang, L. F. (2009b). CH4 inclusions in orogenic harzburgite: Evidence for reduced slab fluids and implication for redox melting in mantle wedge. *Geochimica Et Cosmochimica Acta* **73**, 1737-1754.

Song, S. G., Su, L., Yang, H. Q., Wang, Y. S. (1998). Petrogenesis and emplacement of the Songshugou peridotite in Shangnan, Shaanxi. *Acta Petrologica Sinica* **14**, 212-221.

Song, S. G., Zhang, L. F., Niu, Y. L. (2004a). Ultra-deep origin of garnet peridotite from the North Qaidam ultrahigh-pressure belt, Northern Tibetan Plateau, NW China. *American Mineralogist* **89**, 1330-1336.

Song, S. G., Zhang, L. F., Niu, Y. L., Song, B., Zhang, G. B., Wang, Q. J. (2004b). Zircon U-Pb SHRIMP ages of eclogites from the North Qilian Mountains in NW China and their tectonic implication. *Chinese Science Bulletin* **49**, 848-852.

Song, S. G., Zhang, L. F., Niu, Y. L., Su, L., Jian, P., Liu, D. Y. (2005). Geochronology of diamond-bearing zircons from garnet peridotite in the North Qaidam UHPM belt, Northern Tibetan Plateau: A record of complex histories from oceanic lithosphere subduction to continental collision. *Earth and Planetary Science Letters* **234**, 99-118.

Song, S. G., Zhang, L. F., Niu, Y. L., Su, L., Song, B. A., Liu, D. Y. (2006). Evolution from oceanic subduction to continental collision: a case study from the Northern Tibetan Plateau based on geochemical and geochronological data. *Journal of Petrology* **47**, 435-455.

Song, S. G., Zhang, L. F., Niu, Y. L., Wei, C. J., Liou, J. G., Shu, G. M. (2007b). Eclogite and carpholite-bearing metasedimentary rocks in the North Qilian suture zone, NW China: implications for early palaeozoic cold oceanic subduction and water

transport into mantle. *Journal of Metamorphic Geology* **25**, 547-563.

Song, T.-R. A. & Kawakatsu, H. (2012). Subduction of oceanic asthenosphere: Evidence from sub-slab seismic anisotropy. *Geophysical Research Letters* **39**, L17301.

Soustelle, V. & Tommasi, A. (2010). Seismic properties of the supra-subduction mantle: Constraints from peridotite xenoliths from the Avacha volcano, southern Kamchatka. *Geophysical Research Letters* **37**, 1-5.

Soustelle, V., Tommasi, A., Bodinier, J. L., Garrido, C. J., Vauchez, A. (2009). Deformation and reactive melt transport in the mantle lithosphere above a large-scale partial melting domain: the Ronda peridotite massif, southern Spain. *Journal of Petrology* **50**, 1235-1266.

Soustelle, V., Tommasi, A., Demouchy, S., Franz, L. (2013). Melt-rock interactions, deformation, hydration and seismic properties in the sub-arc lithospheric mantle inferred from xenoliths from seamounts near Lihir, Papua New Guinea. *Tectonophysics* **608**, 330-345.

Soustelle, V., Tommasi, A., Demouchy, S., Ionov, D. A. (2010). Deformation and fluid–rock interaction in the supra-subduction mantle: Microstructures and water contents in peridotite xenoliths from the Avacha volcano, Kamchatka. *Journal of Petrology* **51**, 363-394.

Spandler, C. & Pirard, C. (2013). Element recycling from subducting slabs to arc crust: A review. *Lithos* **170–171**, 208-223.

Stalder, R. (2004). Influence of Fe, Cr and Al on hydrogen incorporation in orthopyroxene. *European Journal of Mineralogy* **16**, 703-711.

Stalder, R. & Skogby, H. (2002). Hydrogen incorporation in enstatite. *European Journal of Mineralogy* **14**, 1139-1144.

Stern, R. J. (2002). Subduction zones. *Reviews of Geophysics* **40**, 1-42.

Su, L., Song, S. G., Song, B., Zhou, D. W., Hao, J. R. (2004). SHRIMP zircon U-Pb ages of garnet pyroxenite and Fushui gabbroic complex in Songshugou region and constraints on tectonic evolution of Qinling orogenic belt. *Chinese Science Bulletin* **49**, 1146-1157.

Sun, S. S., Ji, S. C., Wang, Q., Xu, Z. Q., Salisbury, M., Long, C. X. (2012). Seismic velocities and anisotropy of core samples from the Chinese Continental Scientific Drilling borehole in the Sulu UHP terrane, eastern China. *Journal of Geophysical Research: Solid Earth* **117**, 1-24.

Sun, S. S., Nesbitt, R. W., Sharaskin, A. Y. (1979). Geochemical characteristics of mid-ocean ridge basalts. *Earth And Planetary Science Letters* **44**, 119-138.

Takahashi, E., Uto, K., Schiling, J. G. (1987). Primary magma compositions and Mg/Fe ratios of their mantle residues along Mid Atlantic Ridge 29 ℃N to 73 ℃N. *Technical Reports ISEI*, 1-4.

Tarney, J., Wood, D. A., Saunders, A. D., Cann, J. R., Varet, J. (1980). Nature of mantle heterogeneity in the North Atlantic: Evidence from deep sea drilling. *Philosophical Transactions of the Royal Society of London. Series A, Mathematical and Physical Sciences* **297**, 179-202.

Tasaka, M., Michibayashi, K., Mainprice, D. (2008). B-type olivine fabrics developed in the fore-arc side of the mantle wedge along a subducting slab. *Earth and Planetary Science Letters* **272**, 747-757.

Tatham, D. J., Lloyd, G. E., Butler, R. W. H., Casey, M. (2008). Amphibole and lower crustal seismic properties. *Earth and Planetary Science Letters* **267**, 118-128.

Tatsumi, Y. (2005). The subduction factory: How it operates in the evolving Earth. *GSA Today* **15**, 4-10.

Terada, T., Hiramatsu, Y., Mizukami, T. (2013). Shear wave anisotropy beneath the volcanic front in South Kyushu area, Japan: Development of C-type olivine CPO under H_2O-rich conditions. *Journal of Geophysical Research: Solid Earth* **118**, 4253-4264.

Teyssier, C., Whitney, D. L., Toraman, E., Seaton, N. C. A. (2010). Lawsonite vorticity and subduction kinematics. *Geology* **38**, 1123-1126.

Tibi, R., Wiens, D. A., Yuan, X. (2008). Seismic evidence for widespread serpentinized forearc mantle along the Mariana convergence margin. *Geophysical Research Letters* **35**, L13303.

Tikoff, B. & Teyssier, C. (1994). Strain and fabric analyses based on porphyroclast interaction. *Journal of Structural Geology* **16**, 477-491.

Tommasi, A., Godard, M., Coromina, G., Dautria, J. M., Barsczus, H. (2004). Seismic anisotropy and compositionally induced velocity anomalies in the lithosphere above mantle plumes: a petrological and microstructural study of mantle xenoliths from French Polynesia. *Earth and Planetary Science Letters* **227**, 539-556.

Tommasi, A., Mainprice, D., Canova, G., Chastel, Y. (2000). Viscoplastic self-consistent and equilibrium-based modeling of olivine lattice preferred orientations: Implications for the upper mantle seismic anisotropy. *Journal of Geophysical Research: Solid Earth* **105**, 7893-7908.

Tommasi, A., Tikoff, B., Vauchez, A. (1999). Upper mantle tectonics: three-dimensional deformation, olivine crystallographic fabrics and seismic properties. *Earth and Planetary Science Letters* **168**, 173-186.

Tommasi, A., Vauchez, A., Godard, M., Belley, F. (2006). Deformation and melt transport in a highly depleted peridotite massif from the Canadian Cordillera: Implications to seismic anisotropy above subduction zones. *Earth and Planetary Science Letters* **252**, 245-259.

Tommasi, A., Vauchez, A., Ionov, D. A. (2008). Deformation, static recrystallization, and reactive melt transport in shallow subcontinental mantle xenoliths (Tok Cenozoic volcanic field, SE Siberia). *Earth and Planetary Science Letters* **272**, 65-

77.

Tsuji, Y., Nakajima, J., Hasegawa, A. (2008). Tomographic evidence for hydrated oceanic crust of the Pacific slab beneath northeastern Japan: Implications for water transportation in subduction zones. *Geophysical Research Letters* **35**, L14308.

Tsujimori, T., Sisson, V. B., Liou, J. G., Harlow, G. E., Sorensen, S. S. (2006). Petrologic characterization of Guatemalan lawsonite eclogite: Eclogitization of subducted oceanic crust in a cold subduction zone. *Geological Society of America Special Papers* **403**, 147-168.

van der Laan, S. R., Arculus, R. J., Pearce, J. A., Murton, B. J. (1992). 10. Petrography, mineral chemistry, and phase relations of the basement boninite series of site 786, Izu-Bonin forearc. *Proceedings of the Ocean Drilling Program, Scientific Result* **125**, 171-201.

Van der Wal, D., Chopra, P., Drury, M., Gerald, J. F. (1993). Relationships between dynamically recrystallized grain size and deformation conditions in experimentally deformed olivine rocks. *Geophysical Research Letters* **20**, 1479-1482.

van Keken, P. E. (2003). The structure and dynamics of the mantle wedge. *Earth and Planetary Science Letters* **215**, 323-338.

Vauchez, A., Tommasi, A., Barruol, G., Maumus, J. (2000). Upper mantle deformation and seismic anisotropy in continental rifts. *Physics and Chemistry of the Earth, Part A: Solid Earth and Geodesy* **25**, 111-117.

Vaughan, M. T. & Guggenheim, S. (1986). Elasticity of muscovite and its relationship to crystal structure. *Journal of Geophysical Research: Solid Earth* **91**, 4657-4664.

Vollmer, F. W. (1990). An application of eigenvalue methods to structural domain analysis. *Geological Society of America Bulletin* **102**, 786-791.

Vonlanthen, P., Kunze, K., Burlini, L., Grobety, B. (2006). Seismic properties of the upper mantle beneath Lanzarote (Canary Islands): Model predictions based on texture measurements by EBSD. *Tectonophysics* **428**, 65-85.

Wölbern, I., Löbl, U., Rümpker, G. (2014). Crustal origin of trench-parallel shear-wave fast polarizations in the Central Andes. *Earth and Planetary Science Letters* **392**, 230-238.

Wagner, L. S., Anderson, M. L., Jackson, J. M., Beck, S. L., Zandt, G. (2008). Seismic evidence for orthopyroxene enrichment in the continental lithosphere. *Geology* **36**, 935-938.

Wagner, L. S., Fouch, M. J., James, D. E., Long, M. D. (2013). The role of hydrous phases in the formation of trench parallel anisotropy: Evidence from Rayleigh waves in Cascadia. *Geophysical Research Letters* **40**, 2642-2646.

Wallis, S. (1995). Vorticity analysis and recognition of ductile extension in the Sanbagawa belt, SW Japan. *Journal of Structural Geology* **17**, 1077-1093.

Wallis, S. R., Platt, J. P., Knott, S. D. (1993). Recognition of syn-convergence extension in accretionary wedges with examples from the Calabrian Arc and the Eastern Alps. *American Journal Of Science* **293**, 463-494.

Wang, H. & Simmons, G. (1974). Elasticity of some mantle crystal structures 3. spessartite-almandine garnet. *Journal of Geophysical Research: Solid Earth* **79**, 2607-2613.

Wang, J. & Zhao, D. (2010). Mapping P-wave anisotropy of the Honshu arc from Japan Trench to the back-arc. *Journal of Asian Earth Sciences* **39**, 396-407.

Wang, J. & Zhao, D. P. (2008). P-wave anisotropic tomography beneath Northeast Japan. *Physics of the Earth and Planetary Interiors* **170**, 115-133.

Wang, Q., Burlini, L., Mainprice, D., Xu, Z. Q. (2009). Geochemistry, petrofabrics and seismic properties of eclogites from the Chinese Continental Scientific Drilling boreholes in the Sulu UHP terrane, eastern China. *Tectonophysics* **475**, 251-266.

Wang, Q., Ji, S., Salisbury, M. H., Xia, B., Pan, M., Xu, Z. (2005a). Shear wave properties and Poisson's ratios of ultrahigh-pressure metamorphic rocks from the Dabie-Sulu orogenic belt, China: Implications for crustal composition. *Journal of Geophysical Research* **110**, B08208.

Wang, Q., Xia, Q. K., O'Reilly, S. Y., Griffin, W. L., Beyer, E. E., Brueckner, H. K. (2013a). Pressure- and stress-induced fabric transition in olivine from peridotites in the Western Gneiss Region (Norway): implications for mantle seismic anisotropy. *Journal of Metamorphic Geology* **31**, 93-111.

Wang, X. B., Yang, J. S., Shi, R. D., Chen, S. Y. (2005b). The Songshugou rock body from Qinling - A example of ultramafic cumulate undergone amphibole facies metamorphism. *Acta Geologica Sinica* **79**, 174-189.

Wang, Y. F., Zhang, J. F., Shi, F. (2013b). The origin and geophysical implications of a weak C-type olivine fabric in the Xugou ultrahigh pressure garnet peridotite. *Earth and Planetary Science Letters* **376**, 63-73.

Warner, M. & McGeary, S. (1987). Seismic reflection coefficients from mantle fault zones. *Geophysical Journal of the Royal Astronomical Society* **89**, 223-230.

Warner, M., Morgan, J., Barton, P., Morgan, P., Price, C., Jones, K. (1996). Seismic reflections from the mantle represent relict subduction zones within the continental lithosphere. *Geology* **24**, 39-42.

Warren, J. M. & Hauri, E. H. (2014). Pyroxenes as tracers of mantle water variations. *Journal of Geophysical Research: Solid Earth*, n/a-n/a.

Warren, J. M., Hirth, G., Kelemen, P. B. (2008). Evolution of olivine lattice preferred orientation during simple shear in the mantle. *Earth and Planetary Science Letters* **272**, 501-512.

Wei, C. J. & Song, S. G. (2008). Chloritoid-glaucophane schist in the north Qilian orogen, NW China: phase equilibria and P-T path from garnet zonation. *Journal*

of Metamorphic Geology **26**, 301-316.

Wei, C. J., Yang, Y., Su, X. L., Song, S. G., Zhang, L. F. (2009). Metamorphic evolution of low-*T* eclogite from the North Qilian orogen, NW China: evidence from petrology and calculated phase equilibria in the system NCKFMASHO. *Journal of Metamorphic Geology* **27**, 55-70.

Wenk, H. R., Bennett, K., Canova, G. R., Molinari, A. (1991). Modelling plastic deformation of peridotite with the self-consistent theory. *Journal of Geophysical Research: Solid Earth* **96**, 8337-8349.

Whitney, D. L. & Evans, B. W. (2010). Abbreviations for names of rock-forming minerals. *American Mineralogist* **95**, 185-187.

Wintsch, R. P. & Yi, K. (2002). Dissolution and replacement creep: a significant deformation mechanism in mid-crustal rocks. *Journal of Structural Geology* **24**, 1179-1193.

Withers, A. C. (2013). On the use of unpolarized infrared spectroscopy for quantitative analysis of absorbing species in birefringent crystals. *American Mineralogist* **98**, 689-697.

Withers, A. C., Bureau, H., Raepsaet, C., Hirschmann, M. M. (2012). Calibration of infrared spectroscopy by elastic recoil detection analysis of H in synthetic olivine. *Chemical Geology* **334**, 92-98.

Wu, H. Q., Feng, Y. M., Song, S. G. (1993). Metamorphism and deformation of blueschist belts and their tectonic implications, North Qilian Mountains, China. *Journal of Metamorphic Geology* **11**, 523-536.

Xia, Q.-K., Hao, Y., Li, P., Deloule, E., Coltorti, M., Dallai, L., Yang, X., Feng, M. (2010). Low water content of the Cenozoic lithospheric mantle beneath the eastern part of the North China Craton. *Journal of Geophysical Research* **115**, B07207.

Xu, Z. Q., Chen, J., Wang, Q., Zeng, L. S., Yang, J. S., Chen, F. Y., Li, T. F., Liang, F. H. (2005). Type-C olivine fabric in the Zhimafang garnet peridotite of the southern Sulu ultrahigh-pressure metamorphic terrane: Formation conditions and tectonic implications. *Acta Petrologica Sinica* **21**, 389-397.

Yang, J. J. & Powell, R. (2008). Ultrahigh-pressure garnet peridotites from the devolatilization of sea-floor hydrated ultramafic rocks. *Journal of Metamorphic Geology* **26**, 695-716.

Yang, X., Fischer, K. M., Abers, G. A. (1995). Seismic anisotropy beneath the Shumagin Islands segment of the Aleutian-Alaska subduction zone. *Journal of Geophysical Research: Solid Earth* **100**, 18165-18177.

Yang, Y., Xia, Q. K., Feng, M., Liu, S. C. (2012). OH in natural orthopyroxene: an in situ FTIR investigation at varying temperatures. *Physics and Chemistry of Minerals* **39**, 413-418.

Yin, A., Dang, Y. Q., Zhang, M., Chen, X. H., McRivette, M. W. (2008). Cenozoic

tectonic evolution of the Qaidam basin and its surrounding regions (Part 3): Structural geology, sedimentation, and regional tectonic reconstruction. *Geological Society of America Bulletin* **120**, 847-876.

Zaffarana, C., Tommasi, A., Vauchez, A., Grégoire, M. (2014). Microstructures and seismic properties of south Patagonian mantle xenoliths (Gobernador Gregores and Pali Aike). *Tectonophysics* **621**, 175-197.

Zhang, B., Matsuzaki, T., Wu, X. (2013). Water solubility in orthopyroxene: Dependence on temperature and Al content. *Chinese Science Bulletin*, 1-8.

Zhang, J. F., Green, H. W., Bozhilov, K. N. (2006). Rheology of omphacite at high temperature and pressure and significance of its lattice preferred orientations. *Earth and Planetary Science Letters* **246**, 432-443.

Zhang, J. F., Wang, Y. F., Jin, Z. M. (2008). CPO-induced seismic anisotropy in UHP eclogites. *Science in China Series D-Earth Sciences* **51**, 11-21.

Zhang, J. X. & Meng, F. C. (2006). Lawsonite-bearing eclogites in the north Qilian and north Altyn Tagh: Evidence for cold subduction of oceanic crust. *Chinese Science Bulletin* **51**, 1238-1244.

Zhang, J. X., Meng, F. C., Wan, Y. S. (2007). A cold Early Palaeozoic subduction zone in the North Qilian Mountains, NW China: Petrological and U-Pb geochronological constraints. *Journal of Metamorphic Geology* **25**, 285-304.

Zhang, J. X., Xu, Z. Q., Chen, W., Xu, H. F. (1997). A tentative discussion on the ages of the subduction - accretionary complex/volcanic arcs in the Middle sector of North Qilian Mountain. *Acta Petrologica et Mineralogica* **16**, 112-119.

Zhang, L. F., Wang, Q. J., Song, S. G. (2009). Lawsonite blueschist in Northern Qilian, NW China: P-T pseudosections and petrologic implications. *Journal of Asian Earth Sciences* **35**, 354-366.

Zhang, S. Q. & Karato, S. (1995). Lattice preferred orientation of olivine aggregates deformed in simple shear. *Nature* **375**, 774-777.

Zhang, S. Q., Karato, S., Fitz Gerald, J. D., Faul, U. H., Zhou, Y. (2000). Simple shear deformation of olivine aggregates. *Tectonophysics* **316**, 133-152.

Zhang, Z. J. (1995). The genesis of dunites in the Songshugou ultramafic rock body, North Qinling. *Acta Petrologica Sinica* **11**, 178-189.

Zhao, D. (2004). Global tomographic images of mantle plumes and subducting slabs: insight into deep Earth dynamics. *Physics of the Earth and Planetary Interiors* **146**, 3-34.

Zhao, D. P. (2001). Seismological structure of subduction zones and its implications for arc magmatism and dynamics. *Physics of the Earth and Planetary Interiors* **127**, 197-214.

Zhao, D. P. (2012). Tomography and dynamics of western-Pacific subduction zones.

Monogr. Environ. Earth Planets **1**, 1-70.

Zhou, M.-f., Robinson, P. T., Malpas, J., Edwards, S. J., Qi, L. (2005). REE and PGE Geochemical Constraints on the Formation of Dunites in the Luobusa Ophiolite, Southern Tibet. *Journal of Petrology* **46**, 615-639.

Zhou, M. F., Robinson, P. T., Bai, W. J. (1994). Formation of podiform chromitites by melt/rock interaction in the upper mantle. *Mineralium Deposita* **29**, 98-101.

Zhou, M. F., Robinson, P. T., Malpas, J., Li, Z. J. (1996). Podiform chromitites in the Luobusa ophiolite (Southern Tibet): Implications for melt-rock interaction and chromite segregation in the upper mantle. *Journal of Petrology* **37**, 3-21.

Zucali, M., Chateigner, D., Dugnani, M., Lutterotti, L., Ouladdiaf, B. (2002). Quantitative texture analysis of glaucophanite deformed under eclogite facies conditions (Sesia-Lanzo Zone, Western Alps): comparison between X-ray and neutron diffraction analysis. *Geological Society London Special Publications* **200**, 239-253.

ABSTRACT (IN KOREAN) 국문초록

과거 섭입대였던 두 지역(중국 North Qilian 조산운동대와 Qinling 조산운동대)에서 채취한 청색편암, 에클로자이트, 그리고 맨틀 감람암의 변형 미세구조와 암석구조 분석 및 지화학 분석을 통하여, 섭입대 환경하에서 지구의 동역학적 과정들과 지진파 비등방성을 이해하고자 하였다. 암질과 변형 정도가 각각 다른 청색편암과 에클로자이트에서 계산한 지진파 특성들은 다음과 같은 사실을 지시한다. (1) 청색편암과 엽리가 잘 발달된 에클로자이트들은 지진파 비등방성이 크며, 괴상의 에클로자이트와 감람암들과 비교할 때 대략 3-12% 낮은 지진파 속도를 가진다. 이를 통하여 상부 지진파 저속도층의 점진적인 감소와 섭입 깊이에 따른 지진파 비등방성의 소실을 설명할 수 있다. (2) 해구에 평행한 방향의 지진파 비등방성은 큰 각도로 (> 45–60°) 섭입하는 해양지각에 의하여 야기될 수 있고, 그에 따른 지연시간은 0.03–0.09 초 (괴상 로소나이트 청색편암의 최저값) 에서 0.1–0.3 초 (엽리가 잘 발달된 녹렴석 청색편암의 최대값) 정도이다. (3) 청색편암과 에클로자이트의 지진파 반사 계수 차이가 매우 크기 때문에 (R_c = 0.04–0.20), 얕은 깊이의 청색편암 위주의 부가체 안에 있는 거대한 에클로자이트 암괴가 고분해능 지진파 반사 실험을 통하여 관찰될 가능성이 있다. 맨틀 감람암의 경우 North Qilian 조산운동대와 Qinling 조산운동대에서의 전호 암석권 맨틀에서 ~25-30% 정도의 부분용융 이후에 남은 내열성의 잔여물들로, 하즈버자이트와 더나이트에

해당하며 B, C, A-/D-타입과 같은 다양한 감람석 암석조직이 관찰된다. 다수에 해당하는 A-/D-타입 감람석 암석조직은 해구에 평행한 방향의 지진파 비등방성을 약화시키고, 전호 맨틀에서의 사문석화 작용과 관련된 지진파 특성에 영향을 준다. 반면에, 물이 많은 환경에서 만들어지는 C-타입과 B-타입 감람석 암석조직의 경우 각각 저응력 고온 환경과 고응력 고온 환경에서 발달된다고 알려져있다. C-타입에서 B-타입으로의 감람석 암석조직의 변화는, 섭입대의 맨틀웨지에서 해구방향으로 생기는 삭박작용과 냉각 작용으로 인해 생길 수 있는, 빠른 지진전단파의 편광 방향이 해구에 수직한 방향에서 해구에 평행한 방향으로의 변화를 반영한다. 그러나 전호 맨틀의 발달과정 중에서 물이 많은 환경(B-, C-타입)과 물이 적은 환경(A-, D-타입)에서의 감람석 암석조직 사이의 포괄적인 관계에 대해서는 아직 모호한 부분이 있고, 앞으로 좀 더 실험실에서 암석의 미세구조 연구와 야외 지질조사가 추가되어야 할 것이다.

……..

주요어: 청색편암, 에클로자이트, 감람암, 연성 변형, 섭입대, 지진파 특성

학번: 2011-31268